



Terms and Conditions of Use of Digitised Theses from Trinity College Library Dublin

Copyright statement

All material supplied by Trinity College Library is protected by copyright (under the Copyright and Related Rights Act, 2000 as amended) and other relevant Intellectual Property Rights. By accessing and using a Digitised Thesis from Trinity College Library you acknowledge that all Intellectual Property Rights in any Works supplied are the sole and exclusive property of the copyright and/or other IPR holder. Specific copyright holders may not be explicitly identified. Use of materials from other sources within a thesis should not be construed as a claim over them.

A non-exclusive, non-transferable licence is hereby granted to those using or reproducing, in whole or in part, the material for valid purposes, providing the copyright owners are acknowledged using the normal conventions. Where specific permission to use material is required, this is identified and such permission must be sought from the copyright holder or agency cited.

Liability statement

By using a Digitised Thesis, I accept that Trinity College Dublin bears no legal responsibility for the accuracy, legality or comprehensiveness of materials contained within the thesis, and that Trinity College Dublin accepts no liability for indirect, consequential, or incidental, damages or losses arising from use of the thesis for whatever reason. Information located in a thesis may be subject to specific use constraints, details of which may not be explicitly described. It is the responsibility of potential and actual users to be aware of such constraints and to abide by them. By making use of material from a digitised thesis, you accept these copyright and disclaimer provisions. Where it is brought to the attention of Trinity College Library that there may be a breach of copyright or other restraint, it is the policy to withdraw or take down access to a thesis while the issue is being resolved.

Access Agreement

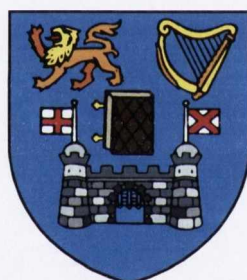
By using a Digitised Thesis from Trinity College Library you are bound by the following Terms & Conditions. Please read them carefully.

I have read and I understand the following statement: All material supplied via a Digitised Thesis from Trinity College Library is protected by copyright and other intellectual property rights, and duplication or sale of all or part of any of a thesis is not permitted, except that material may be duplicated by you for your research use or for educational purposes in electronic or print form providing the copyright owners are acknowledged using the normal conventions. You must obtain permission for any other use. Electronic or print copies may not be offered, whether for sale or otherwise to anyone. This copy has been supplied on the understanding that it is copyright material and that no quotation from the thesis may be published without proper acknowledgement.

Single-Walled Carbon Nanotubes and Photo Switchable Spiroyrans: Novel Multifunctional Platforms for Sensing and Biological Applications

By

Elisa Del Canto



A thesis submitted to the University of Dublin, Trinity College
for the degree of Doctor of Philosophy.

School of Chemistry
September 2011
University of Dublin
Trinity College

Declaration

This thesis is submitted by the undersigned to the University of Dublin, Trinity College for the examination of Doctorate of Philosophy. Except as otherwise stated, this thesis is entirely my own work and has not been submitted as an exercise for a degree to any other university. I agree that the library may lend or copy this thesis freely on request.



Thesis 9710



List of Abbreviations

AA	Amino acid
AFM	Atomic Force Microscopy
ATR FT-IR	Attenuated Total Reflectance Fourier Transform Infra Red
Boc	Tert-butoxycarbonyl group
CNTs	Carbon Nanotubes
CVD	Chemical vapour deposition
D-TGA	Differential Thermogravimetric Analysis
DCM	Dichloromethane
DDS	Drug delivery system
DMF	<i>N, N</i> -dimethylformamide
DOS	Density of states
DWNTs	Double Walled Carbon Nanotubes
EDC·HCl	<i>N</i> -Ethyl- <i>N'</i> -(3-dimethylaminopropyl)carbodiimide hydrochloride
EtOH	Ethanol
Et ₂ O	Diethyl ether
f-SWNTs	Functionalized SWNTs
HiPco	High pressure CO
m	metallic SWNTs
ME	Merocyanine
MeOH	Methanol
MWNTs	Multi Walled Carbon Nanotubes
NHS	<i>N</i> -Hydroxysuccinimide
NMP	1-Methyl-2-pyrrolidinone
NP	Nanoparticle
o-SWNTs	Oxidized SWNTs
p-SWNTs	Purified SWNTs
RBM	Radial breathing mode
s	semiconducting SWNTs
SDBS	Sodium dodecylbenzenesulfonate
SP	Spiropyran
SWNTs	Single Walled Carbon Nanotubes

TEM	Transmission Electron Microscopy
TGA	Thermogravimetric analysis
TFA	Trifluoroacetic acid
UV	Ultraviolet
UV-Vis	Ultraviolet-visible
UV-Vis/NIR	Ultraviolet-visible-near infrared

Summary

Over the last years the applications of chemically modified carbon nanotubes have considerably expanded and progressed in both material and biomedical science. A vast number of SWNTs based materials have been rationally designed and synthesized to combine specific properties of different matters in a single nanoplatform. However, there is still plenty of room for the realization of smart SWNTs composites constituted by molecular devices able to respond to external stimuli with a degree of “intelligence”.

The main aim of this work involves the synthesis and characterization of covalently chemical functionalized single-walled carbon nanotubes (SWNTs) using both defect site and sidewall approaches, in order to develop a material with high solvent dispersibility, suitable for bio applications, and with an elevated number of functional groups on its surface. The latter are utilized as anchors for spiropyran (SP) photoswitchable molecules, which provide “intelligence” to the nanotube scaffold when suitably stimulated. The new photoresponsive SWNTs based receptors are expected to find applications in sensing and drug delivery systems.

Chapter 1 depicts an overview of (1) SWNTs properties, chemical reactivity and covalent functionalization of their defect sites and sidewalls, (2) concept of molecular switches with particular interest to SP photoresponsive molecules, (3) examples of SP on solid state and on SWNTs scaffolds, (4) SP based receptors for metal ions and organic molecules, and finally (5) bioactive molecules on SWNTs for applications in drug delivery systems. This chapter also includes aims of this project and a description of the techniques used to fully characterize the nanotube materials.

In Chapter 2, the preparation and full characterization of SWNTs covalently functionalized with a photo-switchable molecular sensor are reported. After the purification, shortening and tip oxidation of the nanotube material polyethylene glycol (PEG) linker and spiropyran (SP) photochromes are introduced *via* amide coupling procedure. The enrichment of the SWNTs with SP results in light modulated photo-switchable nanocomposite with envisaged sensing properties.

Recent reports have questioned the effective covalent functionalization of the SWNT surface and in Chapter 3 this important question is answered. The investigation onto the effect of NaOH treatment and solvent washing on the functionalization, optical/electronic properties and behavior of chemically modified SWNTs are reported. It is demonstrated how using a well known 2-step purification/oxidation procedure, in the absence of NaOH treatment, COOH functionality is introduced directly onto SWNTs, and not only onto carbonaceous material present in the sample. Moreover, the functionalized materials still exhibit their distinctive optical/electronic properties, as demonstrated by sustained structured spectroscopic absorption and emission features.

Chapter 4 focuses on the development of a multifunctional SWNT-SP nanomaterial, where the nanotubes act as selective intracellular carriers of spiropyran molecules that behave as photo-responsive and selective receptors for metal ions and small organic molecules. In order to ensure a higher degree of photoactive groups in the nanomaterial, the SWNTs are here sidewall functionalized by Tour reaction and further reacted with PEG linker and photo-switchable SP derivative. The light modulated reversible chelation of zinc and acetylsalicylic acid by the SP derivative is reported. In the light of the preliminary results illustrated the SP-SWNTs system can be considered as a promising caging platform and light modulated delivery carrier of biologically important ions and molecules.

Chapter 5 provides a detailed description of the general methods and experimental procedures that have been used in this work.

Finally, in Chapter 6 conclusions and future outlook for our project are reported.

Overall, we believe that this research should contribute to further development of novel smart drug delivery systems based on light responsive covalently modified SWNTs composites.

Acknowledgements

I wish to thank my supervisor Dr. Silvia Giordani for her guidance and invaluable assistance in making this research possible. To the Giordani group both past and present: Manuel, Kevin, Laura, Dania, Ilona, Gabor, Lyn, Sonia, and Jyotiranjana for the tireless help and precious support, and for making this experience unique. I would like to sincerely thank Dr. Tatiana Perova for the help with Raman Spectroscopy and for her kindness, Dr. Juan Camacho (Intel), Dr. Paula Colavita and Dr. Eoin Scanlan for fruitful discussions. To Dr. Manuel Ruther, Dr. John O'Brien and Dr. Martin Feeney for the instrument trainings and their precious assistance with NMR and Mass Spectrometry. I'm really grateful to IRCSET, Intel, Science Foundation Ireland and Trinity College Dublin for the financial support.

Table of Contents

Declaration	II
List of Abbreviations	III
Summary	V
Acknowledgements	VII

Chapter 1. Introduction

1.1	Introduction to carbon nanotubes	2
1.2	Structural properties of CNTs	3
1.3	Physical structure and electronic-optical properties of SWNTs	4
1.4	Chemical reactivity of SWNTs	8
1.5	Chemical modification of SWNTs	11
1.5.1	Covalent functionalization of SWNT: defect site chemistry	13
1.5.2	Covalent functionalization of SWNT: sidewall chemistry	16
1.6	Photoresponsive switchable molecules: spiropyrans	18
1.7	SP on solid state	21
1.8	SP and SWNTs	24
1.9	SP based photoswitchable receptors	27
1.10	SP based receptors for organic molecules	30
1.11	SP-metal complex based receptors for organic molecules	33
1.12	Bioactive organic molecules on SWNTs	36
1.13	Aims of this work	41
1.14	Characterization techniques of SWNTs	43
1.14.1	Thermal gravimetric analysis (TGA)	44
1.14.2	Fourier transform infrared spectroscopy (FT-IR)	45
1.14.3	Raman spectroscopy	46
1.14.4	Ultraviolet-visible (UV-Vis) and ultraviolet-visible-near infrared (UV-Vis/NIR) absorption spectroscopy	48
1.14.5	Near infrared photoluminescence (NIR-PL) spectroscopy	49

1.14.6 Atomic force microscopy (AFM) and transmission electron microscopy (TEM)	49
References	50

Chapter 2. Functionalization of Single-Walled Carbon Nanotubes with Optically Switchable Spiroprans 62

2.1	Introduction	63
2.2	Purification, oxidation and covalent functionalization of SWNTs with PEG linker and spiroprans	64
2.3	Characterization of chemically modified SWNTs	68
	2.3.1 Thermogravimetric analysis and TEM images	68
	2.3.2 FT-IR spectroscopy analysis	71
	2.3.3 Micro Raman spectroscopy analysis	72
	2.3.4 Raman mapping analysis	77
	2.3.5 Atomic force microscopy analysis	78
	2.3.6 UV-Vis/NIR absorbance spectroscopy analysis	79
2.4	On-off switching of SWNTs functionalized with spiropran molecules	80
2.5	Conclusions	83
	References	84

Chapter 3. Critical Investigation of Defect Site Functionalization on Single-Walled Carbon Nanotubes 87

3.1	Introduction	88
3.2	Purification and oxidation of SWNTs	90
3.3	Characterization of purified and oxidized SWNTs	92
	3.3.1 FT-IR spectroscopy analysis	92
	3.3.2 Raman spectroscopy analysis	94
	3.3.3 X-ray photoelectron spectroscopy analysis	95
	3.3.4 NIR-PL and UV-Vis/NIR absorption spectroscopies analysis	97

3.3.5 Thermogravimetric analysis	100
3.3.6 Transmission electron microscopy analysis	102
3.3.7 Atomic force microscopy analysis	103
3.4 Functionalization with fluorescent probe	105
3.5 Spectroscopic analysis of functionalized SWNTs	106
3.6 Microscopic analysis of functionalized SWNTs	110
3.7 Conclusions	111
References	112

**Chapter 4. Single-Walled Carbon Nanotubes as Nanovectors
for Biologically Active Metal Cations and Molecules** 115

4.1 Introduction	116
4.2 Purification and Tour reaction on SWNTs	118
4.3 Functionalization of SWNTs with PEG linker and spiropyrans	119
4.4 Characterization of purified and functionalized SWNTs	120
4.4.1 Thermogravimetric analysis and TEM images	120
4.4.2 FT-IR spectroscopy analysis	123
4.4.3 Raman spectroscopy analysis	125
4.4.4 Atomic force microscopy analysis	126
4.5 On-off switching of SWNTs functionalized with spiropyran molecules	128
4.6 Merocyanine/metal/NSAID complex formation studies	132
4.6.1 NMR and mass spectrometry	132
4.6.2 Absorption and emission spectroscopies	135
4.7 Reversible chelation of zinc by SP f-SWNTs	139
4.8 Epifluorescence microscopy images of SP f-SWNTs	144
4.9 Conclusions	145
References	146

5.1	General Procedures	150
5.2	Experimental for Chapter 2	154
5.2.1	Materials	154
5.2.2	Preparation of o-SWNT (1)	154
5.2.3	Preparation of tert-Butyl 3-(2-(2-(3-aminopropoxy)ethoxy) ethoxy)propylcarbamate (2)	155
5.2.4	Preparation of f-SWNTs (3)	156
5.2.5	Preparation of SP (4)	157
5.2.6	Preparation of f-SWNTs (5)	157
5.3	Experimental for Chapter 3	158
5.3.1	Materials	158
5.3.2	NIR-PL measurements and efficiency calculation	158
5.3.3	Preparation of purified single walled carbon nanotubes p-SWNTs	159
5.3.4	Preparation of oxidized single walled carbon nanotubes o-SWNTs [2]	160
5.3.5	Preparation of base treated purified single walled carbon nanotubes b-SWNTs	161
5.3.6	Preparation of oxidized single walled carbon nanotubes o-SWNTs [1]	161
5.3.7	Preparation of fluorescein functionalized single walled carbon nanotubes f-SWNTs [1]	162
5.3.8	Preparation of fluorescein functionalized single walled carbon nanotubes f-SWNTs [2]	163
5.3.9	Preparation of base treated oxidized single walled carbon nanotubes ob-SWNTs	163
5.4	Experimental for Chapter 4	164
5.4.1	Materials	164
5.4.2	Preparation of purified single walled carbon nanotubes p-SWNTs	164
5.4.3	Preparation of benzoic acid functionalized single walled carbon nanotubes f-SWNTs (1)	166

5.4.4	Preparation of PEG functionalized single walled carbon nanotubes f-SWNTs (2)	167
5.4.5	Preparation of spiropyran functionalized single walled carbon nanotubes f-SWNTs (3)	168
5.4.6	Preparation of SP (5)	169
5.4.7	Characterization of SP (6)	170
5.4.8	NMR studies	171
5.4.9	Mass spectrometry	171
5.4.10	Dispersion of SP f-SWNTs (3)	172
5.4.11	Cell culture	172
5.4.12	Incubation with SP f-SWNTs (3) dispersions	172
	References	173
 Chapter 6. Conclusions and Future Work		174
<hr/>		
6.1	Conclusions	175
6.2	Future work	176
 Chapter 7. Appendix		177
<hr/>		
7.1	Appendix for Chapter 3	178
7.2	Appendix for Chapter 4	182
	7.2.1 ME-Zn complex formation	187
	7.2.2 ME and ASA: no interaction	188
	7.2.3 ASA and Zn ²⁺ metal ion complex formation	189
	7.2.4 ME-Zn-ASA complex formation	191
	7.2.5 SP switchability and Zn ²⁺ chelation in Cl ₂ Bz/CH ₃ CN 9:1	194
 List of Publications, Conference Abstracts and Presentations		196
<hr/>		

List of Figures, Schemes and Tables

Chapter 1. Introduction

Table 1.1: Properties of carbon nanotubes (CNTs).

Figure 1.1: Pictorial representation of SWNT, DWNT and MWNT structures.

Figure 1.2: Graphene honeycomb lattice, chiral vector \vec{C}_h and chiral angle θ .

Figure 1.3: Structural and electronic variety of SWNTs: metallic armchair (5,5) and semiconducting zigzag (10,0) nanotubes.

Figure 1.4: Top] Schematic representation of the density of states (DOS) of HiPco SWNTs contributing to the UV-Vis/NIR absorption. Metallic SWNT: M_{11} is the first metallic transition. Semiconducting SWNT: S_{11} and S_{22} correspond to the first and second interband transitions. Valid for small diameter SWNTs. Bottom] Metal (M_{11}) and semiconductor (S_{11} , S_{22}) transitions in the UV-Vis/NIR absorption spectrum of purified SWNTs (p-SWNTs) dispersed in DMF.

Figure 1.5: UV-Vis/NIR absorption spectra of purified (p-SWNTs) and functionalized (f-SWNTs) nanotubes in DMF showing the loss of structure upon high degree of functionalization.

Figure 1.6: Optical characterization of a HiPco SWNT fraction [Image from ref.59].

Figure 1.7: A] Ideal SWNT structure. B] Typical defects in a SWNT [Image adapted from ref.13]. Intact sidewall, end cap and defects are marked with grey, red and green arrows respectively.

Figure 1.8: π -orbital misalignment angles (ϕ) in the side-wall and in the fullerene like end cap of a (5,5) SWNT [Image from ref.4].

Figure 1.9: Graphical illustrations of non-covalent and covalent chemical modifications of SWNTs.

Figure 1.10: Possible effect of acid-oxidizing purification treatments on the SWNTs morphology.

Figure 1.11: Examples of amidation and esterification reactions on shortened SWNTs bearing carboxylic acid groups. NHS=N-Hydroxysuccinimide, EDC=N-Ethyl-N'-(3-dimethylaminopropyl)carbodiimide, HOBt=N-Hydroxybenzotriazole.

Figure 1.12: Schematic describing some examples of sidewall chemical enrichment of SWNTs.

Figure 1.13: Derivatization approach by aryl diazonium salt additions on SWNTs. ER=electrochemical reduction, IL= ionic liquids.

Figure 1.14: Examples of absorbance patterns in a photochromic process.

Figure 1.15: Structures and switching mechanisms between different electronic configurations of some photochromic compounds.

Figure 1.16: Left] Photo interconversion between the closed (SP) and the open (ME) form of a spiropyran. Right] Absorption spectra of a SP solution before (black line), after irradiation with UV light (wine line) and after storage in the dark (grey line).

Figure 1.17: Examples of SP integrated hybrid materials. A] Fluorescence spectra of organogel formed with LMWG and SP (A), after UV light irradiation for 30 s (B) and 10 min (C), and further visible light irradiation [Image from ref.147]. B] Silylation of hydroxyethyl-SP.¹⁵³ C] Coupling of SP with the Wang resin [Image from ref.154]. D] Light-induced fluorescence modulation of a NP containing a fluorescent dye (NBD) and a SP [Image from ref.157]. E] Modulation of the optical properties of SP-CdSe/ZnS nanocrystals solutions by cycles of UV and Vis irradiation [Images from ref.166].

Figure 1.18: Switches on tubes. A] Photoinduced interconversion of SPO between spiro (closed form) and merocyanine (opened form) on MWNTs, and resistance changes for MWNTs-SPO thin film [Images from ref.174]. B] Synthesis of SP functionalized SWNTs and absorbance changes at 5400 cm^{-1} (S_{11} interband transition) of SP-SWNT film following UV, visible illumination or keeping film in the dark [Images from ref.175].

Figure 1.19: A] One-dimensional SWNTs based semiconductor with photoswitchable molecules assembled on its surface. Light toggles the molecule between a cyclized and charge-separated state. These molecules contain a SWNT recognition domain - (alkyl chain or pyrene). B] Drain current changes of an individual SWNT device following UV and visible illumination cycles [Images from ref.176].

Figure 1.20: Examples of mono and bis SP based metal receptors. 1] First example of SP as ligand for metal cations. $M^{n+} = \text{Cu}^{2+}$ or Fe^{3+} .¹⁸⁶ 2] SP based cryptands with a diazacrown ether bridge. $M^{2+} =$ alkaline earth metals.¹⁸⁷ 3] SP with pendant bis(2-pyridylmethyl)amine (Dpa) chelating arms.¹⁸⁸ 4] SP calix[4]arene derivate carrying two spirobenzopyran moieties. $M^{3+} =$ lanthanides.¹⁸⁹ 5] SP derivatives with hydroxy group

adjacent to the benzopyran oxygen. $M^{2+} = Mg^{2+}, Zn^{2+}, Ni^{2+}, Cu^{2+}, Hg^{2+}$ or Pd^{2+} . $R_1 = H, CH_3$ or NO_2 . $R_2 = CH_3, C_8H_{17}, CH_2Ph$ or $CH_2C(CH_3)_2$.¹⁹⁰

Figure 1.21: Reversible interconversion between the closed SP and a hypothetical merocyanine-zinc complex (ME-Zn). Absorption spectra of SP (black line), of SP added of 1 equiv of $Zn(ClO_4)_2$ (red line) and after the subsequent irradiation with Vis light (green line). Inset] Sequential cycles of conversion between SP and ME-Zn controlled by visible light [Image from ref.191].

Figure 1.22: Essential ionophore sites in the SP structure for a facilitated metal cation ligation.

Figure 1.23: Schematic representation of amino acid transport across liposomal bilayers mediated by SP.

Figure 1.24: Schematic representations of the photochemical ring opening and closing of a spiropyran anchored to gold nanoparticles (NP_{Au} -SP) in the presence and absence of amino acids.

Figure 1.25: Proposed structure of the binary complex between ME and His, and pictures [taken from ref.195] of the colour changes in water by alternate exposure to darkness and visible light.

Figure 1.26: Complexation of GSH by a bis-SP and confocal microscope images [taken from ref.200] of human acute T cell leukemia A] without and B] with spiropyran.

Figure 1.27: Triple hydrogen bond interaction between the open form isomer ME and guanosine derivatives. Molecular recognition of A] SP for guanosine (G) derivatives and B] ferrocene-modified bis-SP for guanine-guanine dinucleosides (GG).

Figure 1.28: A] Proposed structure of the ternary complex containing two merocyanines, Cys (n=1) or Hcy (n=2) linked via disulfide bridge, and metal ions Hg^{2+} or Cu^{2+} . B] Effects of metal ions and amino acids on the absorption spectra of SP in 10% ethanol/water solution at neutral pH. Picture: Colour changes of ethanol/water solutions containing the SP and Hg^{2+} in the presence of: 1] no AA, 2] Gly, 3] Leu, 4] His, 5] Glu, 6] Asp, 7] Met, 8] Cys, 9] Hcy, and 10] GSH (glutathione) [Figure B adapted from the original in ref.180].

Figure 1.29: A] Proposed structure of the ternary complex containing two ME-Zn units and a PPI anion. B] Fluorescence emission spectra of the ME-Zn complex upon addition of increasing concentrations of PPI. The signal changes are indicated by the arrows [Figure B from ref.188].

Table 1.2: Functionalization of SWNTs with pharmaceutical active agents (green box), imaging (purple box) and targeting (blue box) units. The blue wavy line indicates diverse organic linkers or polymers.

Figure 1.30: A] Steps involved in the tumor-targeting drug delivery of taxoid-SWNT-biotin conjugate inside a tumor cell. (1) Internalization of the functionalized nanotube vector, (2) cleavage of the disulfide linker and release of the drug, (3) binding of the free anticancer drug to microtubules. B] Confocal fluorescence microscopy images of cells incubated with the biotin-SWNT-taxoid-fluorescein before (top) and after (bottom) addition of GSH. [Figures adapted from ref.219].

Figure 1.31: TGA measurements of purified nanotubes (p-SWNTs) showing weight change (black line) and its derivative (grey line). The weight loss % at 310 °C is attributed to the decomposition of organic groups in the nanotube samples, and the residue % at 900 °C to the metal content. The experiment is run in air atmosphere with a temperature rate of 10 °C min⁻¹.

Figure 1.32: ATR/Fourier transform IR (FT-IR) transmittance spectra of raw (r-SWNTs) and oxidized (o-SWNTs) nanotube samples. The spectra have not been baseline corrected.

Figure 1.33: Rayleigh and Stokes Raman scattering.

Figure 1.34: Raman spectrum of HiPco [batch R0546 Unidym[®]] SWNTs using a laser wavelength of $\lambda_{exc} = 633$ nm.

Chapter 2.

Figure 2.1: 2-step purification/oxidation of SWNTs.

Figure 2.2: Chemical functionalization of oxidized SWNTs with PEG linker.

Figure 2.2: a] Representation of the SWNTs functionalized with amino terminated chains (1) and (2), b] pictures of the SWNTs dispersions after chemical functionalization with functionalities (1) and (2). [SWNTs]= 0.1 mg/mL DMF.

Figure 2.3: A] Representation of SWNTs functionalized with amino terminated Boc protected chains (1) and (2). B] Pictures of SWNTs dispersions after chemical functionalization with functionalities (1) and (2). [SWNTs]= 0.1 mg/mL DMF, sonication time 30 minutes at minimum power.

Figure 2.4: Functionalization of SWNTs with SP molecular switch.

Figure 2.5: UV-Vis absorption profiles of TFA treated f-SWNTs and f-SWNTs (5) compared with a blank solution (all but nanotubes) which has been treated in the same way.

Figure 2.6: Graph] TGA traces in nitrogen of raw, purified, oxidized and functionalized SWNTs. Table] Weight losses, estimated number of carbon atoms per organic group and residue percentages for the same samples.

Figure 2.7: HR-TEM images of A] raw SWNTs, B] p-SWNTs, and C] o-SWNTs (1) on 200 mesh Cu holey carbon grids demonstrating the removal of the metal impurities (black particles) by 2-step purification/oxidation procedures. Scale bar: 100 nm. Figure C inset: detail of a small bundle of o-SWNTs (1) with a diameter of 20 nm circa (scale bar: 20 nm). [HR-TEM images from ref.26].

Figure 2.8: TGA first derivative traces of raw, purified and oxidized SWNTs performed in air atmosphere. The shift of the graphitic decomposition temperature to progressively higher values going from raw to o-SWNTs (1) is indicative of the increasing purity of the material.

Figure 2.9: TGA first derivative traces of f-SWNTs (5) and spiropyran (4) recorded under air flow.

Figure 2.10: A] Full range FT-IR spectra of (I) raw SWNTs, (II) o-SWNTs (1) and (III) f-SWNTs (5). B] Stretching vibrations assignment for (II) o-SWNTs (1) and (III) f-SWNTs (5). The peaks intensities are more than 3 times the peak to peak noise observed. To improve data visualization the spectra have been baseline corrected.

Figure 2.11: FT-IR spectra of (I) HiPco R0546, (II) oxidized and (III) SP functionalized SWNTs. The spectra have not been baseline corrected to show the decrease in transmittance observed in the region $1700\text{-}650\text{ cm}^{-1}$ when comparing the o-SWNTs (1) and SP f-SWNTs (5) to the raw HiPco SWNTs.

Figure 2.12: Micro Raman analyses ($\lambda_{\text{exc}} = 633\text{ nm}$) of (I) raw SWNTs, (II) o-SWNTs (1) and (III) f-SWNTs (5). In the insets the RBM analyses are reported. $I_{\text{D}}/I_{\text{G}}$ ratios indirectly confirmed the successful covalent functionalization of the nanotube material.

Figure 2.13: Raman spectra of A] raw HiPco SWNTs, B] oxidized and C] SP functionalized SWNTs collected using 457, 514 and 633 nm excitation wavelengths. In the insets the RBM analyses are reported.

Table 2.1: Diameter values and structural assignment of raw, purified, oxidized and functionalized SWNTs calculated from the highest intensity RBM shifts using equation

(1) and the chart for the instant structural assignment of the SWNT respectively. Excitation with 457, 514 and 633 nm laser lines and relative data are coloured in blue, green and red respectively. In the table s = semiconducting, m= metallic.

Figure 2.14: NIR-PL spectra of raw, purified and oxidized SWNTs dispersed in SDBS aqueous solution. A] $\lambda_{exc} = 638$ nm; B] $\lambda_{exc} = 683$ nm; C] $\lambda_{exc} = 785$ nm [Figures from ref.26].

Figure 2.15: Raman mapping analysis ($\lambda_{exc} = 488$ nm) of f-SWNTs (5). A] Full map image. B] Single Raman spectra from the region marked in the full Raman map. C] RBM mapping in the range 198-221 cm^{-1} . D] D-band mapping. E] G-band mapping. Time exposure 0.2 sec, one accumulation, point number 128 x 128.

Figure 2.16: Micro Raman analysis ($\lambda_{exc} = 488$ nm) of f-SWNTs (5) in the functional group region.

Figure 2.17: AFM topographic images of A] bundles of raw HiPco SWNTs, and B] individual SP f-SWNTs (5). C] Cross-section profile illustrating the height of the SP functionalized nanotube.

Figure 2.18 : UV-Vis/NIR absorption spectra of A] raw SWNTs, p-SWNTs, o-SWNTs (1) and f-SWNTs (5) collected on the supernatant of initial 10^{-2} mg/mL nanotubes in DMF ; B] raw SWNTs, p-SWNTs and o-SWNTs (1) in SDBS aqueous solution [SWNTs]_i = 2.1×10^{-2} mg/mL, SWNTs:SDBS weight ratio 1:25 [Figure adapted from ref.26].

Figure 2.19: A] Photo interconversion of the closed spiropyran (SP, 6) into the open form merocyanine (ME). B] Absorption spectra of SP (6) 10^{-4} M in DMF after 30 seconds UV illumination (long wavelength, 365 nm) and after 8 minutes storage in the dark.

Figure 2.20: UV-Vis absorption spectra of f-SWNTs (5) and o-SWNTs (1) collected on the supernatant of initial 10^{-2} mg/mL nanotubes in DMF.

Figure 2.21: A] f-SWNTs (5) response to UV (365 nm) and Vis (560-900 nm) illumination for 30 seconds. Inset: difference absorption spectra of f-SWNTs (5) after 30 seconds UV, Vis and UV illuminations. B] UV-Vis absorption spectra of o-SWNTs (1) after UV and Vis light illumination. Spectra collected on the supernatant of initial 0.1 mg/mL nanotubes in DMF.

Figure 2.22: Top] On-off switching cartoon of f-SWNTs (5). Bottom] Absorbance changes at 556 nm of f-SWNTs (5) solutions following UV (365 nm) and visible (560-900 nm) illumination cycles. Gray and white bars indicate the UV and the Vis

irradiation respectively. The spectra were collected on the supernatant of initial 0.1 mg/mL nanotubes in DMF.

Chapter 3.

Scheme 3.1: Representation of purification and oxidation of SWNTs. A] HNO₃ 2.6 M, 100 °C, 48 h. B] NaOH 8M, 100 °C, 48 h in triplicate. C] Neutralization with HCl and concentration to a solid. D, E] H₂SO₄: H₂O₂ 4:1, 35 °C, 1 h. F] NaOH 8M, 100 °C, 48 h.

Scheme 3.2: Detailed NaOH/solvent washing procedures and pictures of the filtrates.

Figure 3.1: ATR/FT-IR spectra of A] raw (r-SWNTs) and purified (p-SWNTs), B] base treated (b-SWNTs) and oxidized (o-SWNTs [1]), C] oxidized (o-SWNTs [2]) and oxidized base treated (ob-SWNTs) nanotubes. Spectra have been baseline corrected to improve data visualization.

Figure 3.2: A] ATR/Fourier transform IR (FT-IR) spectrum of carboxylated carbonaceous fragments (CCFs). IR (ATR) $\nu_{\max}^{\text{cm}^{-1}}$: 3600-3200 (O-H str), 2964 (C-H str), 1586 (C=C str, or C=O str), 1396 (C-H bend, or C=O str), 1051 (C-O str), 795 (Na-O or C-H bend).³⁵⁻³⁷ To improve data visualization the spectrum has been baseline corrected. B] Raman spectrum of CCFs. I_D/I_G ratio = 1, indicating high degree of defects in the carbonaceous material.

Figure 3.3: Pictures of the filtrates following NaOH treatments of A] p-SWNTs and B] o-SWNTs [2].

Figure 3.4: Raman spectra ($\lambda_{\text{exc}} = 633$ nm) of A] r-SWNTs and p-SWNTs, B] b-SWNTs and o-SWNTs [1], C] o-SWNTs [2] and ob-SWNTs. All the spectra have been normalized on the G-band. Insets show the RBM bands (scale: 0-0.24 a.u.).

Figure 3.5: XPS C 1s and O 1s spectra of r-SWNTs, p-SWNTs, b-SWNTs, o-SWNTs [1] and o-SWNTs [2]. Where fitted components are labelled as: **C1**: C-C sp², **C2**: plasmon loss, **C3**: C-C sp³, **C4**: (C=O)-O-, and **O1**: Fe₂O₃/Fe₃O₄, **O2**: C-O-C/(C=O)-O-/C-OH, **O3**: (C=O), **O4**: (C=O)-O-Na,⁴¹ **O5**: H₂O.

Figure 3.6: NIR photoluminescence (PL) spectra ($\lambda_{\text{exc}} = 785$ nm) of A] r-SWNTs and p-SWNTs, B] b-SWNTs and o-SWNTs [1], C] o-SWNTs [2] and ob-SWNTs. D] Histograms showing the average NIR-PL efficiency at $\lambda_{\text{exc}} = 785$ nm ($n_{\text{measurements}} = 3$).

Figure 3.7: UV-Vis/NIR absorption profiles of all samples in DMF. Absorption values (Y-axes) have been varied in order to better visualize the van Hove singularities. Spectra with actual absorption intensity values are reported in Figure 3.10.

Figure 3.8: TGA traces of r-SWNTs and p-SWNTs. The weight losses % at 310 °C attributed to the decomposition of organic groups in the nanotube samples are reported. All the experiments have been run in air atmosphere with a temperature rate of 10 °C min⁻¹.

Table 3.1: Weight loss % at 310 °C attributed to the decomposition of organic groups in the nanotube samples are reported for r-SWNTs, p-SWNTs, b-SWNTs, CCFs, o-SWNTs [1] and [2].

Figure 3.9: TGA traces of r-SWNTs, p-SWNTs and b-SWNTs. The experiments have been run in nitrogen atmosphere with a temperature rate of 10 °C min⁻¹.

Table 3.2: Weight loss % at 400 °C attributed to the decomposition of organic groups in the nanotube samples are reported for r-SWNTs, p-SWNTs, b-SWNTs, CCFs, o-SWNTs [1] and [2].

Figure 3.10: HR-TEM of 1] r-SWNTs, 2] p-SWNTs, 3] b-SWNTs, 4] o-SWNTs [1], 5] o-SWNTs [2], 6] CCFs, 7] f-SWNTs [1] and 8] f-SWNTs [2] on 200 mesh Cu holey carbon grids.

Figure 3.11: AFM topographic images and height profiles of 1] r-SWNTs, 2] p-SWNTs, 3] b-SWNTs. Z-slide 0-12 nm for r-SWNTs, and 0-4 nm for p-SWNTs and b-SWNTs images.

Figure 3.12: AFM topographic images of 1] o-SWNTs [1] and 2] o-SWNTs [2]. Average length, calculated on 100 SWNTs, is 482 ± 170 nm for o-SWNTs [1] and 528 ± 159 nm for o-SWNTs [2]. Z-slide 0-4nm.

Scheme 3.3: Coupling reaction of oxidized SWNTs [1] and [2] with fluoresceinamine.

Figure 3.13: UV-Vis/NIR absorption profiles of f-SWNTs [1] and f-SWNTs [2]. The van Hove singularities are still present in both the samples. [SWNTs]_i = 1 x 10⁻¹ mg/mL DMF. The absorption band associated to the fluorescent dye is not present, as an indication of the small amount of fluoresceinamine coupled to the nanotubes.

Figure 3.14: Emission profiles (λ_{exc} = 490 nm) of fluoresceinamine, f-SWNTs [1] and [2] and fluoresceinamine π - π stacked to o-SWNTs [2]. The nanotube samples have been diluted until same optical absorption values in DMF.

Figure 3.15: Emission profiles ($\lambda_{\text{exc}} = 490 \text{ nm}$) of fluoresceinamine functionalized nanotubes f-SWNTs [1] and f-SWNTs [2] compared to r-SWNTs, p-SWNTs, b-SWNTs, o-SWNTs [1], o-SWNTs [2] and CCFs [4]. $[\text{SWNTs}]_i = 1 \times 10^{-1} \text{ mg/mL DMF}$, $[\text{CCFs}]_i = 1 \times 10^{-1} \text{ mg/mL DMF}$. Emission peaks at 545 nm are present only in the fluoresceinamine functionalized nanotubes.

Figure 3.16: Raman spectra ($\lambda_{\text{exc}} = 633 \text{ nm}$) of A] o-SWNTs [1] and f-SWNTs [1] and B] o-SWNTs [2] and f-SWNTs [2] normalized on the G-band. Insets show the RBM bands (scale: 0-0.25 a.u.).

Figure 3.17: A] NIR-PL spectra ($\lambda_{\text{exc}} = 785 \text{ nm}$) of r-SWNTs, f-SWNTs [1] and f-SWNTs [2]. B] Histograms showing the average NIR-PL efficiency at $\lambda_{\text{exc}} = 785 \text{ nm}$ ($n_{\text{measurements}} = 3$).

Figure 3.18: XPS C 1s and O 1s spectra of A] o-SWNTs [1] and f-SWNTs [1], and B] o-SWNTs [2] and f-SWNTs [2]. Fitted components are labelled as: **C1:** C-C sp^2 , **C2:** C-C sp^3 , **C3:** C-O, **C4:** C=O, **C5:** (C=O)-O-, **C6:** plasmon loss, and **O1:** (C=O), **O2:** C-O-C/(C=O)-O-/C-OH, **O4:** (C=O)-O-Na.

Figure 3.19: AFM topographic images and height profiles of fluoresceinamine functionalized nanotubes. 1] f-SWNTs [1] and 2] f-SWNTs [2]. Z-slide 0-2 nm.

Chapter 4.

Figure 4.1: Purification of raw SWNTs by nitric acid, sodium hydroxide and hydrogen peroxide treatment.

Figure 4.2: Sidewall functionalization of SWNTs with benzoic acid, via the Tour reaction.

Figure 4.3: Functionalization of Tour reacted nanotubes f-SWNTs (1) with PEG chain and spiropyran photoswitchable derivative.

Figure 4.4: Pictures of SWNTs dispersions after A] purification and functionalization with B] benzoic acid and C] SP derivative. $[\text{SWNTs}] = 0.1 \text{ mg/mL distilled H}_2\text{O}$, sonication time 30 min at minimum power. Pictures taken 1 h after sonication ceased.

Figure 4.5: Evidences of effective purification of raw SWNTs after treatment with HNO_3 , NaOH and H_2O_2 . TGA (solid lines) and first derivative (dotted lines) traces of raw (r-SWNTs) and purified (p-SWNTs) nanotubes run in air atmosphere.

Figure 4.6: HR-TEM images of raw (left) and purified (right) SWNTs on 200 mesh Cu holey carbon grids demonstrating the removal of the metal impurities (black particles) after nitric acid purification and treatment with NaOH and H₂O₂. Scale bar: 20 nm [analyses run by Dania Movia].

Table 4.1: Weight losses % at 500 °C attributed to the decomposition of organic functionalities, estimated number of carbon atoms per organic group and residue percentages after decomposition in nitrogen atmosphere are reported for raw, purified and functionalized SWNTs.

Figure 4.7: TGA first derivative traces in the 100-750 °C range of raw, purified, Tour reacted f-SWNTs (1) and SP functionalized f-SWNTs (5) recorded under nitrogen flow.

Figure 4.8: ATR/FT-IR spectra of A] raw (r-SWNTs), purified (p-SWNTs) and Tour functionalized (f-SWNTs (1)), B] TFA treated and SP functionalized (SP f-SWNTs (3)) nanotubes. Spectra have been baseline corrected to improve data visualization.

Figure 4.9: Raman analyses ($\lambda_{exc}= 633$ nm). Figure] Raman spectra (normalized on the G-band) of r-SWNTs, p-SWNTs and f-SWNTs (1). Table] I_D/I_G ratio calculations for all the samples.

Figure 4.10: Raman analyses ($\lambda_{exc}= 633$ nm) of enlarged A] D- and G- bands, and B] RBM bands of raw, purified and functionalized SWNTs. Spectra normalized on the G-band.

Figure 4.11: AFM topographic images of r-SWNTs, p-SWNTs, f-SWNTs (1), (2) and (3). Z-slide: r-SWNTs 0-10 nm, p-SWNTs and f-SWNTs (1) 0-2.5 nm, f-SWNTs (2) 0-3.7 nm, SP f-SWNTs (3) 0-4 nm.

Figure 4.12: A] Photo interconversion of the closed SP (6) into the ME open form. B] Absorption spectra of SP (6) 10⁻⁴ M in DMF after 1 min UV illumination (365 nm) and after 3 min storage in the dark.

Figure 4.13: UV-Vis absorption spectra of r-SWNTs, p-SWNTs, f-SWNTs (1), (2) and (3) collected on the supernatant of initial 0.1 mg/mL nanotubes in DMF. The arrow indicates the absorption peak ascribable to SP in the nanomaterial.

Figure 4.14: On-off switching cartoon of SP f-SWNTs (3) and absorption studies. A] SP f-SWNTs (3) response to UV (365 nm) illumination for 2 min and dark for 3 min. Inset: difference absorption spectra of SP f-SWNTs (3) after 2 min UV, 3 min dark and additional 2 min UV illuminations. B] Absorbance changes at 585 nm of SP f-SWNTs (3) solutions following UV (365 nm) and dark cycles. Gray and white bars indicate the

UV and the darkness intervals respectively. The spectra were collected on the supernatant of initial 0.1 mg/mL nanotubes in DMF.

Figure 4.15: Emission studies. A] SP f-SWNTs (**3**) response to UV (365 nm) illumination for 2 minutes and dark for 3 minutes. B] Emission changes at 670 nm of SP f-SWNTs (**3**) solutions following UV (365 nm) and darkness cycles. Gray and white bars indicate the UV and the darkness intervals respectively. The spectra were collected on the supernatant of initial 0.1 mg/mL nanotubes in DMF.

Figure 4.16: Hypothetical structure of the triad **ME-Zn-ASA**, and ¹H-NMR partial spectra of spiropyran prior to (**SP**) and after the addition of 1 eq of Zn(ClO₄)₂ (**ME-Zn**), 1 eq of aspirin (**SP+ASA**), and 1 eq of Zn(ClO₄)₂ plus 1 eq of aspirin (**ME-Zn-ASA**).

Figure 4.17: Absorption spectra of 10⁻⁴ M SP (**6**) in CH₃CN (blue) after the addition of 1 equivalent of Zn²⁺ (orange), and an additional 1 equivalent of ASA (dark yellow). Pictures of the correspondent solutions are reported in the inset and labelled as A, B and C respectively.

Figure 4.18: Kinetic of **ME-Zn** and **ME-Zn-ASA** complexes formation. A] Emission spectra of a SP solution (10⁻⁵ M, CH₃CN) after addition of 1 eq of Zn(ClO₄)₂ (10⁻² M, H₂O) and Vis irradiation for 1 min. Data interval 30 sec for 50 min. B] Emissions at 633 nm of SP solutions added of Zn, Zn+ ASA or ASA in equimolar amounts.

Figure 4.19: Kinetic of **ME-Zn-ASA** complexes formation and release of Zn/ASA by Vis light. A] Absorption spectra of a **ME-Zn-ASA** before and after irradiation with Vis light (3300K) for 1 minute. B] Kinetic of **ME-Zn-ASA** complex formation at 430 nm after Vis light illumination.

Figure 4.20: A] Emission spectra of ME (**6**) (10⁻⁵ M, CH₃CN) recorded every 30 sec for 50 min. B] Kinetic of ME (**6**) decay at 705 nm in the presence or absence of ASA.

Figure 4.21: Pictorial representation of the cycle of chelation and light modulated release of zinc and ASA by the SP-based receptor.

Figure 4.22: Absorption studies. A] Spectra of a SP solution (10⁻⁴ M, Cl₂Bz/CH₃CN 9:1) after addition of 1 eq of Zn(ClO₄)₂ (10⁻¹ M, H₂O). Data recorded for 1 h every 1 min, and after 3h. In the inset the colour of the solution after addition of zinc is shown. B] Changes in absorption intensity of **ME-Zn** at 440 nm after Vis light illumination.

Figure 4.23: Emission studies. A] Spectra of a SP solution (10⁻⁵ M, Cl₂Bz/CH₃CN 9:1) after addition of 1 eq of Zn(ClO₄)₂ (10⁻² M, H₂O) and Vis irradiation for 1 min. Data

recorded for 30 min every 30 sec. B] Changes in emissions intensity of a SP solutions added of Zn in equimolar amount at 578 nm.

Figure 4.24: Emission studies. A] SP f-SWNTs (**3**) before and after UV (365 nm) illumination for 2 min. B] Emission changes at 667 nm of SP f-SWNTs (**3**) solutions following UV (365 nm) and darkness cycles. Gray and white bars indicate UV (2 min) and darkness (5 min) intervals respectively. Spectra were collected on the supernatant of initial 0.1 mg/mL nanotubes in Cl₂Bz/CH₃CN 9:1.

Figure 4.25: Release of zinc by SP f-SWNTs (**3**) triggered by light. A] Emission spectra ($\lambda_{exc}=440$ nm) of SP f-SWNTs (**3**) added of Zn(ClO₄)₂ (10⁻¹ M, H₂O, 1 μ l/mL of NTs) and of the **ME-Zn** complex in Cl₂Bz/CH₃CN 9:1. B] Emission changes at 508 nm of the same SP f-SWNTs (**3**) solution added of zinc, following Vis (3300 K) illumination (5 min, grey bars) and dark cycles (5 min, white bars). The spectra were collected on the supernatant of initial 0.1 mg/mL nanotubes in Cl₂Bz/CH₃CN 9:1.

Figure 4.26: Pictorial representation of the envisaged release of bioactive payloads from SWNTs bearing SP photoactive receptors.

Figure 4.27: Representative epifluorescent microscopy images of PMA-activated, “macrophage-like” THP-1 cells stained with Phalloidin-Alexa 546 conjugate after 24 h exposure to SP f-SWNTs (**3**). (B, D) Arrows point out SP f-SWNTs (**3**) aggregates in close contact with cells. (C) Macrophage engulfing a SWNTs aggregate (red arrow). (B-D) Intensely stained punctate foci of F-actin are visible across the entire cells surface. The punctate F-actin fluorescence along the cell is associated with monocyte-to-macrophage differentiation and it is indicative of adhesive structure formation.³ Scale bar: 20 μ m: (A) 10 \times , (C-D) 50 \times magnification.

Chapter 6.

Figure 6.1: Pictorial representation of the light modulated cycle of chelation and release of Zn²⁺ and AA by a SP-based receptor.

Chapter 7.

Figure 3.1a: Raman spectra ($\lambda_{\text{exc}} = 633 \text{ nm}$) of o-SWNTs [1] and o-SWNTs [2]. Spectra have been normalized on the G-band. The insets show RBMs enlargement (scale: 0-0.25 a.u.).

Figure 3.2a: NIR photoluminescence (PL) spectra of r-SWNTs, p-SWNTs, b-SWNTs, o-SWNTs [1], o-SWNTs [2], ob-SWNTs and CCFs. ($[\text{SWNTs}]_i = 8 \times 10^{-2} \text{ mg/mL}$; $[\text{CCFs}]_i = 8 \times 10^{-2} \text{ mg/mL}$; SWNTs:SDBS weight ratio = 1:25; CCFs: SDBS weight ratio = 1 :25). 1] $\lambda_{\text{exc}} = 638 \text{ nm}$ 2] $\lambda_{\text{exc}} = 683 \text{ nm}$. On the bottom, histograms showing the average NIR-PL efficiency at $\lambda_{\text{exc}} = 638 \text{ nm}$ and $\lambda_{\text{exc}} = 683 \text{ nm}$ ($n_{\text{measurements}} = 3$).

Figure 3.3a: UV-Vis/NIR absorption profiles of r-SWNTs, p-SWNTs, b-SWNTs, o-SWNTs [1], o-SWNTs [2] and CCFs. $[\text{SWNTs}]_i = 1 \times 10^{-1} \text{ mg/mL DMF}$. Spectra with actual absorption intensity values are reported.

Figure 3.4a: TGA first derivative traces of r-SWNTs, p-SWNTs and b-SWNTs performed in air atmosphere. The shift of the graphitic decomposition temperature to higher values going from raw to p-SWNTs is indicative of the increasing purity of the material.

Figure 3.5a: TGA traces of r-SWNTs, p-SWNTs, b-SWNTs, CCFs, o-SWNTs [1] and [2], f-SWNTs [1] and [2]. The weight losses % at $310 \text{ }^\circ\text{C}$ attributed to the decomposition of organic groups in the nanotube samples are reported. All the experiments have been run in air atmosphere with a temperature rate of $10 \text{ }^\circ\text{C min}^{-1}$.

Figure 3.6a: NIR photoluminescence (PL) spectra of f-SWNTs [1] and f-SWNTs [2]. ($[\text{SWNTs}]_i = 8 \times 10^{-2} \text{ mg/mL}$; SWNTs:SDBS weight ratio = 1:25). A] $\lambda_{\text{exc}} = 638 \text{ nm}$ B] $\lambda_{\text{exc}} = 683 \text{ nm}$. On the bottom, histograms showing the average NIR-PL efficiency at $\lambda_{\text{exc}} = 638 \text{ nm}$ and $\lambda_{\text{exc}} = 683 \text{ nm}$ ($n_{\text{measurements}} = 3$).

Figure 4.1a: UV-Vis absorption profiles of TFA treated f-SWNTs (2) and SP f-SWNTs (3) compared with a blank solution (all but nanotubes) which has been treated in the same way.

Figure 4.2a: TGA traces of r-SWNTs, p-SWNTs, f-SWNTs (1), f-SWNTs (2), TFA treated f-SWNTs (2) and SP f-SWNTs (3). The weight losses % at $700 \text{ }^\circ\text{C}$ attributed to the decomposition of organic groups in the nanotube samples are reported. All the experiments have been run in N_2 atmosphere with a temperature rate of $10 \text{ }^\circ\text{C min}^{-1}$.

Figure 4.3a: ATR/FT-IR spectra of A] raw (r-SWNTs), purified (p-SWNTs) and Tour functionalized (f-SWNTs (1)), B] TFA treated and SP functionalized (SP f-SWNTs (3)) nanotubes.

Figure 4.4a: UV-Vis absorption spectra of r-SWNTs, p-SWNTs, f-SWNTs (1), f-SWNTs (2) and TFA treated f-SWNT (2) after UV illumination for 2 min and storage in the dark for 7 min.

Figure 4.5a: Emission profiles ($\lambda_{\text{exc}} = 593$ nm) of f-SWNTs (2) before and after removal of the Boc protecting group by TFA recorded after UV illumination for 2 min and storage in the dark for 5 min.

Figure 4.6a: Comparison of emission profiles ($\lambda_{\text{exc}} = 593$ nm) of SP f-SWNTs (2) and SP (5) after UV illumination (365 nm) for 2 min in DMF. [SWNTs] = supernatant of initial 0.1 mg/mL, [SP] = 10^{-5} M.

Figure 4.7a: Top] NMR tubes containing SP before and after the addition of zinc. Bottom] MALDI-TOF mass spectrum of ME-Zn complex in CDCl_3 .

Figure 4.8a: $^1\text{H-NMR}$ partial spectra of a CDCl_3 solution of SP (6) containing ASA after overnight (top spectra) and two month time (bottom spectra) storage in the dark. The arrows indicate the peaks that would have changed if an interaction between the two molecules occurred.

Figure 4.9a: ES mass spectra of SP (6) A] before and B] after the addition of 1 eq of ASA in CDCl_3 .

Figure 4.10a: $^1\text{H-NMR}$ partial spectra (top) and mass spectra (bottom) of a CDCl_3 solution of ASA A] before and B] after the addition of 1 eq of $\text{Zn}(\text{ClO}_4)_2$ in D_2O .

Figure 4.11a: MALDI-TOF mass spectrum of ME-Zn-ASA in CDCl_3 .

Figure 4.12a: Absorption spectra of 10^{-4} M SP (6) in CH_3CN after A] addition of Zn^{2+} and ASA in equimolar amounts recorded after 1 hour and 1 day, B] addition of Zn^{2+} and ASA in equimolar amounts and excess of ASA.

Figure 4.13a: Absorption spectra of 10^{-4} M SP (6) in CH_3CN recorded before and after the addition of 1 eq of trifluoroacetic acid (TFA) at 1 hour and 1 day. The absence of an increased absorption band at 430 nm following addition of TFA after 1 day, excluded its correlation to newly formed MEH. Inset] Pictures of SP (6) solution before and after the addition of Zn^{2+} /ASA and TFA. The different colours further confirmed the non similarity of the three SP samples.

Figure 4.14a: Light modulation of the ME-Zn complex. Absorption and emission spectra of ME-Zn before and after Vis irradiation (3300K) for 1 min.

Figure 4.15a: Absorption spectra of CH₃CN solutions added of Zn(ClO₄)₂, ASA or the two together. The absorption shoulder at 310 nm suggests the complexation of zinc by the drug.

Table 4.1a: Solvents and mixtures of solvents tested for the solubilization and detection of performances of SP-based DDS anchored to SWNTs or in solution. Positive and negative results are schematized with a green v or a red x respectively. DBPS: Dulbecco's phosphate buffered saline.

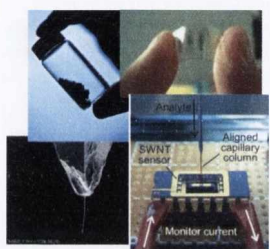
Figure 4.16a: Comparison of absorption and emission spectra of SP (**6**) dissolved in CH₃CN (1, 3) or Cl₂Bz/CH₃CN 9:1 (2, 4). 1,2] Absorption profiles of 10⁻⁴ M SP solutions before and after UV (356 nm) irradiation for 1 min, and after storage in the dark. 3,4] Fluorescence decay of 10⁻⁵ M SP solutions after irradiation with UV light (365 nm) for 1 min recorded at intervals of 30 sec.

Figure 4.17a: Absorption spectra of **ME-Zn** in Cl₂Bz/CH₃CN 9:1 before and after irradiation with Vis light (3300K) for 1 min. The band at 440 nm disappeared indicating release of the metal ion and closure of the receptor to the SP isomer.

Figure 4.18a: Absorption spectra of a SP (**6**) solution (10⁻⁴ M, Cl₂Bz/CH₃CN 9:1) before and after the addition of 1 eq of Zn(ClO₄)₂ (10⁻¹ M, H₂O) and 1 eq of TFA. Pictures of the SP solutions after addition of the acid (SP+TFA) and the metal ion (ME-Zn) are reported on the right.

Figure 4.19a: Emission spectra ($\lambda_{exc} = 440$ nm) of A] p-SWNTs, f-SWNTs (**1**) and SP f-SWNTs (**3**) before and after the addition of Zn(ClO₄)₂ (10⁻¹ M, H₂O, 1 μ l/mL of NTs), B] p-SWNTs before and after irradiation with Vis light (3300K) for 5 min. Spectra collected on the supernatant of initial 0.1 mg/mL nanotubes in Cl₂Bz/CH₃CN 9:1.

Chapter 1. Introduction



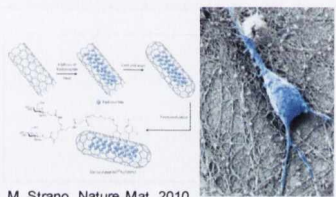
C. H. Lee, *et al.* *Angew Chem Int Ed*, 2008

Material science

Nanotechnology



Electronics



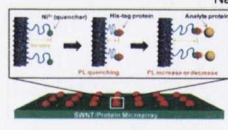
M. Strano. *Nature Mat*, 2010

G. A. Silva. *Nature Nanotech*, 2009

Medicine



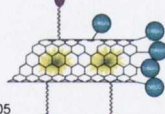
Pantarotto D. *et al.* *Angew Chem. Int. Ed.*, 2004



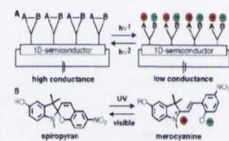
Ahn JN, *NanoLetters*, 2011



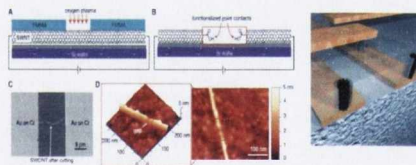
N.W.S Kam, *PNAS*, 2005



Prato M *et al.* *Acc Chem Res*, 2008



X. Guo, *et al.* *JACS* 2005



X. Guo, *et al.* *Science* 2006

Graham AP *et al.* *Small* 2005

1.1 Introduction to carbon nanotubes

Carbon nanotubes (CNTs)^{1,2} are macromolecules belonging to the family of carbon allotropes which includes diamond, graphite, graphene and fullerenes.³ Since their inception, CNTs have been regarded as a promising material in the fields of physics, chemistry, material science, electronics, and nanotechnology thanks to their remarkable properties (Table 1.1).⁴⁻²²

Table 1.1: Properties of carbon nanotubes (CNTs).

Properties of CNTs	
<i>STRUCTURAL</i>	1D system ⁷
<i>OPTICAL</i>	Transitions sharp and strong ^{8,20}
<i>ELECTRONIC</i>	Semiconducting/metallic ⁹⁻¹¹
<i>CHEMICAL</i>	Non planar geometry/easy decoration ^{4,12-16}
<i>THERMAL</i>	Ballistic conduction ^{17,18}
<i>MECHANICAL</i>	High stiffness and unique axial strength ¹⁹

For some years now, the biological and medical applications of CNTs are an area of considerable scientific interest, thanks to the ability of CNTs to cross the cellular membrane and act both as bioimaging agents and as carriers of biologically and therapeutically active substances in cells.²³⁻³⁰

As a consequence of their outstanding features CNTs have been and will be extensively exploited as promising platforms for interdisciplinary applications covering different domains, where nanoelectronics and photovoltaic devices, superconductors, reinforcing agents, nanostructured biomaterials, imaging probes and drug delivery carriers are just a few noteworthy examples.^{22,29,31-46}

1.2 Structural properties of CNTs

CNTs possess a unique tubular nano-structured shape that can be thought of as narrow strips of graphene rolled up into seamless tubes. The latter represent a molecular system which is nanometer-sized in diameter but up to centimetres long, yielding a length/diameter ratio that can exceed 10^7 . Thanks to this structural peculiarity CNTs can be considered as nearly one-dimensional (1D) materials, whose dimensionality is intermediate between the 0D fullerenes and the 2D graphene layers.⁵

Depending on the number of rolled up graphene sheets CNTs are classified in structural subclasses (Figure 1.1):

- Single-walled nanotubes (SWNTs): one graphene sheet is wrapped around forming CNTs with diameters close to 1 nm and lengths up to many thousands nm
- Double-walled nanotubes (DWNTs): two graphene cylinders are concentrically arranged giving rise to CNTs with diameters ranging from 1 to a few nm
- Multi-walled nanotubes (MWNTs): more than two graphene sheets are arranged in concentric cylinders generating CNTs with diameters up to 100 nm and lengths as variable as SWNTs.

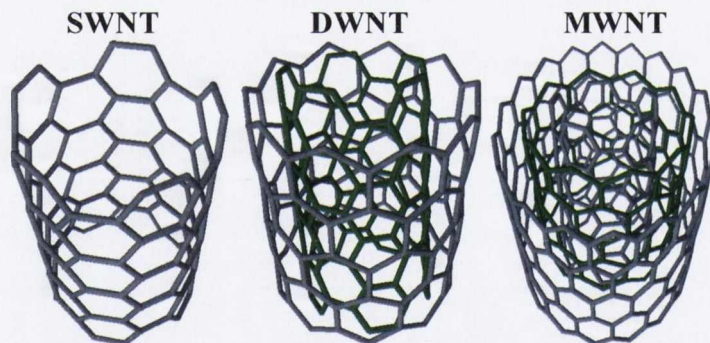


Figure 1.1: Pictorial representation of SWNT, DWNT and MWNT structures.

The properties of CNTs are directly influenced by the number of graphene sheets and the way in which they are wrapped. Therefore SWNTs and MWNTs are characterized by different mechanical, electrical, thermal and optical features. In this research our attention is focused on nanotubes made of a single graphene shell.

1.3 Physical structure and electronic-optical properties of SWNTs

The structural parameters⁴⁷ (Figure 1.2) that are essential in order to uniquely specify the physical and electrical properties that a SWNT will exhibit are:

- chiral or Hamada vector \vec{C}_h
- chiral angle θ .

The chiral vector \vec{C}_h is a linear combination of the unit vectors of the graphene sheets and is defined by the relation:

$$\vec{C}_h = n \vec{a}_1 + m \vec{a}_2$$

where n and m are integers and \vec{a}_1 and \vec{a}_2 are the unit vector of the graphene lattice. \vec{C}_h length represents the SWNT circumference.

The chiral angle θ is the angle between the chiral vector \vec{C}_h and the vector \vec{a}_1 and is defined by the relation:

$$\theta = \tan^{-1}[(m\sqrt{3}/(m + 2n))]$$

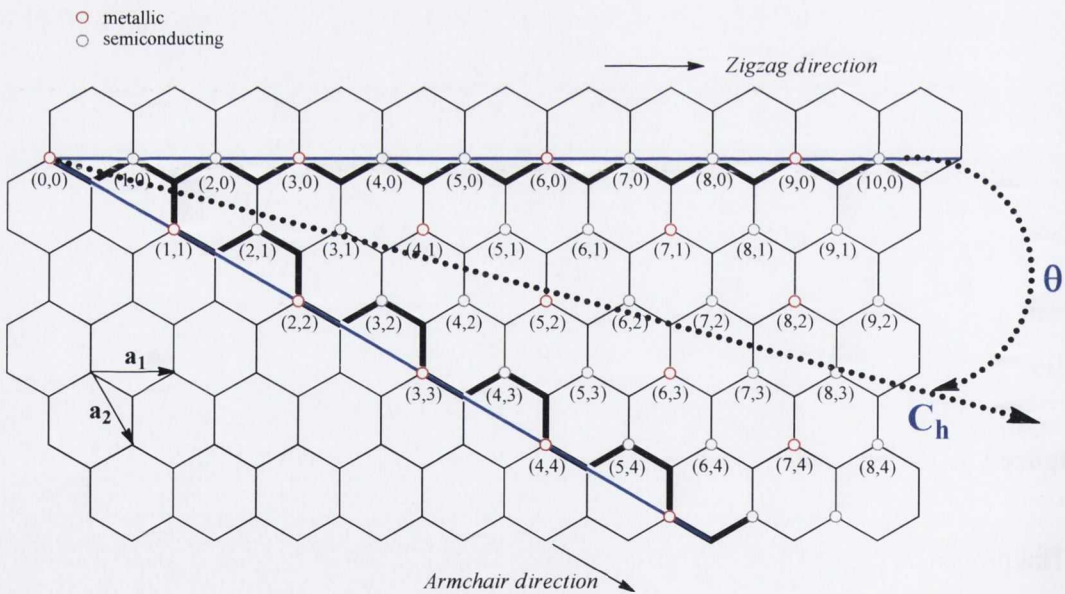


Figure 1.2: Graphene honeycomb lattice, chiral vector \vec{C}_h and chiral angle θ .

Depending on the values assumed by the pair of integers (n , m) three types of SWNTs, which differ both in physical properties and configurations, can be depicted:

- armchair $n = m \neq 0$ e $\theta = 30^\circ$ (chair pattern along the circumference)
- zigzag $n \neq 0$ $m = 0$ e $\theta = 0^\circ$ (zig-zag pattern along the circumference)
- chiral (n , m) pair where $0^\circ < \theta < 30^\circ$.

Moreover SWNTs can be either metallic or semiconducting depending on the arrangement of the hexagon rings along the tubular surface. Therefore, from the integer (n , m) values the SWNTs' electrical behaviour can be determined (Figure 1.3). A nanotube for being defined metallic or semiconducting needs to fulfil the rule $n-m/3$ is an integer or is a non-integer, respectively. Consequently, all the armchair tubes are metallic, while one-third of the zigzag and chiral tubes are metallic and the remaining two-third are semiconducting.⁴⁸ Additionally, a simple chart for the instant structural assignment of the SWNTs has been prepared by Ramesh Sivarajan.*

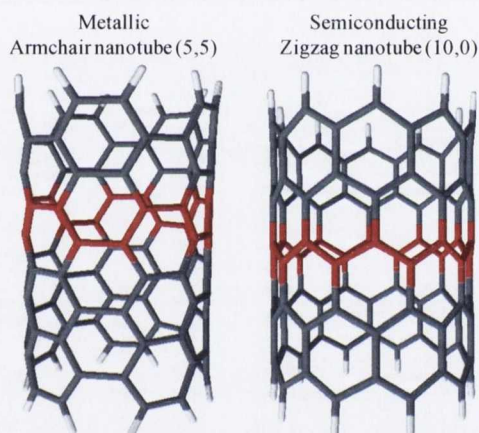


Figure 1.3: Structural and electronic variety of SWNTs: metallic armchair (5,5) and semiconducting zigzag (10,0) nanotubes.

The optical properties of SWNTs (Figure 1.4) are determined by the integers (n , m) values and derive from the electronic transitions between the first and the second pair of van Hove singularities (“spikes”) in the SWNTs density of states (DOS).^{9,47,49,50} The SWNTs gap energy is related to their chirality and diameter,⁵¹ therefore each (n , m)

* available on www.carbonwall.com

SWNT shows a different set of van Hove singularities in the valence and conduction bands.⁵²

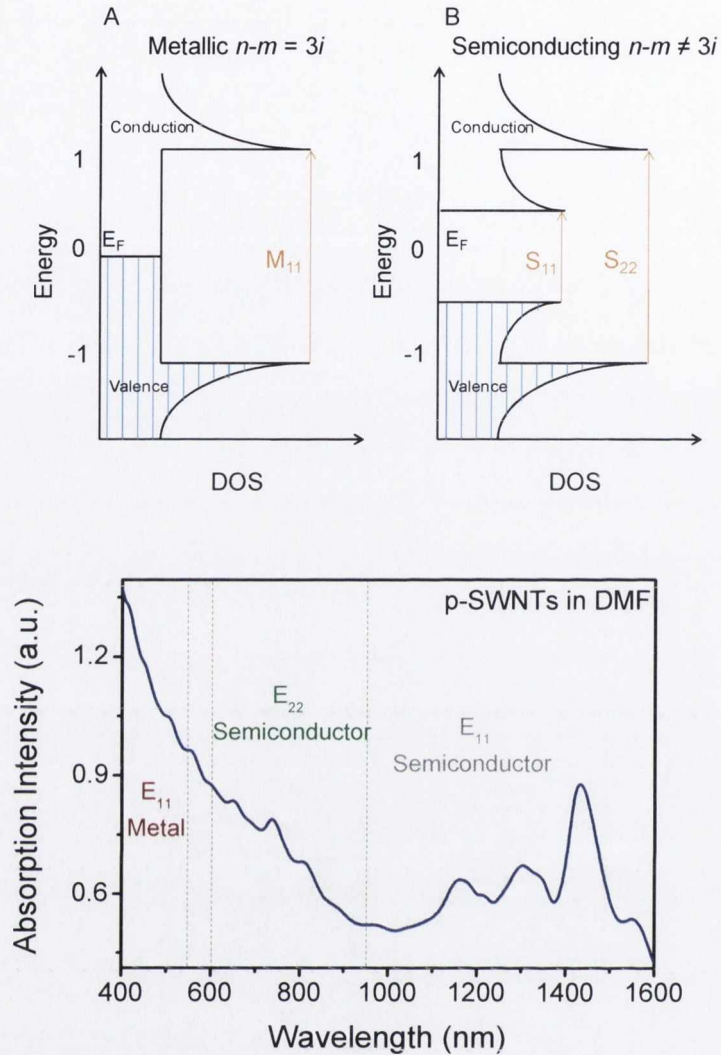


Figure 1.4: Top] Schematic representation of the density of states (DOS) of HiPco SWNTs contributing to the UV-Vis/NIR absorption. Metallic SWNT: M_{11} is the first metallic transition. Semiconducting SWNT: S_{11} and S_{22} correspond to the first and second interband transitions. Valid for small diameter SWNTs. Bottom] Metal (M_{11}) and semiconductor (S_{11} , S_{22}) transitions in the UV-Vis/NIR absorption spectrum of purified SWNTs (p-SWNTs) dispersed in DMF.

It has been widely reported that defects, vacancies, dopants and covalently bound functionalities onto the nanotube surface change its electronic structure because of the disruption of the carbon π -conjugation in the tube lattice.⁵²⁻⁵⁴ Usually a high degree of

functionalization, such as in the sidewall approach discussed later on, results in the complete loss of the S_{11} , S_{22} and M_{11} features,⁵⁵ as reported in Figure 1.5.

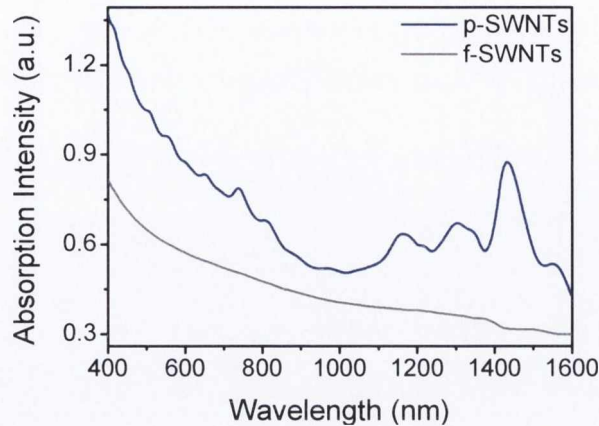


Figure 1.5: UV-Vis/NIR absorption spectra of purified (p-SWNTs) and functionalized (f-SWNTs) nanotubes in DMF showing the loss of structure upon high degree of functionalization.

Knowing the energies of the van Hove singularities transitions for specific pairs of integers (n , m) is essential when absorption, Raman and photoluminescence (PL) spectroscopies data need a comprehensive interpretation. The optical frequencies and the Raman shifts of measured peaks can be assigned to specific diameter and chirality tubes thanks to comparative analysis based on Kataura plot and radial breathing mode (RBM) correlation tables.^{8,20,56-58} An example of optical characterization of a SWNT fraction is reported in Figure 1.6.⁵⁹

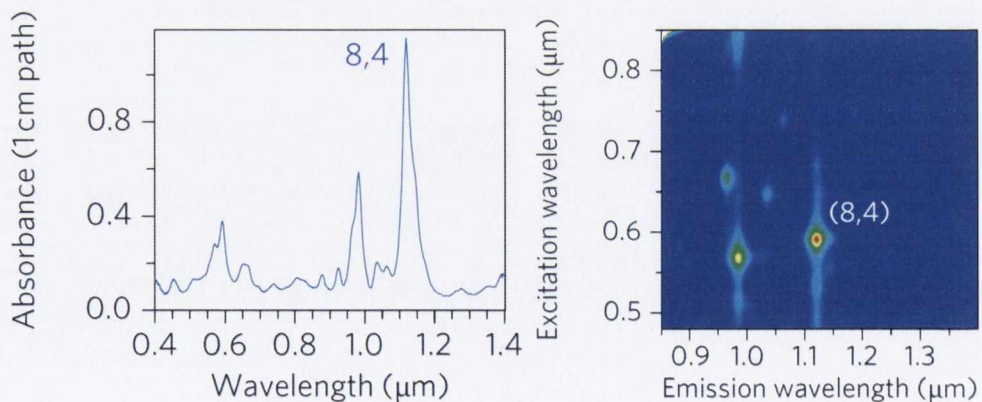


Figure 1.6: Optical characterization of a HiPco SWNT fraction [Image from ref.59].

In order to investigate if a process preferentially affects metallic or semiconducting tubes or to explore whether nanotube diameter selection occurs during chemical functionalization, the RBM regions in Raman spectra are usually analyzed. Raman spectroscopy is one of the most extensively used characterization techniques for SWNTs and it is further discussed later on in this introductory chapter.

1.4 Chemical reactivity of SWNTs

SWNTs are characterized by three different chemical reactive regions: the intact sidewall, the end caps and the defects on the sidewall (Figure 1.7).^{4,6}

The intact sidewall region is characterized by the presence of carbon hexagonal rings hybridized sp^2 , the end caps are formed by a pentagonal and hexagonal carbon rings distribution, while the defect sites on the sidewalls are mainly characterized by pairs of five- and seven- membered rings (Stone-Wales defects), sp^3 -hybridized defects and vacancies on the nanotube lattice.¹³

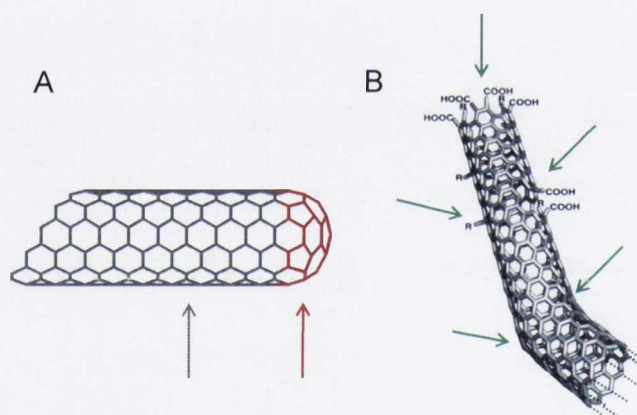


Figure 1.7: A] Ideal SWNT structure. B] Typical defects in a SWNT [Image adapted from ref.13]. Intact sidewall, end cap and defects are marked with grey, red and green arrows respectively.

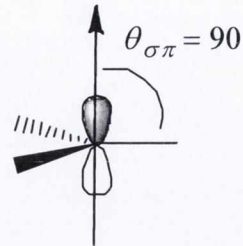
The SWNT chemical reactivity is principally driven by the carbon atoms local strain which is due to the non planar geometry of its structure. Pyramidalization angles and misalignment of the π -orbitals between adjacent pairs of conjugated carbon atoms have a central role on the SWNTs structural stability and reactivity.⁴

The pyramidalization angle (θ_p) is defined by the relation:

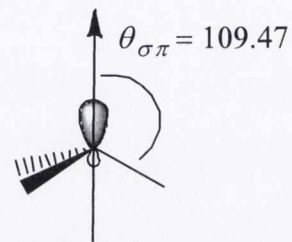
$$\theta_p = (\theta_{\sigma\pi} - 90)^\circ$$

where $\theta_{\sigma\pi}$ is the angle between the π -orbital and the σ -bond, and it has value of:

- 0° for trigonal (sp^2 hybridized) carbon atoms



- 19.5° for tetrahedral (sp^3 hybridized) carbon atoms



In a flat graphene sheet θ_p has a value of 0° because of the trigonal hybridization due to the highly stabilized C=C π -conjugation. All fullerene carbon atoms have a $\theta_p = 11.6^\circ$ and their geometry is more appropriate for tetrahedral than trigonal hybridization. Therefore, in fullerene chemistry, every reaction able to saturate the carbon atoms can relieve the local strain and decrease the strain of the remaining carbon atoms.⁶⁰ The result of the decreased local strain is the easier further addition chemistry and an increased reactivity. SWNTs end caps resemble a hemispherical fullerene structure, and their chemical reactivity can therefore be compared. Considering that it is impossible to reduce fullerenes pyramidalization angle below the value of 9.7° , and the structural similarity between fullerenes and the SWNTs end caps, the latter will always present a certain amount of chemical reactivity. Hamon *et al.*⁶¹ reported end cap and sidewall pyramidalization angles belonging to different diameters and chiralities of SWNTs. The results obtained confirm that SWNTs are more reactive than a flat graphene sheet and that the end caps are the most reactive regions in the SWNT structure.

In SWNTs two types of bonds can be observed (Figure 1.8):

- bonds that are perpendicular to the SWNT axis
- bonds that have an inclination angle to the circumference.

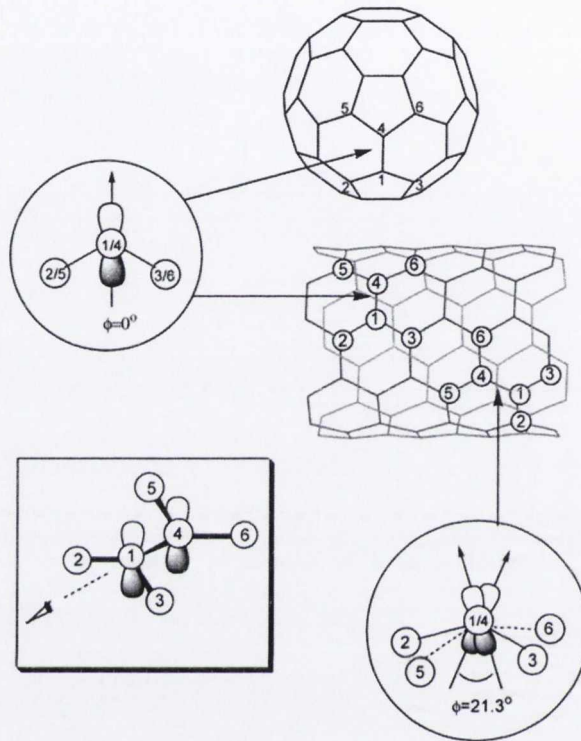


Figure 1.8: π -orbital misalignment angles (ϕ) in the side-wall and in the fullerene like end cap of a (5,5) SWNT [Image from ref.4].

These bonds possess different π -orbital misalignment angles (ϕ), and thanks to torsional strain energies calculations,⁶² the misalignment angle looks to be the main source of strain in SWNTs. π -orbitals misalignment angles and pyramidalization angle (θ_p) scale inversely with the SWNT tube diameter, therefore a different chemical reactivity is expected in tubes in which dimension and chirality differ.

1.5 Chemical modification of SWNTs

Most of the currently used methods for the SWNT synthesis (including chemical vapour deposition (CVD), high pressure carbon monoxide (HiPco), laser ablation and arc discharge) produce a raw multi component solid (pristine SWNTs) characterized by the presence of:

- impurities such as residual catalyst metal particles, metal clusters coated with carbon, amorphous carbon and in some cases fullerenes
- a mixture of tubes with different lengths, diameters and chiral angles
- bundles of different diameter SWNTs
- SWNTs with defects both at the tube ends and on the sidewalls.

As a consequence the possibility of finding a pair of identical SWNTs in a macroscopic sample is really small, like looking for a needle in a haystack. This sample heterogeneity can cause a serious limit for the characterization of SWNT derivatives and thus their further applications. It is therefore necessary to introduce an effective purification step and chemical-mechanical homogenization procedure in order to produce a material which can be successfully processed thereafter.

Different methods can be employed to purify pristine SWNTs where thermal annealing, chromatography, ultrasonically assisted filtration, microwave heating, centrifugation, oxidation with strong acids (mainly nitric acid) and organic functionalization are only some noteworthy examples.⁶³⁻⁷² However, even after successful purification (that in some cases severely affects the nanotube structure) one of the limitations towards the extensive use of SWNTs is the difficult manipulation and the lack of solubility in common solvents due to strong van der Waals interactions that stick them together in bundles.

One of the conventional approaches in recent years to improve both the solubility/dispersibility and the processibility of SWNTs is through chemical derivatization^{73,74} which could be, as schematized in Figure 1.9, divided in two main categories:

- non-covalent functionalization

- covalent functionalization.

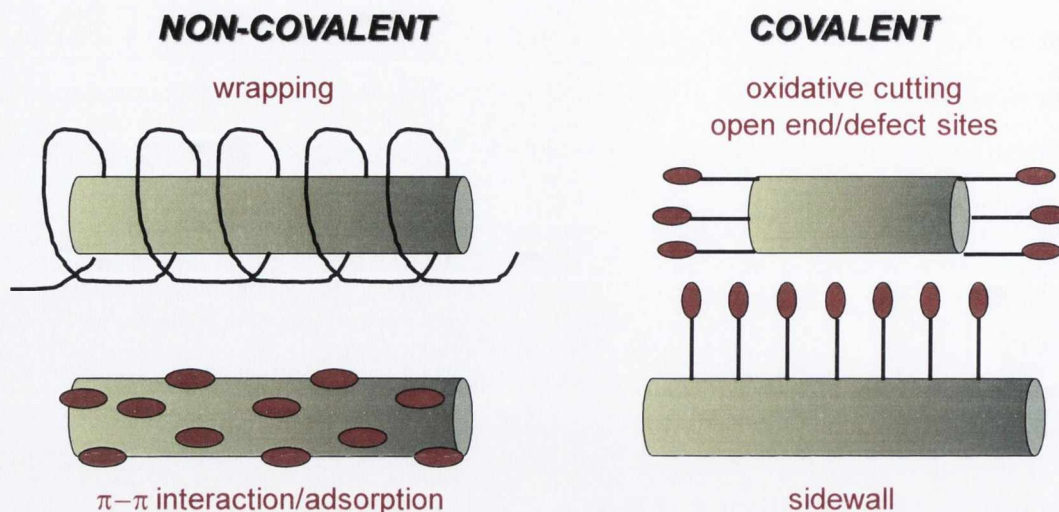


Figure 1.9: Graphical illustrations of non-covalent and covalent chemical modifications of SWNTs.

In the non-covalent functionalization approach, as example surfactants, biomolecules (such as peptides, oligonucleotides and DNA), polymers and aromatic molecules are capable of forming π - π interactions with the graphitic SWNTs surface or being adsorbed or wrapped around it.^{14,15,75-79} Besides the decoration of the nanotube surface with disparate bulky functional groups, the main and very attractive advantage of the non-covalent interaction is the complete preservation of the electronic properties of the carbon network. However this supramolecular approach is not within the interest of this thesis, therefore it will not be delved further on.

Regarding the covalent approach, which is the one considered in this work, SWNTs can be functionalized either on the sidewall or at the open ends/defect sites.^{14-16,80,81} Among the sidewall chemistry a considerable number of functional groups can be directly attached to the SWNT surface thanks to the countless reactions that have been reported in the literature. On the other hand, the open ended SWNTs are characterized by the presence of free carboxylic groups therefore esterifications or amidations reactions represent the open ends chemistry.

Besides the improved dispersibility and processibility, one of the key objectives in the covalent chemical modification of SWNTs consists in the quantitative control of the functionalities introduced onto the nanotube surface, as a substantial structural modification may adversely alter their properties.⁸¹ A high degree of functionalization is

directly linked to a variation of the conductive and electrical properties, which is undesirable for electronic uses but might be required in drug delivery applications when a high functionality loading is preferable. However, by selecting *a priori* the sidewall or the open ended functionalization route and the operative conditions, the covalent approach allows the tailoring of a nanotube material with specific structural, functional and electronic properties. Additionally, the recent discovery of reversible covalent modification processes has shown to be an important step towards the quantitative control of the chemical groups attached to the nanotube surface⁸¹ by opening real opportunities toward the production of SWNTs with controlled and specific properties.

This thesis will approach to both defect site/open ends (Chapter 2 and 3) and sidewall (Chapter 4) chemical methods for the synthesis of SWNTs covalently modified with photoactive molecules.

1.5.1 Covalent functionalization of SWNT: defect site chemistry

As previously mentioned, one of the structural characteristics of a raw SWNT material is the presence of impurities and defects on its surface. Further defects are usually produced while removing the metal catalyst residues from the raw SWNTs, where one of the most commonly employed techniques, which is also the one reported in this work, is the sample treatment under acid-oxidizing conditions.^{63,82} This process has as a secondary effect the formation of oxygenated functions on the defect sites that consist mostly in heptagonal and pentagonal carbon rings. The carbon atoms in the defect sites possess a higher reactivity than the one present in the “intact” hexagonal rings because of the sharing of C=C double bonds with higher strain. As a consequence of the purification step a number of oxygenated functions, such as ketones, alcohols and ester groups are generated and can be found on the nanotube surface, as schematized in Figure 1.10.⁸³

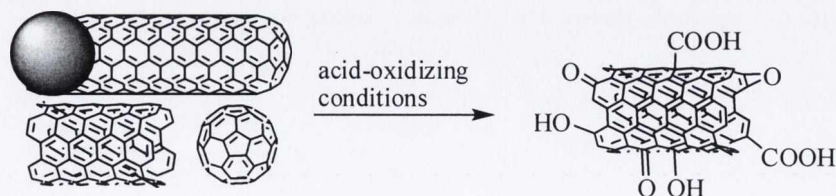


Figure 1.10: Possible effect of acid-oxidizing purification treatments on the SWNTs morphology.

The purification under strong acidic-oxidative conditions is very popular among the nanotube community and is widely employed as initial step for further modification and decoration of the SWNTs. Additional chemistry that converts the oxygenated functionalities into carboxylic acids is however needed, as only these carbonyl groups are capable of reacting with alcohols and amines to give ester and amides derivatives respectively.¹⁶ Depending on the harshness of the chemical conditions selected, the oxidized vacancies present onto the surface of p-SWNTs can be consumed and behave as triggering point for the so-called “oxidative cutting” process which yields shortened SWNTs bearing –COOH groups, also called fullerene pipes.⁸⁴ Different types of oxidizing procedures can be mentioned, such as oxygen plasma treatments, thermal oxidations in air or oxygen atmosphere, ozonolysis and gas phase or liquid phase oxidations.^{6,15,85} Oxidation times and conditions used are extremely important and have to be meticulously chosen as they directly affect (1) the density of carboxylic residues on the open ends, (2) the number of defect sites onto the SWNTs surface and (3) the nanotube lengths.^{86,87} However, one of the most commonly used methods consists of refluxing SWNTs in HNO₃ followed by ultrasonication in a H₂SO₄/HNO₃ mixture^{84,86} or by a treatment in H₂SO₄/H₂O₂,^{14,88,89} else in a milder treatment with just the refluxing step in HNO₃.¹³ In this thesis, and specifically in chapter 2 and 3, the above mentioned 2 step purification/oxidation in HNO₃ and piranha solution will be reported as first measure toward the production of a clean, short and covalently functionalized SWNT material.

Since their first inception in 1998, fullerene pipes have been widely exploited by the nanotube community as easy and standard methods, such as conversion of the carboxyl group to acid chloride or to carbodiimide activated ester, allow their further covalent decoration. The latter leads up to key benefits that can be listed as:

- enhancement of the debundling process⁹⁰
- improvement of the solubility either in organic solvents or in water^{91,92}
- reduction of the cytotoxicity^{93,94}
- applications in biomedicine^{30,95}
- combination of unique properties of different materials in one single multifunctional nanotube-based platform.^{96,97}

A vast number of papers and reviews that report the above mentioned approach have been published in the last years,¹⁴⁻¹⁶ and an exemplification of a number of possible amidation and esterification reactions on shortened SWNTs bearing carboxylic acid groups is reported in Figure 1.11.

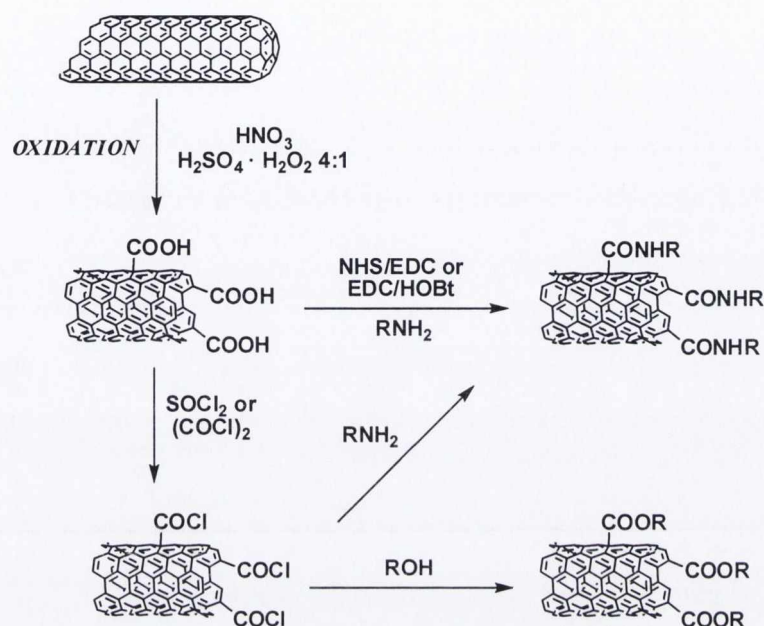


Figure 1.11: Examples of amidation and esterification reactions on shortened SWNTs bearing carboxylic acid groups. NHS=N-Hydroxysuccinimide, EDC=N-Ethyl-N'-(3-dimethylaminopropyl)carbodiimide, HOBt=N-Hydroxybenzotriazole.

The chemical modification of shortened and oxidized SWNTs with organic amines *via* carbodiimide coupling reactions has been widely reported as reliable procedure to integrate nanotubes with *e.g.* biomolecules,⁹⁸⁻¹⁰⁰ electron-acceptor complexes,⁹⁷ semiconductor nanocrystals¹⁰¹ and fullerenes.^{96,102} In the two following chapters of this thesis the chemical approach that involves the NHS/EDC activation of the $-COOH$ will be used to combine nanotubes and photoactive molecules.

1.5.2 Covalent functionalization of SWNT: sidewall chemistry

Chemical modification of the SWNTs sidewalls is more difficult to accomplish if compared to that of the fullerene-like ends because of the lower curvature and therefore lower reactivity of the nanotube walls. As a consequence harsher conditions and/or highly reactive species are needed to functionalize them. Most of the functionalization methods reported so far makes use of electrophilic reagents that react with the partial deactivated carbon-carbon double bonds in the sidewall surface, but not to intact benzene.¹⁰³⁻¹⁰⁵ A considerable number of derivatization schemes have been developed and are quoted in a number of recent reviews.^{4,14-16,80,106} Some of these are schematized in Figure 1.12 and include the use of fluorine,^{107,108} the addition of carbenes and nitrenes,¹⁰⁹⁻¹¹² Bingel cyclopropanation,¹¹³ 1,3 dipolar and Diels-alder cycloadditions,¹¹⁴⁻¹¹⁶ Birch reduction conditions¹¹⁷ and the generation of alkyl and aryl radicals.^{53,55,118}

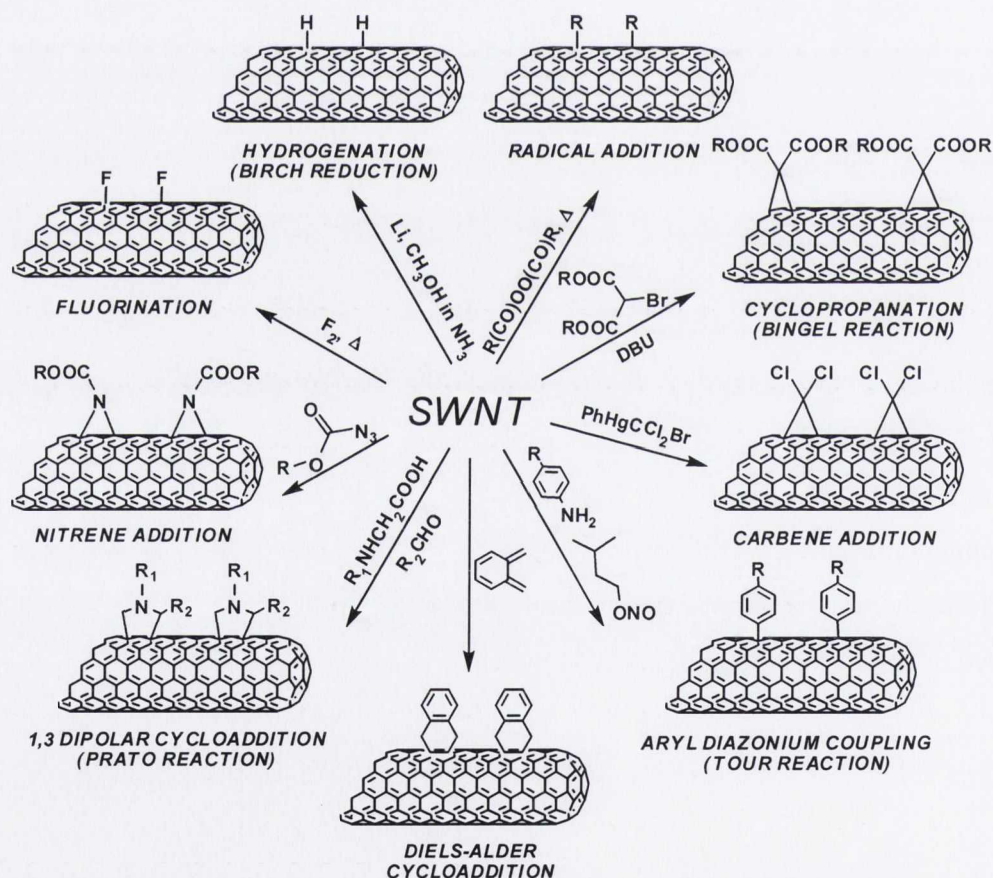


Figure 1.12: Schematic describing some examples of sidewall chemical enrichment of SWNTs.

Aryl diazonium coupling, commonly named Tour reaction, proceeds via radical intermediates and it is one of the most examined addition reactions to SWNTs. It allows to produce a nanotube material that (1) is highly enriched in functionalities, calculated as one organic group every 20 carbon atoms of SWNT, (2) has highly enhanced dispersibility in common solvents and water, depending on the nature of the aryl -R substituent, (3) is selectively functionalized onto the metallic tubes under controlled conditions.^{14,52,73,119} Aryl adducts of SWNTs can be formed by following different routes, as schematized in Figure 1.13.¹⁶

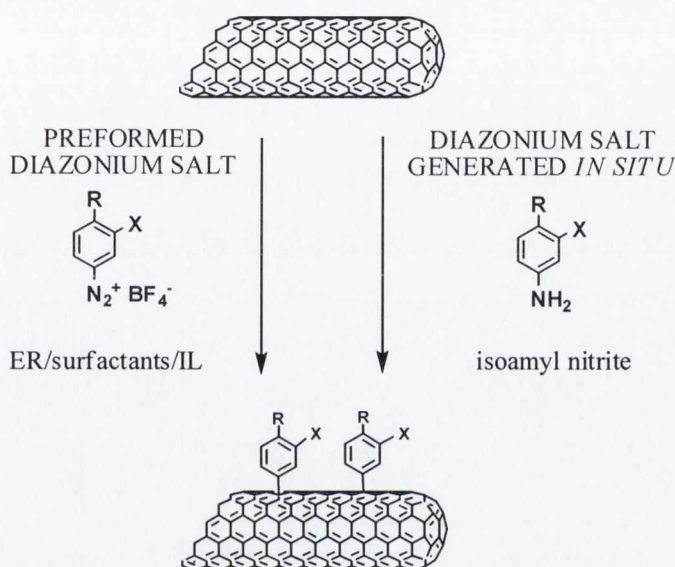


Figure 1.13: Derivatization approach by aryl diazonium salt additions on SWNTs. ER= electrochemical reduction, IL= ionic liquids.

Diazonium salts can be electrochemically reduced in organic media,⁵³ react efficiently with individual surfactant-coated SWNTs in water¹²⁰ or in ionic liquids,¹⁰⁶ and can be generated *in situ* by action of isoamyl nitrite on aniline with or without solvent.^{55,121,122} This wide variety of chemical conditions allowed the widespread use of this approach for the chemical modification of SWNT sidewalls, as confirmed by a vast number of published works.^{14-16,80,91,119} In chapter 4 of this thesis SWNTs will be sidewall functionalized by a treatment with *in situ* generated 4-carboxybenzenediazonium due to the high degree of functionalization required for the potential uses of the proposed nanotube material as light controllable drug delivery platform.

1.6 Photoresponsive switchable molecules: spiropyrans

Molecular switches are molecules that can be reversibly shifted between two or more stable states. Light, pH, temperature, electrical current, and ligands are some of the stimuli which can effectively lead the molecular switches to convert between the different states. Molecular switches are well known for their useful properties such as optical data storage, ion sensing and photoregenerable surface modifications.¹²³⁻¹²⁵

Among this class of molecules, photochromic compounds are widely studied as they possess the peculiarity to switch between two different electronic configurations upon irradiation at an appropriate wavelength.¹²⁶ The term photochromism was coined in 1955 by Hirshberg¹²⁷ and by IUPAC definition is “a reversible transformation of a chemical species induced in one or both directions by absorption of electromagnetic radiation between two forms, A and B, having different absorption spectra” (Figure 1.14).

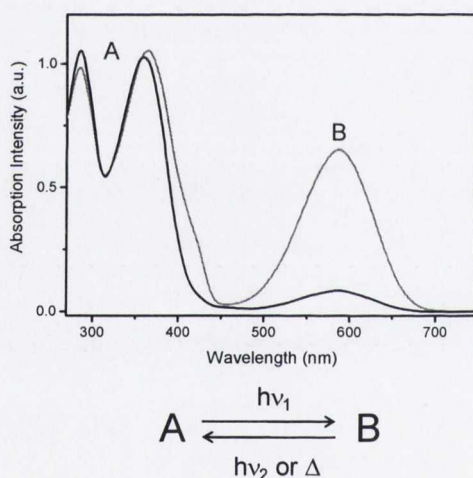


Figure 1.14: Examples of absorbance patterns in a photochromic process.

Thanks to this exclusive property, photochromic compounds have been extensively included in a variety of supramolecular assemblies ranging from polymers^{128,129} to optical memories¹³⁰ and molecular devices.^{131,132} Photochromes are classified based on their structure and switching mechanism: stilbenes and azobenzenes,¹³³ diarylethenes and dithienylethenes,^{134,135} fulgides,¹³⁶ anils,¹³⁷ spiropyrans and spirooxazines¹³⁸⁻¹⁴⁰ are only some examples.¹²⁶ Few of the latter are illustrated in Figure 1.15.

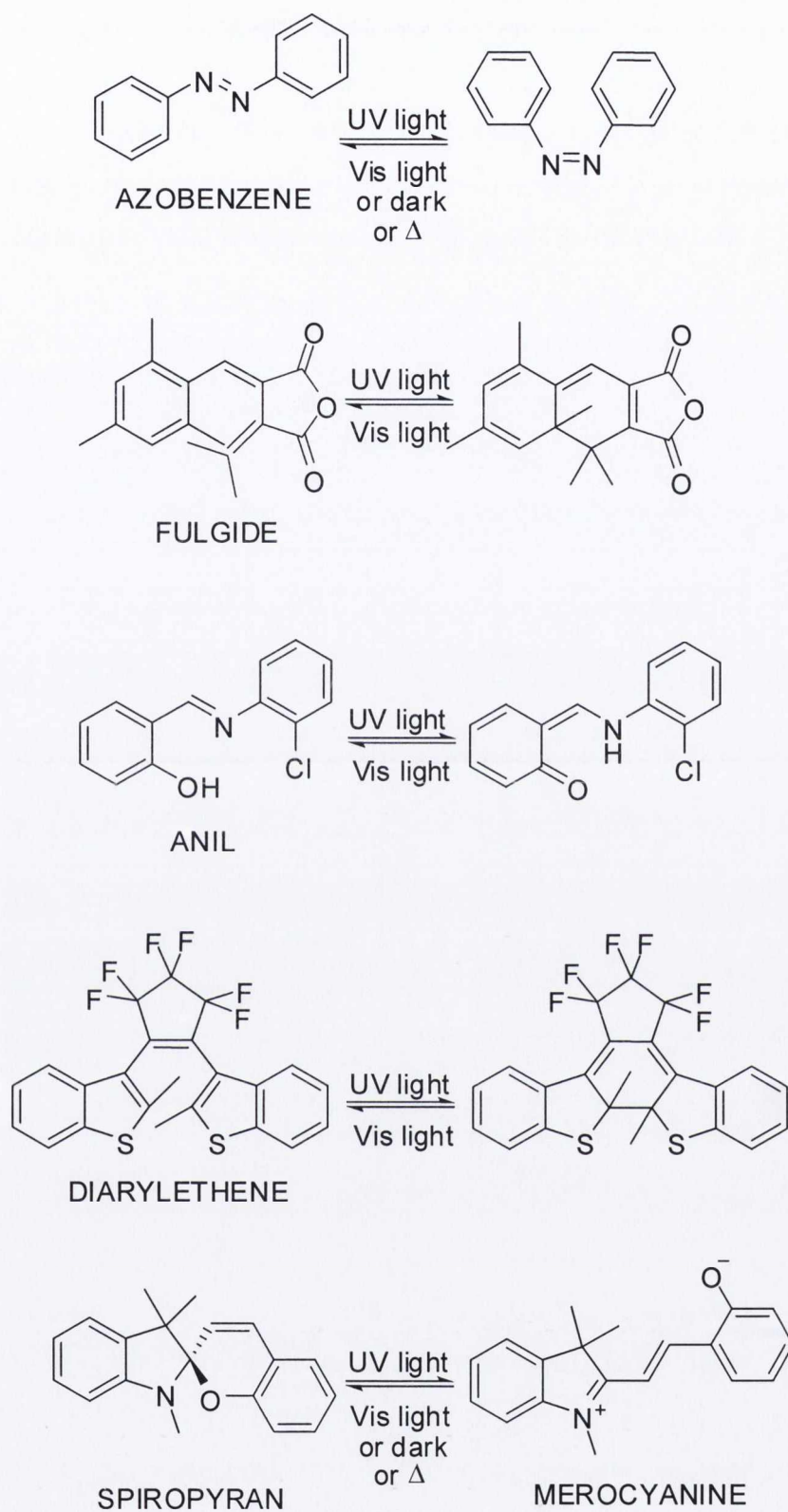


Figure 1.15: Structures and switching mechanisms between different electronic configurations of some photochromic compounds.

This thesis is focused exclusively on spiropyrans (SP) and on the study of their photochromic behaviour in solution when coupled to SWNTs (Chapter 2 and 4). SPs have been specifically chosen because they have shown the ability to isomerise to their corresponding merocyanine (ME) “opened” form upon UV light illumination (Figure 1.15), and to revert back to the starting “closed” structural conformation following irradiation with visible light, storage in the dark or heating, typically with high sensitivity.¹⁴¹⁻¹⁴⁴ Each state is characterized by a particular absorbance and by definition both transformations must be reversible, as schematized in Figure 1.16.

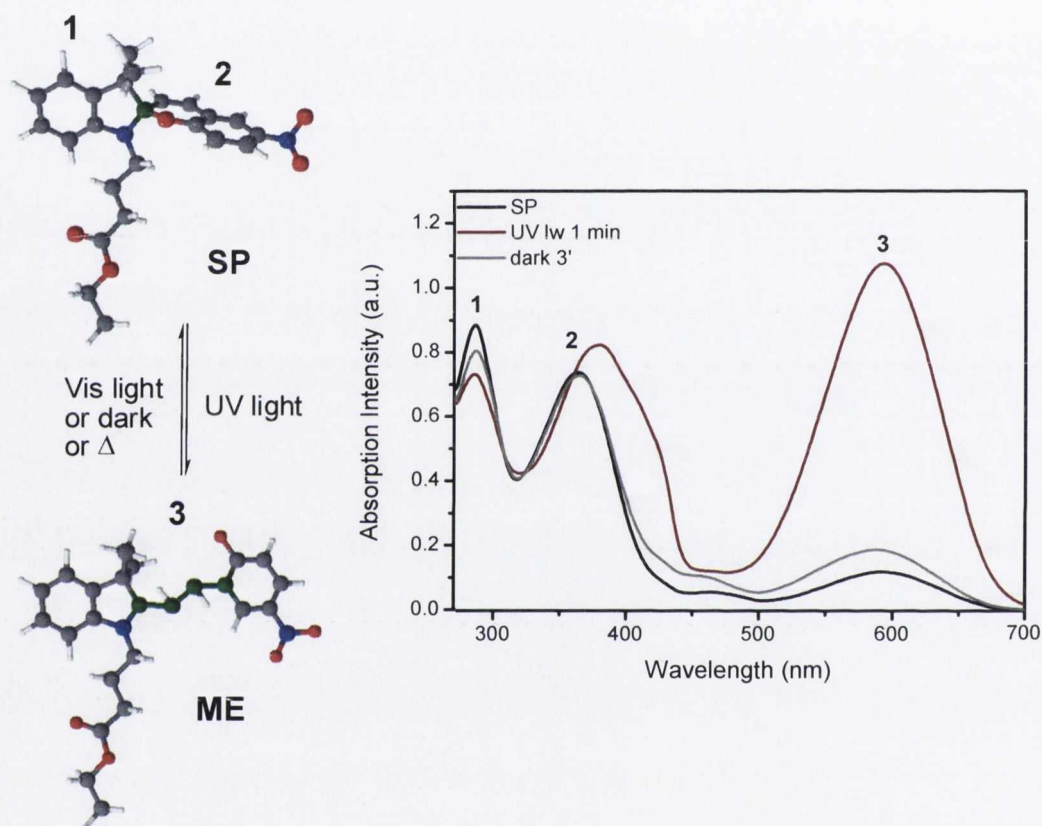


Figure 1.16: Left] Photo interconversion between the closed (SP) and the open (ME) form of a spiropyran. Right] Absorption spectra of a SP solution before (black line), after irradiation with UV light (wine line) and after storage in the dark (grey line).

Structurally SPs consist of two heterocyclic moieties (indole and benzopyran) that are positioned in two perpendicular planes and are linked to each other through a sp^3 -hybridized spiro carbon atom C_{spiro} (green atom in SP, Figure 1.16).¹⁴⁵ The “closed” form isomer is the thermodynamically favourable in non polar solvents and it absorbs below 400 nm, where the contributions from the indolic and the benzopyran halves of

the molecule are labelled with **1** and **2** respectively (graph in Figure 1.16).¹⁴⁶ The absorption of a photon in the 200-400 nm region induces the cleavage of the C_{spiro}-O bond leading to the formation of the fully conjugated zwitterionic “opened” ME isomer that strongly absorbs in the visible region (labelled as **3**). By following either a photochemical or a thermal path the ME form isomerizes back to the colourless SP form.

1.7 SP on solid state

Hybrid nanomaterials composed of photoactive molecules and a variety of organic and inorganic components have been the subject of several studies over the past decade due to their potential applications in optical data storage, optical switches, chem/bio sensors and the fabrication of photoresponsive devices.¹⁴⁷⁻¹⁵⁰ The mixing of components at the nanometer scale still attracts the scientific community’s interest because of its potential appealing opportunities to build new materials with specifically tailored chemical and physical properties. Among these, SP derivatives are very attractive as they retain their optical and caging properties when incorporated in hybrid materials.¹⁴⁸ The SP-ME system although well studied in solution has not been extensively investigated in the solid state. Nonetheless, in recent research studies SP derivatives have been integrated in a number of materials for the most disparate uses, which can be listed as:

- organogels based on low-molecular weight gelators (LMWG) for applications in data recording (Figure 1.17 A)¹⁴⁷
- polymers, such as (1) poly(*N*-isopropylacrylamide) for the production of microgels with photo-, thermally, and pH-responsive properties in aqueous suspension¹⁵¹ and (2) polymethyl methacrylate for the detection of metal ions¹⁵²
- silica- and/or polystyrene based materials for energy transfer, fundamental spectroscopy and stability studies in solid matrices respectively (Figure 1.17 B and C)¹⁵³⁻¹⁵⁵
- polymeric nanoparticles (NP) for the potential (1) production of smart inks and time sensitive displays¹⁵⁶ and (2) imaging and biological labelling (Figure 1.17 D)^{157,158}

- gold NP for potential controlled release of amino acids¹⁵⁹ and for the realization of spiropyran-AuNP-based logic gates¹⁶⁰
- gold nanoclusters for potential applications in biological imaging and labelling, as well as in reversible data storage/erasing¹⁶¹
- gold electrodes for (1) electrooxidation of dopamine and metabolites by means of electrostatic interactions¹⁶² and (2) concentration and release of metal ions on surfaces in a controlled process¹⁶³
- glass and silicon surfaces in microfluidic devices^{164,165}
- CdSe/ZnS nanocrystals for optically addressable devices with improved fatigue resistance (Figure 1.17 E)¹⁶⁶
- organic thin film transistors for complex integrated electronic logic circuits or future new computing systems.¹⁶⁷

Owing to the variety of hybrid devices and the several applications proposed in the above mentioned works, plus the constant need of smaller smart devices, it is licit to envisage the use of SPs in one-dimensional photoresponsive integrated systems.

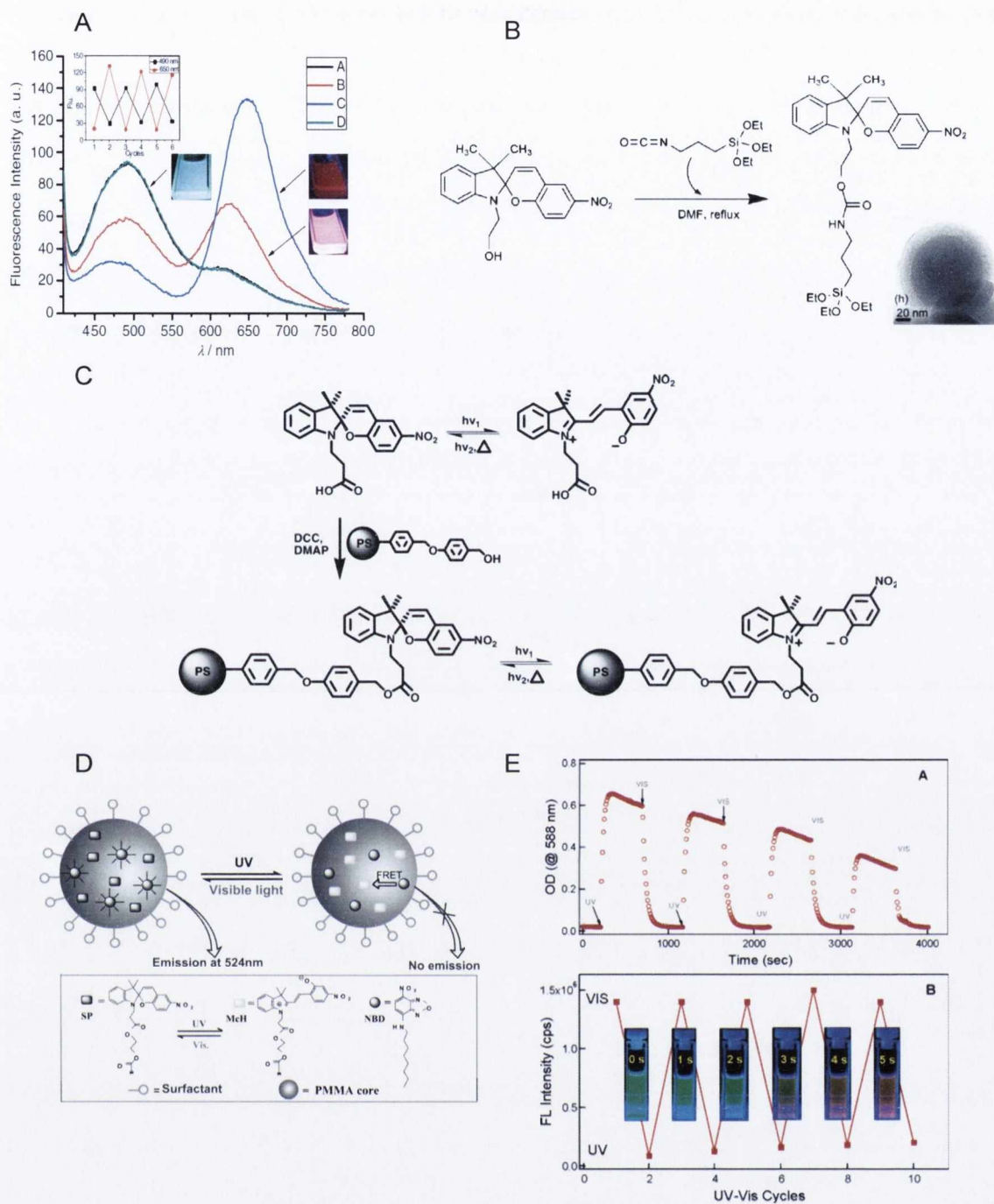


Figure 1.17: Examples of SP integrated hybrid materials. A) Fluorescence spectra of organogel formed with LMWG and SP (A), after UV light irradiation for 30 s (B) and 10 min (C), and further visible light irradiation [Image from ref.147]. B) Silylation of hydroxyethyl-SP.¹⁵³ C) Coupling of SP with the Wang resin [Image from ref.154]. D) Light-induced fluorescence modulation of a NP containing a fluorescent dye (NBD) and a SP [Image from ref.157]. E) Modulation of the optical properties of SP-CdSe/ZnS nanocrystals solutions by cycles of UV and Vis irradiation [Images from ref.166].

1.8 SP and SWNTs

The integration of photo and chemo responsive molecules in one-dimensional CNT based materials, where the principal intent consists of switching and sensing applications in solid state devices, is a topic of current interest.¹⁶⁸⁻¹⁷⁰

The Nuckolls group in 2006 demonstrated for the first time the capability to switch the conductance of a molecule in a one-dimensional electrical device based on cut functionalized SWNTs.³³ This opened the way to molecular-scale nanotube based functionalized electrodes/transistors, and a number of reviews have been reported in the last years.^{169,171-173} Although considerable work has been done to integrate stimuli-responding functionalities on SWNTs via both covalent and non-covalent approaches, nanotubes are still regarded as ideal scaffold for optoelectronic integrated devices. This because such nanosized systems can find applications not only in sensing but also in detecting and delivering applications according to the nature of the functionalities anchored to the tubes.

Even though CNT-photoswitchable molecules integrated systems have not been extensively investigated so far, a number of examples are worth to mention because of their promising applications as engineering switches on the molecular level and solid-state technologies.

MWNTs covalently functionalized with a photochromic spironaphthoxazines (SPO) derivative were reported and the reversible photoresponsive conductance switching of the material under UV light irradiation demonstrated.¹⁷⁴ The interconversion of SPO between the closed and the open form when attached to MWNTs is schematized in Figure 1.18A, where the resistance changes for MWNTs-SPO thin film are also reported.

A study related to the light modulation of electronic transitions in semiconducting SWNTs was reported few years ago. It was demonstrated that the electronic characteristics of SWNTs can be tailored by light and additionally that the interband transition intensities of functionalized SWNTs (f-SWNTs) with a SP derivative can be modulated via photoinduced changes in the SP polarity.¹⁷⁵ The schematic for the synthesis of SP f-SWNTs and the light modulated absorbance changes at the S_{11} interband transition wavelength of the thin film are reported in Figure 1.18B. The

results reported in this study can be considered pioneering for the further development of SWNT based chemical sensors.

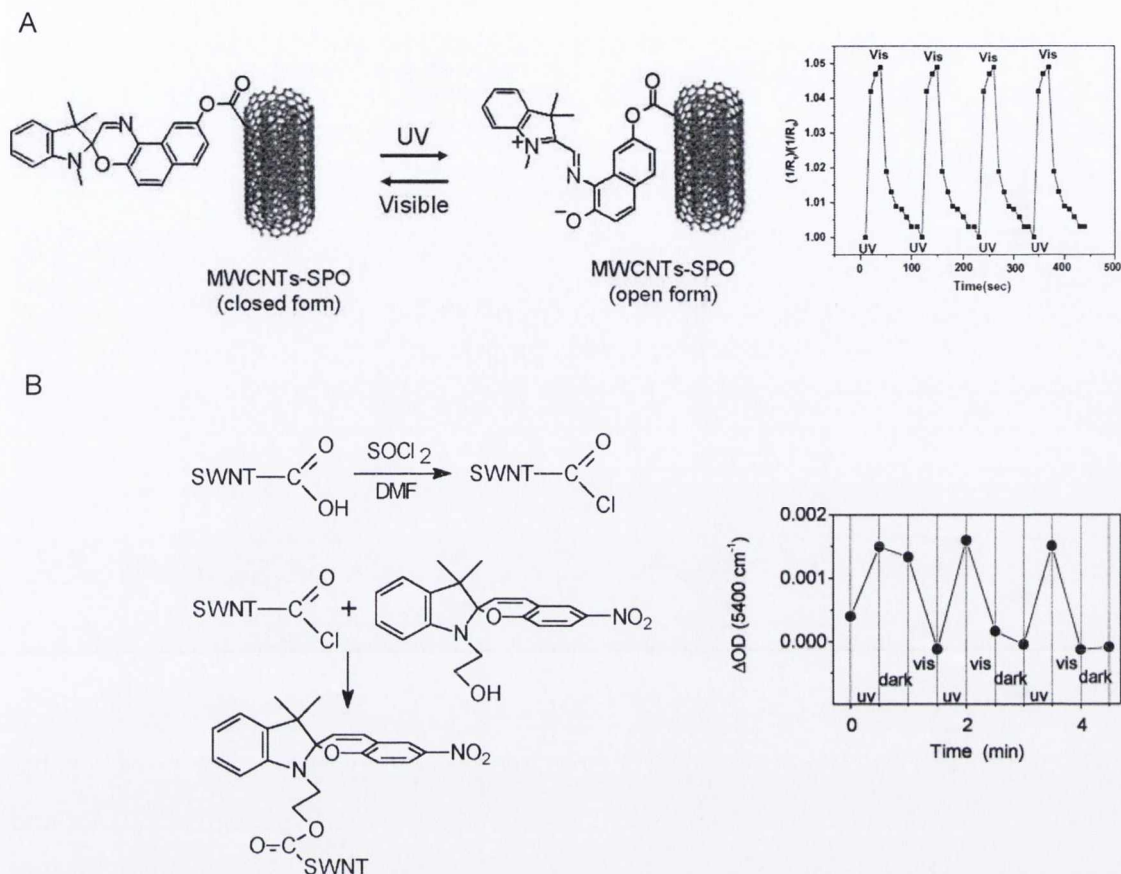


Figure 1.18: Switches on tubes. A) Photoinduced interconversion of SPO between spiro (closed form) and merocyanine (opened form) on MWNTs, and resistance changes for MWNTs-SPO thin film [Images from ref.174]. B) Synthesis of SP functionalized SWNTs and absorbance changes at 5400 cm^{-1} (S_{11} interband transition) of SP-SWNT film following UV, visible illumination or keeping film in the dark [Images from ref.175].

More recently it has been shown that in a SWNT based transistor SP non covalently associated with its surface can be used as conductance switches.¹⁷⁶ By toggling the photoactive molecule back-and-forth between the open and close conformations the device characteristic can be changed, as showed in Figure 1.19. This study provides an example of how to combine unique properties coming from two different components in a single nanodevice. In such nanosystems light is sensed and converted into a signal, and therefore, at a rudimentary level, they can be compared to biological processes such as vision and photosynthesis.¹⁶⁹

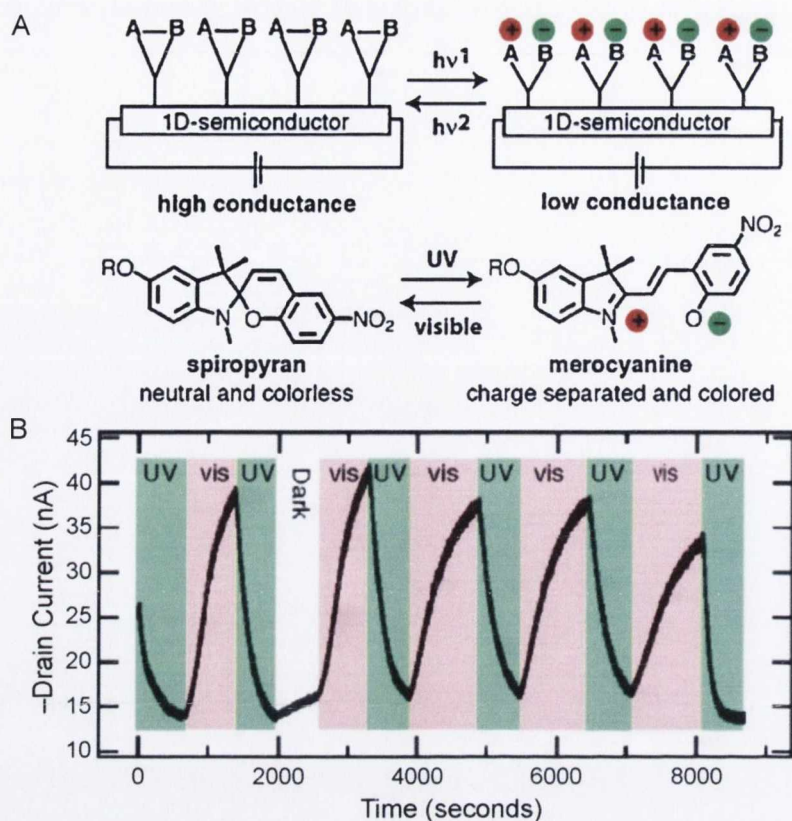


Figure 1.19: A) One-dimensional SWNTs based semiconductor with photoswitchable molecules assembled on its surface. Light toggles the molecule between a cyclized and charge-separated state. These molecules contain a SWNT recognition domain - (alkyl chain or pyrene). B) Drain current changes of an individual SWNT device following UV and visible illumination cycles [Images from ref.176].

To the best of our knowledge, the above mentioned works are the only reported examples where the unique properties of SP derivatives and SWNTs have been coupled together. Moreover only one used these two components covalently linked together,¹⁷⁵ that is our same approach. However, while the work reported by the Haddon group related to the light modulation of electronic transitions in semiconducting SWNTs, our focus (discussed in detail in Chapter 2) consists in the design and production of a nanosized smart light modulated material that consists of a nanotube scaffold and an “intelligent” molecular switch.

Additionally, in all the examples reported so far CNT-photoswitchable systems have been assembled on thin films, while we are intrigued by the modulation of the SP optical properties in solution to better simulate potential responses in bio environments.

1.9 SP based photoswitchable receptors

In organic solvents the conversion of SP into ME can be induced by complexation with divalent cations,¹⁷⁷ and a vast number of variously substitute's mono and bis SP derivatives that behave as metal ion chelating receptors have been reported in the literature.¹⁷⁸⁻¹⁸⁵ To have an overview of the wide range of structures tested in the last years few schematic examples of SP-metal complexes are depicted in Figure 1.20. Since the synthesis of the first photochromic chelating agent, that dates back to 1965 and is labelled with **1**, big effort has been made to optimize the SP structure for getting selective metal receptors. Only some noteworthy examples that closely correlate to our project will be discussed later on in this section.

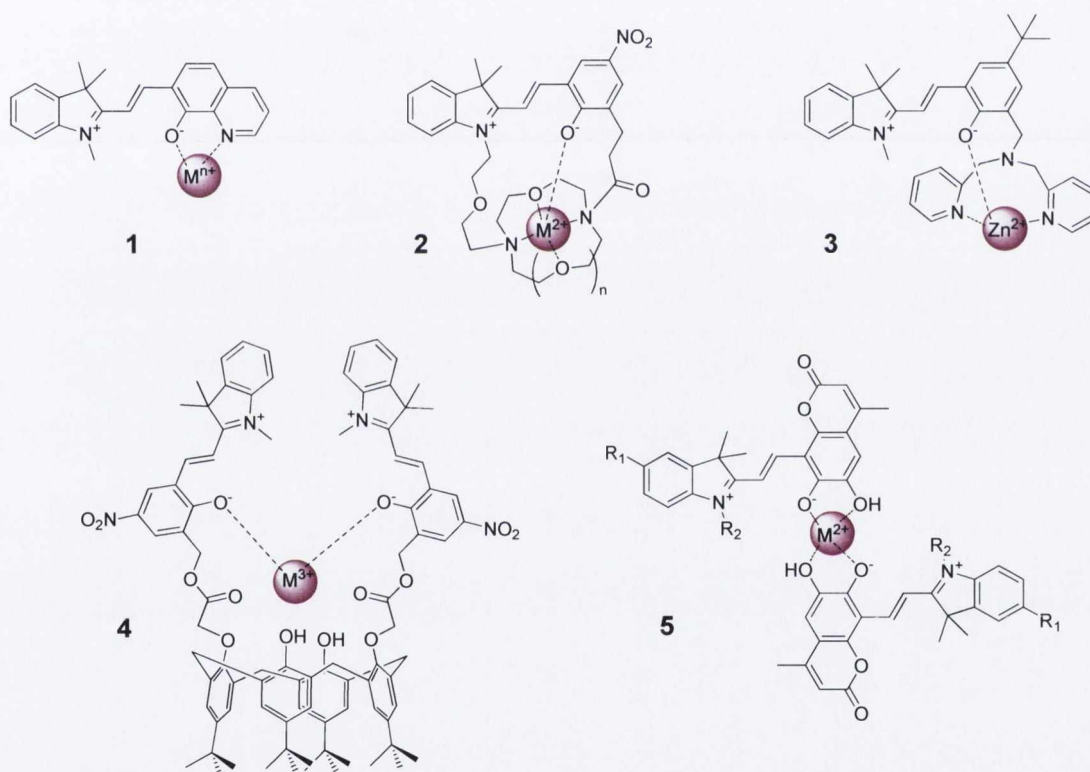


Figure 1.20: Examples of mono and bis SP based metal receptors. 1] First example of SP as ligand for metal cations. $M^{n+} = Cu^{2+}$ or Fe^{3+} .¹⁸⁶ 2] SP based cryptands with a diazacrown ether bridge. $M^{2+} =$ alkaline earth metals.¹⁸⁷ 3] SP with pendant bis(2-pyridylmethyl)amine (Dpa) chelating arms.¹⁸⁸ 4] SP calix[4]arene derivate carrying two spirobenzopyran moieties. $M^{3+} =$ lanthanides.¹⁸⁹ 5] SP derivatives with hydroxy group adjacent to the benzopyran oxygen. $M^{2+} = Mg^{2+}, Zn^{2+}, Ni^{2+}, Cu^{2+}, Hg^{2+}$ or Pd^{2+} . $R_1 = H, CH_3$ or NO_2 . $R_2 = CH_3, C_8H_{17}, CH_2Ph$ or $CH_2C(CH_3)_2$.¹⁹⁰

When a metal receptor is designed, the reversibility is one of the characteristic that has to be taken into consideration if versatility is needed. If then the receptor can be regenerated by a simple and fast stimulus, such as a light impulse, high performance devices can be envisaged. Recently in our group we reported a SP based fluorescent receptor that is selective towards Zn^{2+} ions and that is rapidly photo regenerated (Figure 1.21).¹⁹¹ When $Zn(ClO_4)_2$ is added to the SP solution, the metal pushes the equilibrium toward the open form isomer thus generating the reactive phenolate anion. The latter participates to the coordination of the electronically poor metal together with the accessible methoxy group. This receptor has shown to be highly selective and fully reversible upon visible light illumination, and the sequential conversion cycles between SP and ME-Zn are reported in the inset in Figure 1.21.

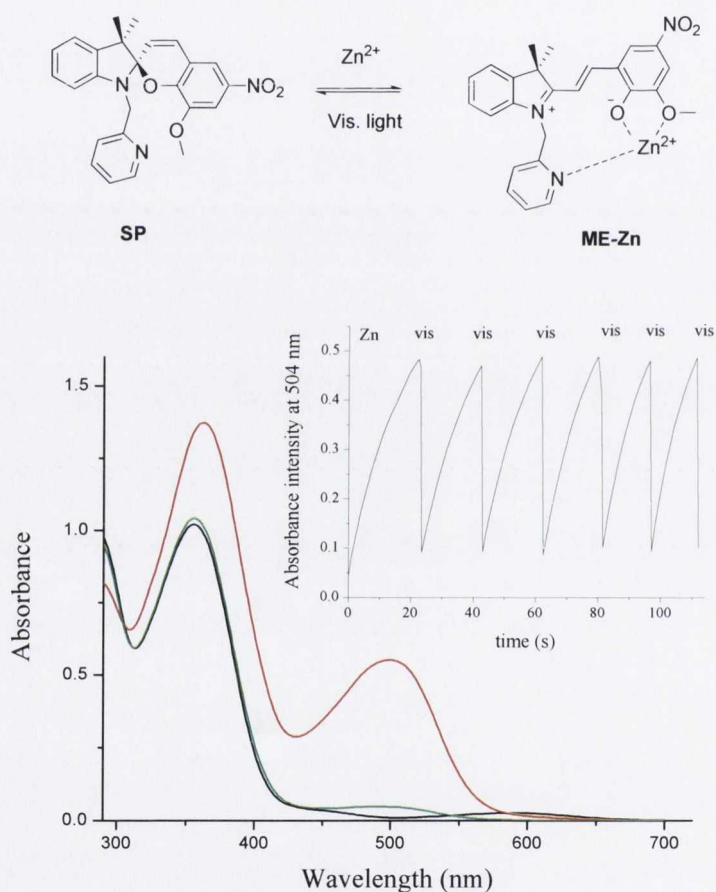


Figure 1.21: Reversible interconversion between the closed SP and a hypothetical merocyanine-zinc complex (ME-Zn). Absorption spectra of SP (black line), of SP added of 1 equiv of $Zn(ClO_4)_2$ (red line) and after the subsequent irradiation with Vis light (green line). Inset] Sequential cycles of conversion between SP and ME-Zn controlled by visible light [Image from ref.191].

Upon addition of Zn^{2+} the SP solution turned from colourless to deep orange as a result of the ME-Zn complex formation. This peculiarity can be used for the naked-eye detection of Zn(II) and offers promising versatility as it is robust with respect to a wide range of other metal ions.

Specific ionophore sites revealed to be indispensable in the SP structure to create a chelating moiety and thus facilitating the cation-ME interaction and promoting the photo-induced control of the metal ligation.¹⁹² Strong electron withdrawing groups (*e.g.* nitro) in *para* position with respect to the benzopyran oxygen, carboxylated chains in N indolic position and a methoxy group in the benzopyran 8' position have been proposed for (1) the release of the cation by Vis light,¹⁹³ (2) a higher flexibility and a more stable interaction with the metal cation¹⁹⁴ and (3) the cooperation with the phenolate anion in the chelation of the ion¹⁷⁷ respectively (Figure 1.22).

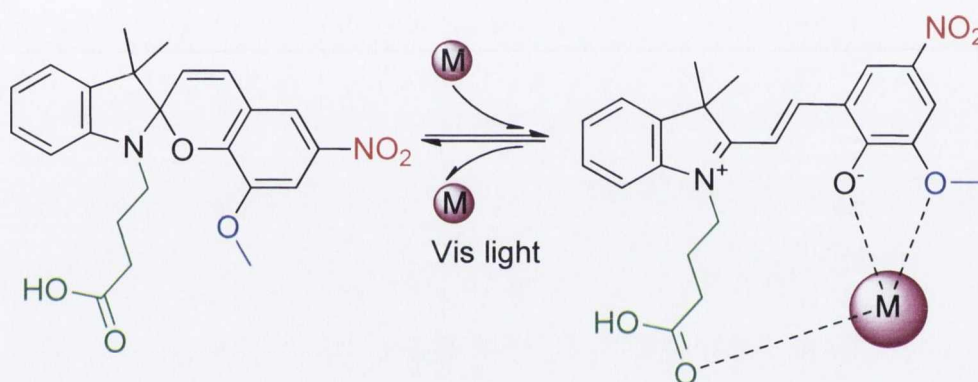


Figure 1.22: Essential ionophore sites in the SP structure for a facilitated metal cation ligation.

The uptake and the release of cationic species can be modulated by irradiation with light at different wavelengths in the visible range, and the metal complex formation can be easily detected by a distinctive optical signal¹⁸⁴ (*e.g.* band at 500 nm in Figure 1.21) and/or by the colour change of the solution upon addition of the metal (*e.g.* from colourless to orange).^{191,192} The light modulated reversible chelation of metals by a SP derivative opens the way for the use of such fluorescent and photoregenerable receptor for ion sensing applications.

On the light of these recent reports, in this thesis we will investigate the use of a SP derivative that bears the above mentioned ionophore sites as receptors for metal ions,

and Zn in the specific, when anchored to SWNTs (Chapter 4). The final aim of this nanosized SP-nanotube based material will not be the ion sensing, but the controlled release of the metal by light irradiation. In this way functionalized nanotubes will behave as novel light modulated delivery carriers of biologically important cations.

1.10 SP based receptors for organic molecules

SP derivatives have also been investigated as receptors for the recognition and quantification of biomolecules such as amino acids,^{179,180,195-197} nucleosides,^{198,199} glutathione²⁰⁰ and pyrophosphates.¹⁸⁸ However, if a comparison is made with the sensors developed for metal ions, the examples reported for the sensing of organic molecules are really limited.

In the eighties, the pioneering study of electrostatic interaction between the zwitterionic open form of SPs and amino acid (AA) molecules was reported, making photoresponsive SPs attractive candidates for the photo-controlled transport of AA across biological membranes (Figure 1.23).^{196,197}

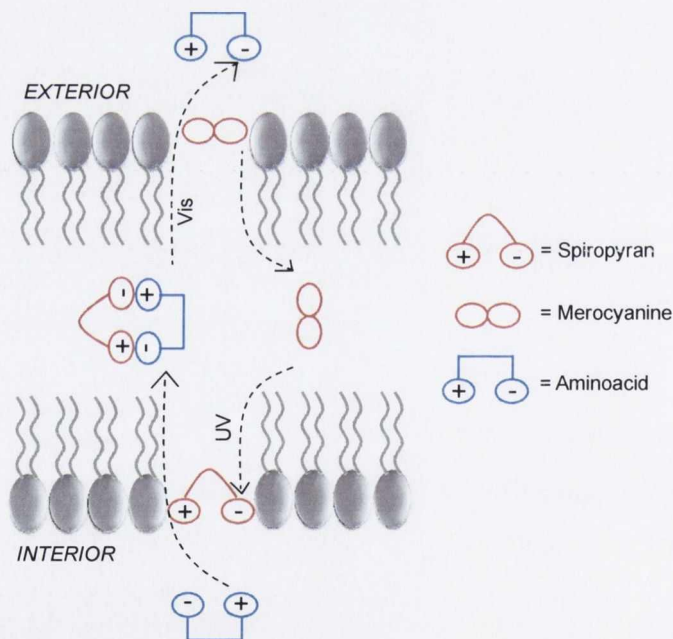


Figure 1.23: Schematic representation of amino acid transport across liposomal bilayers mediated by spiropyran.

Two decades later, the ability of SP to bind and release AA derivatives in a controlled way was demonstrated when the photoactive SP dyes are anchored to gold nanoparticles

(NP_{Au}).¹⁵⁹ The authors showed that upon irradiation, the SP molecules present at the first NP_{Au} shell can regulate the assembly ($\lambda_{\text{exc}} = 360 \text{ nm}$) and release ($\lambda_{\text{exc}} = 520 \text{ nm}$) of different AA derivatives that constitute the outer NP_{Au} layer (Figure 1.24). The photoswitching of the spiropyran anchored to gold nanoparticles (NP_{Au}-SP) was investigated in the presence of L-tryptophan, L-tyrosine, L-DOPA and R-methyl-L-DOPA. In dark conditions, the absorption of NP_{Au}-SP remained unaffected upon addition of AA solutions, thus excluding any ground state interactions. When the NP_{Au}-SP was irradiated with UV light ($\lambda_{\text{exc}} = 360 \text{ nm}$) the absorption band of the ME open form was observed as expected, and a quick ring closure was recorded afterwards. Interestingly when amino acid derivatives were added to the NP_{Au}-ME solution the ring closure was impeded, due to the two-point electrostatic interaction between the ME and the AA zwitterionic forms. This led to the formation of a complex (NP_{Au}-ME-AA complex in Figure 1.24) that can be dissociated and reconstituted upon photoirradiation with visible and UV light respectively. The light modulation of this NP_{Au}-ME-AA system opened the way to the design of controlled release drug delivery systems based on light controllable SP-based complexes.

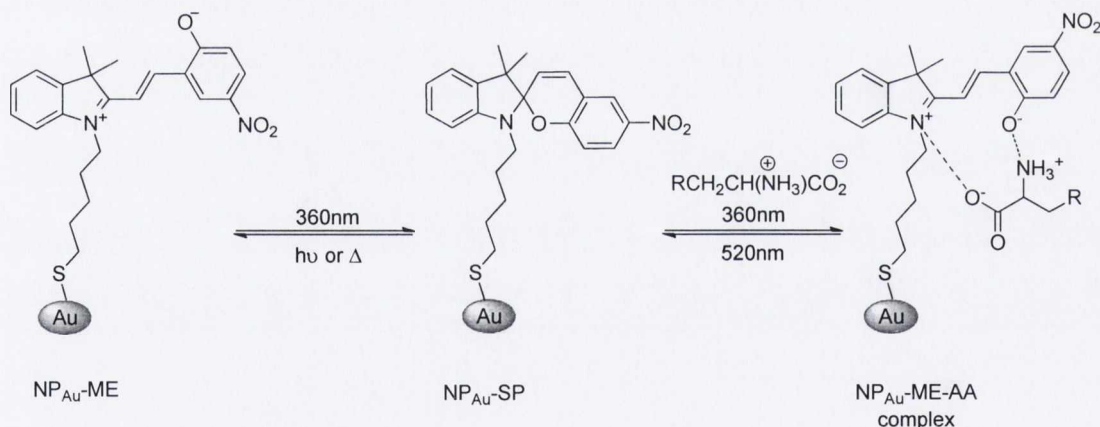


Figure 1.24: Schematic representations of the photochemical ring opening and closing of a spiropyran anchored to gold nanoparticles (NP_{Au}-SP) in the presence and absence of amino acid.

Later, the isomerization of a spiropyran derivative by an histidine (His) amino acid derivative dissolved in pure water was investigated (Figure 1.25),¹⁹⁵ and a simple method to recognise His through visual colour change of a SP solution after storage in the dark was presented.

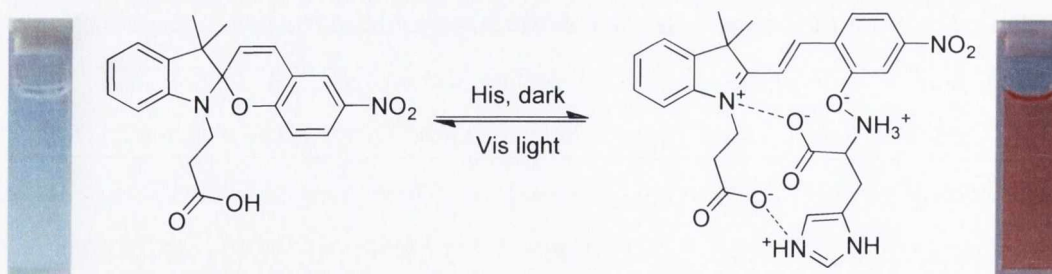


Figure 1.25: Proposed structure of the binary complex between ME and His, and pictures [taken from ref.195] of the colour changes in water by alternate exposure to darkness and visible light.

Last year the interaction of a novel SP receptor with thiol containing amino acids and with reduced glutathione (GSH) was investigated. The first selective SP based receptor for GSH was developed that shows strong fluorescence emission upon binding both in vitro and in vivo.²⁰⁰ Being the fluorescence output not strongly affected by cysteine, homocysteine and other thiol containing peptides this bis-SP sensor can be used as a marker of intracellular GSH in living cells. The molecular recognition, which is based on multipoint electrostatic interactions between the ME and the GSH, is reported in Figure 1.26 together with a confocal fluorescence microscope image (B) that shows the fluorescence of the SP molecule upon complexation with the GSH in cells.

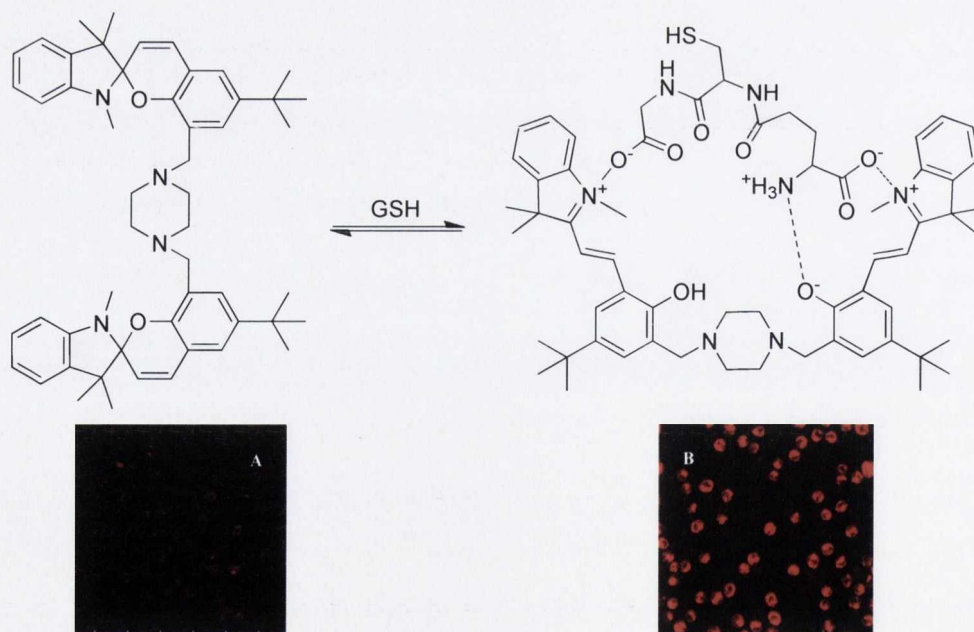


Figure 1.26: Complexation of GSH by a bis-SP and confocal microscope images [taken from ref.200] of human acute T cell leukemia A) without and B) with spiropyran.

Among the SP based receptors for nucleosides, in the early nineties the synthesis and coloration of a selective SP for guanosine (G) derivatives was reported for the first time.¹⁹⁹ The compound binds selectively the nucleoside through a triple hydrogen bond interaction between the acetamidopyridone unit of its ME open form and the guanine, as reported in Figure 1.27A. The so-called “recognition/structural change/signalling” receptor showed to dramatically change in its UV-Vis absorption spectrum upon interaction with guanosine derivatives, signalled by the appearance of a strong band at 550 nm. The same authors more recently developed a ferrocene-modified bis-SP derivative that acted as highly selective signalling receptor for guanine–guanine dinucleosides (GG). Also in this case the binding is governed by the hydrogen bonding complementarity between the ME isomer and the nucleoside. Upon addition of G or GG a strong absorption band in the visible region (575 nm) is observable and the solution turns red (Figure 1.27B).

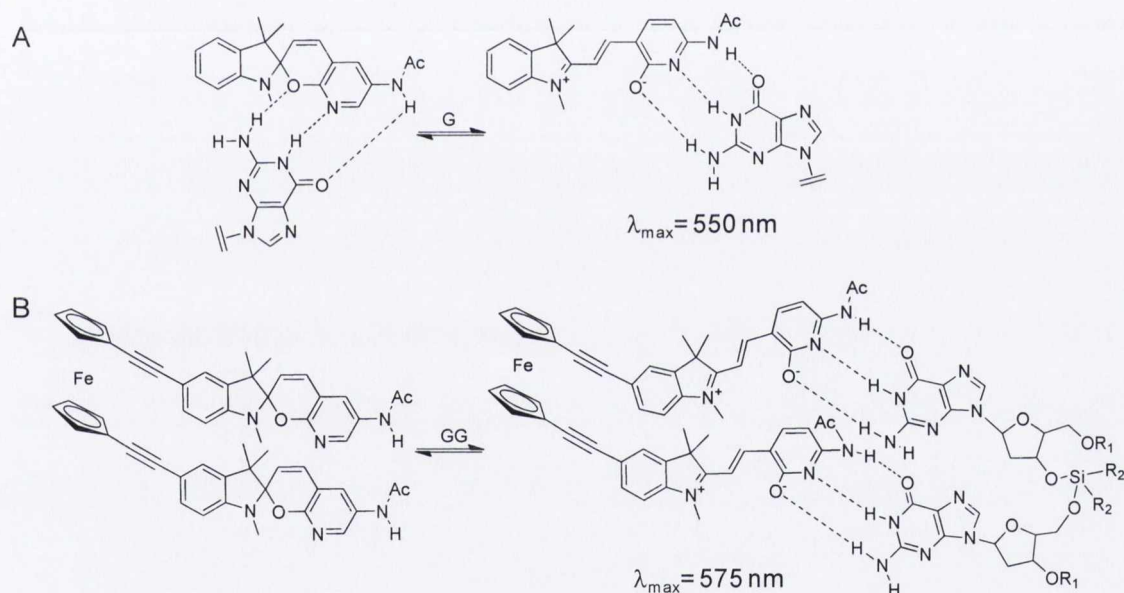


Figure 1.27: Triple hydrogen bond interaction between the open form isomer ME and guanosine derivatives. Molecular recognition of A] SP for guanosine (G) derivatives and B] ferrocene-modified bis-SP for guanine–guanine dinucleosides (GG).

1.11 SP-metal complex based receptors for organic molecules

A new strategy to recognise and quantify amino acids by SP derivatives has been introduced in 2006.¹⁸⁰ The interaction between cysteine (Cys) and homocysteine (Hcy)

with the photoactive dye showed to be weak in neutral aqueous conditions, but the ligation of a metal cation to the ME open form of the dye demonstrated to play a key role in the recognition process. In the proposed approach, mercury (Hg^{2+}) or copper (Cu^{2+}) have shown to be capable to bind both the SP and the AA molecules through a cooperative ligation, as depicted in Figure 1.28A. The recognition process is selective and sensitive toward Cys and Hcy over a number of amino acids, as evidenced by the changes in both absorption spectra and colour of the SP solutions upon addition of Hg^{2+} and different AA (Figure 1.28B).

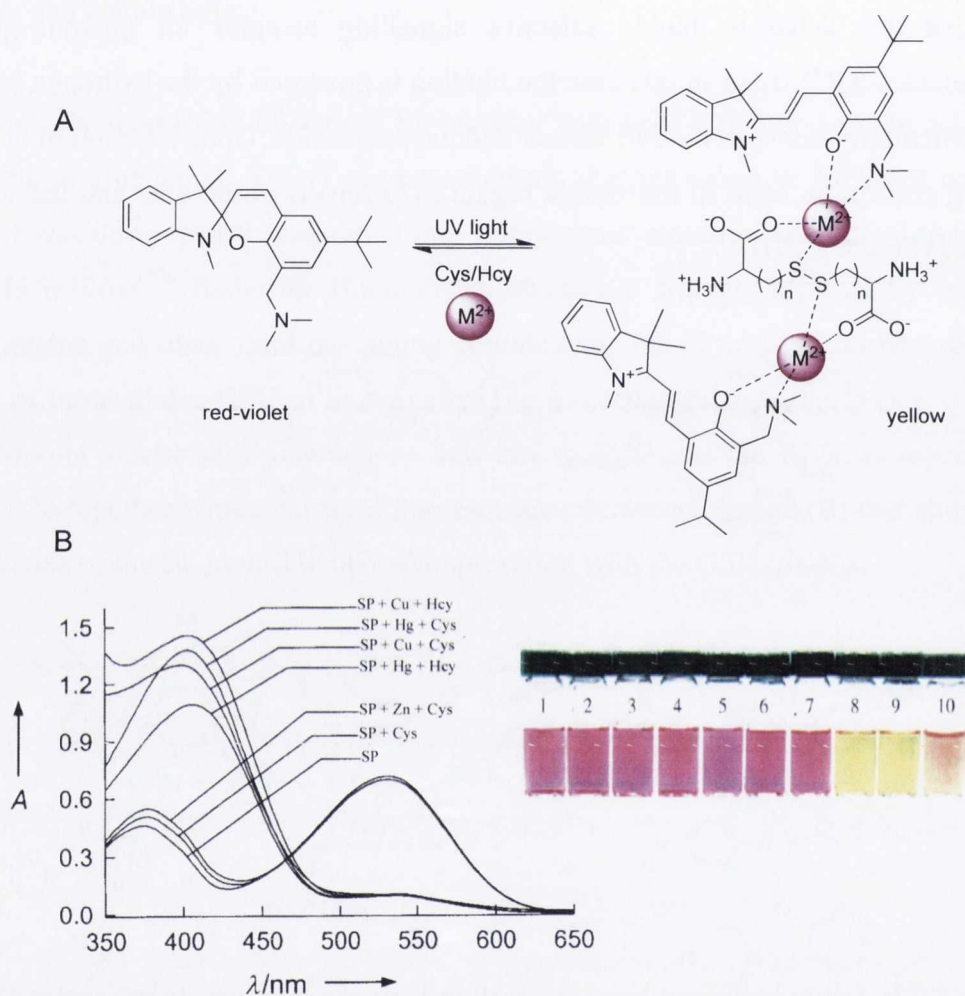


Figure 1.28: A] Proposed structure of the ternary complex containing two merocyanines, Cys ($n=1$) or Hcy ($n=2$) linked via disulfide bridge, and metal ions Hg^{2+} or Cu^{2+} . B] Effects of metal ions and amino acids on the absorption spectra of SP in 10% ethanol/water solution at neutral pH. Picture: Colour changes of ethanol/water solutions containing the SP and Hg^{2+} in the presence of: 1] no AA, 2] Gly, 3] Leu, 4] His, 5] Glu, 6] Asp, 7] Met, 8] Cys, 9] Hcy, and 10] GSH (glutathione) [Figure B adapted from the original in ref.180].

When the three components (SP, metal and AA) exist together the selectivity of interaction has shown to be determined by the binding affinity between the metal ion and the AA, as well as the relative size of the analyte. The effect of different ligation functions at the 8'-position of the spiropyran skeleton on the capability of sensing diverse metal ions, when an amino acid intermediate is present in solution, have been examined by the same authors.¹⁷⁹ It turned out that, in the presence of Cys, the Dpa substituted merocyanine (derivative 3 in Figure 1.20) responds with high sensitivity and specificity toward Hg^{2+} , thus opening the way to direct sensing and detection of metal ions in aqueous solution.

SP with pendant bis(2-pyridylmethyl)amine (Dpa) chelating arms is capable to form a complex with Zn^{2+} in aqueous solution, and this metal complexation favours the selective ligation of a pyrophosphate anion (PPi).¹⁸⁸ The cooperative ligation interactions between the metal ion and the organic molecules are reported in Figure 1.29A. The PPi is coordinated by two merocyanine-zinc (ME-Zn) units, and the formation of the ternary complex can be monitored by the decrease of fluorescence intensity at 630 nm (attributed to ME-Zn complex) together with the increase of the original ME fluorescence at 560 nm (Figure 1.29B).

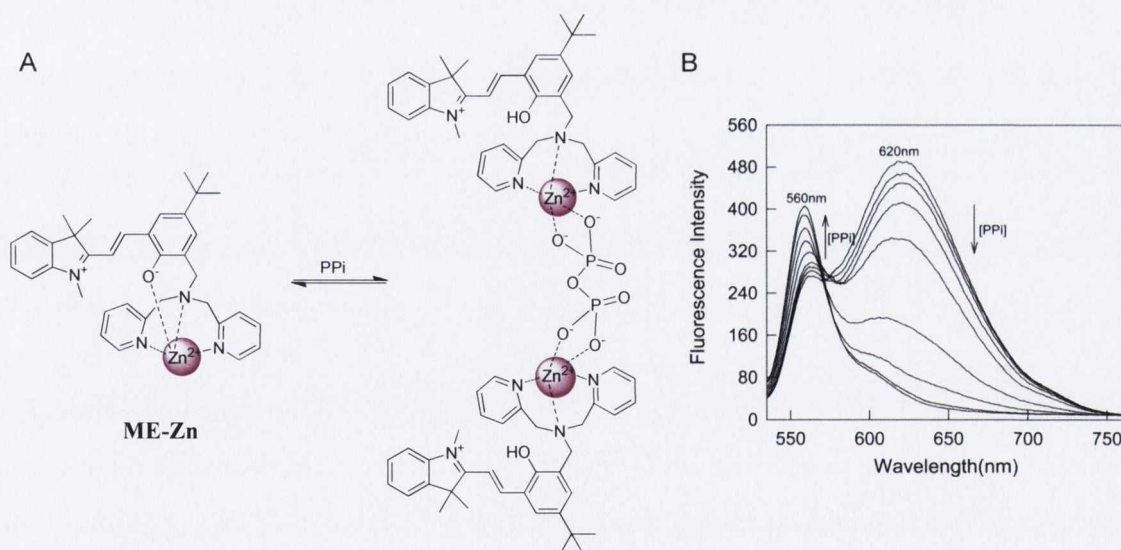


Figure 1.29: A) Proposed structure of the ternary complex containing two ME-Zn units and a PPi anion. B) Fluorescence emission spectra of the ME-Zn complex upon addition of increasing concentrations of PPi . The signal changes are indicated by the arrows [Figure B from ref.188].

The long wavelength excitation and emission of the ME-Zn complex reported here, opens the way for potential in vivo screening applications of SP based receptors.

On the light of these relevant reports, in Chapter 4 of this thesis a SP based fluorescent receptor that selectively and reversibly chelates Zn^{2+} ions will be investigated as potential photo-modulated delivery system of biologically important molecules when anchored to SWNTs.

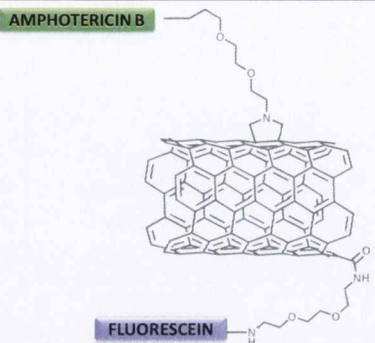
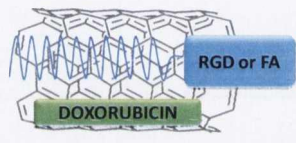
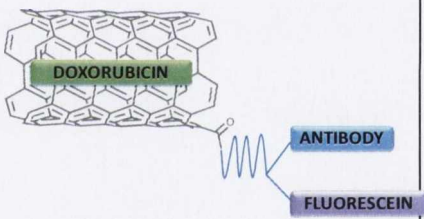
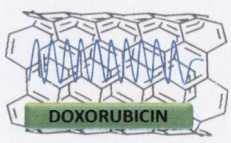
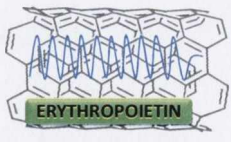
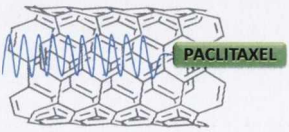
1.12 Bioactive organic molecules on SWNTs

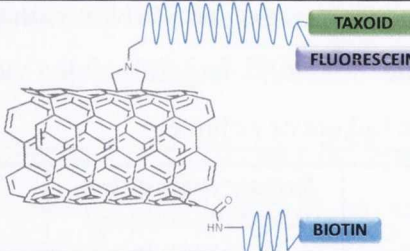
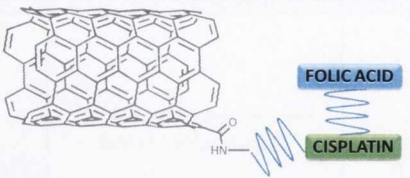
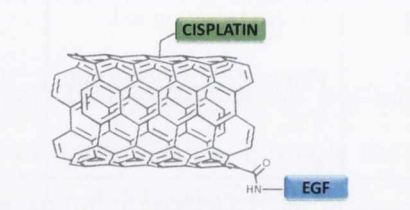
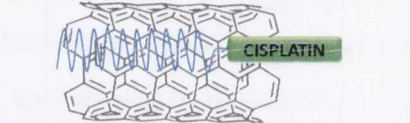

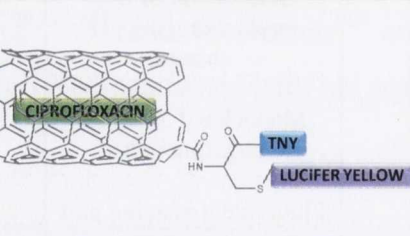

SWNTs have shown the ability to transport biologically active payloads across cell membranes.^{24,26} Even if the mechanism of translocation through the phospholipid bilayers is still controversial,^{25,28} direct and indirect proofs of the presence of SWNTs inside cells have been reported.^{23,24,27,201} Moreover, given the capacity of SWNTs to interact with amino acids,¹¹⁵ proteins,²⁰¹⁻²⁰³ carbohydrates,²⁰⁴ polymers,²⁰⁵ DNA,^{24,206-208} siRNA,²⁰⁹ genes²¹⁰ and drugs^{25,211,212} the applications in medicinal chemistry and biology are consequently of pronounced interest.^{30,213,214}

Drug delivery,^{95,214-217} targeting therapy^{39,211,218} and biosensing²⁰⁶ are only some examples of the promising applications that SWNTs enriched with bio active molecules have been proposed and explored for.⁴⁰

The advantage of SWNTs covalent and non covalent functionalization with variable size and type cargos, allows the rational design of nanosized carriers of pharmaceutically active molecules. Moreover, nanotubes can be strategically enriched with different functional groups to bear targeting, imaging and therapeutic moieties at the same time, as reported in many recently published works.^{30,40,214,215,219} Covalent, non covalent or encapsulation approaches are the different functionalization strategies applied to couple pharmaceutical active agents to SWNTs, and the examples reported so far of such functional nanovectors are summarized in Table 1.2. The exploration of SWNTs as carriers of pharmaceutically active payloads is still in its early days and, as a consequence, the design and the realization of new drug delivery composites is highly appealing.

Table 1.2: Functionalization of SWNTs with pharmaceutical active agents (green box), imaging (purple box) and targeting (blue box) units. The blue wavy line indicates diverse organic linkers or polymers.

<i>Drug and properties</i>	<i>Release mechanism, targeting/imaging approach</i>	<i>Material</i>	<i>Reference</i>
<i>Amphotericin B</i> [antimycotic]	Enzymatic cleavage of the covalent bond No targeting unit Fluorescein imaging unit		25,220
<i>Doxorubicin</i> [anti-cancer]	Detachment of π - π stacked drug by pH change RGD (Arg-Gly-Asp) or FA (folic acid) targeting unit No imaging unit		221-223
	Detachment of π - π stacked drug by pH change Monoclonal antibody targeting unit Fluorescein imaging unit		224
	Detachment of π - π stacked drug by pH change or NIR laser irradiation No targeting/imaging units		225,226
<i>Erythropoietin (EPO)</i> [performance-enhancing]	Detachment of π - π stacked drug by pH change No targeting/imaging units		227
<i>Paclitaxel (Taxol®)</i> [anti-cancer]	Enzymatic cleavage of the covalent bond No targeting/imaging units		228

<p><i>Taxoid</i> [anti-cancer]</p>	<p>Enzymatic cleavage of the covalent bond</p> <p>Biotin targeting unit</p> <p>Fluorescein imaging unit</p>		<p>219</p>
<p><i>Cisplatin</i> [anti-cancer]</p>	<p>Enzymatic cleavage of the covalent bond</p> <p>Folic acid targeting unit</p> <p>No imaging unit</p>		<p>211</p>
	<p>Enzymatic cleavage of the covalent bond</p> <p>Epidermal growth factor (EGF) targeting unit</p> <p>No imaging unit</p>		<p>229,230</p>
	<p>Enzymatic reduction</p> <p>No targeting/imaging units</p>		<p>212</p>
	<p>Release with time</p> <p>No targeting/imaging units</p>		<p>231</p>
<p><i>Ciprofloxacin</i> [bactericide]</p>	<p>Release by NIR radiation</p> <p>EphB4-binding peptide (TNY) targeting unit</p> <p>Lucifer yellow imaging unit</p>		<p>232</p>
<p><i>Amantadine</i> [antiparkinson]</p>			
<p><i>Metformin</i> [antidiabetic]</p>			
<p><i>Gabapentin</i> [antiepileptic]</p>			
<p><i>Betahistine</i> [antivertigo]</p>	<p>Enzymatic cleavage of the covalent bond</p> <p>No targeting/imaging units</p>		<p>217</p>
<p><i>Dipyridamol</i> [antiplatelet]</p>			
<p><i>Lisinopril</i> [antihypertensive]</p>			
<p><i>Atorvastatin</i> [antilipemic]</p>			

The exploitation of the properties of nanotubes as nanovectors has been primarily applied for the delivery of anticancer drugs to specific cancer cells.^{211,214,219,233-235} Amino acids,^{232,233} antibodies^{224,234} and vitamins such as folic acid²¹¹ and biotin²¹⁹ have been conjugated to SWNTs functionalized with anti-tumoral drugs or prodrugs, for the development of tumor-targeted drug delivery system (DDS). In the above-mentioned cases, the lock and key interaction between the substrate and the receptor present on nanotubes and on cancer cells respectively, permits the specific binding and local action of drugs attached to the tubes surface. In theory an analogous targeted-delivery approach can be used to load a variety of pharmaceutically active molecules onto nanotubes constructs if specific receptors are known to be expressed in tissues affected by abnormal functioning.

Although the investigation onto selective binding sites and complementary substrates is not within the interest of this thesis, the elegant example of multifunctional nanotube based vehicle for tumor-targeted therapy is worth to mention.²¹⁹ Besides the synthesis and full characterization of the material, the study of interaction and release of the active molecules inside the cells have also been demonstrated. Figure 1.30A depicts a schematic illustration of the steps involved in the transport and release of the taxol derivative inside a tumor cell by a SWNT carrier. The internalization of the functionalized nanotube vector is made possible by the selective binding of biotin to the cell membrane that triggers the receptor-mediated endocytosis. Once the f-SWNT is inside, the drug can be released following cleavage of the disulfide linker by intracellular GSH and explicate its action, which consists in the block of the mitotic process and in the promotion of the apoptosis by stabilization of the microtubules. A fluorescent label was anchored to the taxoid to monitor the presence of the drug in the living system with time. Confocal fluorescence microscopy images of cells incubated with the biotin-SWNT-(taxoid-fluorescein) conjugate are reported in Figure 1.30B. The images refer to cells incubated before (top) and after (bottom) the addition of the cleavage agent GSH: the binding of the microtubules stands out in the second case, thus confirming the achievement of the targeted therapeutic effect.

These results together with the one summarized in Table 1.2 laid the foundations for the development of more complex multifunctional drug delivery vectors based on SWNTs. No matter if the latter are functionalized with a specific recognition unit into their surface, DDSs necessitate to (1) be constituted by a biocompatible platform, and

(2) be conjugated with a drug or prodrug that can be easily released and explicate its action *in situ*.

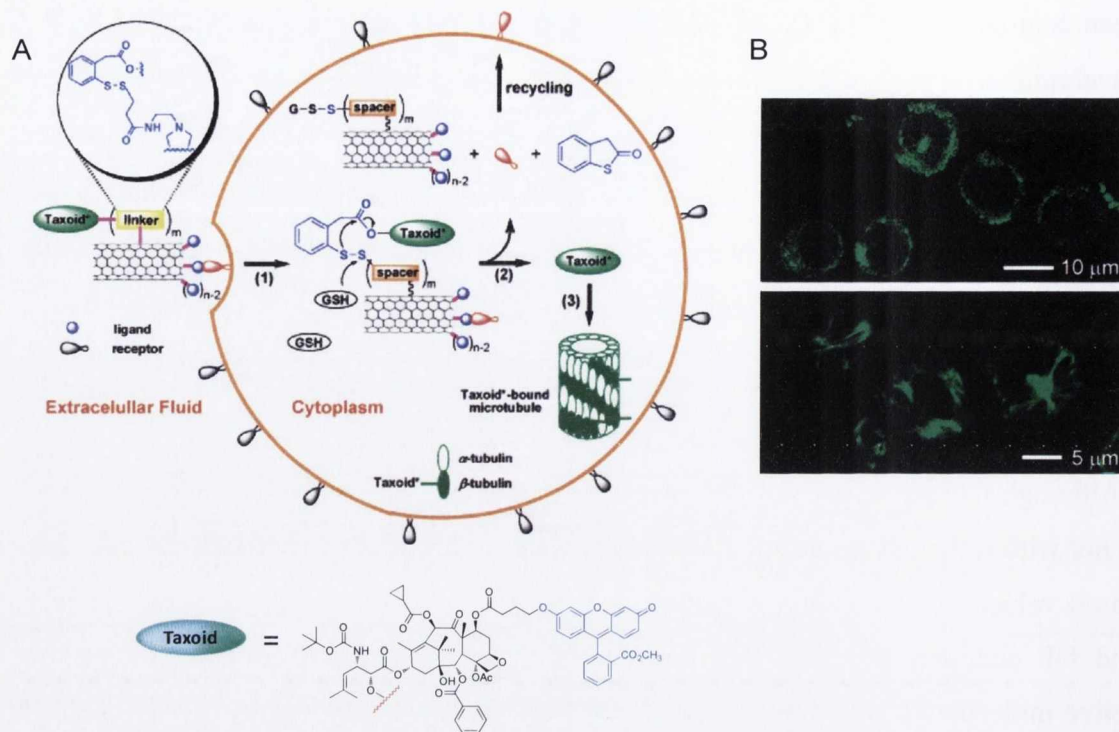


Figure 1.30: A] Steps involved in the tumor-targeting drug delivery of taxoid-SWNT-biotin conjugate inside a tumor cell. (1) Internalization of the functionalized nanotube vector, (2) cleavage of the disulfide linker and release of the drug, (3) binding of the free anticancer drug to microtubules. B] Confocal fluorescence microscopy images of cells incubated with the biotin-SWNT-taxoid-fluorescein before (top) and after (bottom) addition of GSH. [Figures adapted from ref.219].

As emphasized by a number of progresses reported by renowned research groups,^{30,40,213,218,235,236} the use of nanotubes in medicine is at a crossroads where the concrete applications will depend on the risk-benefit ratio they pose. Even if dissenting opinions still exist, the chemical modification of SWNTs surface with organic functional groups has proven to be a valid approach to improve their biocompatibility, as SWNTs become non-immunogenic when are shortened, functionalized and/or water dispersible.^{23,40,93,94,237-239} Additionally, irrespectively of which functionality they are covalently enriched, SWNTs have shown the ability to be internalized by a wide variety of cell types and to traffic through different cell barriers,²⁵ which is of great importance if new functional nanomaterials are aimed to be used as DDS.

In the present research work, and specifically in Chapter 4, we investigate the use of sidewall covalent functionalized SWNTs by SP derivative as potential DDS for anti-inflammatory agents, where their release mechanism will be ruled by light radiation.

1.13 Aims of this work

Over the last years the applications of chemically modified carbon nanotubes have considerably expanded and progressed in both material and biomedical science. A vast number of SWNTs based materials have been rationally designed and synthesized to combine specific properties of different matters in a single nanoplatform. However, there is still plenty of room for the realization of smart SWNTs composites constituted by molecular devices able to respond to external stimuli with a degree of “intelligence”.

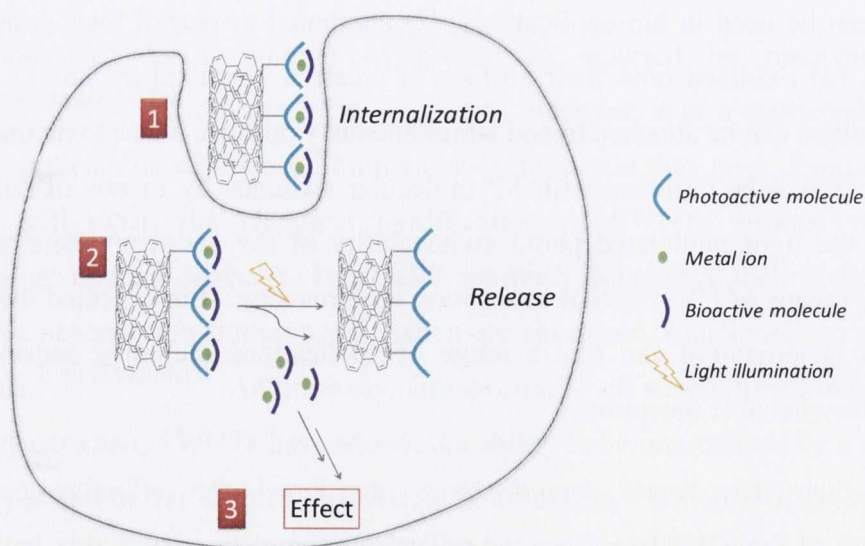
The main aim of our research project involves the development of novel nanosized and photoresponsive SP/SWNT based materials which unique switching and caging properties are regarded as promising for applications in sensing and drug delivery.

SWNTs cannot be easily manipulated because of their lack of solubility in common solvents and this represents a significant limitation towards their extensive use, especially if the final aim is the application of SWNTs as carriers of biologically active molecules. To overcome this problem the first task of this thesis will be the rational design of a chemical functionalization protocol of SWNTs with different length polyoxyethylene chain with the aim of enhancing the debundling process and simultaneously create water soluble (or dispersible) f-SWNTs. Before the enrichment with hydrophilic spacers, SWNTs will be (1) purified to have a material free of metal catalysts that can be used in bio applications, (2) shortened to permit their easier cell internalization, (3) oxidized onto their surface to create a chemical anchor to which other functionalities can be attached to and simultaneously produce a less toxic material. Finally the tubes will be enriched with SP molecular switches by means of coupling reactions, and the light modulated photo switchability of the nanocomposite will be investigated by means of UV-Vis/NIR absorption spectroscopy. It is expected that such modular smart nanomaterial can find a range of applications including sensing and reversible photoswitchable receptors.

Considering then that recent reports have questioned the effective covalent functionalization of the SWNTs surface we will also attempt to answer this important

question beside the investigation onto the preservation of optical and electronic properties of SWNTs after chemical treatments. In the specific, we will critically compare a batch of oxidized and functionalized SWNTs obtained by following two different chemical protocols. In the first the tubes will be subjected to the extensively reported 2-step purification/oxidation protocol and an exhaustive solvent washing, whereas in the second approach the purified SWNTs will be treated with aqueous NaOH solution before the second oxidative step. In both cases the oxidized SWNTs will be further functionalized with a fluorescent label in order to compare the final materials. We believe that the resulting findings will be extremely relevant for the nanotube community, bearing in mind that the decoration of the nanotube surface with carboxylic groups has been and still is one of the most utilized anchors for the further chemical functionalization *via* amidation and esterifications reactions.

Another objective of our research will be the functionalization of a highly pure SWNT material on its sidewalls by a SP based receptor that can act as a light modulated caging platform for metal ions and small organic molecules. We will utilize a SP based fluorescent receptor, developed in our lab that has shown to chelate reversibly Zn^{2+} ions. In parallel, we will investigate the formation of a supramolecular complex between SP, Zn^{2+} ions and a nonsteroidal anti-inflammatory drug (NSAID) by absorption and emission spectroscopies combined with mass spectrometry and 1H -NMR. Finally the light modulated release of Zn^{2+} and NSAID from the SP derivative anchored to SWNTs will be examined, and the outcome will be transferred to the fluorescent receptor anchored to SWNTs. A pictorial representation of the envisaged process is reported here below:



The steps involved can be listed as (1) internalization of the drug delivery system based on SWNTs covalently functionalized with spiropyran photoactive molecules that carries bioactive metal ions and molecules, (2) release of metal ions and bioactive molecules from the SP triggered by irradiation with light, and (3) subsequent induction of a therapeutic effect by the released moieties.

The light modulated release of both Zn^{2+} and NSAID from the SP derivative would open promising opportunities in drug delivery especially when the photoactive molecule is anchored to an appropriate nanosized carrier such as SWNTs. To the best of our knowledge it would be the first time that a triad SP: Zn^{2+} : NSAID is reported (with or without a nanotube vector) and the first time that a SP based DDS is presented.

We hope that successful results from this work will contribute to the development of novel smart drug delivery systems based on light responsive covalently modified SWNTs composites.

1.14 Characterization techniques of SWNTs

Beside the production of a covalently chemically modified nanotube material, the further intent of this project was the development of a characterization procedure which could demonstrate a comprehensive picture of the structural, electronic and chemical properties of the material synthesised. To confirm the presence of functionality on the SWNTs structure several analytical techniques are commonly employed.^{6,16,47,240}

In this research project we use complementary spectroscopic and microscopic techniques together with thermal gravimetric analyses to characterize the raw, purified, oxidized and chemically modified SWNTs after every chemical step. Only in this way the assessment of their structural properties and behaviour in different solvents as well as their degree of purity, functionalization and dispersion can be valued.

In the paragraphs to follow the analytical techniques will be briefly presented and they will include: thermal gravimetric analysis (TGA), FT-IR, Raman, UV-Vis and UV-Vis/NIR absorption and NIR photoluminescence spectroscopies as well as atomic force and transmission electron microscopies.

1.14.1 Thermal gravimetric analysis (TGA)

TGA is a simple analytical technique that measures the weight loss of a material as a function of the temperature. This technique is used to obtain information on the SWNT purity, thermal stability and degree of functionalization. TGA measurements are generally conducted in air or in an inert atmosphere, such as helium, nitrogen or argon. The number of functionalities introduced on the SWNTs can be calculated under a nitrogen atmosphere by the equation reported later on in Chapter 2, as the burning process is limited to the chemical moieties bound to the nanotube graphitic structure. It is well documented that diverse functional groups on a surface show different thermal stabilities,⁸³ and typically the organic non-nanotube material decomposes below 600 °C. In air the whole graphitic structure is combustible, and the sample purity can therefore be evaluated using this method. The residual mass, also referred as ash content, consists mainly of metal particles coming from the catalyst. Figure 1.31 shows an example of thermogravimetric analysis run in air of purified SWNTs containing oxygenated functional groups on their surface. It is evident from the first derivative trace that the organic functionalities decompose rapidly and more effectively than the carbon framework (480 °C), and that the sample is free from residual metal catalyst as the residue left at 900 °C is nought.

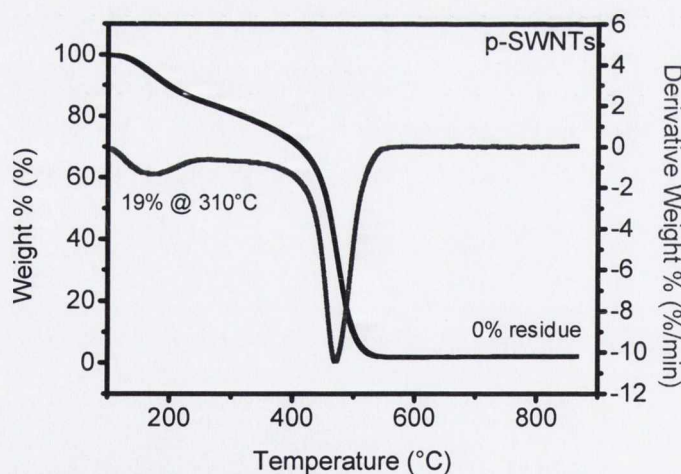


Figure 1.31: TGA measurements of purified nanotubes (p-SWNTs) showing weight change (black line) and its derivative (grey line). The weight loss % at 310 °C is attributed to the decomposition of organic groups in the nanotube samples, and the residue % at 900 °C to the metal content. The experiment is run in air atmosphere with a temperature rate of 10 °C min⁻¹.

1.14.2 Fourier transform infrared spectroscopy (FT-IR)

Infrared (IR) spectroscopy is a chemical analytical technique which measures the infrared intensity versus wavelength of light, detecting the vibration characteristics of chemical functional groups in a sample. Two different vibrational modes exist: stretching (rhythmical movement along the bond axes that leads to a variation in the interatomic distance) and bending (torsion and oscillation of the bonds with no change in the reciprocal atom position). Vibrational, rotational and conformational changes that lead to a rhythmic change of the molecular dipole moment can be observed in the IR. After irradiation with an IR source, a molecule tends to absorb the radiation in certain wavenumber ranges that are specific for the functional groups present in the structure. Therefore the resulting IR spectrum represents a molecular fingerprint of the sample.

SWNTs strongly absorb in the IR range, it is for this reason that very little information can be gained with regards to the vibrational properties of SWNTs with this technique. However the determination of chemical groups present in appropriate concentration on the nanotube structure can be successfully determined using this technique. Figure 1.32 compares FT-IR spectra of raw and oxidized SWNTs, where the stretching vibration assignable to C=O groups ($\sim 1720\text{ cm}^{-1}$) is clearly visible for o-SWNTS.

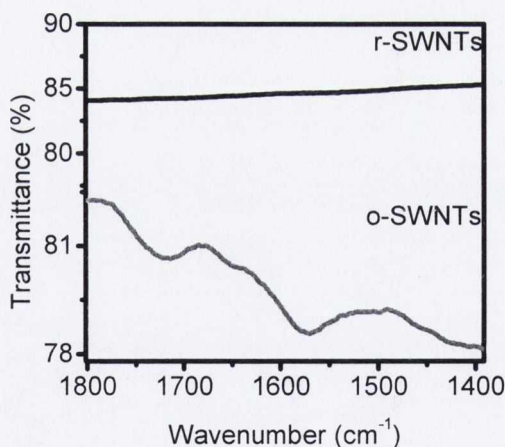


Figure 1.32: ATR/Fourier transform IR (FT-IR) transmittance spectra of raw (r-SWNTs) and oxidized (o-SWNTs) nanotube samples. The spectra have not been baseline corrected.

1.14.3 Raman spectroscopy

When electromagnetic radiation passes through matter, most of the radiation continues in its original direction but a small fraction is scattered in other directions. The redirection of light due to its interaction with matter is called *scattering* and may or may not occur with transfer of energy. The scattered radiation could have the same or a slightly different wavelength of the incoming light (Figure 1.33): light that is scattered at the same wavelength as the incoming light is called *Rayleigh scattering* and light that is scattered with a different wavelength is called *Stokes* or *Raman scattering*.

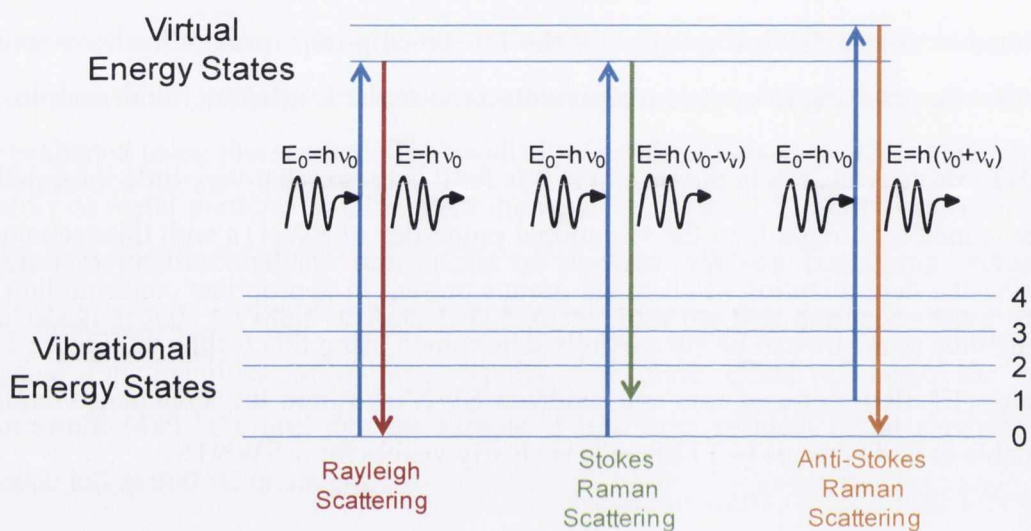


Figure 1.33: Rayleigh and Stokes Raman scattering.

In Raman Spectroscopy the radiation is emitted by a laser-beam which interacts with molecular roto-vibrational motions and the photon could re-emerge with a lower or a higher energy. In Raman spectra the *Stokes scattering* is observable and a fingerprint of the molecule under examination is easily obtainable. In order to be Raman active a molecule needs to display a variation in molecular polarizability.

Raman spectroscopy is one of the most extensively employed methods for the characterization of carbon nanotubes²⁴¹⁻²⁴³ and it gives information about impurities, tube damage and disorder, degree of functionalization, diameter and chirality of the nanotubes analyzed. Furthermore it is a fast and non-destructive technique without the need for complex sample preparation. As an example Figure 1.34 shows a Raman

spectrum from 100 to 4000 cm^{-1} taken from SWNTs that were produced by catalytic decomposition of carbon monoxide (HiPco-process).

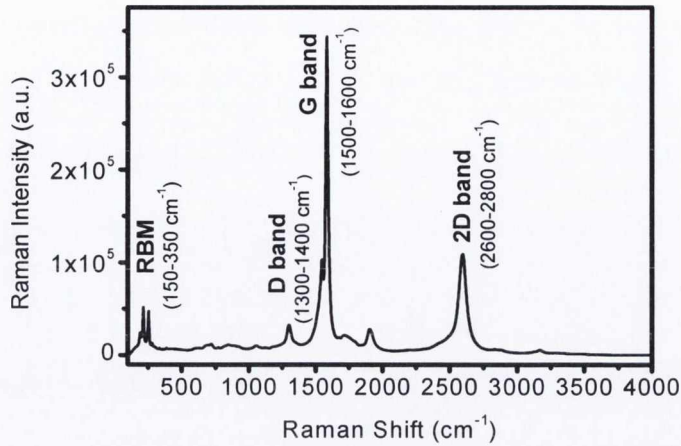


Figure 1.34: Raman spectrum of HiPco [batch R0546 Unidym[®]] SWNTs using a laser wavelength of $\lambda_{\text{exc}} = 633 \text{ nm}$.

The most significant spectral features observable in a Raman spectrum of SWNTs are:

- the radial breathing mode (RBM) band ($150\text{-}350 \text{ cm}^{-1}$), which corresponds to the radial vibration of the carbon atoms in phase.²⁴⁴ It is unique to single-walled carbon nanotubes and it enables SWNTs diameter measurements with the following equation:

$$\omega_{RBM} = \frac{A}{d} + B$$

The constants A and B can have variable values, which are attributed to environmental effects.²⁴⁵ Assuming the presence of individual freestanding tubes values of $A=204 \text{ cm}^{-1}$ and $B=27 \text{ cm}^{-1}$ have been determined.²⁴⁶

From the RBM values and the Kataura plot⁵⁶ the electronic properties of the nanotubes resonant for a given excitation wavelength can be also deduced.

- the D-band ($1300\text{-}1400 \text{ cm}^{-1}$), also called the “disorder” band that is activated when the symmetry of the graphitic structure is disrupted. This can be due to the introduction of defects and edge planes on the nanotube sp^2 -hybridized carbon network, and to the increase of sp^3 -hybridized carbon content. Being a defect induced signal, it is supposed to change proportionally with the degree of covalent functionalization.²⁴⁷

- the G-band (1500-1600 cm^{-1}), also called “tangential” mode that is related to the tangential motion of the carbon atoms on the nanotube surface. It consists of two main sub-bands: the G^+ and the G^- , which relate to the axial and circumferential in plane vibrations in semiconducting nanotubes respectively.²⁴⁸ The G^- band allows the determination of the diameter distribution in the sample by the following equation:

$$\omega_{G^-} = 1591 - \frac{47.7}{d^2}$$

The distinction of semiconducting from metallic SWNTs is also possible from the analysis of the G^- band line shape: Breit-Wigner-Fano is metallic, Lorentzian is semiconducting.

- the 2D-band (2600-2800 cm^{-1}) which is the overtone of the D-band and that is a fingerprint of the graphitic structure, and is independent of disorder.²⁴⁹

The D- and G-bands intensity ratio (I_D/I_G) gives information about the degree of functionalization and the defects in the tubes. Usually it increases with the number of functionalities and defects introduced in the nanotube structure after chemical modification. In this thesis we take into consideration the I_D/I_G ratio as an indirect measure of the degree of functionalization.^{16,61,241,248}

1.14.4 Ultraviolet-visible (UV-Vis) and ultraviolet-visible-near infrared (UV-Vis/NIR) absorption spectroscopy

As already discussed in paragraph 1.3 of this introductory chapter, pristine SWNTs show characteristic bands in the UV-Vis and UV-Vis/NIR absorption spectra. Those bands are due to the transitions between the first and the second pair of van Hove singularities in the SWNTs density of states (Figure 1.4).⁹ It has been reported that after covalent chemical modification the SWNTs electronic structure changes because of the disruption of the carbon π -conjugation in the tube structure. Usually a high degree of functionalization results in the complete loss of the S_{11} , S_{22} and M_{11} features (Figure 1.5).¹² The analysis of SWNTs solutions by absorption spectroscopy is therefore a powerful technique to investigate into the preservation of their characteristic and unique electronic structure.

1.14.5 Near infrared photoluminescence (NIR-PL) spectroscopy

O'Connell *et al.* firstly observed that semiconducting SWNTs emit band gap photoluminescence (PL) in the NIR region when present as individual entities.⁵⁰ The possibility to assign optical transitions to specific SWNTs chiralities has confirmed that fluorescence is a valid method to assess nanotubes electronic configurations, as already shown in Figure 1.6 in paragraph 1.3 of this chapter.^{20,59}

The intensity of the NIR-PL of individual SWNTs can be affected by acid treatment, chemical reagents and metal ions. The quenching of the PL has shown to be completely reversible upon addition of base or chelating agents if it is a result of protonation reaction at the nanotube surface or metal complexation respectively.²⁵⁰⁻²⁵² On the contrary, irreversible quenching is observed if the SWNTs are exposed to diazonium salts.^{50,252,253} The investigation into quenching of the NIR-PL is therefore useful to examine the extent of defects onto the nanotube surface.

1.14.6 Atomic force microscopy (AFM) and transmission electron microscopy (TEM)

Atomic force microscopy (AFM) and transmission electron microscopy (TEM) are powerful tools to visualize the morphology and purity of SWNTs samples.¹⁶ In the present thesis, AFM topographic images are recorded to estimate the average length distribution of the oxidized and functionalized SWNTs, while TEM images are recorded to investigate the effectiveness of purification protocols in progressively removing catalyst impurities from the starting material.

References

- (1) Iijima, S. *Nature* **1991**, *354*, 56.
- (2) Iijima, S.; Ichihashi, T. *Nature* **1993**, *363*, 603.
- (3) Martin, N.; Guldi, D. M.; Echegoyen, L. *Chemical Communications* **2011**, *47*, 604.
- (4) Niyogi, S.; Hamon, M. A.; Hu, H.; Zhao, B.; Bhowmik, P.; Sen, R.; Itkis, M. E.; Haddon, R. C. *Accounts of Chemical Research* **2002**, *35*, 1105.
- (5) Tomanek, D.; Jorio, A.; Dresselhaus, M. S.; Dresselhaus, G. In *Carbon Nanotubes* 2008; Vol. 111, p 1.
- (6) Burghard, M. *Surface Science Reports* **2005**, *58*, 1.
- (7) Tans, S. J.; Devoret, M. H.; Dai, H. J.; Thess, A.; Smalley, R. E.; Geerligs, L. J.; Dekker, C. *Nature* **1997**, *386*, 474.
- (8) Kataura, H.; Kumazawa, Y.; Maniwa, Y.; Umezu, I.; Suzuki, S.; Ohtsuka, Y.; Achiba, Y. *Synthetic Metals* **1999**, *103*, 2555.
- (9) Itkis, M. E.; Niyogi, S.; Meng, M. E.; Hamon, M. A.; Hu, H.; Haddon, R. C. *Nano Letters* **2002**, *2*, 155.
- (10) Sgobba, V.; Guldi, D. M. *Chemical Society Reviews* **2009**, *38*, 165.
- (11) Ando, T. *NPG Asia Materials* **2009**, *1*, 17.
- (12) Chen, J.; Hamon, M. A.; Hu, H.; Chen, Y. S.; Rao, A. M.; Eklund, P. C.; Haddon, R. C. *Science* **1998**, *282*, 95.
- (13) Hirsch, A. *Angewandte Chemie-International Edition* **2002**, *41*, 1853.
- (14) Tasis, D.; Tagmatarchis, N.; Bianco, A.; Prato, M. *Chemical Reviews* **2006**, *106*, 1105.
- (15) Karousis, N.; Tagmatarchis, N.; Tasis, D. *Chemical Reviews* **2010**, *110*, 5366.
- (16) Singh, P.; Campidelli, S.; Giordani, S.; Bonifazi, D.; Bianco, A.; Prato, M. *Chemical Society Reviews* **2009**, *38*, 2214.
- (17) White, C. T.; Todorov, T. N. *Nature* **1998**, *393*, 240.
- (18) Berber, S.; Kwon, Y. K.; Tomanek, D. *Physical Review Letters* **2000**, *84*, 4613.
- (19) Treacy, M. M. J.; Ebbesen, T. W.; Gibson, J. M. *Nature* **1996**, *381*, 678.
- (20) Bachilo, S. M.; Strano, M. S.; Kittrell, C.; Hauge, R. H.; Smalley, R. E.; Weisman, R. B. *Science* **2002**, *298*, 2361.
- (21) Hecht, D. S.; Hu, L.; Irvin, G. *Advanced Materials* **2011**, *23*, 1482.
- (22) Hu, L.; Hecht, D. S.; Grüner, G. *Chemical Reviews* **2010**, *110*, 5790.
- (23) Shi Kam, N. W.; Jessop, T. C.; Wender, P. A.; Dai, H. *Journal of the American Chemical Society* **2004**, *126*, 6850.
- (24) Pantarotto, D.; Singh, R.; McCarthy, D.; Erhardt, M.; Briand, J. P.; Prato, M.; Kostarelos, K.; Bianco, A. *Angewandte Chemie-International Edition* **2004**, *43*, 5242.

- (25) Kostarelos, K.; Lacerda, L.; Pastorin, G.; Wu, W.; Wieckowski, S.; Luangsivilay, J.; Godefroy, S.; Pantarotto, D.; Briand, J. P.; Muller, S.; Prato, M.; Bianco, A. *Nature Nanotechnology* **2007**, *2*, 108.
- (26) Pantarotto, D.; Briand, J. P.; Prato, M.; Bianco, A. *Chemical Communications* **2004**, 16.
- (27) Jin, H.; Heller, D. A.; Sharma, R.; Strano, M. S. *Acs Nano* **2009**, *3*, 149.
- (28) Pogodin, S.; Baulin, V. A. *Acs Nano* **2010**, *4*, 5293.
- (29) Liu, Z.; Yang, K.; Lee, S.-T. *Journal of Materials Chemistry* **2011**, *21*, 586.
- (30) Kostarelos, K.; Bianco, A.; Prato, M. *Nature Nanotechnology* **2009**, *4*, 627.
- (31) Opatkiewicz, J.; LeMieux, M. C.; Bao, Z. N. *Acs Nano* **2010**, *4*, 2975.
- (32) Liu, C. H.; Wu, C. C.; Zhong, Z. *Nano Letters* **2011**, ASAP.
- (33) Guo, X. F.; Small, J. P.; Klare, J. E.; Wang, Y. L.; Purewal, M. S.; Tam, I. W.; Hong, B. H.; Caldwell, R.; Huang, L. M.; O'Brien, S.; Yan, J. M.; Breslow, R.; Wind, S. J.; Hone, J.; Kim, P.; Nuckolls, C. *Science* **2006**, *311*, 356.
- (34) Choi, W.; Hong, S.; Abrahamson, J. T.; Han, J. H.; Song, C.; Nair, N.; Baik, S.; Strano, M. S. *Nature Materials* **2010**, *9*, 423.
- (35) Lee, H. J.; Park, J.; Yoon, O. J.; Kim, H. W.; Lee, D. Y.; Kim, D. H.; Lee, W. B.; Lee, N.-E.; Bonventre, J. V.; Kim, S. S. *Nature Nanotechnology* **2011**, *6*, 121.
- (36) Jin, H.; Heller, D. A.; Kalbacova, M.; Kim, J. H.; Zhang, J. Q.; Boghossian, A. A.; Maheshri, N.; Strano, M. S. *Nature Nanotechnology* **2010**, *5*, 302.
- (37) Schnorr, J. M.; Swager, T. M. *Chemistry of Materials* **2011**, 646.
- (38) Bianco, A.; Kostarelos, K.; Prato, M. *Current Opinion in Chemical Biology* **2005**, *9*, 674.
- (39) Kam, N. W. S.; O'Connell, M.; Wisdom, J. A.; Dai, H. *Proceedings of the National Academy of Sciences of the United States of America* **2005**, *102*, 11600.
- (40) Liu, Z.; Tabakman, S.; Welsher, K.; Dai, H. J. *Nano Research* **2009**, *2*, 85.
- (41) Strano, M. S.; Boghossian, A. A.; Kim, W. J.; Barone, P. W.; Jeng, E. S.; Heller, D. A.; Nair, N.; Jin, H.; Sharma, R.; Lee, C. Y. *Mrs Bulletin* **2009**, *34*, 950.
- (42) Sahoo, N. G.; Rana, S.; Cho, J. W.; Li, L.; Chan, S. H. *Progress in Polymer Science* **2010**, *35*, 837.
- (43) Byrne, M. T.; Gun'ko, Y. K. *Advanced Materials* **2010**, *22*, 1672.
- (44) Singh, S.; Ray, S. S. *Journal of Nanoscience and Nanotechnology* **2007**, *7*, 2596.
- (45) De La Zerda, A.; Zavaleta, C.; Keren, S.; Vaithilingam, S.; Bodapati, S.; Liu, Z.; Levi, J.; Smith, B. R.; Ma, T. J.; Oralkan, O.; Cheng, Z.; Chen, X. Y.; Dai, H. J.; Khuri-Yakub, B. T.; Gambhir, S. S. *Nature Nanotechnology* **2008**, *3*, 557.
- (46) Ghosh, D.; Ghosh, P.; Tanemura, M.; Haysahi, A.; Hayashi, Y.; Shinji, K.; Miura, N.; Yusop, M. Z.; Asaka, T. *Chemical Communications* **2011**, *47*, 4980.

- (47) Belin, T.; Epron, F. *Materials Science and Engineering B-Solid State Materials for Advanced Technology* **2005**, *119*, 105.
- (48) Saito, R.; Dresselhaus, G.; Dresselhaus, M. S. *Imperial College Press, London* **1998**.
- (49) Joselevich, E. *Chemphyschem* **2004**, *5*, 619.
- (50) O'Connell, M. J.; Bachilo, S. M.; Huffman, C. B.; Moore, V. C.; Strano, M. S.; Haroz, E. H.; Rialon, K. L.; Boul, P. J.; Noon, W. H.; Kittrell, C.; Ma, J. P.; Hauge, R. H.; Weisman, R. B.; Smalley, R. E. *Science* **2002**, *297*, 593.
- (51) Liu, X.; Pichler, T.; Knupfer, M.; Golden, M. S.; Fink, J.; Kataura, H.; Achiba, Y. *Physical Review B* **2002**, *66*.
- (52) Strano, M. S.; Dyke, C. A.; Usrey, M. L.; Barone, P. W.; Allen, M. J.; Shan, H. W.; Kittrell, C.; Hauge, R. H.; Tour, J. M.; Smalley, R. E. *Science* **2003**, *301*, 1519.
- (53) Bahr, J. L.; Yang, J. P.; Kosynkin, D. V.; Bronikowski, M. J.; Smalley, R. E.; Tour, J. M. *Journal of the American Chemical Society* **2001**, *123*, 6536.
- (54) Charlier, J. C. *Accounts of Chemical Research* **2002**, *35*, 1063.
- (55) Bahr, J. L.; Tour, J. M. *Chemistry of Materials* **2001**, *13*, 3823.
- (56) Weisman, R. B.; Bachilo, S. M. *Nano Letters* **2003**, *3*, 1235.
- (57) Telg, H.; Maultzsch, J.; Reich, S.; Thomsen, C. *Physical Review B* **2006**, *74*.
- (58) Strano, M. S.; Doorn, S. K.; Haroz, E. H.; Kittrell, C.; Hauge, R. H.; Smalley, R. E. *Nano Letters* **2003**, *3*, 1091.
- (59) Ghosh, S.; Bachilo, S. M.; Weisman, R. B. *Nature Nanotechnology* **2010**, *5*, 443.
- (60) Haddon, R. C. *Science* **1993**, *261*, 1545.
- (61) Hamon, M. A.; Itkis, M. E.; Niyogi, S.; Alvaraez, T.; Kuper, C.; Menon, M.; Haddon, R. C. *Journal of the American Chemical Society* **2001**, *123*, 11292.
- (62) Haddon, R. C. *Journal of the American Chemical Society* **1987**, *109*, 1676.
- (63) Pillai, S. K.; Ray, S. S.; Moodley, M. *Journal of Nanoscience and Nanotechnology* **2007**, *7*, 3011.
- (64) Georgakilas, V.; Voulgaris, D.; Vazquez, E.; Prato, M.; Guldi, D. M.; Kukovecz, A.; Kuzmany, H. *Journal of the American Chemical Society* **2002**, *124*, 14318.
- (65) Rinzler, A. G.; Liu, J.; Dai, H.; Nikolaev, P.; Huffman, C. B.; Rodriguez-Macias, F. J.; Boul, P. J.; Lu, A. H.; Heymann, D.; Colbert, D. T.; Lee, R. S.; Fischer, J. E.; Rao, A. M.; Eklund, P. C.; Smalley, R. E. *Applied Physics a-Materials Science & Processing* **1998**, *67*, 29.
- (66) Chiang, I. W.; Brinson, B. E.; Huang, A. Y.; Willis, P. A.; Bronikowski, M. J.; Margrave, J. L.; Smalley, R. E.; Hauge, R. H. *Journal of Physical Chemistry B* **2001**, *105*, 8297.
- (67) Dillon, A. C.; Gennett, T.; Jones, K. M.; Alleman, J. L.; Parilla, P. A.; Heben, M. J. *Advanced Materials* **1999**, *11*, 1354.
- (68) Hu, H.; Zhao, B.; Itkis, M. E.; Haddon, R. C. *Journal of Physical Chemistry B* **2003**, *107*, 13838.

- (69) Zhao, B.; Hu, H.; Niyogi, S.; Itkis, M. E.; Hamon, M. A.; Bhowmik, P.; Meier, M. S.; Haddon, R. C. *Journal of the American Chemical Society* **2001**, *123*, 11673.
- (70) MacKenzie, K.; Dunens, O.; Harris, A. T. *Separation and Purification Technology* **2009**, *66*, 209.
- (71) Wang, Y. H.; Shan, H. W.; Hauge, R. H.; Pasquali, M.; Smalley, R. E. *Journal of Physical Chemistry B* **2007**, *111*, 1249.
- (72) Vivekchand, S. R. C.; Jayakanth, R.; Govindaraj, A.; Rao, C. N. R. *Small* **2005**, *1*, 920.
- (73) Dyke, C. A.; Tour, J. M. *Chemistry-a European Journal* **2004**, *10*, 813.
- (74) Campidelli, S.; Klumpp, C.; Bianco, A.; Guldi, D. M.; Prato, M. *Journal of Physical Organic Chemistry* **2006**, *19*, 531.
- (75) Britz, D. A.; Khlobystov, A. N. *Chemical Society Reviews* **2006**, *35*, 637.
- (76) Holzinger, M.; Baur, J.; Haddad, R.; Wang, X.; Cosnier, S. *Chemical Communications* **2011**, *47*, 2450.
- (77) Chung, C.-L.; Campidelli, S.; Filoramo, A. *Chemical Communications* **2010**, *46*, 6539.
- (78) Nakayama-Ratchford, N.; Bangsaruntip, S.; Sun, X. M.; Welsher, K.; Dai, H. J. *Journal of the American Chemical Society* **2007**, *129*, 2448.
- (79) Sprafke, J. K.; Stranks, S. D.; Warner, J. H.; Nicholas, R. J.; Anderson, H. L. *Angewandte Chemie International Edition* **2011**, *50*, 2313.
- (80) Banerjee, S.; Hemraj-Benny, T.; Wong, S. S. *Advanced Materials* **2005**, *17*, 17.
- (81) Prato, M. *Nature* **2010**, *465*, 172.
- (82) Hou, P. X.; Liu, C.; Cheng, H. M. *Carbon* **2008**, *46*, 2003.
- (83) Ros, T. G.; van Dillen, A. J.; Geus, J. W.; Koningsberger, D. C. *Chemistry – A European Journal* **2002**, *8*, 1151.
- (84) Liu, J.; Rinzler, A. G.; Dai, H. J.; Hafner, J. H.; Bradley, R. K.; Boul, P. J.; Lu, A.; Iverson, T.; Shelimov, K.; Huffman, C. B.; Rodriguez-Macias, F.; Shon, Y. S.; Lee, T. R.; Colbert, D. T.; Smalley, R. E. *Science* **1998**, *280*, 1253.
- (85) Marques, R. R. N.; Machado, B. F.; Faria, J. L.; Silva, A. M. T. *Carbon* **2010**, *48*, 1515.
- (86) Ziegler, K. J.; Gu, Z. N.; Peng, H. Q.; Flor, E. L.; Hauge, R. H.; Smalley, R. E. *Journal of the American Chemical Society* **2005**, *127*, 1541.
- (87) Romanos, G. E.; Likodimos, V.; Marques, R. R. N.; Steriotis, T. A.; Papageorgiou, S. K.; Faria, J. L.; Figueiredo, J. L.; Silva, A. n. M. T.; Falaras, P. *The Journal of Physical Chemistry C* **2011**, *115*, 8534.
- (88) Bonifazi, D.; Nacci, C.; Marega, R.; Campidelli, S.; Ceballos, G.; Modesti, S.; Meneghetti, M.; Prato, M. *Nano Letters* **2006**, *6*, 1408.
- (89) Bergeret, C.; Cousseau, J.; Fernandez, V.; Mevellec, J. Y.; Lefrant, S. *Journal of Physical Chemistry C* **2008**, *112*, 16411.

- (90) Hamon, M. A.; Chen, J.; Hu, H.; Chen, Y. S.; Itkis, M. E.; Rao, A. M.; Eklund, P. C.; Haddon, R. C. *Advanced Materials* **1999**, *11*, 834.
- (91) Bahr, J. L.; Tour, J. M. *Journal of Materials Chemistry* **2002**, *12*, 1952.
- (92) Kahn, M. G. C.; Banerjee, S.; Wong, S. S. *Nano Letters* **2002**, *2*, 1215.
- (93) Dumortier, H.; Lacotte, S.; Pastorin, G.; Marega, R.; Wu, W.; Bonifazi, D.; Briand, J.-P.; Prato, M.; Muller, S.; Bianco, A. *Nano Letters* **2006**, *6*, 1522.
- (94) Porter, A. E.; Gass, M.; Bendall, J. S.; Muller, K.; Goode, A.; Skepper, J. N.; Midgley, P. A.; Welland, M. *Acs Nano* **2009**, *3*, 1485.
- (95) Pastorin, G. *Pharmaceutical Research* **2009**, *26*, 746.
- (96) Giordani, S.; Colomer, J. F.; Cattaruzza, F.; Alfonsi, J.; Meneghetti, M.; Prato, M.; Bonifazi, D. *Carbon* **2009**, *49*, 578.
- (97) Bottini, M.; Magrini, A.; Di Venere, A.; Bellucci, S.; Dawson, M. I.; Rosato, N.; Bergamaschi, A.; Mustelin, T. *Journal of Nanoscience and Nanotechnology* **2006**, *6*, 1381.
- (98) Asuri, P.; Bale, S. S.; Pangule, R. C.; Shah, D. A.; Kane, R. S.; Dordick, J. S. *Langmuir* **2007**, *23*, 12318.
- (99) Piran, M.; Kotlyar, V.; Medina, D. D.; Pirlot, C.; Goldman, D.; Lellouche, J.-P. *Journal of Materials Chemistry* **2009**, *19*, 631.
- (100) Gu, L.; Elkin, T.; Jiang, X.; Li, H.; Lin, Y.; Qu, L.; Tzeng, T.-R. J.; Joseph, R.; Sun, Y.-P. *Chemical Communications* **2005**, 874.
- (101) Banerjee, S.; Kahn, M. G. C.; Wong, S. S. *Chemistry-a European Journal* **2003**, *9*, 1899.
- (102) Wu, W.; Zhu, H.; Fan, L.; Yang, S. *Chemistry – A European Journal* **2008**, *14*, 5981.
- (103) Seyferth, D. *Accounts of Chemical Research* **1972**, *5*, 65.
- (104) Haddon, R. C.; Chichester, S. V.; Stein, S. M.; Marshall, J. H.; Muijsce, A. M. *The Journal of Organic Chemistry* **1987**, *52*, 711.
- (105) Srivastava, D.; Brenner, D. W.; Schall, J. D.; Ausman, K. D.; Yu, M.; Ruoff, R. S. *The Journal of Physical Chemistry B* **1999**, *103*, 4330.
- (106) Dyke, C. A.; Tour, J. M. *Journal of Physical Chemistry A* **2004**, *108*, 11151.
- (107) Pehrsson, P. E.; Zhao, W.; Baldwin, J. W.; Song, C. H.; Liu, J.; Kooi, S.; Zheng, B. *Journal of Physical Chemistry B* **2003**, *107*, 5690.
- (108) Mickelson, E. T.; Huffman, C. B.; Rinzler, A. G.; Smalley, R. E.; Hauge, R. H.; Margrave, J. L. *Chemical Physics Letters* **1998**, *296*, 188.
- (109) Hu, H.; Zhao, B.; Hamon, M. A.; Kamaras, K.; Itkis, M. E.; Haddon, R. C. *Journal of the American Chemical Society* **2003**, *125*, 14893.
- (110) Holzinger, M.; Abraham, J.; Whelan, P.; Graupner, R.; Ley, L.; Hennrich, F.; Kappes, M.; Hirsch, A. *Journal of the American Chemical Society* **2003**, *125*, 8566.

- (111) Leinonen, H.; Rintala, J.; Siitonen, A.; Lajunen, M.; Pettersson, M. *Carbon* **2010**, *48*, 2425.
- (112) Chen, Y.; Haddon, R. C.; Fang, S.; Rao, A. M.; Lee, W. H.; Dickey, E. C.; Grulke, E. A.; Pendergrass, J. C.; Chavan, A.; Haley, B. E.; Smalley, R. E. *Journal of Materials Research* **1998**, *13*, 2423.
- (113) Coleman, K. S.; Bailey, S. R.; Fogden, S.; Green, M. L. H. *Journal of the American Chemical Society* **2003**, *125*, 8722.
- (114) Georgakilas, V.; Kordatos, K.; Prato, M.; Guldi, D. M.; Holzinger, M.; Hirsch, A. *Journal of the American Chemical Society* **2002**, *124*, 760.
- (115) Georgakilas, V.; Tagmatarchis, N.; Pantarotto, D.; Bianco, A.; Briand, J. P.; Prato, M. *Chemical Communications* **2002**, 3050.
- (116) Delgado, J. L.; de la Cruz, P.; Langa, F.; Urbina, A.; Casado, J.; Navarrete, J. T. L. *Chemical Communications* **2004**, 1734.
- (117) Pekker, S.; Salvétat, J. P.; Jakab, E.; Bonard, J. M.; Forró, L. *The Journal of Physical Chemistry B* **2001**, *105*, 7938.
- (118) Nakamura, T.; Ishihara, M.; Ohana, T.; Tanaka, A.; Koga, Y. *Chemical Communications* **2004**, 1336.
- (119) Flavin, K.; Lawrence, K.; Bartelmess, J.; Tasiar, M.; Navio, C.; Bittencourt, C.; O'Shea, D. F.; Guldi, D. M.; Giordani, S. *Acs Nano* **2011**, *5*, 1198.
- (120) Dyke, C. A.; Tour, J. M. *Nano Letters* **2003**, *3*, 1215.
- (121) Hudson, J. L.; Casavant, M. J.; Tour, J. M. *Journal of the American Chemical Society* **2004**, *126*, 11158.
- (122) Dyke, C. A.; Tour, J. M. *Journal of the American Chemical Society* **2003**, *125*, 1156.
- (123) Kawata, S.; Kawata, Y. *Chemical Reviews* **2000**, *100*, 1777.
- (124) Jones, I. M.; Hamilton, A. D. *Organic Letters* **2010**, *12*, 3651.
- (125) Gust, D.; Moore, T. A.; Moore, A. L. *Chemical Communications* **2006**, 1169.
- (126) Bouas-Laurent, H.; Durr, H. *Pure and Applied Chemistry* **2001**, *73*, 639.
- (127) Hirshberg, Y.; Fischer, E. *Journal of Chemical Physics* **1955**, *23*, 1723.
- (128) Wilson, A. E. J. *Physics in Technology* **1984**, *15*, 232.
- (129) Seefeldt, B.; Kasper, R.; Beining, M.; Mattay, J.; Arden-Jacob, J.; Kemnitzer, N.; Drexhage, K. H.; Heilemann, M.; Sauer, M. *Photochemical & Photobiological Sciences* **2010**, *9*, 213.
- (130) Tsivgoulis, G. M.; Lehn, J.-M. *Angewandte Chemie International Edition in English* **1995**, *34*, 1119.
- (131) Feringa, B. L. *Molecular Switches 2001*, Wiley-VCH. **2001**.
- (132) Guglielmetti, R. *Photochromism: Molecules and Systems* **1990**, Elsevier: Amsterdam.
- (133) Wyman, G. M. *Chemical Reviews* **1955**, *55*, 625.

- (134) Kellogg, R. M.; Groen, M. B.; Wynberg, H. *The Journal of Organic Chemistry* **1967**, *32*, 3093.
- (135) Irie, M. *Chemical Reviews* **2000**, *100*, 1685.
- (136) Yokoyama, Y. *Chemical Reviews* **2000**, *100*, 1717.
- (137) Cohen, M. D.; Schmidt, G. M. J. *The Journal of Physical Chemistry* **1962**, *66*, 2442.
- (138) Hirshberg, Y. *Journal of the American Chemical Society* **1956**, *78*, 2304.
- (139) Fox, M. A.; Voynick, T. A. *The Journal of Organic Chemistry* **1981**, *46*, 1235.
- (140) Berkovic, G.; Krongauz, V.; Weiss, V. *Chemical Reviews* **2000**, *100*, 1741.
- (141) Raymo, F. M.; Giordani, S. *Journal of the American Chemical Society* **2002**, *124*, 2004.
- (142) Fischer, E.; Hirshberg, Y. *Journal of the Chemical Society* **1952**, 4522.
- (143) Raymo, F. M.; Giordani, S. *Proceedings of the National Academy of Sciences of the United States of America* **2002**, *99*, 4941.
- (144) Buback, J.; Kullmann, M.; Langhojer, F.; Nuernberger, P.; Schmidt, R.; Würthner, F.; Brixner, T. *Journal of the American Chemical Society* **2010**, *132*, 16510.
- (145) Guglielmetti, R. *Photochromism: Molecules and Systems*; Elsevier, 2003.
- (146) Tyer, N. W.; Becker, R. S. *Journal of the American Chemical Society* **1970**, *92*, 1289.
- (147) Chen, Q.; Zhang, D. Q.; Zhang, G. X.; Yang, X. Y.; Feng, Y.; Fan, Q. H.; Zhu, D. B. *Advanced Functional Materials* **2010**, *20*, 3244.
- (148) Sanchez, C.; Lebeau, B.; Chaput, F.; Boilot, J. P. *Advanced Materials* **2003**, *15*, 1969.
- (149) Wang, M.-S.; Xu, G.; Zhang, Z.-J.; Guo, G.-C. *Chemical Communications* **2010**, *46*, 361.
- (150) Byrne, R.; Diamond, D. *Nature Materials* **2006**, *5*, 421.
- (151) Garcia, A.; Marquez, M.; Cai, T.; Rosario, R.; Hu, Z. B.; Gust, D.; Hayes, M.; Vail, S. A.; Park, C. D. *Langmuir* **2007**, *23*, 224.
- (152) Byrne, R. J.; Stitzel, S. E.; Diamond, D. *Journal of Materials Chemistry* **2006**, *16*, 1332.
- (153) Allouche, J.; Le Beulze, A.; Dupin, J.-C.; Ledeuil, J.-B.; Blanc, S.; Gonbeau, D. *Journal of Materials Chemistry* **2010**, *20*, 9370.
- (154) Whelan, J.; Wojtyk, J. T. C.; Buncel, E. *Chemistry of Materials* **2008**, *20*, 3797.
- (155) Whelan, J.; Abdallah, D.; Wojtyk, J.; Buncel, E. *Journal of Materials Chemistry* **2010**, *20*, 5727.
- (156) Zhu, M.-Q.; Zhu, L.; Han, J. J.; Wu, W.; Hurst, J. K.; Li, A. D. Q. *Journal of the American Chemical Society* **2006**, *128*, 4303.
- (157) Chen, J.; Zeng, F.; Wu, S. Z.; Su, J.; Tong, Z. *Small* **2009**, *5*, 970.
- (158) Su, J. H.; Chen, J.; Zeng, F.; Chen, Q. M.; Wu, S. Z.; Tong, Z. *Polymer Bulletin* **2008**, *61*, 425.
- (159) Ipe, B. I.; Mahima, S.; Thomas, K. G. *Journal of the American Chemical Society* **2003**, *125*, 7174.

- (160) Liu, D.; Chen, W.; Sun, K.; Deng, K.; Zhang, W.; Wang, Z.; Jiang, X. *Angewandte Chemie International Edition* **2011**, *50*, 4103.
- (161) Liao, B.; Chen, J. A.; Huang, H. W.; Li, X. F.; He, B. Q. *Journal of Materials Chemistry* **2011**, *21*, 5867.
- (162) Doron, A.; Katz, E.; Tao, G.; Willner, I. *Langmuir* **1997**, *13*, 1783.
- (163) Riskin, M.; Katz, E.; Gutkin, V.; Willner, I. *Langmuir* **2006**, *22*, 10483.
- (164) Rosario, R.; Gust, D.; Hayes, M.; Jahnke, F.; Springer, J.; Garcia, A. A. *Langmuir* **2002**, *18*, 8062.
- (165) Dattilo, D.; Armelao, L.; Fois, G.; Mistura, G.; Maggini, M. *Langmuir* **2007**, *23*, 12945.
- (166) Zhu, L.; Zhu, M.-Q.; Hurst, J. K.; Li, A. D. Q. *Journal of the American Chemical Society* **2005**, *127*, 8968.
- (167) Shen, Q.; Cao, Y.; Liu, S.; Steigerwald, M. L.; Guo, X. F. *Journal of Physical Chemistry C* **2009**, *113*, 10807.
- (168) Liu, S.; Li, J. M.; Shen, Q.; Cao, Y.; Guo, X. F.; Zhang, G. M.; Teng, C. Q.; Zhang, J.; Liu, Z. F.; Steigerwald, M. L.; Xu, D. S.; Nuckolls, C. *Angewandte Chemie-International Edition* **2009**, *48*, 4759.
- (169) Liu, S.; Shen, Q.; Cao, Y.; Gan, L.; Wang, Z. X.; Steigerwald, M. L.; Guo, X. F. *Coordination Chemistry Reviews* **2010**, *254*, 1101.
- (170) Malic, E.; Weber, C.; Richter, M.; Atalla, V.; Klamroth, T.; Saalfrank, P.; Reich, S.; Knorr, A. *Physical Review Letters* **2011**, *106*, 097401.
- (171) Del Valle, M.; Gutierrez, R.; Tejedor, C.; Cuniberti, G. *Nature Nanotechnology* **2007**, *2*, 176.
- (172) Wei, D.; Liu, Y. *Advanced Materials* **2008**, *20*, 2815.
- (173) Guo, X. F.; Myers, M.; Xiao, S. X.; Lefenfeld, M.; Steiner, R.; Tulevski, G. S.; Tang, J. Y.; Baumert, J.; Leibfarth, F.; Yardley, J. T.; Steigerwald, M. L.; Kim, P.; Nuckolls, C. *Proceedings of the National Academy of Sciences of the United States of America* **2006**, *103*, 11452.
- (174) Cheong, I. W.; Wang, S.; Ki, H. S.; Kim, S. H. *Current Applied Physics* **2009**, *9*, 1269.
- (175) Khairutdinov, R. F.; Itkis, M. E.; Haddon, R. C. *Nano Letters* **2004**, *4*, 1529.
- (176) Guo, X. F.; Huang, L. M.; O'Brien, S.; Kim, P.; Nuckolls, C. *Journal of the American Chemical Society* **2005**, *127*, 15045.
- (177) Gorner, H.; Chibisov, A. K. *Journal of the Chemical Society-Faraday Transactions* **1998**, *94*, 2557.
- (178) Shao, N.; Zhang, Y.; Cheung, S. M.; Yang, R. H.; Chan, W. H.; Mo, T.; Li, K. A.; Liu, F. *Analytical Chemistry* **2005**, *77*, 7294.
- (179) Shao, N.; Gao, X.; Wang, H.; Yang, R.; Chan, W. *Analytica Chimica Acta* **2009**, *655*, 1.

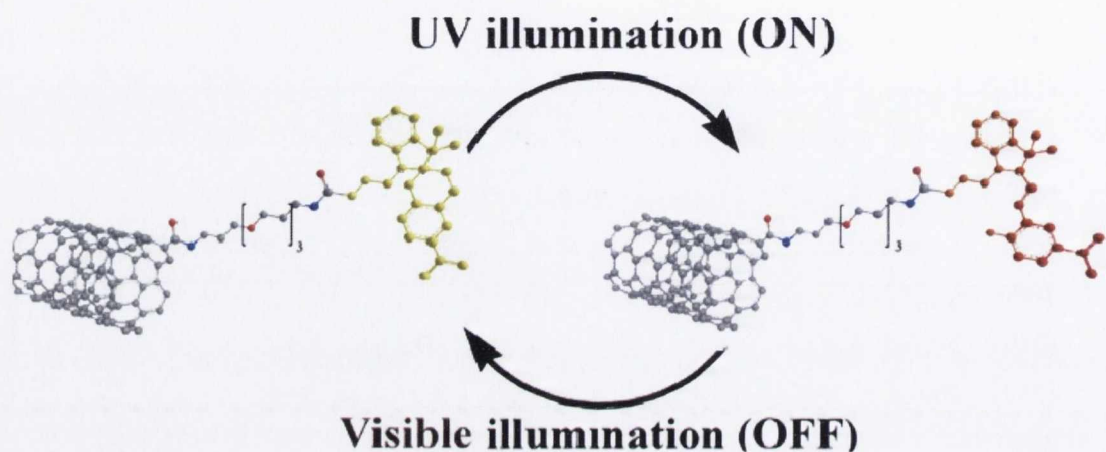
- (180) Shao, N.; Jin, J. Y.; Cheung, S. M.; Yang, R. H.; Chan, W. H.; Mo, T. *Angewandte Chemie-International Edition* **2006**, *45*, 4944.
- (181) Inouye, M.; Ueno, M.; Kitao, T.; Tsuchiya, K. *Journal of the American Chemical Society* **1990**, *112*, 8977.
- (182) Chernyshev, A. V.; Metelitsa, A. V.; Gaeva, E. B.; Voloshin, N. A.; Borodkin, G. S.; Minkin, V. I. *Journal of Physical Organic Chemistry* **2007**, *20*, 908.
- (183) Tu, C.; Osborne, E. A.; Louie, A. Y. *Tetrahedron* **2009**, *65*, 1241.
- (184) Fries, K. H.; Driskell, J. D.; Samanta, S.; Locklin, J. *Analytical Chemistry* **2010**, *82*, 3306.
- (185) Winkler, J. D.; Bowen, C. M.; Michelet, V. *Journal of the American Chemical Society* **1998**, *120*, 3237.
- (186) Phillips, J. P.; Mueller, A.; Przystal, F. *Journal of the American Chemical Society* **1965**, *87*, 4020.
- (187) Inouye, M.; Noguchi, Y.; Isagawa, K. *Angewandte Chemie International Edition in English* **1994**, *33*, 1163.
- (188) Shao, N.; Wang, H.; Gao, X.; Yang, R.; Chan, W. *Analytical Chemistry* **2010**, *82*, 4628.
- (189) Liu, Z.; Jiang, L.; Liang, Z.; Gao, Y. *Tetrahedron* **2006**, *62*, 3214.
- (190) Nikolaeva, O. G.; Tsukanov, A. V.; Shepelenko, E. N.; Lukyanov, B. S.; Metelitsa, A. V.; Kostyrina, O. Y.; Dubonosov, A. D.; Bren, V. A.; Minkin, V. I. *International Journal of Photoenergy* **2009**, 238615.
- (191) Natali, M.; Soldi, L.; Giordani, S. *Tetrahedron* **2010**, *66*, 7612.
- (192) Natali, M.; Aakeroy, C.; Desper, J.; Giordani, S. *Dalton Transactions* **2010**, *39*, 8269.
- (193) E. Collins, G.; Choi, L.-S.; J. Ewing, K.; Michelet, V.; M. Bowen, C.; D. Winkler, J. *Chemical Communications* **1999**, 321.
- (194) Wojtyk, J. T. C.; Kazmaier, P. M.; Buncel, E. *Chemistry of Materials* **2001**, *13*, 2547.
- (195) Liu, Y.; Fan, M.; Zhang, S.; Sheng, X.; Yao, J. *New Journal of Chemistry* **2007**, *31*, 1878.
- (196) Sunamoto, J.; Iwamoto, K.; Mohri, Y.; Kominato, T. *Journal of the American Chemical Society* **1982**, *104*, 5502.
- (197) Marxtibbon, S.; Willner, I. *Journal of the Chemical Society-Chemical Communications* **1994**, 1261.
- (198) Takase, M.; Inouye, M. *Chemical Communications* **2001**, 2432.
- (199) Inouye, M.; Kim, K.; Kitao, T. *Journal of the American Chemical Society* **1992**, *114*, 778.
- (200) Shao, N.; Jin, J. Y.; Wang, H.; Zheng, J.; Yang, R. H.; Chan, W. H.; Abliz, Z. *Journal of the American Chemical Society* **2010**, *132*, 725.
- (201) Kam, N. W. S.; Dai, H. J. *Journal of the American Chemical Society* **2005**, *127*, 6021.

- (202) Pantarotto, D.; Partidos, C. D.; Graff, R.; Hoebeke, J.; Briand, J. P.; Prato, M.; Bianco, A. *Journal of the American Chemical Society* **2003**, *125*, 6160.
- (203) Chen, R. J.; Zhang, Y. G.; Wang, D. W.; Dai, H. J. *Journal of the American Chemical Society* **2001**, *123*, 3838.
- (204) Gorityala, B. K.; Ma, J.; Wang, X.; Chen, P.; Liu, X. W. *Chemical Society Reviews* **2010**, *39*, 2915.
- (205) Cherukuri, P.; Bachilo, S. M.; Litovsky, S. H.; Weisman, R. B. *Journal of the American Chemical Society* **2004**, *126*, 15638.
- (206) Heller, D. A.; Jin, H.; Martinez, B. M.; Patel, D.; Miller, B. M.; Yeung, T. K.; Jena, P. V.; Hobartner, C.; Ha, T.; Silverman, S. K.; Strano, M. S. *Nature Nanotechnology* **2009**, *4*, 114.
- (207) Zheng, M.; Jagota, A.; Strano, M. S.; Santos, A. P.; Barone, P.; Chou, S. G.; Diner, B. A.; Dresselhaus, M. S.; McLean, R. S.; Onoa, G. B.; Samsonidze, G. G.; Semke, E. D.; Usrey, M.; Walls, D. J. *Science* **2003**, *302*, 1545.
- (208) Heller, D. A.; Jeng, E. S.; Yeung, T. K.; Martinez, B. M.; Moll, A. E.; Gastala, J. B.; Strano, M. S. *Science* **2006**, *311*, 508.
- (209) Liu, Z.; Winters, M.; Holodniy, M.; Dai, H. *Angewandte Chemie* **2007**, *119*, 2069.
- (210) Bianco, A.; Kostarelos, K.; Partidos, C. D.; Prato, M. *Chemical Communications* **2005**, 571.
- (211) Dhar, S.; Liu, Z.; Thomale, J. r.; Dai, H.; Lippard, S. J. *Journal of the American Chemical Society* **2008**, *130*, 11467.
- (212) Feazell, R. P.; Nakayama-Ratchford, N.; Dai, H.; Lippard, S. J. *Journal of the American Chemical Society* **2007**, *129*, 8438.
- (213) Liang, F.; Chen, B. *Current Medicinal Chemistry* **2010**, *17*, 10.
- (214) Su, Z.; Zhu, S.; Donkor, A. D.; Tzoganakis, C.; Honek, J. F. *Journal of the American Chemical Society* **2011**, *113*, 6874.
- (215) Prato, M.; Kostarelos, K.; Bianco, A. *Accounts of Chemical Research* **2008**, *41*, 60.
- (216) Bianco, A. *Expert Opinion on Drug Delivery* **2004**, *1*, 57.
- (217) Khazaei, A.; Rad, M. N.; Borazjani, M. K. *International journal of nanomedicine* **2010**, *5*, 639.
- (218) Liu, Y. F.; Wang, H. F. *Nature Nanotechnology* **2007**, *2*, 20.
- (219) Chen, J.; Chen, S.; Zhao, X.; Kuznetsova, L. V.; Wong, S. S.; Ojima, I. *Journal of the American Chemical Society* **2008**, *130*, 16778.
- (220) Wu, W.; Wieckowski, S.; Pastorin, G.; Benincasa, M.; Klumpp, C.; Briand, J.-P.; Gennaro, R.; Prato, M.; Bianco, A. *Angewandte Chemie International Edition* **2005**, *44*, 6358.
- (221) Liu, Z.; Fan, A. C.; Rakhra, K.; Sherlock, S.; Goodwin, A.; Chen, X.; Yang, Q.; Felsher, D. W.; Dai, H. *Angewandte Chemie International Edition* **2009**, *48*, 7668.
- (222) Zhang, X.; Meng, L.; Lu, Q.; Fei, Z.; Dyson, P. J. *Biomaterials* **2009**, *30*, 6041.

- (223) Liu, Z.; Sun, X. M.; Nakayama-Ratchford, N.; Dai, H. J. *Acs Nano* **2007**, *1*, 50.
- (224) Heister, E.; Neves, V.; Tilmaciu, C.; Lipert, K.; Beltrán, V. S.; Coley, H. M.; Silva, S. R. P.; McFadden, J. *Carbon* **2009**, *47*, 2152.
- (225) Fujigaya, T.; Morimoto, T.; Nakashima, N. *Soft Matter* **2011**, *7*, 2647.
- (226) Park, S.; Yang, H.-S.; Kim, D.; Jo, K.; Jon, S. *Chemical Communications* **2008**, 2876.
- (227) Ito, Y.; Venkatesan, N.; Hirako, N.; Sugioka, N.; Takada, K. *International Journal of Pharmaceutics* **2007**, *337*, 357.
- (228) Liu, Z.; Chen, K.; Davis, C.; Sherlock, S.; Cao, Q. Z.; Chen, X. Y.; Dai, H. J. *Cancer Research* **2008**, *68*, 6652.
- (229) Bhirde, A. A.; Patel, V.; Gavard, J.; Zhang, G.; Sousa, A. A.; Masedunskas, A.; Leapman, R. D.; Weigert, R.; Gutkind, J. S.; Rusling, J. F. *Acs Nano* **2009**, *3*, 307.
- (230) Bhirde, A. A.; Patel, S.; Sousa, A. A.; Patel, V.; Molinolo, A. A.; Ji, Y. M.; Leapman, R. D.; Gutkind, J. S.; Rusling, J. F. *Nanomedicine* **2010**, *5*, 1535.
- (231) Tripisciano, C.; Kraemer, K.; Taylor, A.; Borowiak-Palen, E. *Chemical Physics Letters* **2009**, *478*, 200.
- (232) Chaban, V. V.; Savchenko, T. I.; Kovalenko, S. M.; Prezhdo, O. V. *The Journal of Physical Chemistry B* **2010**, *114*, 13481.
- (233) Liu, Z.; Cai, W. B.; He, L. N.; Nakayama, N.; Chen, K.; Sun, X. M.; Chen, X. Y.; Dai, H. J. *Nature Nanotechnology* **2007**, *2*, 47.
- (234) McDevitt, M. R.; Chattopadhyay, D.; Kappel, B. J.; Jaggi, J. S.; Schiffman, S. R.; Antczak, C.; Njardarson, J. T.; Brentjens, R.; Scheinberg, D. A. *Journal of Nuclear Medicine* **2007**, *48*, 1180.
- (235) Ménard-Moyon, C.; Venturelli, E.; Fabbro, C.; Samori, C.; Da Ros, T.; Kostarelos, K.; Prato, M.; Bianco, A. *Expert Opinion on Drug Discovery* **2010**, *5*, 691.
- (236) Berlin, J. M.; Leonard, A. D.; Pham, T. T.; Sano, D.; Marcano, D. C.; Yan, S.; Fiorentino, S.; Milas, Z. L.; Kosynkin, D. V.; Price, B. K.; Lucente-Schultz, R. M.; Wen, X.; Raso, M. G.; Craig, S. L.; Tran, H. T.; Myers, J. N.; Tour, J. M. *Acs Nano* **2010**, *4*, 4621.
- (237) Sayes, C. M.; Liang, F.; Hudson, J. L.; Mendez, J.; Guo, W.; Beach, J. M.; Moore, V. C.; Doyle, C. D.; West, J. L.; Billups, W. E.; Ausman, K. D.; Colvin, V. L. *Toxicology Letters* **2006**, *161*, 135.
- (238) Nimmagadda, A.; Thurston, K.; Nollert, M. U.; McFetridge, P. S. *Journal of Biomedical Materials Research Part A* **2006**, *76A*, 614.
- (239) Schipper, M. L.; Nakayama-Ratchford, N.; Davis, C. R.; Kam, N. W. S.; Chu, P.; Liu, Z.; Sun, X.; Dai, H.; Gambhir, S. S. *Nature Nanotechnology* **2008**, *3*, 216.
- (240) Arepalli, S.; Nikolaev, P.; Gorelik, O.; Hadjiev, V. G.; Bradlev, H. A.; Holmes, W.; Files, B.; Yowell, L. *Carbon* **2004**, *42*, 1783.
- (241) Graupner, R. *Journal of Raman Spectroscopy* **2007**, *38*, 673.

- (242) Jorio, A.; Pimenta, M. A.; Souza, A. G.; Saito, R.; Dresselhaus, G.; Dresselhaus, M. S. *New Journal of Physics* **2003**, *5*, 139.1.
- (243) Mussi, V.; Biale, C.; Visentin, S.; Barbero, N.; Rocchia, M.; Valbusa, U. *Carbon* **2010**, *48*, 3391.
- (244) Rao, A. M.; Richter, E.; Bandow, S.; Chase, B.; Eklund, P. C.; Williams, K. A.; Fang, S.; Subbaswamy, K. R.; Menon, M.; Thess, A.; Smalley, R. E.; Dresselhaus, G.; Dresselhaus, M. S. *Science* **1997**, *275*, 187.
- (245) Jorio, A.; Fantini, C.; Pimenta, M. A.; Capaz, R. B.; Samsonidze, G. G.; Dresselhaus, G.; Dresselhaus, M. S.; Jiang, J.; Kobayashi, N.; Gruneis, A.; Saito, R. *Physical Review B* **2005**, *71*.
- (246) Meyer, J. C.; Paillet, M.; Michel, T.; Moreac, A.; Neumann, A.; Duesberg, G. S.; Roth, S.; Sauvajol, J. L. *Physical Review Letters* **2005**, *95*.
- (247) Ferrari, A. C.; Robertson, J. *Physical Review B* **2000**, *61*, 14095.
- (248) Lazzeri, M.; Piscanec, S.; Mauri, F.; Ferrari, A. C.; Robertson, J. *Physical Review B* **2006**, *73*, 155426.
- (249) Ferrari, A. C. *Solid State Communications* **2007**, *143*, 47.
- (250) Brege, J. J.; Gallaway, C.; Barron, A. R. *Journal of Physical Chemistry C* **2009**, *113*, 4270.
- (251) Brege, J. J.; Gallaway, C.; Barron, A. R. *The Journal of Physical Chemistry C* **2007**, *111*, 17812.
- (252) Cagnet, L.; Tsyboulski, D. A.; Rocha, J. D. R.; Doyle, C. D.; Tour, J. M.; Weisman, R. B. *Science* **2007**, *316*, 1465.
- (253) Strano, M. S.; Huffman, C. B.; Moore, V. C.; O'Connell, M. J.; Haroz, E. H.; Hubbard, J.; Miller, M.; Rialon, K.; Kittrell, C.; Ramesh, S.; Hauge, R. H.; Smalley, R. E. *Journal of Physical Chemistry B* **2003**, *107*, 6979.

Chapter 2. Functionalization of Single-Walled Carbon Nanotubes with Optically Switchable Spiroyrans



In this chapter the design, synthesis and complete characterization of a smart material composed of SWNTs functionalized with SP-based photo switchable molecules are reported. Due to the chemical complexity of the system a range of complementary spectroscopic and microscopic techniques was required to provide a complete picture of the composition and performance of the nanomaterial. Specifically, TEM and TGA confirmed the successful purification of the nanotube sample; TGA supported the presence of molecular switches in the functionalized material; Raman indirectly confirmed the successful oxidation of the tubes; FT-IR proved the nature of the functional groups introduced onto the nanotube surface and AFM demonstrated nanotube shortened lengths. The photo responsive behaviour of the nanomaterial was evaluated by UV-Vis/NIR absorption spectroscopy, and the first example of a continuous ON-OFF switching of a SP-SWNT material in solution is reported.

2.1 Introduction

The development of nanosized devices that respond to the environment in a manner that suggest a degree of “intelligence” is a topic of modern interest. In this context, robust molecular sensors that can detect changes in their environment with a high degree of selectivity and sensitivity represent important building blocks of target-oriented smart materials. A modular system composed of a nanosized scaffold with appropriate physical/chemical properties, and a molecular system which desired signals can be readily modulated by external stimuli, offer good promise for the development of a multi-tasking and target-oriented nanodevice. With this intent, the objective of this chapter is the development of a modular smart nanomaterial that couples the unique properties of SWNTs¹⁻⁴ and photochromic molecular switches in a single device, where the nanotubes act as the scaffolding, and spiropyrans (SP) provide the ‘intelligence’. SP were specifically chosen because of their tremendous versatility, fast stimuli responsiveness⁵⁻⁸ and high sensitivities⁹ that makes them legitimate candidates for a number of profitable applications in nanoelectronics and sensing.

As previously mentioned, SWNTs cannot be easily manipulated because of their lack of solubility in common solvents which represents a significant limitation towards their extensive use. To overcome this problem we rationally designed a chemical functionalization protocol of SWNTs with different length PEGylated chains with the aim of promoting the unraveling process¹⁰ and, at the same time, create a water dispersible material for potential biological applications.^{11,12} Before this, purification, shortening and oxidation of the SWNTs will be performed with the aim of (1) having a material free of metal catalysts that can be used in bio applications, (2) permit their easier cell internalization, and (3) create a chemical anchor to which other functionalities can be attached to and simultaneously produce a less toxic material.¹³⁻¹⁶ The shortened tubes decorated with carboxylic acid groups will be integrated with SP molecular switches by means of coupling reactions, and the light modulated photo switchability of the nanocomposite will be investigated by means of UV-Vis/NIR absorption spectroscopy.

The preparation of integrated nanomaterials where switchable molecular units are coupled to SWNTs has received some interest recently (as reviewed in the introductory

chapter of this thesis),¹⁷⁻²¹ with Haddon and co-workers initially demonstrating the possibility of photo-inducing electronic transitions in semiconducting nanotubes covalently modified with SP derivatives on solid state.

Our objective considerably differs from the achievements of the Haddon group as we are intrigued by the cyclic modulation of the optical properties of SP derivatives covalently coupled to SWNTs in solution to better simulate potential responses in biological environments. It is expected that such modular smart nanomaterial can find a range of applications among the many already demonstrated,²² including sensing and reversible photoswitchable receptors.

Materials of this type are likely to display considerable chemical and structural complexity; therefore the development of a comprehensive and reliable characterization protocol is imperative. An array of fundamentally different techniques such as TGA, FT-IR, Raman, UV-Vis/NIR absorption spectroscopies and atomic force and transmission electron microscopies will be used, in order to provide a complete picture of the composition and performance of the modular smart material developed.

2.2 Purification, oxidation and covalent functionalization of SWNTs with PEG linker and spiropyrans.

Commercially available raw HiPco SWNTs (Unidym[®]) were utilized during this research, which usually contain a variable degree of impurity coming from the synthetic process. Before proceeding with any chemical modification it was therefore necessary to purify the sample. As mentioned in chapter 1 of this thesis, a number of different procedures are commonly used. The one utilized by our group consisted in the treatment of as received pristine SWNTs with a solution 2.6 M of HNO₃ that was stirred under reflux at 100°C for 48 hours (Figure 2.1).²³⁻²⁶

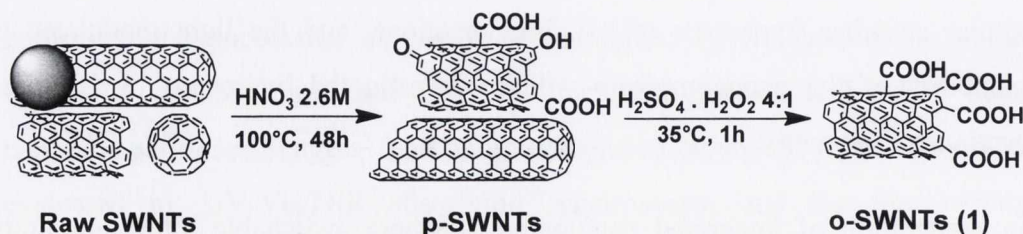
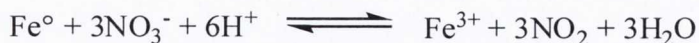


Figure 2.1: 2-step purification/oxidation of SWNTs.

The main impurity present in raw HiPco SWNTs (Unidym[®]) is elemental iron, and the purification procedure in strong acid-oxidizing conditions was therefore used in the elimination of the Fe nanoparticles as soluble species (Fe_2O_3) by means of the following redox reaction:



The purification procedure lead to the formation of a certain amount of open ends as well as oxidized defect sites on the SWNTs surface, consequently a mixture of purified and oxidized SWNTs were present in the sample. The solubilisation of Fe impurities in aqueous media permitted an easy separation of the purified SWNTs (p-SWNTs) by means of a filtration under reduced pressure.

To homogenize and to reduce the dimensional dispersion of the purified nanotube material, and to obtain SWNTs enriched with $-\text{COOH}$ functional groups at the end caps (which are the most reactive regions in the SWNT structure), a widely reported oxidative protocol has been applied, which consisted of a strong oxidation treatment with piranha solution ($\text{H}_2\text{SO}_4 \cdot \text{H}_2\text{O}_2$ 30% 4:1 ratio) at 35°C for 60 minutes (Figure 2.1).²⁷⁻²⁹ The oxidation time is of major importance and it has been carefully controlled as it determines the number of carboxylic residues produced both on the open ends and the defect sites of the SWNTs, besides the nanotube lengths.

The functionalization procedure utilized in this work is based on the reactivity of the carboxylic groups which have been introduced with the 2-step purification/oxidation protocol, and amidation reactions represent the open ends chemistry applied. The covalent functionalization of o-SWNTs (**1**) was performed using an amide coupling procedure in which an amine terminated short chain polyethylene glycol (PEG) linker (**2**) was introduced onto the SWNTs, which was first protected using a tert-butoxycarbonyl (Boc) moiety to ensure single ended chain attachment (Figure 2.2).

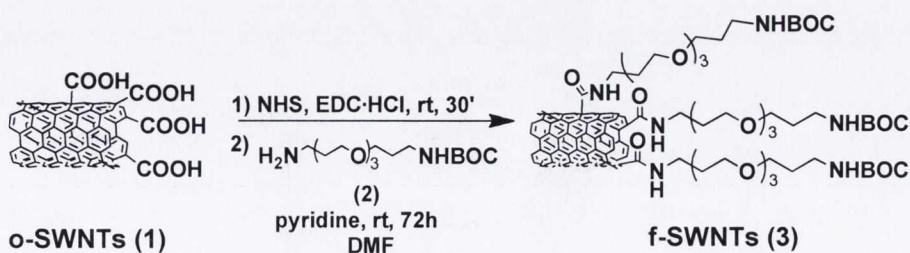


Figure 2.2: Chemical functionalization of oxidized SWNTs with PEG linker.

In order to effectively improve the performance of the covalently modified SWNT material, an important prerequisite is its solubility in common solvents and aqueous media. Different molecular weight PEGylated compounds have demonstrated not only to be valuable solubilising agents for SWNTs, but also to increase their biocompatibility by reducing the trigger of apoptotic processes in mice.^{12,30,31}

In our case, the hydrophilic PEG linker (2) was specifically chosen as it showed to better enhance the nanotube solubility after a short time of mild sonication, when compared to a sample previously synthesized in our lab that contains a shorter and non oxygenated functional chain (Figure 2.3 A). From the picture reported in Figure 2.3B it can be appreciate how the nanotubes coupled with the PEG hydrophilic spacer (2) present a better dispersibility among the two samples.

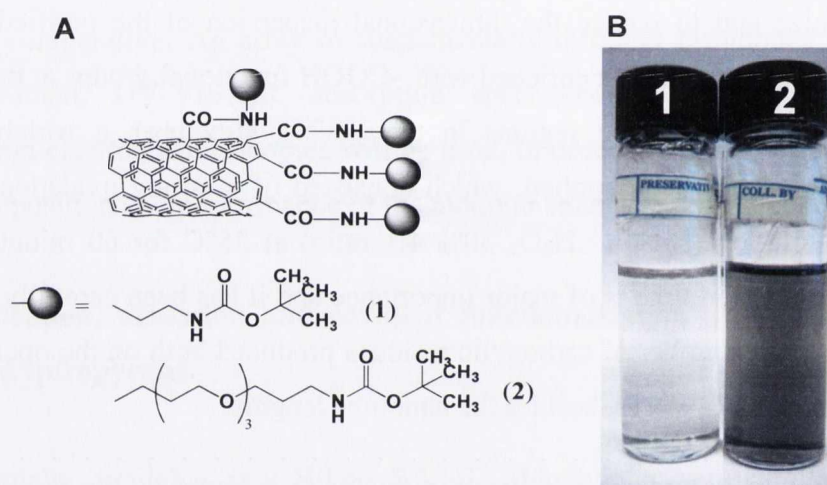


Figure 2.3: A] Representation of SWNTs functionalized with amino terminated Boc protected chains (1) and (2). B] Pictures of SWNTs dispersions after chemical functionalization with functionalities (1) and (2). [SWNTs]= 0.1 mg/mL DMF, sonication time 30 minutes at minimum power.

Following removal of the Boc protecting group using trifluoroacetic acid, the spiropyran derivative (4) synthesized in our lab,³² was converted to an activated ester using EDC·HCl and NHS, as schematized in Figure 2.4. A coupling procedure was again used to afford the spiropyran functionalized nanotubes f-SWNTs (5).

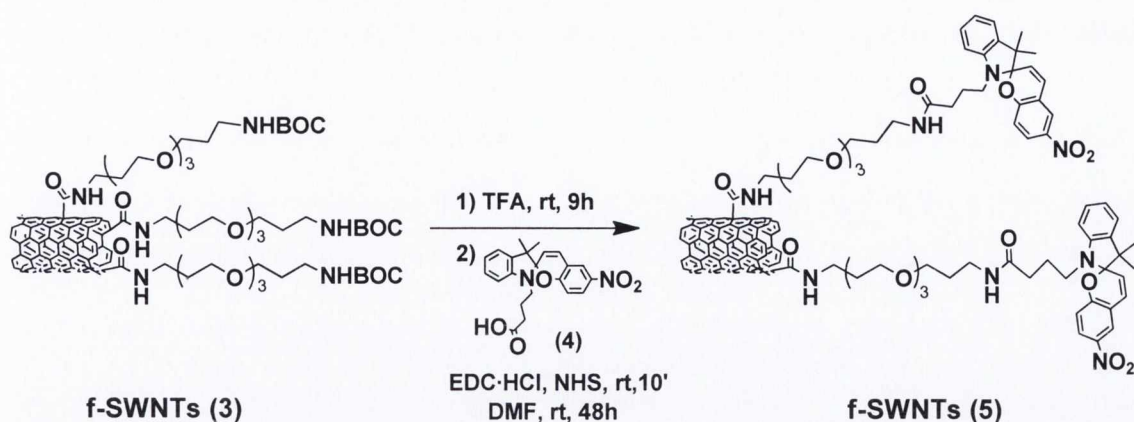


Figure 2.4: Functionalization of SWNTs with SP molecular switch.

Kaiser test is a colorimetric assay that reveals quantitatively the presence of primary amino groups.^{33,34} It was performed before and after the coupling reaction of SWNTs with SP to have a balance of the amount of functionalities introduced. The number of amine groups that reacted with the SP was estimated at 59%, and the SP loading was calculated as $\sim 79 \mu\text{g}/\text{mg}$ SWNTs.³⁵ The absorbance of TFA treated f-SWNTs and f-SWNTs (5) were measured relative to a blank solution at 570 nm that correspond to the chromophore generated by the reaction of ninhydrin with primary amines (Figure 2.5).

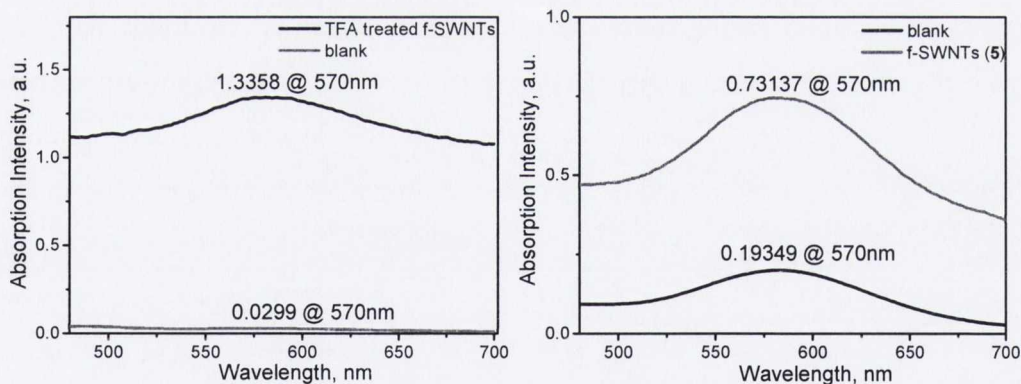


Figure 2.5: UV-Vis absorption profiles of TFA treated f-SWNTs and f-SWNTs (5) compared with a blank solution (all but nanotubes) which has been treated in the same way.

The amine loading was calculated from the equation:

$$\frac{\mu\text{mol}}{\text{g}} = \frac{[Abs \text{ sample} - Abs \text{ blank}] \cdot \text{dilution (ml)} \cdot 10^6}{\text{extinction coeff.} \cdot \text{sample weight (mg)}}$$

where the extinction coefficient, also known as molar absorptivity, represents how efficiently a chemical species absorbs light at a given wavelength. For CNTs this coefficient has a value of $15000 \text{ M}^{-1} \text{ cm}^{-1}$. The amine loading was calculated as 433.46 mmol/g for TFA treated f-SWNTs and as 233.82 mmol/g for f-SWNTs (5), therefore the difference of 199.64 mmol/g constituted the amino groups that reacted with the SP derivative.

2.3 Characterization of chemically modified SWNTs.

In order to provide a complete picture of the composition of purified, oxidized and functionalized SWNT the following complementary techniques were used: TGA, FT-IR, Raman, UV-Vis/NIR absorbance spectroscopies, AFM and TEM.

2.3.1 Thermogravimetric analysis and TEM images. Thermogravimetric analyses have been run both in air and in nitrogen atmosphere, to evaluate the purity and degree of functionalization of raw, purified, oxidized and functionalized SWNTs. It should be noted that the removal of all non-reacted reagents was ensured by sonication and exhaustive solvent washing cycles after each chemical treatment: as a consequence the weight loss below the graphitic decomposition temperature is correlated to organic functional groups on the nanotube surface. TGA traces in nitrogen atmosphere for all the samples are reported in Figure 2.6 together with weight losses, estimated number of carbon atoms per organic group and residue percentages at 900 °C after burning in air.

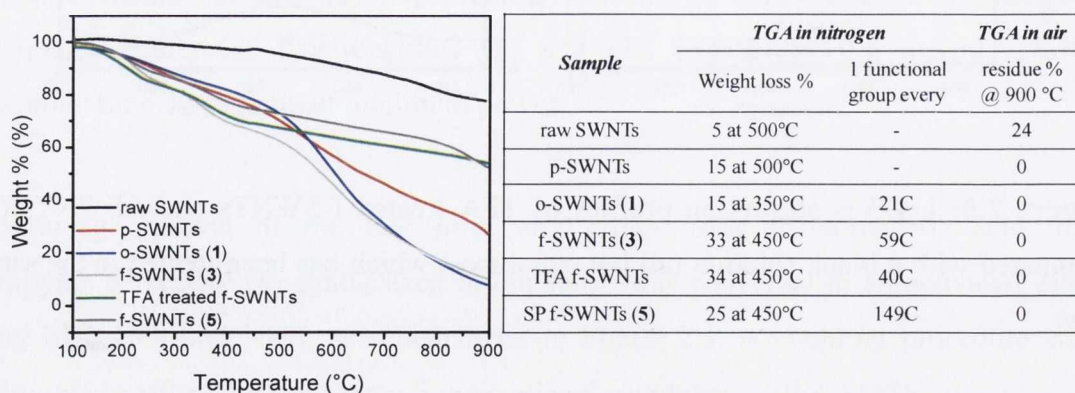


Figure 2.6: Graph] TGA traces in nitrogen flow of raw, purified, oxidized and functionalized SWNTs. Table] Weight losses, estimated number of carbon atoms per organic group and residue percentages for the same samples.

To evaluate the extent of impurity due to metal catalyst in the SWNTs samples, the residual ash at 900 °C after combustion in air was taken into account, besides HR-TEM analyses. The TGA residue is reduced from 24% in the raw nanotubes to 0% in purified and oxidized SWNTs, confirming the successful purification from metal particles *via* the 2-step purification/oxidation protocol. HR-TEM images confirmed this, as appreciable from Figure 2.7. Raw SWNTs (Figure 2.7A) show a high content of iron catalyst that is visible as black particles (thanks to the high diffraction contrast of metals), while p-SWNT and o-SWNT (1) show a purified material composed mainly of bundles of SWNTs free from metal residues (Figure 2.7B and 2.7C, respectively).

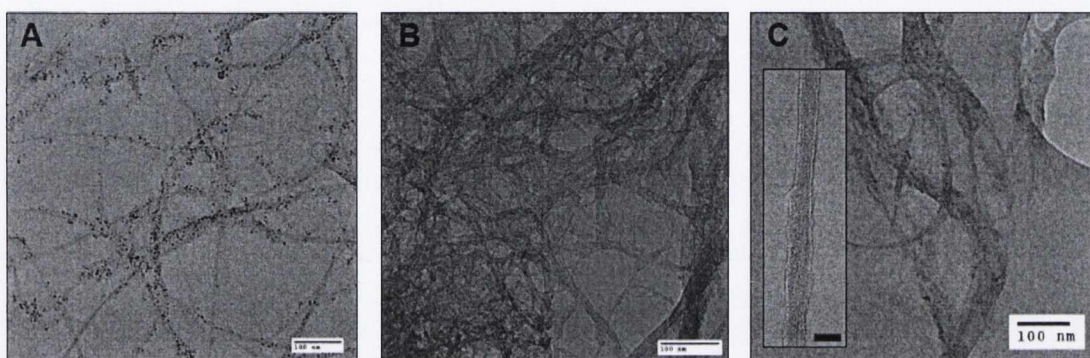


Figure 2.7: HR-TEM images of A) raw SWNTs, B) p-SWNTs, and C) o-SWNTs (1) on 200 mesh Cu holey carbon grids demonstrating the removal of the metal impurities (black particles) by 2-step purification/oxidation procedures. Scale bar: 100 nm. Figure C inset: detail of a small bundle of o-SWNTs (1) with a diameter of 20 nm circa (scale bar: 20 nm). [HR-TEM images from ref.26].

The TGA of the oxidized (1) and functionalized SWNTs (5) performed in nitrogen show a weight loss of about 15% at 350 °C and 25% at 450 °C, respectively, as compared to about only 5% at 500 °C of the raw SWNTs. We assume that this weight loss occurring during fragmentation is due to pyrolysis of the hydrogenated carbon residues. On the basis of this assumption, we estimated that the degree of functionalization is of one organic functional group every 21 and 149 carbon atoms respectively, by applying the following equation:

$$X = \frac{(100 - L) \cdot M_w}{L \cdot 12}$$

where X is the number of carbon atoms in the SWNT sample per covalent functional group, L is the % weight loss in the range of 100-450 °C, and M_w is the molecular weight of the functionality attached to the nanotube. The number 12 refers to the atomic mass of carbon, which is the main constituent of SWNT structure. The notable decrease of calculated functionalities per carbon atom following functionalization with the molecular switch (Figure 2.6), can be explained with the progressive removal of functionalized carbonaceous fragments following washing and sonication cycles.^{46,47}

When impurities such as amorphous carbon and metal particles are present in the nanotube material, they can act as oxidation initiators creating hotspots on the graphitic surface which, as a consequence, combusts at lower temperatures.³⁶ Hence, the significant shift of the graphitic decomposition temperatures of raw, p-SWNTs and o-SWNTs (1) from 443 °C to 491 °C and 553 °C respectively (Figure 2.8) in the TGA first derivative traces is an additional proof of the efficacy of the purification process.

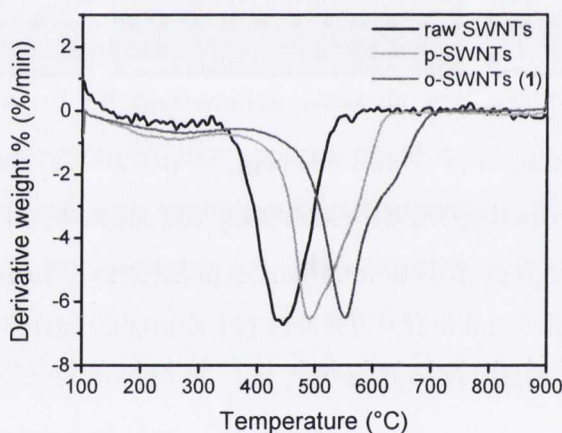


Figure 2.8: TGA first derivative traces of raw, purified and oxidized SWNTs performed in air atmosphere. The shift of the graphitic decomposition temperature to progressively higher values going from raw to o-SWNTs (1) is indicative of the increasing purity of the material.

To determine as to whether covalent functionalization was achieved, the first derivative curves from the TGA analyses have been again taken into consideration. We focused on the temperature difference maxima between raw SWNTs, o-SWNTs (1) and the f-SWNTs (5) below the graphitic decomposition temperatures³⁷ and we also performed TGA experiments on the pure SP (4). Figure 2.9 shows a comparison of first

derivative traces of the photoactive molecule with that of the f-SWNTs (5). It is evident that SP (4) is almost completely decomposed at 400 °C displaying two temperature maximum weight loss rates at 178 °C and 236 °C. These maxima also appear for the f-SWNTs (5), although shifted to higher values of 216 °C and 341 °C, indicating the presence of SPs on the nanotube material, which is not present as a non reacted species.

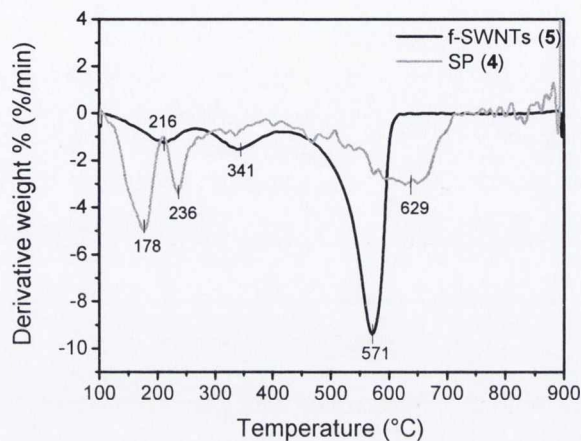


Figure 2.9: TGA first derivative traces of f-SWNTs (5) and spiropyran (4) recorded under air flow.

2.3.2 FT-IR spectroscopy analysis. FT-IR spectra of raw SWNTs, o-SWNTs (1) and f-SWNTs (5) are illustrated in Figure 2.10. The stretching vibrations observed between 1750 cm^{-1} and 1700 cm^{-1} are characteristic of the carboxyl group, and can be assigned to the oxygenated moieties introduced during the oxidative treatment of the SWNTs.³⁷

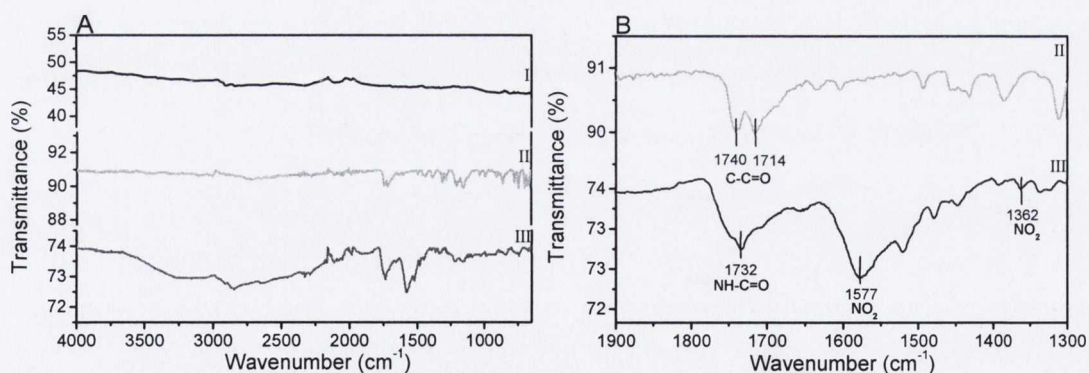


Figure 2.10: A] Full range FT-IR spectra of (I) raw SWNTs, (II) o-SWNTs (1) and (III) f-SWNTs (5). B] Stretching vibrations assignment for (II) o-SWNTs (1) and (III) f-SWNTs (5). The peaks intensities are more than 3 times the peak to peak noise observed. To improve data visualization the spectra have been baseline corrected.

On comparison of the f-SWNTs (**5**) spectrum with that of the oxidized material additional bands are observed indicating the presence of aliphatic chains, amidic, ether and amino groups (peak assignments for all the nanotube samples are reported in the experimental part in chapter 5). In addition the two distinctive nitro absorption bands at 1577 and 1362 cm^{-1} are clearly evident (Figure 2.10B III), indicating the presence of the spiropyran molecule in the nanomaterial.

An additional indication of successful covalent functionalization is a decrease in transmittance observed in the region $1700\text{--}650\text{ cm}^{-1}$ when comparing the o-SWNTs (**1**) to the raw SWNTs, as purification and doping processes introduce holes into the valence band of the SWNTs that lead to an increase in the IR absorption bands (Figure 2.11).³

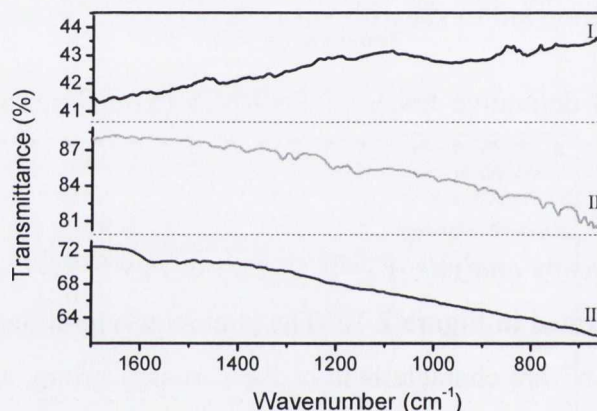


Figure 2.11: FT-IR spectra of (I) HiPco R0546, (II) oxidized and (III) SP functionalized SWNTs. The spectra have not been baseline corrected to show the decrease in transmittance observed in the region $1700\text{--}650\text{ cm}^{-1}$ when comparing the o-SWNTs (**1**) and SP f-SWNTs (**5**) to the raw HiPco SWNTs.

2.3.3 Micro-Raman spectroscopy analysis. The covalent functionalization of the SWNTs [I_D/I_G ratios calculations] and the detection of spiropyran molecules attached to the tubes [functional groups shift assignment] were confirmed by performing Raman spectroscopy analysis.³⁸⁻⁴⁰ Micro-Raman scattering measurements were carried out on all samples at room temperature using three different excitation wavelengths (457 , 514 and 633 nm)⁴¹ in order to collect all the varying diameter contributions. Figure 2.12 illustrates the Raman spectra of raw SWNTs, o-SWNTs (**1**) and f-SWNTs (**5**) using an

excitation wavelength of 633 nm and laser power as low as possible to avoid structural degradation.

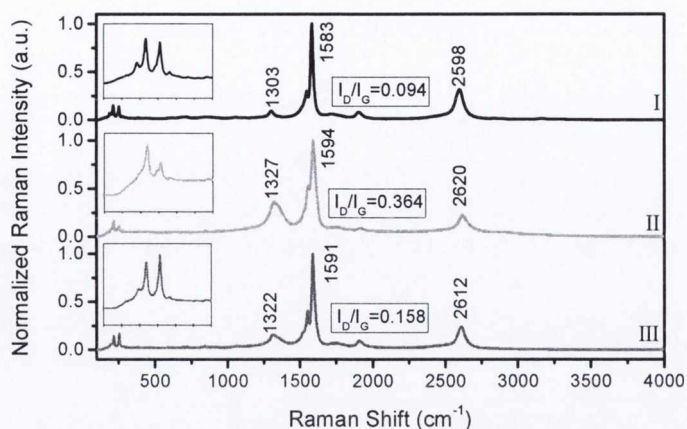


Figure 2.12: Micro Raman analyses ($\lambda_{exc} = 633$ nm) of (I) raw SWNTs, (II) o-SWNTs (1) and (III) f-SWNTs (5). In the insets the RBM analyses are reported. I_D/I_G ratios indirectly confirmed the successful covalent functionalization of the nanotube material.

It is clearly evident from Figure 2.12 that the I_D/I_G ratio increases when comparing raw to oxidized nanotubes. This increase is indicative of the breakage of the graphene sheet symmetry that in the present case can be associated with the introduction of oxygenated functionalities onto the nanotube surface. From the result reported we can thus assume that the covalent functionalization of the SWNTs was indeed successful. Conversely, comparing o-SWNTs (1) and f-SWNTs (5) a decrease in the I_D/I_G ratio is observed. This is most likely due to removal of the carboxylated carbonaceous fragments (CCFs)^{46,47} during chemical treatment and the subsequent stringent washing procedure employing a range of organic solvents.

The resonance Raman enhancement effect, for a specific SWNT type, happens when the laser excitation wavelength approaches the wavelength of the van Hove singularity of that nanotube, therefore every laser can be used to examine a limited set of SWNTs types. SWNT samples never present a homogeneous diameter distribution and often, even after functionalization and sonic treatment, are present in bundles. For this reason we have chosen to use multiple excitation wavelengths to collect all the varying

diameter contributions. Figure 2.13 displays Raman spectra of raw, oxidized and purified SWNTs with the three different excitation wavelengths (457, 514 and 633 nm).

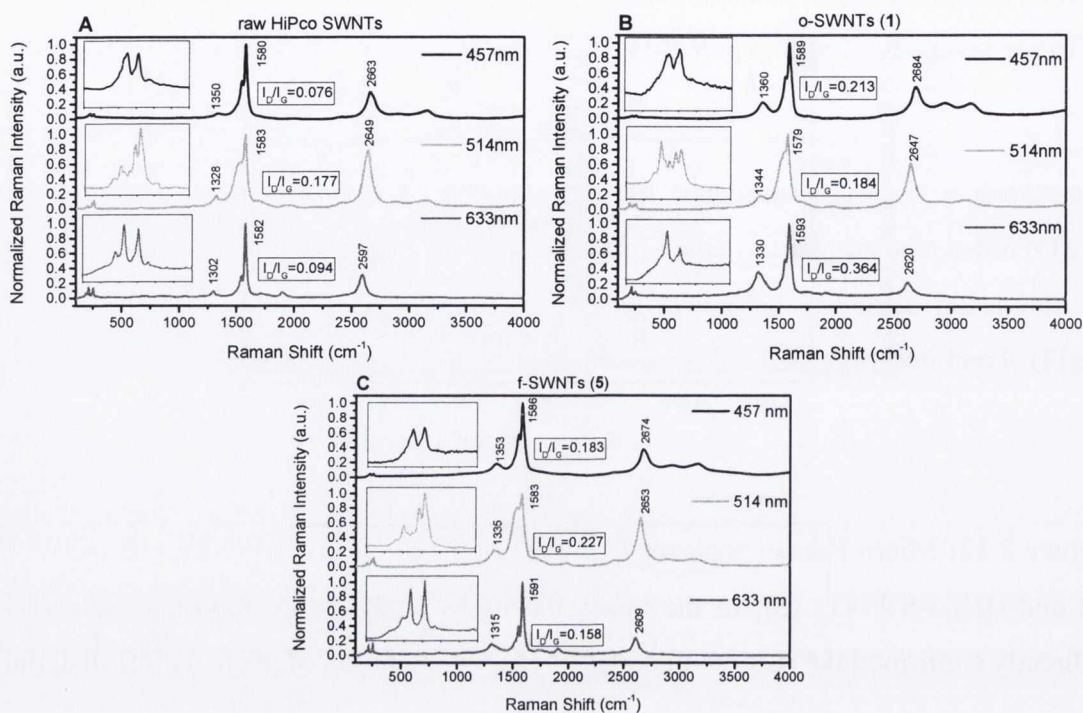


Figure 2.13: Raman spectra of A] raw HiPco SWNTs, B] oxidized and C] SP functionalized SWNTs collected using 457, 514 and 633 nm excitation wavelengths. In the insets the RBM analyses are reported.

Metallic SWNTs possess a higher electron density near the Fermi level, resulting in an increased reactivity over the semiconducting SWNTs.³ In the light of this, we analyzed the Raman RBM and G^+/G^- bands to investigate whether the o-SWNTs and f-SWNTs (5) samples were enriched in metallic or semiconducting tubes. Blue (457 nm) and green (514 nm) laser lines have been used to probe metallic and large diameter semiconducting tubes,⁴⁸ while the red (633 nm) laser line has been used to probe smaller diameter metallic and semiconducting tubes. The symmetry and the line shape of the G-band components G^+ and G^- have been analyzed. From the results obtained we can assume that all the f-SWNT samples consist of a mixture of metallic and semiconducting tubes, as the G^- components do not show a symmetric line shape but appear broadened and asymmetric toward the low wavenumber side when the samples are excited with the 514 nm laser line.⁴⁰ Structural assignments of SWNTs referred to

higher RBM resonant peaks for each excitation wavelength were additionally calculated using the integer (n, m) values from the RBM shifts observed (Table 2.1). Following analysis of both the G-band components and the integers (n, m) values, we have concluded that a preferential functionalization does not occur on the SWNTs using this synthetic method.

Considering that the chemical reactivity of the SWNTs is principally driven by the carbon atoms local strain (and therefore proportional to the tube diameter), we additionally calculated the diameter of resonant tubes by analysing the RBM modes. The RBM wavenumbers (ω_{RBM}) depend only on the diameter d of the SWNTs and not on the way they are rolled up to form the tube (chiral angles). Additionally, considering that the ω_{RBM} is inversely proportional to the tube diameter d and that the lower energy G-band component (G^-) shows clear diameter dependence, the two following equations^{40,49} can be applied to calculate SWNTs diameters:

$$\omega_{RBM} = \frac{A}{d} + B \quad (1) \qquad \omega_{G^-} = 1591 - \frac{47.7}{d^2} \quad (2)$$

Different values of the constants, A and B, have been reported where the variations in A and B are often attributed to environmental effects.⁵⁰ Assuming the presence of individual freestanding tubes recently values of $A=204 \text{ cm}^{-1}$ and $B=27 \text{ cm}^{-1}$ have been determined.⁴⁹ These values were used to calculate the diameters of the nanotube samples, and the values obtained from the highest intensity RBM shifts are reported in Table 2.1.

Sample name	RBM highest intensity shift (cm^{-1})	Diameter (nm)	Structural assignment (n,m)
raw SWNTs	225, 262, 215	1.03, 0.87, 1.08	(10,5) s, (7,6) s, (9,7) s
p-SWNTs	257, 263, 220	0.89, 0.87, 1.06	(11,1) s, (10,2) s, (13,1) m
o-SWNTs (1)	253, 201, 220	0.90, 1.17, 1.06	(10,3) s, (11,6) s, (13,1) m
f-SWNTs (3)	226, 201, 258	1.02, 1.17, 0.88	(10,5) s, (11,6) s, (11,1) s
TFA treated f-SWNTs	255, 263, 258	0.89, 0.86, 0.88	(10,5) s, (10,2) s, (11,1) s
f-SWNTs (5)	223, 261, 258	1.04, 0.87, 0.88	(11,4) s, (7,6) s, (11,1) s

Table 2.1: Diameter values and structural assignment of raw, purified, oxidized and functionalized SWNTs calculated from the highest intensity RBM shifts using equation (1) and the chart for the instant structural assignment of the SWNT* respectively. Excitation with 457, 514 and 633 nm laser lines and relative data are coloured in blue, green and red respectively. In the table s = semiconducting, m= metallic.

The results coming from (1) above calculations, (2) assignment of optical frequencies of NIR-PL emission peaks by Kataura plot⁵¹ (Figure 2.14), and (3) Raman RBM band intensity analyses, suggest a partial loss of small diameter SWNTs during the 2-step purification/oxidation procedure and that any preferential diameter selection occurred.

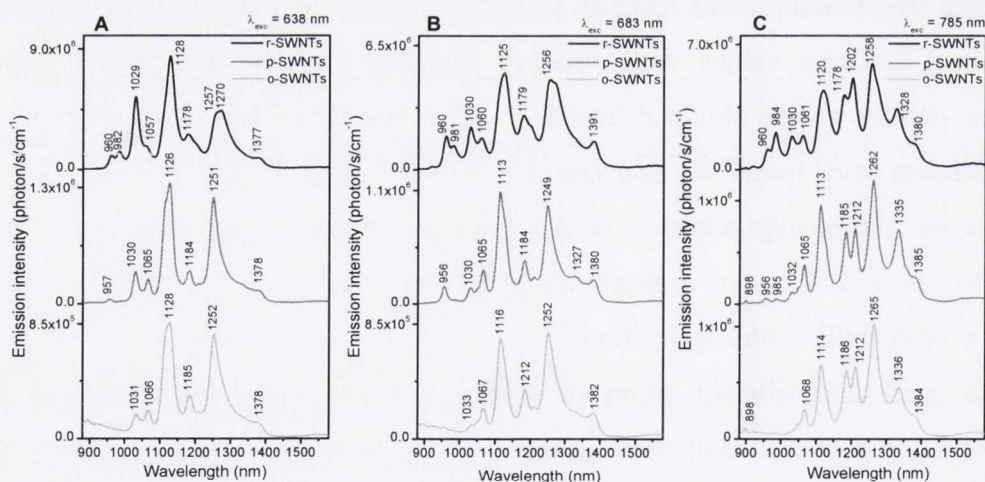


Figure 2.14: NIR-PL spectra of raw, purified and oxidized SWNTs dispersed in SDBS aqueous solution. A] $\lambda_{\text{exc}} = 638$ nm; B] $\lambda_{\text{exc}} = 683$ nm; C] $\lambda_{\text{exc}} = 785$ nm [Figures from ref.26].

* Calculations were performed using “A simple chart for the instant structural assignment of the SWNTs” by Ramesh Sivarajan available on www.carbonwall.com.

2.3.4 *Raman mapping*. Raman mapping measurement was performed at room temperature on the SP f-SWNTs (**5**). To ensure that the material deposited by the microscopy cover slide consisted of SWNTs the three characteristic Raman regions, RBM, D- and G- bands, were mapped beside the full range spectrum (Figure 2.15).

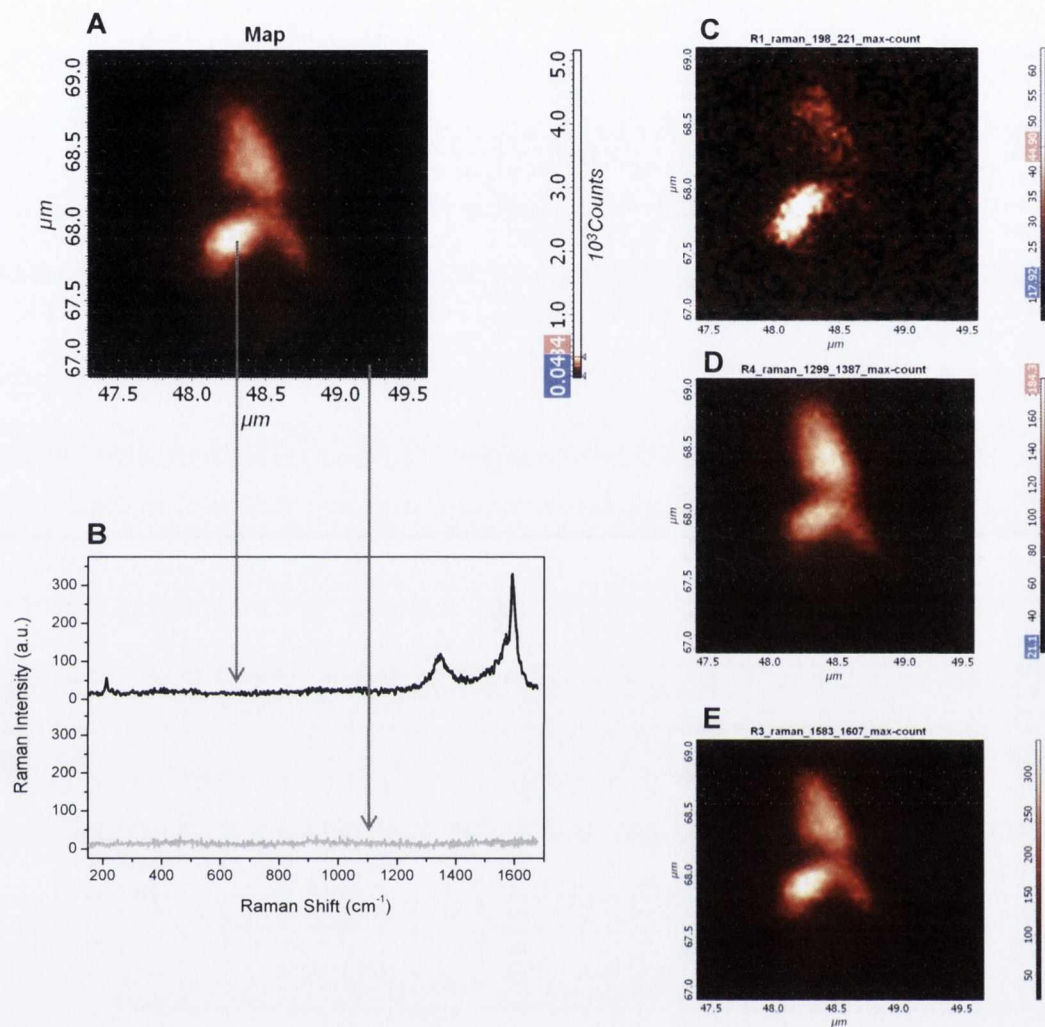


Figure 2.15: Raman mapping analysis ($\lambda_{\text{exc}} = 488 \text{ nm}$) of f-SWNTs (**5**). A] Full map image. B] Single Raman spectra from the region marked in the full Raman map. C] RBM mapping in the range 198-221 cm^{-1} . D] D-band mapping. E] G-band mapping. Time exposure 0.2 sec, one accumulation, point number 128 x 128.

The presence of functionalities bound to the tubes was confirmed after single Raman measurements with high exposure time in a different mapped area. Some typical vibrations of the functional groups introduced on the tubes were recorded in the range from 300 to 1100 cm^{-1} and are reported in Figure 2.16.

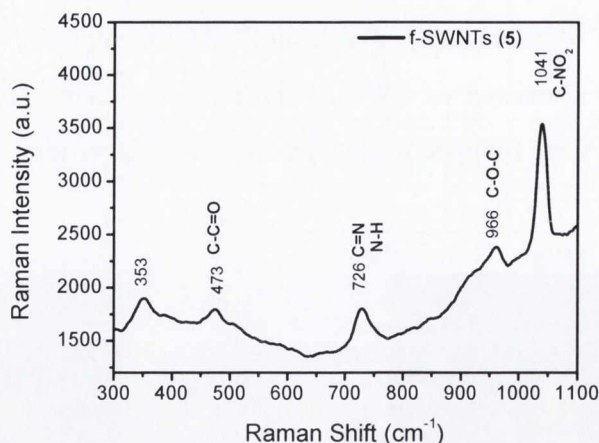


Figure 2.16: Micro Raman analysis ($\lambda_{\text{exc}} = 488 \text{ nm}$) of f-SWNTs (**5**) in the functional group region.

Raman shifts assigned to stretching and deformation vibrations of amidic groups ($473, 726 \text{ cm}^{-1}$), stretching vibrations of ethers linkages (966 cm^{-1}) and nitro aromatic groups (1041 cm^{-1}) ensure that the PEG chain and the spiropyran derivative have been effectively introduced onto nanotube surface.

2.3.5 Atomic force microscopy analysis. AFM analyses were performed to estimate nanotube dimensions after the 2-step purification/oxidation protocol. Raw SWNTs and f-SWNTs (**5**) were dispersed in DMF via sonication and subsequently spin-coated onto freshly cleaned mica substrates. Figure 2.17 illustrates typically dispersed bundles of raw SWNTs (2.17A) and an individual f-SWNT (**5**) (2.17B) on the substrate surface.

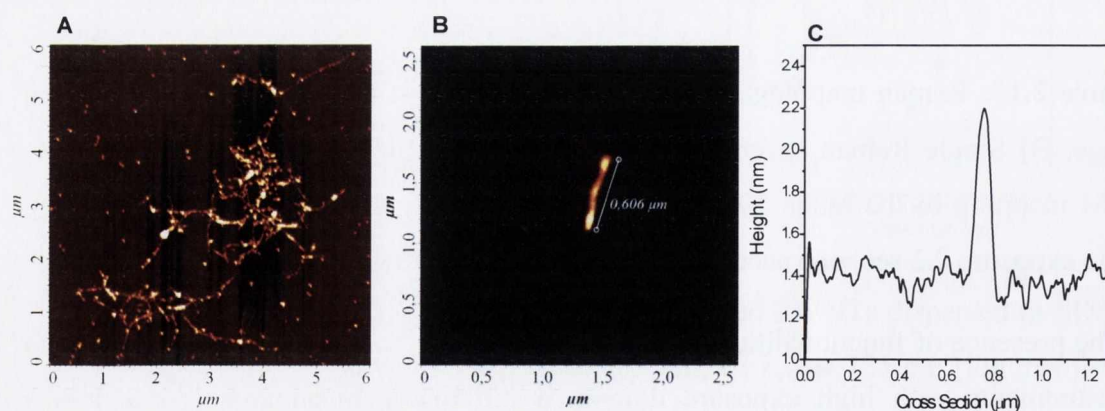


Figure 2.17: AFM topographic images of A] bundles of raw HiPco SWNTs, and B] individual SP f-SWNTs (**5**). C] Cross-section profile illustrating the height of the SP functionalized nanotube.

The reported lengths of raw SWNTs (Unidym[®] specification data) are up to 1 μm and average length calculations on 100 single f-SWNTs (5) from AFM images, confirmed the shortening of the tubes to a value of 593 ± 0.139 nm.

2.3.6 UV-Vis/NIR absorbance spectroscopy analysis. Optical absorption spectroscopy has been used to evaluate the effect of chemical treatment on the characteristic properties of the nanotubes by analysis of the electronic structure changes.^{3,52} UV-Vis/NIR absorption spectra of raw nanotubes and after nitric acid purification, oxidation (1) and functionalization (5) have been recorded on the supernatant of centrifuged samples (10^{-2} mg/mL) dispersed in DMF (Figure 2.18A). The electronic structure of the SWNTs are only slightly perturbed following chemical modification and a partial loss in number and intensity of the van Hove transitions is observed. This result not only indicates the effective chemical modification of the tubes,^{52,53} but also confirms the preservation of the structured electronic properties of our covalently modified tubes.

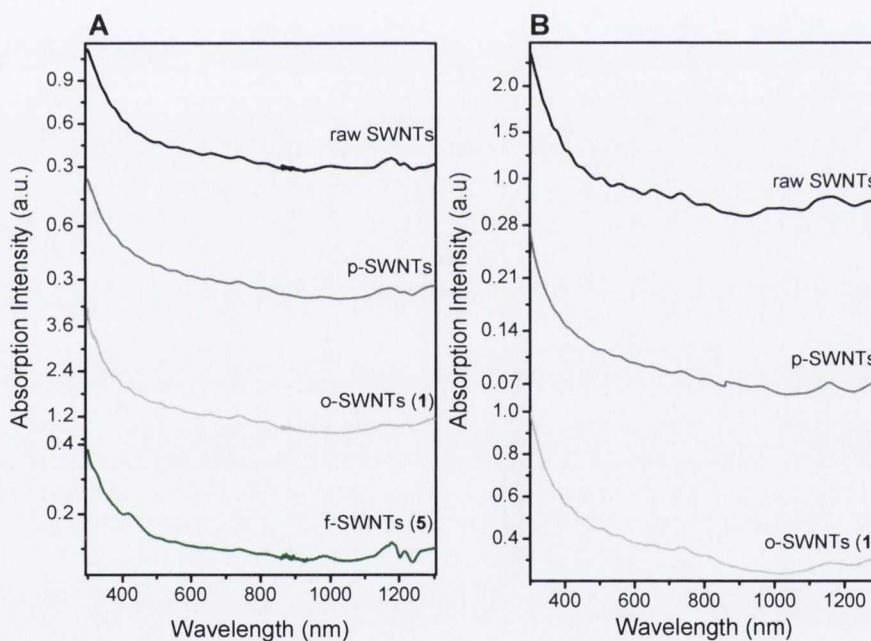


Figure 2.18: UV-Vis/NIR absorption spectra of A] raw SWNTs, p-SWNTs, o-SWNTs (1) and f-SWNTs (5) collected on the supernatant of initial 10^{-2} mg/mL nanotubes in DMF ; B] raw SWNTs, p-SWNTs and o-SWNTs (1) in SDBS aqueous solution [SWNTs]_i= 2.1×10^{-2} mg/mL, SWNTs:SDBS weight ratio 1:25 [Figure adapted from ref. 26].

The same outcome has been shown in another our work, where absorption studies have been run on SDBS aqueous solutions of the same raw, purified and oxidized nanotubes (Figure 2.18B),²⁶ and NIR-PL spectra (already shown in Figure 2.14) strengthened this assumption. It is worth to mention that the 2-step purification/oxidation protocol used in this work has shown to be a valuable way to produce a nanotube material with potential use as novel NIR fluorescent probes for molecular imaging.²⁶

2.4 On-off switching of SWNTs functionalized with spiropyran molecules.

In order to observe the switching of the f-SWNT (**5**) construct we have first studied the optical changes which could be induced on a molecular SP in solution upon UV irradiation and storage in the dark. A reversible reaction between the spiropyran (**6**) and merocyanine (ME) is observable upon irradiation with UV light (365 nm) and subsequent storage in the dark. The absorption spectra are reported in Figure 2.19 where it can be seen that after 30 seconds of UV irradiation, the absorption band of the merocyanine (at 594 nm) increases in intensity and after 8 minutes of storage in the dark it returns to its initial value.

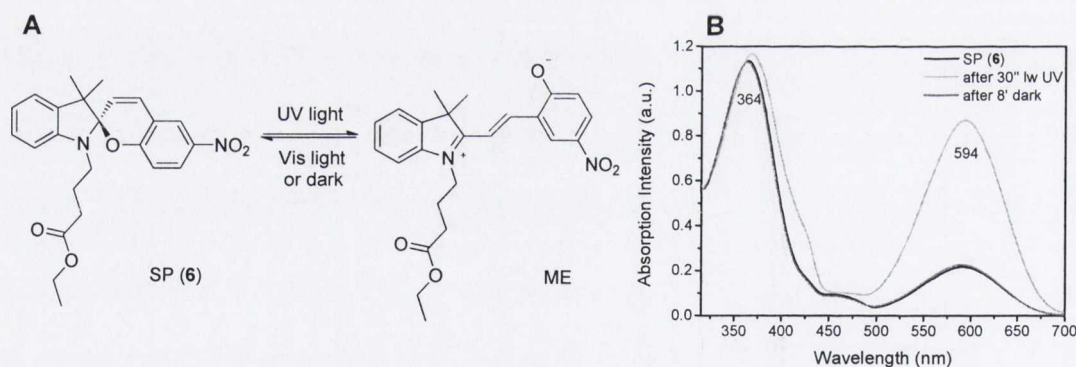


Figure 2.19: A] Photo interconversion of the closed spiropyran (SP, **6**) into the open form merocyanine (ME). B] Absorption spectra of SP (**6**) 10^{-4} M in DMF after 30 seconds UV illumination (long wavelength, 365 nm) and after 8 minutes storage in the dark.

On comparison of the UV-Vis absorption spectra of the o-SWNTs (**1**) and f-SWNTs (**5**) a peak is clearly observable at 417 nm in the latter, corresponding to the bound spiropyran (**6**) (Figure 2.20).

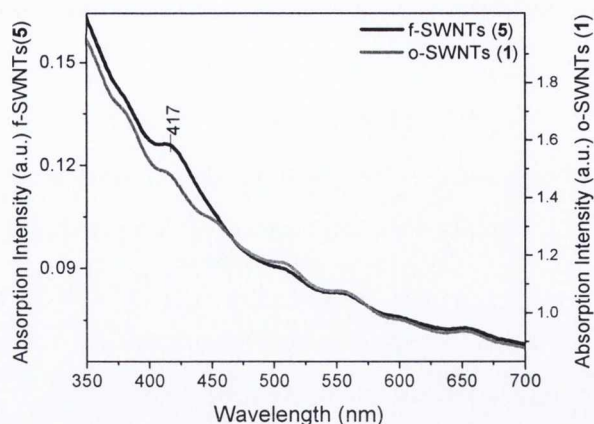


Figure 2.20: UV-Vis absorption spectra of f-SWNTs (**5**) and o-SWNTs (**1**) collected on the supernatant of initial 10^{-2} mg/mL nanotubes in DMF.

This absorption band is shifted with respect to molecular spiropyran (**6**) in solution, which is regarded as stemming from π - π interactions between the spiropyran and the graphitic nanotube surface. This is similar to shifts reported for ME bound to bulk materials.⁵⁴

The photoresponsiveness of f-SWNTs (**5**) in solution has been demonstrated by measuring the optical changes that occurred after UV and Vis light irradiations. Figure 2.21A illustrates the nature of such changes before and after UV illumination.

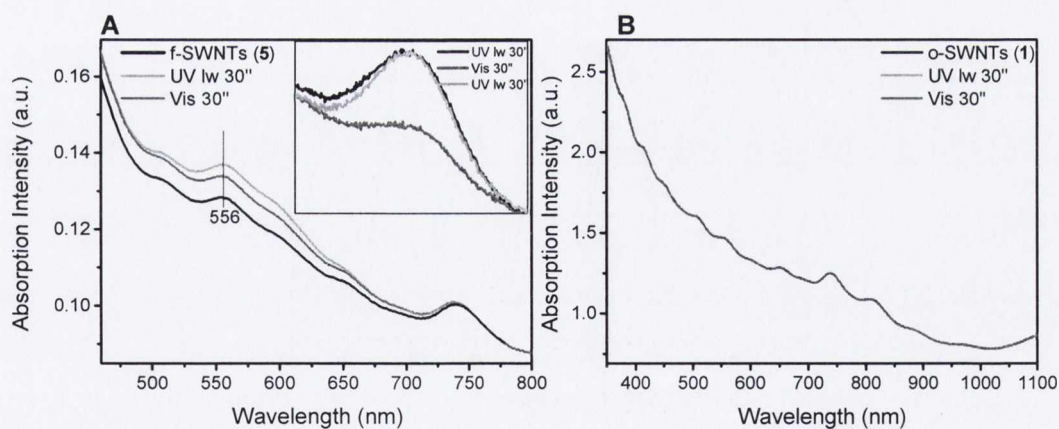


Figure 2.21: A) f-SWNTs (**5**) response to UV (365 nm) and Vis (560-900 nm) illumination for 30 seconds. Inset: difference absorption spectra of f-SWNTs (**5**) after 30 seconds UV, Vis and UV illuminations. B) UV-Vis absorption spectra of o-SWNTs (**1**) after UV and Vis light illumination. Spectra collected on the supernatant of initial 0.1 mg/mL nanotubes in DMF.

As a result of UV irradiation (365 nm) an increase in absorbance in the region characteristic to the merocyanine isomer is recorded. It is demonstrated that the merocyanine absorption band at 556 nm switches back to the starting value following 30 seconds of illumination with visible light (560-900 nm) as illustrated in Figure 2.21A. For improved data visualization, absorption spectra of f-SWNTs (**5**) have been subtracted from the spectra recorded after UV and Vis illumination, as reported in the inset in Figure 2.21A. The same experiments performed on oxidized nanotubes (**1**), have shown no photoresponsiveness as displayed in Figure 2.21B.

The reversible switching of the spiro molecule is demonstrated schematically in Figure 2.22A and the changes in the absorbance band intensity of SP f-SWNTs (**5**) are reproducible and the on-off switching cycles are reported in Figure 2.22B.

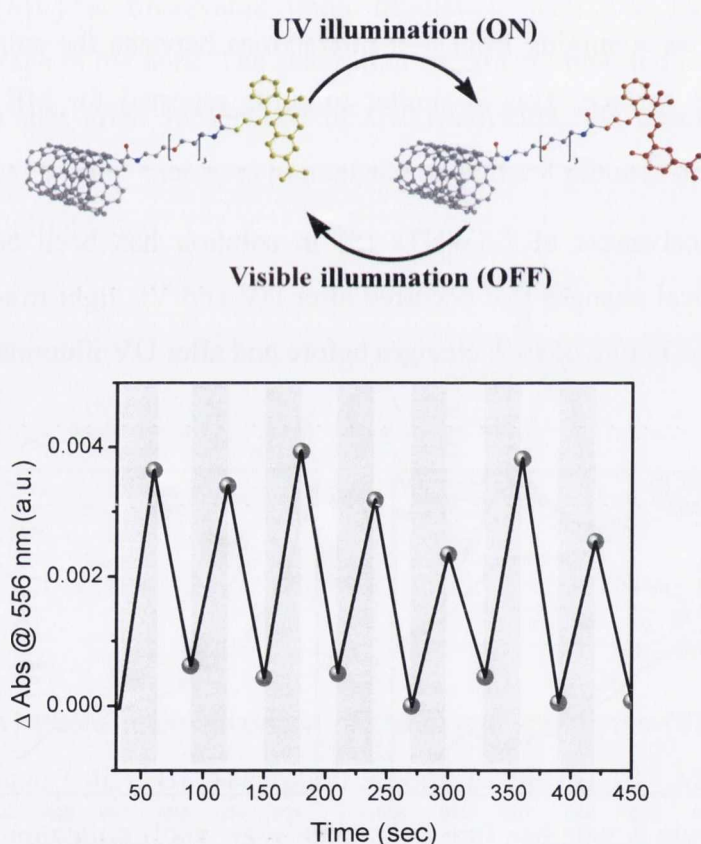


Figure 2.22: Top] On-off switching cartoon of f-SWNTs (**5**). Bottom] Absorbance changes at 556 nm of f-SWNTs (**5**) solutions following UV (365 nm) and visible (560-900 nm) illumination cycles. Gray and white bars indicate the UV and the Vis irradiation respectively. The spectra were collected on the supernatant of initial 0.1 mg/mL nanotubes in DMF.

2.5 Conclusions

We have demonstrated the preparation of a smart material composed of spiropyran functionalized SWNTs. All stages of the synthetic process have been characterized by means of TGA, spectroscopic and microscopic techniques to obtain a comprehensive overview of their structural, electronic and chemical properties. TGA analysis was used to demonstrate that the residue remaining following complete pyrolysis decreased from 24% in the raw nanotubes to 0% in the functionalized samples, confirming purification of the nanomaterial. The latter was supported by HR-TEM images, where black particles of residual metal catalyst are not anymore visible after nitric acid treatment. Weight losses calculated from TGA analyses suggested the presence of a high degree of functionalization of the tubes, estimated at approximately about one organic functional group every 149 carbon atoms. The analyses of TGA first derivative curve ensured that the SP moieties were present in the functionalized sample. The presence of aliphatic chains, amidic, ether and amino groups are confirmed by the stretching vibrations observed in the FT-IR spectrum of f-SWNTs as well as the nitro group present on the spiropyran aromatic ring. From AFM topographic images the nanotube average lengths have been calculated as approximately 600 nm. Raman Spectroscopy has been determinant in indirectly confirming the covalent functionalization of the SWNTs; the I_D/I_G ratio increases when comparing raw to chemically modified SWNTs. Micro Raman measurements have been performed on all nanotube samples with three different laser excitation wavelengths (457, 514 and 633 nm) in order to examine all diameter/chirality contributions. Sustained structured spectroscopic absorption and emission features of the chemically modified nanotubes have been confirmed by UV-Vis/NIR absorption spectroscopy and NIR-PL. The photoresponsiveness of our f-SWNTs in solution was demonstrated by measuring the optical changes that occurred after UV and Vis light illuminations. UV irradiation resulted in a substantial increase of the band at 556 nm and Vis light irradiation induced restoration of the initial intensity. We report light induced reversible conversion of spiropyran molecules attached to the SWNT from the close spiro conformation to the open merocyanine form in solution.

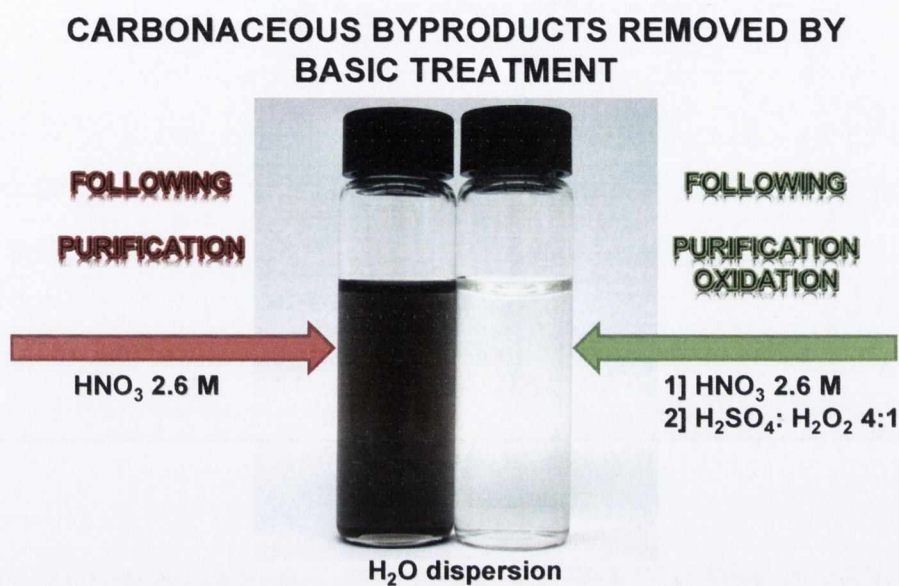
References

- (1) Niyogi, S.; Hamon, M. A.; Hu, H.; Zhao, B.; Bhowmik, P.; Sen, R.; Itkis, M. E.; Haddon, R. C. *Accounts of Chemical Research* **2002**, *35*, 1105.
- (2) Burghard, M. *Surface Science Reports* **2005**, *58*, 1.
- (3) Itkis, M. E.; Niyogi, S.; Meng, M. E.; Hamon, M. A.; Hu, H.; Haddon, R. C. *Nano Letters* **2002**, *2*, 155.
- (4) Hasan, T.; Sun, Z. P.; Wang, F. Q.; Bonaccorso, F.; Tan, P. H.; Rozhin, A. G.; Ferrari, A. C. *Advanced Materials* **2009**, *21*, 3874.
- (5) Raymo, F. M.; Giordani, S. *Proceedings of the National Academy of Sciences of the United States of America* **2002**, *99*, 4941.
- (6) Raymo, F. M.; Giordani, S. *Journal of the American Chemical Society* **2001**, *123*, 4651.
- (7) Ren, J. Q.; Tian, H. *Sensors* **2007**, *7*, 3166.
- (8) Natali, M.; Soldi, L.; Giordani, S. *Tetrahedron* **2010**, *66*, 7612.
- (9) Kawata, S.; Kawata, Y. *Chemical Reviews* **2000**, *100*, 1777.
- (10) Hamon, M. A.; Chen, J.; Hu, H.; Chen, Y. S.; Itkis, M. E.; Rao, A. M.; Eklund, P. C.; Haddon, R. C. *Advanced Materials* **1999**, *11*, 834.
- (11) Kostarelos, K.; Bianco, A.; Prato, M. *Nature Nanotechnology* **2009**, *4*, 627.
- (12) Pastorin, G. *Pharmaceutical Research* **2009**, *26*, 746.
- (13) Dumortier, H.; Lacotte, S.; Pastorin, G.; Marega, R.; Wu, W.; Bonifazi, D.; Briand, J.-P.; Prato, M.; Muller, S.; Bianco, A. *Nano Letters* **2006**, *6*, 1522.
- (14) Porter, A. E.; Gass, M.; Bendall, J. S.; Muller, K.; Goode, A.; Skepper, J. N.; Midgley, P. A.; Welland, M. *Acs Nano* **2009**, *3*, 1485.
- (15) Koyama, S.; Kim, Y. A.; Hayashi, T.; Takeuchi, K.; Fujii, C.; Kuroiwa, N.; Koyama, H.; Tsukahara, T.; Endo, M. *Carbon* **2009**, *47*, 1365.
- (16) Kolosnjaj-Tabi, J.; Hartman, K. B.; Boudjemaa, S.; Ananta, J. S.; Morgant, G.; Szwarc, H.; Wilson, L. J.; Moussa, F. *Acs Nano* **2010**, *4*, 1481.
- (17) Khairutdinov, R. F.; Itkis, M. E.; Haddon, R. C. *Nano Letters* **2004**, *4*, 1529.
- (18) Guo, X. F.; Small, J. P.; Klare, J. E.; Wang, Y. L.; Purewal, M. S.; Tam, I. W.; Hong, B. H.; Caldwell, R.; Huang, L. M.; O'Brien, S.; Yan, J. M.; Breslow, R.; Wind, S. J.; Hone, J.; Kim, P.; Nuckolls, C. *Science* **2006**, *311*, 356.
- (19) Guo, X. F.; Huang, L. M.; O'Brien, S.; Kim, P.; Nuckolls, C. *Journal of the American Chemical Society* **2005**, *127*, 15045.
- (20) Yildiz, I.; Deniz, E.; Raymo, F. M. *Chemical Society Reviews* **2009**, *38*, 1859.
- (21) Malic, E.; Weber, C.; Richter, M.; Atalla, V.; Klamroth, T.; Saalfrank, P.; Reich, S.; Knorr, A. *Physical Review Letters* **2011**, *106*, 097401.
- (22) Schnorr, J. M.; Swager, T. M. *Chemistry of Materials* **2011**, *646*.

- (23) Liu, J.; Rinzler, A. G.; Dai, H. J.; Hafner, J. H.; Bradley, R. K.; Boul, P. J.; Lu, A.; Iverson, T.; Shelimov, K.; Huffman, C. B.; Rodriguez-Macias, F.; Shon, Y. S.; Lee, T. R.; Colbert, D. T.; Smalley, R. E. *Science* **1998**, *280*, 1253.
- (24) Giordani, S.; Colomer, J. F.; Cattaruzza, F.; Alfonsi, J.; Meneghetti, M.; Prato, M.; Bonifazi, D. *Carbon* **2009**, *49*, 578.
- (25) Movia, D.; Del Canto, E.; Giordani, S. *Physica Status Solidi B-Basic Solid State Physics* **2009**, *246*, 2704.
- (26) Movia, D.; Del Canto, E.; Giordani, S. *The Journal of Physical Chemistry C* **2010**, *114*, 18407.
- (27) Hamon, M. A.; Itkis, M. E.; Niyogi, S.; Alvaraez, T.; Kuper, C.; Menon, M.; Haddon, R. C. *Journal of the American Chemical Society* **2001**, *123*, 11292.
- (28) Haddon, R. C. *Science* **1993**, *261*, 1545.
- (29) Haddon, R. C. *Journal of the American Chemical Society* **1987**, *109*, 1676.
- (30) Bhirde, A. A.; Patel, S.; Sousa, A. A.; Patel, V.; Molinolo, A. A.; Ji, Y. M.; Leapman, R. D.; Gutkind, J. S.; Rusling, J. F. *Nanomedicine* **2010**, *5*, 1535.
- (31) Kalinina, I.; Worsley, K.; Lugo, C.; Mandal, S.; Bekyarova, E.; Haddon, R. C. *Chemistry of Materials* **2011**, *23*, 1246.
- (32) Aakeroy, C. B.; Hurley, E. P.; Desper, J.; Natali, M.; Douglawi, A.; Giordani, S. *CrystEngComm* **2010**, *12*, 1027.
- (33) Kaiser, E.; Colescot, R. I.; Bossing, C. D.; Cook, P. I. *Analytical Biochemistry* **1970**, *34*, 595.
- (34) Quintana, M.; Prato, M. *Chemical Communications* **2009**, 6005.
- (35) Pantarotto, D.; Browne, W. R.; Feringa, B. L. *Chemical Communications* **2008**, 1533.
- (36) Rinaldi, A.; Frank, B.; Su, D. S.; Hamid, S. B. A.; Schloegl, R. *Chemistry of Materials* **2011**, *23*, 926.
- (37) Ros, T. G.; van Dillen, A. J.; Geus, J. W.; Koningsberger, D. C. *Chemistry – A European Journal* **2002**, *8*, 1151.
- (38) Landi, B. J.; Cress, C. D.; Evans, C. M.; Raffaele, R. P. *Chemistry of Materials* **2005**, *17*, 6819.
- (39) Costa, S.; Borowiak-Palen, E.; Kruszynska, M.; Bachmatiuk, A.; Kalenczuk, R. J. *Materials Science-Poland* **2008**, *26*, 433.
- (40) Graupner, R. *Journal of Raman Spectroscopy* **2007**, *38*, 673.
- (41) Singh, P.; Campidelli, S.; Giordani, S.; Bonifazi, D.; Bianco, A.; Prato, M. *Chemical Society Reviews* **2009**, *38*, 2214.
- (42) Rao, A. M.; Richter, E.; Bandow, S.; Chase, B.; Eklund, P. C.; Williams, K. A.; Fang, S.; Subbaswamy, K. R.; Menon, M.; Thess, A.; Smalley, R. E.; Dresselhaus, G.; Dresselhaus, M. S. *Science* **1997**, *275*, 187.

- (43) Ferrari, A. C.; Robertson, J. *Physical Review B* **2000**, *61*, 14095.
- (44) Lazzeri, M.; Piscanec, S.; Mauri, F.; Ferrari, A. C.; Robertson, J. *Physical Review B* **2006**, *73*, 155426.
- (45) Ferrari, A. C. *Solid State Communications* **2007**, *143*, 47.
- (46) Salzmann, C. G.; Llewellyn, S. A.; Tobias, G.; Ward, M. A. H.; Huh, Y.; Green, M. L. H. *Advanced Materials* **2007**, *19*, 883.
- (47) Shao, L.; Tobias, G.; Salzmann, C. G.; Ballesteros, B.; Hong, S. Y.; Crossley, A.; Davis, B. G.; Green, M. L. H. *Chemical Communications* **2007**, 5090.
- (48) Dyke, C. A.; Stewart, M. P.; Tour, J. M. *Journal of the American Chemical Society* **2005**, *127*, 4497.
- (49) Meyer, J. C.; Paillet, M.; Michel, T.; Moreac, A.; Neumann, A.; Duesberg, G. S.; Roth, S.; Sauvajol, J. L. *Physical Review Letters* **2005**, 95.
- (50) Jorio, A.; Fantini, C.; Pimenta, M. A.; Capaz, R. B.; Samsonidze, G. G.; Dresselhaus, G.; Dresselhaus, M. S.; Jiang, J.; Kobayashi, N.; Gruneis, A.; Saito, R. *Physical Review B* **2005**, 71.
- (51) Weisman, R. B.; Bachilo, S. M. *Nano Letters* **2003**, *3*, 1235.
- (52) Chen, J.; Hamon, M. A.; Hu, H.; Chen, Y. S.; Rao, A. M.; Eklund, P. C.; Haddon, R. C. *Science* **1998**, *282*, 95.
- (53) Liu, X. P., T.; Knupfer, M.; Fink, J. *Physical Review B* **2004**, *70*, 205405.
- (54) Sayama, K. H., K.; Ohga, Y.; Shinpou, A.; Suga, S.; Arakawa, H. *New Journal of Chemistry* **2001**, *25*, 200.

Chapter 3. Critical Investigation of Defect Site Functionalization on Single-Walled Carbon Nanotubes



The presence of carboxylated carbonaceous material in nitric acid treated SWNT samples has recently brought renewed focus on the processes by which covalent functionalization of such materials are carried out. In this chapter, using a widely reported 2-step purification/oxidation procedure, we investigate the effect of treatment with base and solvent washing on the functionalization, final properties and behavior of SWNTs. We demonstrate, using a number of spectroscopic and microscopic techniques, that in the absence of NaOH treatment, COOH functionality is introduced directly onto SWNTs, and not only onto carbonaceous material present in the sample. Covalent functionalization of the oxidized materials is also investigated by attachment of a fluorescent probe, and ultimately, whether treated with base or solvent washed the resulting materials will show to be close to identical with respect to both their appearance and properties. The evidence that using either of these purification/oxidation strategies functionalized materials can be produced that still exhibit distinctive optical/electronic properties is here reported, as demonstrated by sustained structured spectroscopic absorption and emission features.

3.1 Introduction

The widespread exploitation of the unique properties of SWNTs is still impeded by a number of practical aspects such as purity, solubility and processibility. Great effort has recently been exerted with regards to their chemical treatment and functionalization in order to overcome these problems, and also to drive towards the production of more manageable multi-functional materials.

As already mentioned in the introductory chapter of this thesis, two approaches have been widely reported in the literature for the chemical modification of SWNTs, which involve either the non-covalent adsorption onto the nanotube surface^{1,2} or the covalent attachment to the π -conjugated skeleton.^{3,4} There are obvious advantages related to the covalent strategy, such as control over the number of functional moieties which may be attached,⁵⁻⁷ in addition to the well defined nature and stability of the linker which connects them to the nanotube. Care must be taken however, as the optical, electronic and thermal properties depend heavily upon the highly conjugated form in which the SWNTs exist,⁸⁻¹⁰ and their covalent modification, depending on its location, can result in loss of those properties.¹¹ The two general strategies for covalently attaching functional molecules to the nanotube structure involve, as already described, or (1) the reaction at the sidewall of the tube, or (2) the addition of functional moieties to oxidized defect sites already present or produced during acidic/oxidative purification of the material.¹²

In the first strategy the introduction of a covalent bond at the sidewall provokes the substantial disruption of the C=C conjugation, and as a consequence the loss of the distinctive electronic/optical properties of the tubes. On the contrary, the second strategy, which has been extensively used by the nanotube community, permits the preservation of the latter depending on both the time of reaction and the nitric acid concentration. Nitric acid is used as a standard reagent to remove synthetic by-products such as residual metal catalyst and amorphous carbon from raw SWNT samples,¹³⁻¹⁷ and varying numbers of oxygenated functionalities (mainly carbonyl and carboxylic acid groups) can be introduced onto defect sites, to which further functionality are commonly subsequently attached.¹⁶

Recently it has been reported that during the acidic/oxidative purification procedure small polycyclic aromatic sheets edge-terminated with carboxyl groups, coined as

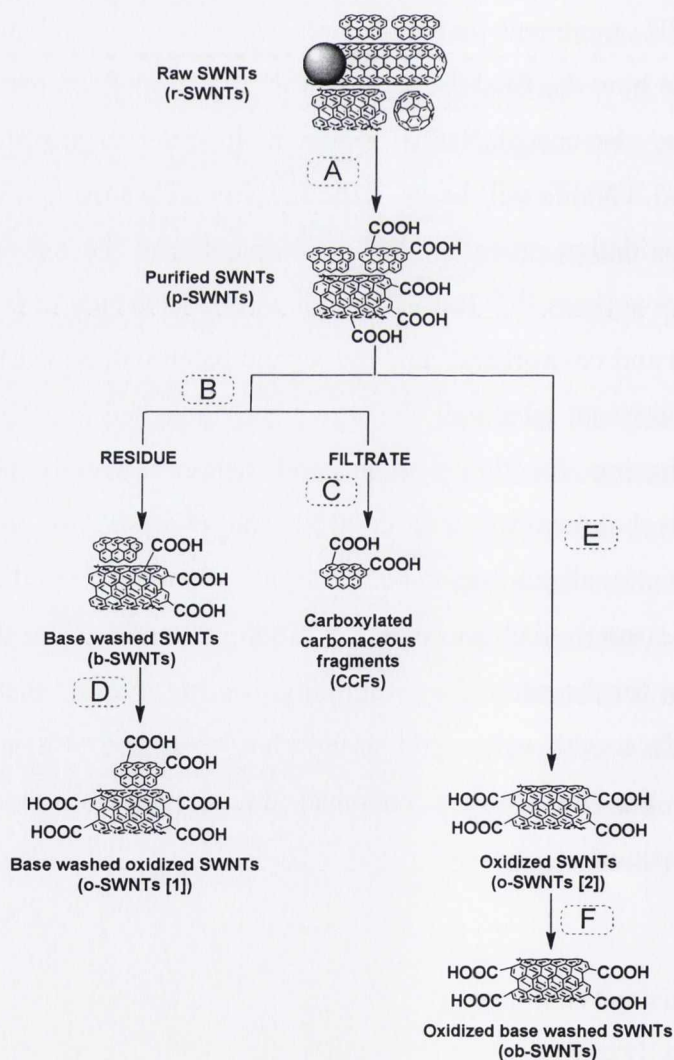
carboxylated carbonaceous fragments (CCFs), are also generated and it is understood that they form a “uniform and reactive coating on the SWNTs”.^{15,18,19} The effective removal of the CCFs from acid purified samples by NaOH treatment has been demonstrated,¹⁹⁻²¹ and it has therefore come into contention as to whether reactions carried out, following the purification step, actually result in covalent modification of the nanotubes or only result in functionalization of the CCFs. Haddon and co-workers have more recently shown that nitric acid purified samples exhaustively washed with aqueous base nevertheless contained a sufficient number of carboxylic acid groups to prepare high quality covalently functionalized nanotubes.²² Only this year, Romanos *et al.* confirmed that the thermal treatment of SWNTs in mild oxidative conditions leads to the formation of amorphous carbon, although a considerable fraction of functional groups remains attached onto the SWNTs walls rather than on CCFs.²³

These recent studies raise some important questions as to whether previously reported procedures presenting covalent functionalization using defect site chemistry,²⁴⁻²⁸ in the absence of NaOH treatment, were actually producing covalently functionalized materials, and also how the final properties of the functionalized materials are affected by the presence or absence of NaOH treatment. In order to attempt to answer these questions, oxidized SWNTs will be prepared in two batches using a widely reported 2-step purification/oxidation procedure,^{12,29-32} comparable to the one initially developed by Smalley and co-workers.^{33,34} The first batch will be subjected to the NaOH treatment reported by Green and co-workers¹⁹ and the second batch will be washed with a number of solvents. A fluorescent label will be subsequently attached to each batch as a simple method of monitoring functionalization, and using a variety of complementary characterization techniques we will contrast and compare the final properties of oxidized and functionalized nanotube materials obtained *via* the two “washing” approaches. We strongly believe that the findings reported in this work will be extremely relevant for the nanotube community, bearing in mind that the decoration of the nanotube surface with carboxylic groups has been and still is one of the most utilized anchors for the further chemical functionalization *via* amidation and esterifications reactions.

3.2 Purification and oxidation of SWNTs

The purification of as purchased raw SWNTs was performed using the widely reported protocol, already utilized and described in chapter 2, which consists of refluxing the nanotubes in an aqueous dispersion of nitric acid for 48 hours (Scheme 3.1).³³ The strong acidic conditions are used to remove catalytic iron nanoparticles and also to oxidize defect sites on the SWNTs, with carboxylated carbonaceous fragments (CCFs) being produced as a by-product. The purified sample (p-SWNTs) was split into two batches, of which the first was subjected to the NaOH treatment to produce b-SWNTs and the second was sonicated in organic solvents followed by filtration.

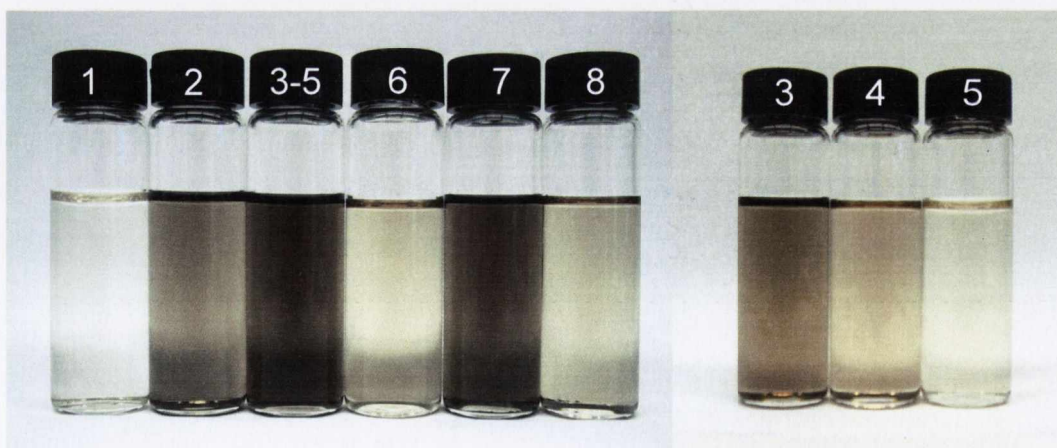
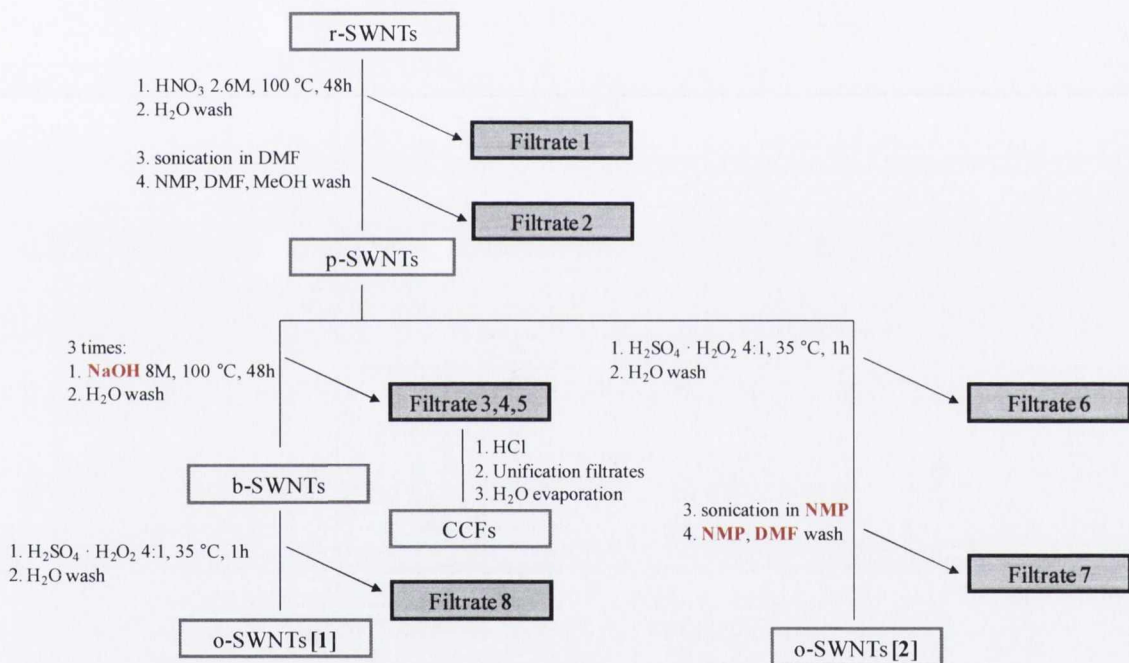
Scheme 3.1: Representation of purification and oxidation of SWNTs. A] HNO_3 2.6 M, 100 °C, 48 h. B] NaOH 8M, 100 °C, 48 h in triplicate. C] Neutralization with HCl and concentration to a solid. D, E] H_2SO_4 : H_2O_2 4:1, 35 °C, 1 h. F] NaOH 8M, 100 °C, 48 h.



Thereafter both batches were further oxidized for 1 hour at 35 °C in a mixture of sulphuric acid and hydrogen peroxide to produce o-SWNTs [1] and [2] (Scheme 3.1). Following each synthetic step it was ensured that the nanotubes were washed thoroughly with water until a neutral pH was reached, and subsequently dispersed in DMF by sonication and washed with DMF and methanol until the filtrate ran clear.

The detailed washing procedures and the filtrate pictures are reported in Scheme 3.2, where the presence of carbonaceous material is evident in all the collected fractions coming from both NaOH and solvent washing routes. When filtrates 3-5 and 7 are compared, their similar colour suggests an analogous amount of carbonaceous material removal.

Scheme 3.2: Detailed NaOH/solvent washing procedures and pictures of the filtrates.



3.3 Characterization of purified and oxidized SWNTs

3.3.1 FT-IR analysis

The introduction and removal of specific functional groups following each treatment was monitored by infrared spectroscopy. The appearance of absorption bands related to carbonyl stretching (1724 cm^{-1}) and the stretching of C=C bonds in the polyaromatic backbone of the tubes ($1570\text{--}1580\text{ cm}^{-1}$),^{22,35} are clearly evident following treatment with nitric acid (Figure 3.1A).

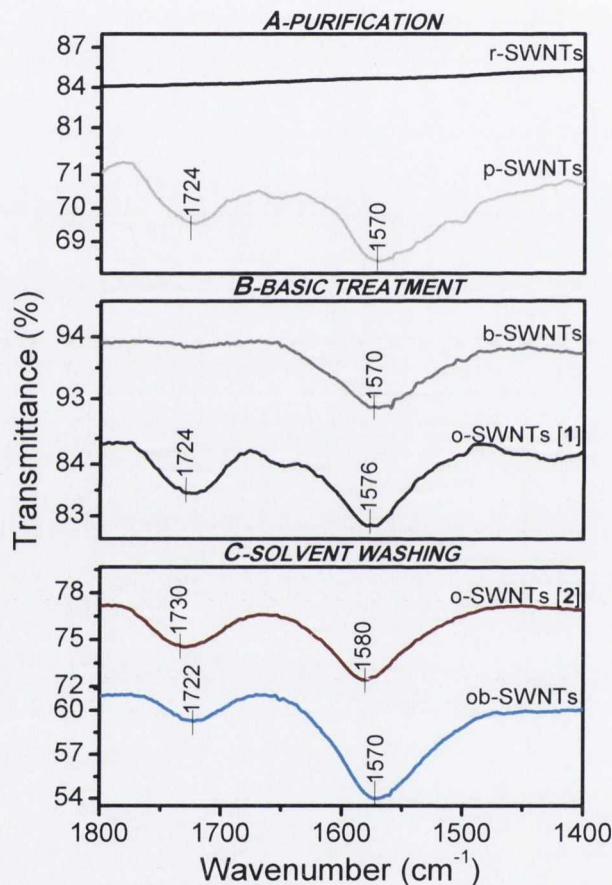


Figure 3.1: ATR/FT-IR spectra of A] raw (r-SWNTs) and purified (p-SWNTs), B] base treated (b-SWNTs) and oxidized (o-SWNTs [1]), C] oxidized (o-SWNTs [2]) and oxidized base treated (ob-SWNTs) nanotubes. Spectra have been baseline corrected to improve data visualization.

The carbonyl stretching vibration may be assigned to carboxylic acid groups (COOH) produced either at defect sites on the nanotubes or on other carbonaceous material in the sample. This band notably decreased after NaOH treatment (Figure 3.1B), indicating

that COOH functionalities in the sample were mainly present on the carbonaceous fragments which could be washed away after conversion to the more soluble sodium salt. FT-IR and Raman analyses of the filtrate (unified fractions 3-5 pictured in Scheme 3.2) demonstrated the presence of CCFs in accordance with the literature,³⁶ as reported in Figure 3.2.

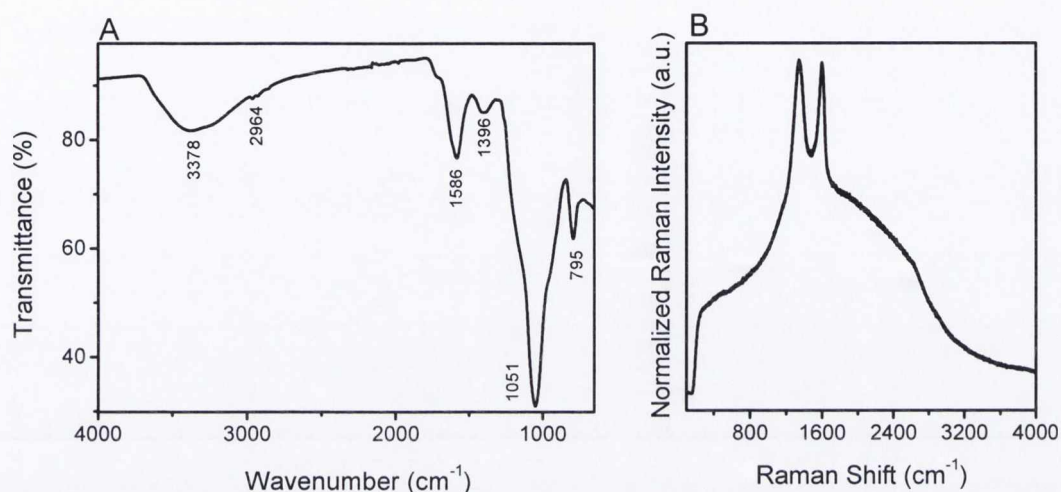


Figure 3.2: A) ATR/Fourier transform IR (FT-IR) spectrum of carboxylated carbonaceous fragments (CCFs). IR (ATR) ν_{\max} /cm⁻¹: 3600-3200 (O-H str), 2964 (C-H str), 1586 (C=C str, or C=O str), 1396 (C-H bend, or C=O str), 1051 (C-O str), 795 (Na-O or C-H bend).³⁶⁻³⁸ To improve data visualization the spectrum has been baseline corrected. B) Raman spectrum of CCFs. I_D/I_G ratio = 1, indicating high degree of defects in the carbonaceous material.

Following oxidation to o-SWNTs [1] the carbonyl stretching vibration is seen to reappear. As infrared spectroscopy cannot distinguish between COOH groups attached to the nanotubes and those attached to carbonaceous material, o-SWNTs [1] and [2] appear almost identical (Figure 3.1B and 3.1C). A small portion of o-SWNTs [2] was treated with base in order to investigate the presence of CCFs following the solvent washing procedure. Only a small reduction in the carbonyl band is observed going from o-SWNTs [2] to oxidized base washed nanotubes ob-SWNTs (Figure 3.1C), strongly indicating that the COOH functionalities present in the sample are indeed on the SWNTs. The filtrates from both NaOH treatments are illustrated in Figure 3.3, and the difference in the quantity of CCFs washed from each sample is evident from the filtrate

color, demonstrating the influence of the solvent washing and the oxidation procedure on the composition of the sample.

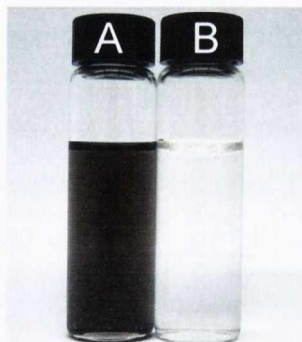


Figure 3.3: Pictures of the filtrates following NaOH treatments of A] p-SWNTs and B] o-SWNTs [2].

3.3.2 Raman spectroscopy analysis

Raman spectroscopy was used to monitor the introduction of defects into each sample, by monitoring changes in the intensity ratio of the characteristic D- (defect) and G- (graphitic) bands (Figure 3.4).^{39,40}

Following the purification procedure the I_D/I_G ratio increased from 14 to 44% indicating breakage of the graphene sheet symmetry (Figure 3.4A). In this case the symmetry disruption is associated with the introduction of defects on both the nanotubes and the carbonaceous fragments. The relative intensity of the D-band subsequently decreased from 44 to 21% following NaOH treatment, in accordance with literature values (Figure 3.4B).^{19,22,36} The persistence of amorphous carbon (not containing acidic functionality) in the sample is however clear from the magnitude and shape of the D-band. The relative intensity again increased to 26% following the oxidation to o-SWNTs [1], indicating the introduction of defects on both the nanotubes and amorphous carbon (Figure 3.4B). When compared to o-SWNTs [2], where the sample was washed with NMP instead of aqueous base, the relative D-band intensity dropped to below that of the raw material (Figure 3.4C). This coupled with the restored sharpness and symmetry of the band, strongly indicates that the oxidation step in combination with the NMP treatment results in removal of both the CCFs and amorphous carbon from the sample. The NaOH treatment of o-SWNTs [2] confirms

this, demonstrating only a small reduction of the I_D/I_G ratio (Figure 3.4C). Enlarged spectra, shown in Appendix (Figure 3.1a) clearly contrast the broad unsymmetrical D-band of o-SWNTs [1] with the sharper more symmetrical D-band of o-SWNTs [2].

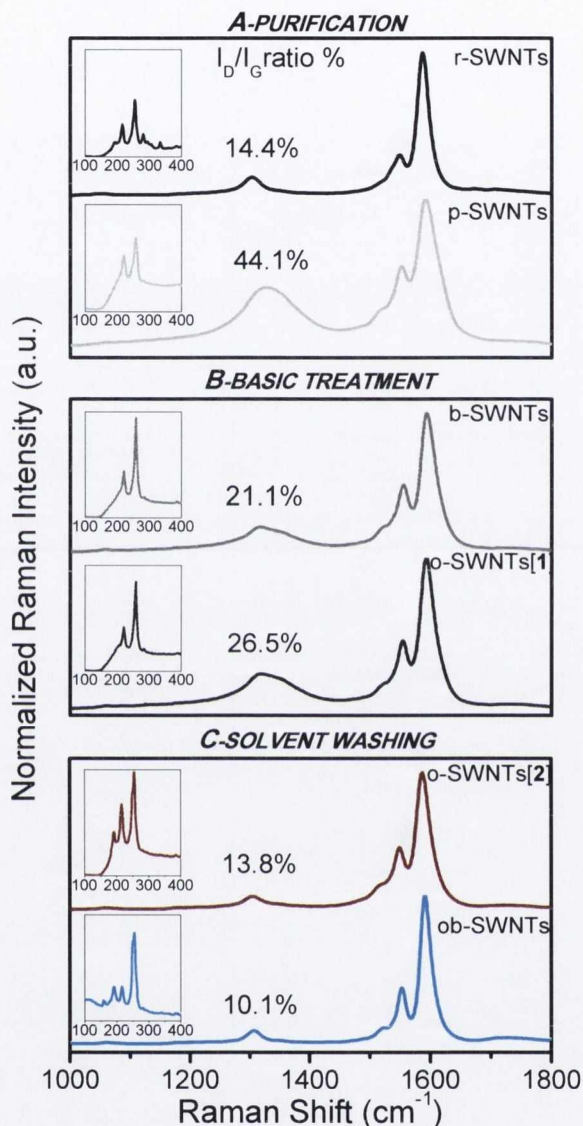


Figure 3.4: Raman spectra ($\lambda_{exc}=633$ nm) of A) r-SWNTs and p-SWNTs, B) b-SWNTs and o-SWNTs [1], C) o-SWNTs [2] and ob-SWNTs. All the spectra have been normalized on the G-band. Insets show the RBM bands (scale: 0-0.24 a.u.).

3.3.3 X-ray photoelectron spectroscopy analysis

X-ray photoelectron spectroscopy (XPS) is a common surface analysis for the characterization of carbonaceous materials,^{41,42} as it allows to determine (1) chemical

composition, (2) presence of impurities, and (3) nature of chemical bonds. In the present work XPS was used to evaluate the changes in the chemical nature of the functional groups present in the sample following the different steps of the purification/oxidation process. Figure 3.5 illustrates the C 1s and O 1s core level spectra for each sample in addition to the fitting into the various components used to reproduce the spectra [all XPS experiments performed by our collaborators at the University of Mons, Belgium].

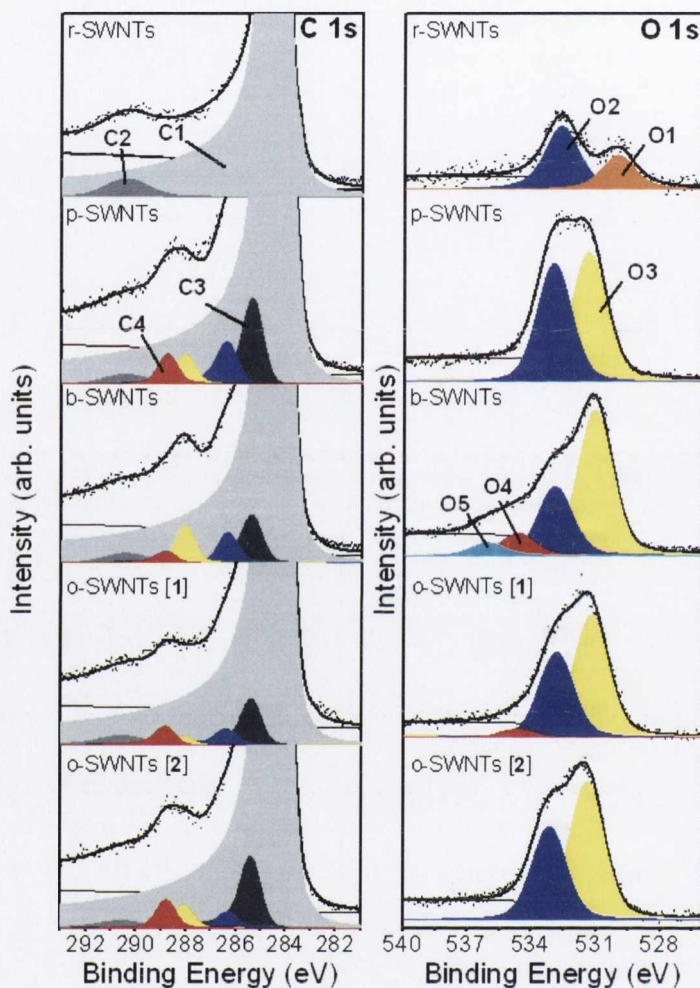


Figure 3.5: XPS C 1s and O 1s spectra of r-SWNTs, p-SWNTs, b-SWNTs, o-SWNTs [1] and o-SWNTs [2]. Where fitted components are labelled as: **C1**: C-C sp^2 , **C2**: plasmon loss, **C3**: C-C sp^3 , **C4**: (C=O)-O-, and **O1**: Fe_2O_3/Fe_3O_4 , **O2**: C-O-C/(C=O)-O-/C-OH, **O3**: (C=O), **O4**: (C=O)-O-Na,⁴³ **O5**: H_2O .

Characteristic contributions including the primary graphitic peak (284.4 eV) and plasmon loss (290.6 eV) are evident from the C 1s peak of the r-SWNTs. Following nitric acid purification a number of new contributions appear, which can be associated

to the increasing sp^3 content (285.3 eV)⁴¹ and the grafting of oxygen containing functionality (286 -289 eV) onto the sample, most notably carboxylic acid groups at 288.8 eV.⁴² Following NaOH treatment a reduction in the intensity of both the sp^3 and carboxylic acid components is observed indicating removal of CCFs, while after oxidation to o-SWNTs [1], as expected, the intensity of the component associated to carboxylic acid increases. When o-SWNTs [1] and [2] are compared the C 1s peak and its components appear much the same, indicating the similarity in the type and quantity of functionality present whether or not NaOH treatment is performed.

Analysis of the O 1s peak reveals the presence of iron oxide catalyst (530 eV)⁴⁴ in the raw material, which disappears following the purification procedure. A four-fold increase in the oxygen content of the sample also occurs as expected, which is accompanied by the appearance of an additional component at 531.3 eV representing oxygen species of lower binding energy.⁴² Following NaOH treatment a reduction in the relative intensity of the carboxylic acid containing component is evident, presumably due to the removal of CCFs. In accordance with the IR and Raman results this contribution again increases following the oxidation procedure indicating introduction of carboxylic acid functionality onto the SWNTs. On comparison of o-SWNTs [1] and [2] it is again evident that the oxygen containing functionality in each sample is similar both in the presence or absence of NaOH treatment.

3.3.4 NIR-PL and UV-Vis/NIR absorption spectroscopies analysis

In order to fully exploit the remarkable properties of SWNTs, the preservation of optical and electronic properties following chemical treatments is an important factor.⁸⁻¹⁰ The effect of each treatment on the structured emission and absorption features of the SWNTs was monitored by NIR-PL and UV-Vis/NIR absorption spectroscopies, and the results are illustrated in Figures 3.6 and 3.7, respectively.

The NIR-PL spectra clearly show that all nanotubes samples display a structured emission in the NIR (Figure 3.6 and 3.2a in Appendix).

In addition UV-Vis/NIR absorption data demonstrate the persistence of the van Hove singularities (Figure 3.7), which is in accordance with our previously reported results.³¹

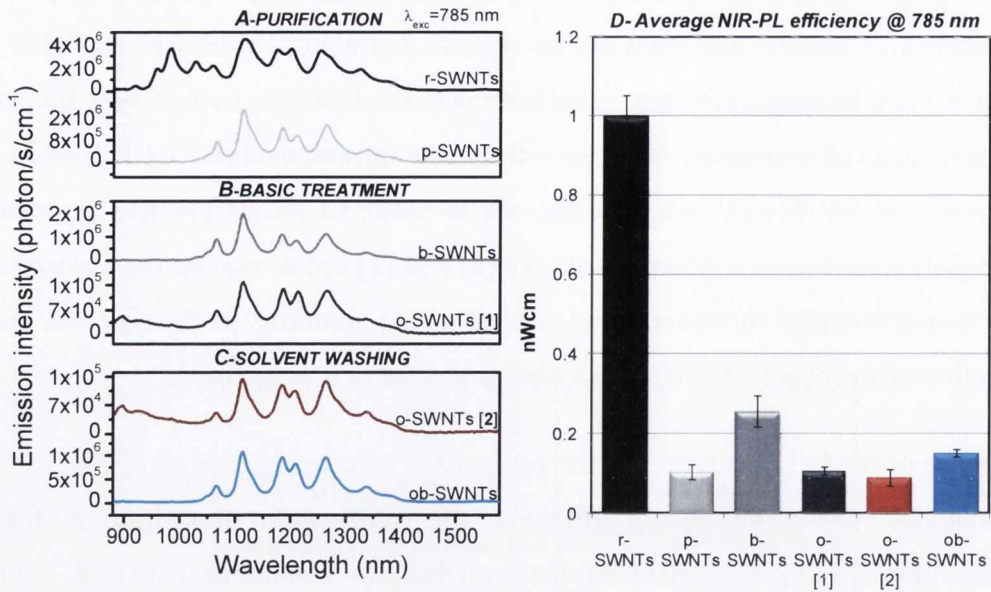


Figure 3.6: NIR photoluminescence (PL) spectra ($\lambda_{exc} = 785$ nm) of A) r-SWNTs and p-SWNTs, B) b-SWNTs and o-SWNTs [1], C) o-SWNTs [2] and ob-SWNTs. D) Histograms showing the average NIR-PL efficiency at $\lambda_{exc} = 785$ nm ($n_{measurements} = 3$).

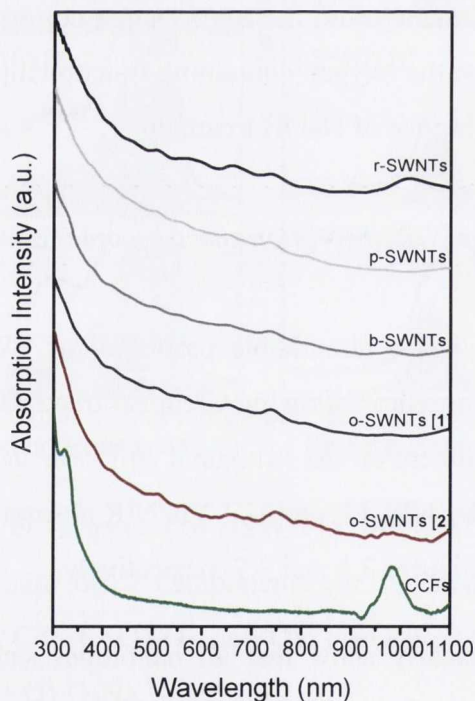


Figure 3.7: UV-Vis/NIR absorption profiles of all samples in DMF. Absorption values (Y-axes) have been varied in order to better visualize the van Hove singularities. Spectra with actual absorption intensity values are reported in Appendix Figure 3.3a.

The assignment of the optical frequencies from NIR-PL spectra, demonstrate that the bands at smaller wavelengths (900-1050 nm), corresponding to small diameter SWNTs, are completely destroyed during the purification procedure. This is in agreement with the loss of smaller diameter bands from the RBM region of the Raman spectra (Figure 3.4). The complete destruction of these SWNTs implies that all nanotubes in the sample have been affected by the acidic treatment and indicates that the PL observed is not simply due to the presence of unaltered nanotubes.

The investigation into quenching of the NIR-PL, following each chemical treatment (Figure 3.6D and histograms in Figure 3.2A), has also given us a useful insight into the extent of defect introduction on the SWNTs with minimal interference from the other carbonaceous impurities present in the sample. The average NIR emission efficiency was evaluated for all SWNT samples (Figure 3.6D) and it is clear that a 90 % quenching of the photoluminescence was observed following the purification procedure (NIR-PL efficiency calculations reported in Chapter 5). Under acidic conditions this is known to occur as a result of protonation reactions at the nanotube surface.⁴⁵⁻⁴⁷ However, Weisman and co-workers have demonstrated that this doping process is completely reversible upon addition of base.^{46,47} Following NaOH treatment of the p-SWNTs, reappearance of the PL is observed, but only to 30 % of the original intensity, demonstrated by the raw material. We thus propose that the irreversible quenching observed, originates from defects produced in the nanotube structure during the purification procedure, as opposed to reversible doping by protonation. If we also consider that functionality introduced onto the nanotube structure during the purification procedure, for a large extent, does not seem to consist of carbonyl containing moieties (Figure 3.1B), the highly oxidative treatment seems necessary, in order to convert the defects into reactive COOH groups.

Following the oxidation procedure the NIR-PL of o-SWNTs [1] and [2] again drops to a value of approximately 10 %, which is most probably the result of both defect introduction and doping processes. After NaOH treatment of o-SWNTs [2] an increase in the PL efficiency is evident, however it is still smaller than b-SWNTs suggesting the introduction of additional defects during the oxidation step.

3.3.5 Thermogravimetric analysis

TGAs were performed on each sample in air, and following treatment with nitric acid nearly quantitative removal of the catalyst was demonstrated, where the residual ash content at 900 °C dropped from 34% in the raw material to 1% (Figure 3.8 and Table 3.1).

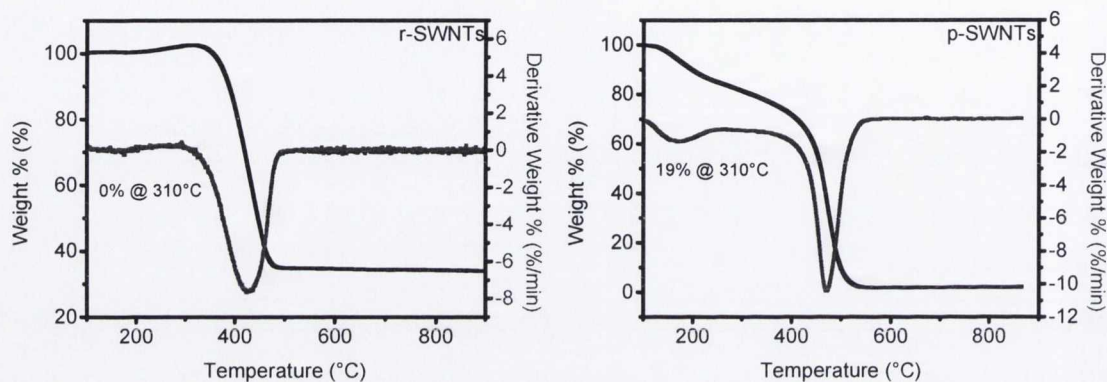


Figure 3.8: TGA traces of r-SWNTs and p-SWNTs. The weight losses % at 310 °C attributed to the decomposition of organic groups in the nanotube samples are reported. All the experiments have been run in air atmosphere with a temperature rate of 10 °C min⁻¹.

<i>Sample</i>	<i>Weight loss @ 310 °C</i>
r-SWNTs	0%
p-SWNTs	19%
b-SWNTs	5%
CCFs	7%
o-SWNTs [1]	11%
o-SWNTs [2]	10%

Table 3.1: Weight loss % at 310 °C attributed to the decomposition of organic groups in the nanotube samples are reported for r-SWNTs, p-SWNTs, b-SWNTs, CCFs, o-SWNTs [1] and [2].

TGAs were also performed under a nitrogen atmosphere (Figure 3.9 and Table 3.2). On comparison of both the curve shape and the weight loss below 400 °C, before and

after treatment with NaOH, a significant change is observable which is indicative of the effectiveness of the NaOH treatment in the removal of carbonaceous material from the p-SWNTs.

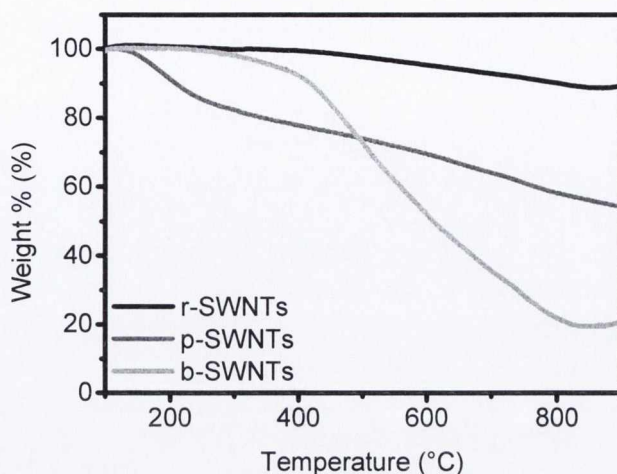


Figure 3.9: TGA traces of r-SWNTs, p-SWNTs and b-SWNTs. The experiments have been run in nitrogen atmosphere with a temperature rate of $10\text{ }^{\circ}\text{C min}^{-1}$.

<i>Sample</i>	<i>Weight loss @ 400 °C</i>
r-SWNTs	0.5 %
p-SWNTs	22 %
b-SWNTs	8 %
CCFs	13 %
o-SWNTs [1]	12 %
o-SWNTs [2]	11 %

Table 3.2: Weight loss % at 400 °C attributed to the decomposition of organic groups in the nanotube samples are reported for r-SWNTs, p-SWNTs, b-SWNTs, CCFs, o-SWNTs [1] and [2].

Another indication of the successful removal of impurities and CCFs from the nanotube sample comes from the increased oxidative stability of the material after purification and treatment with NaOH (Appendix Figure 3.4a, 3.5a). This result is in agreement with recently reported data, where CCFs have shown to act as oxidation initiators creating hotspots on the nanotube surface which induce their combustion to lower temperatures.⁴⁸

3.3.6 Transmission electron microscopy analysis

HR-TEM confirmed the effective purification of the nanotube material, where the high content of iron catalyst, visible as black particles in the r-SWNTs, is absent in the purified material (Figure 3.10).

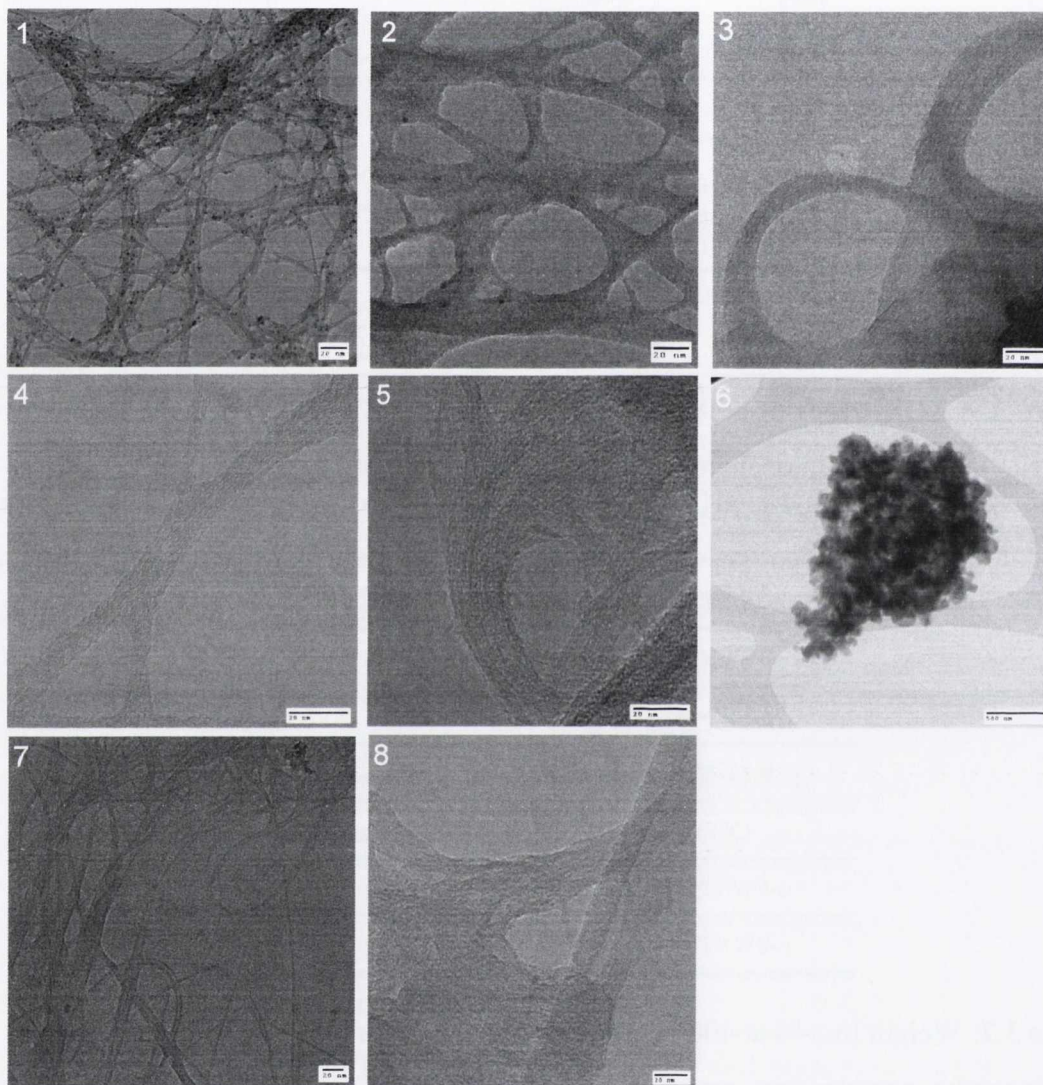


Figure 3.10: HR-TEM of 1] r-SWNTs, 2] p-SWNTs, 3] b-SWNTs, 4] o-SWNTs [1], 5] o-SWNTs [2], 6] CCFs, 7] f-SWNTs [1] and 8] f-SWNTs [2] on 200 mesh Cu holey carbon grids.

3.3.7 Atomic force microscopy analysis

AFM topographic images of r-SWNTs, p-SWNTs and b-SWNTs displayed the effectiveness of purification and washing protocols in progressively removing catalyst and carbonaceous impurities going from r-SWNTs to b-SWNTs (Figure 3.11).

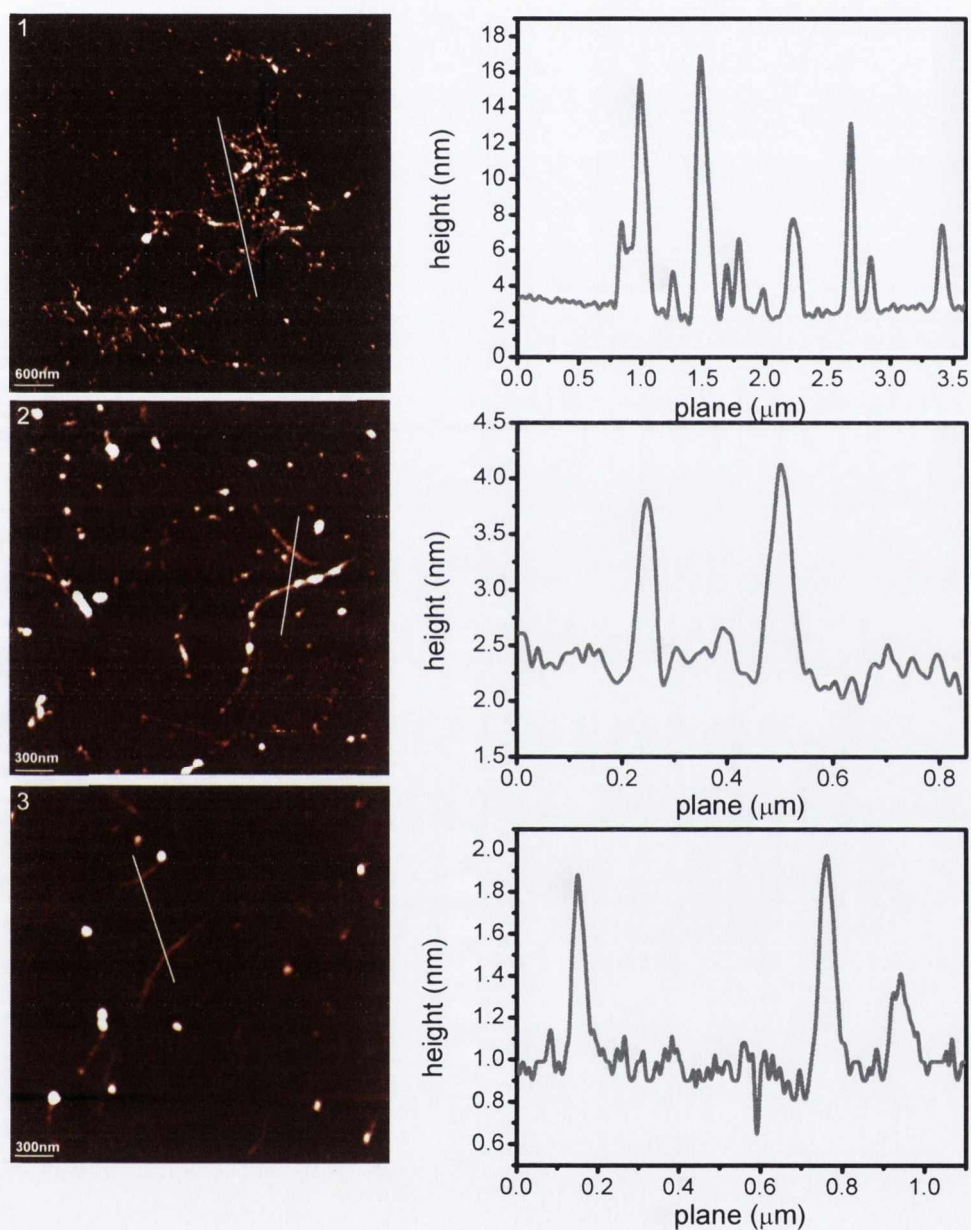


Figure 3.11: AFM topographic images and height profiles of 1] r-SWNTs, 2] p-SWNTs, 3] b-SWNTs. Z-slide 0-12 nm for r-SWNTs, and 0-4 nm for p-SWNTs and b-SWNTs images.

Additionally, AFM images of o-SWNTs [1] and [2] confirmed the shortening of the tubes after oxidation treatments, where average lengths were estimated at 482 ± 170 nm and 528 ± 159 nm, respectively (Figure 3.12).

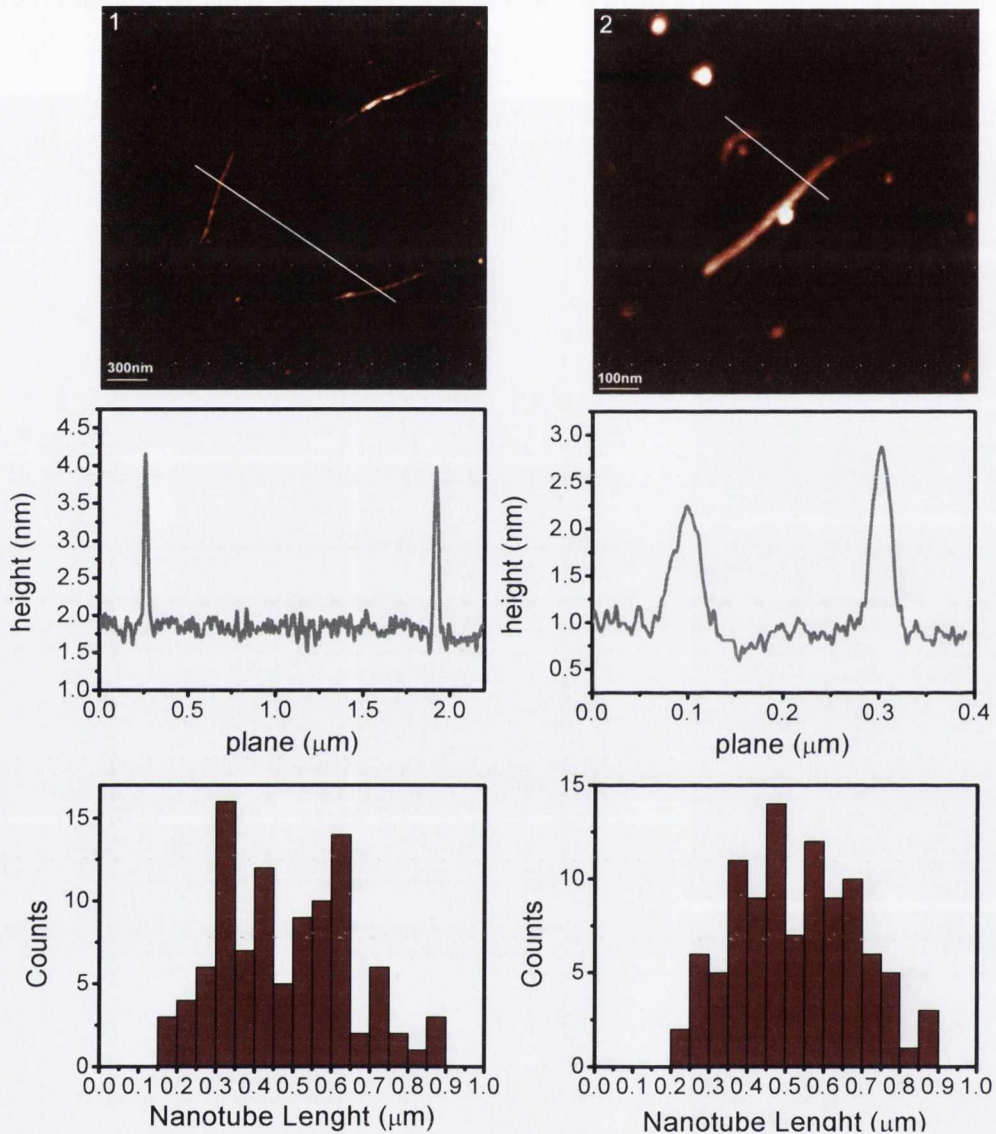
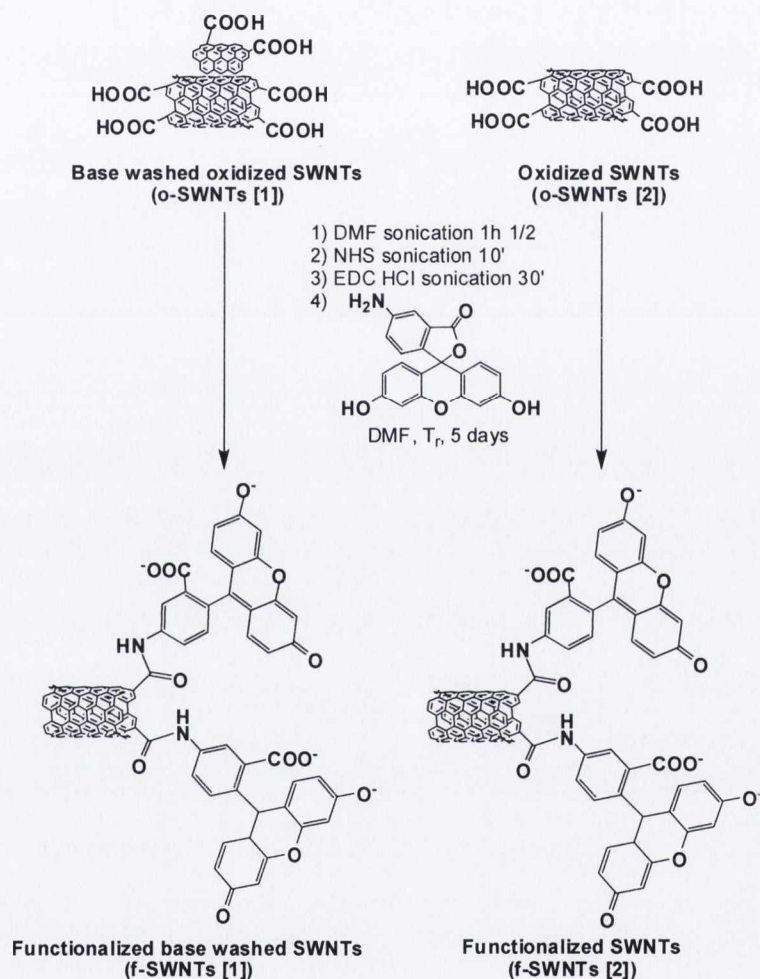


Figure 3.12: AFM topographic images of 1] o-SWNTs [1] and 2] o-SWNTs [2]. Average length, calculated on 100 SWNTs, is 482 ± 170 nm for o-SWNTs [1] and 528 ± 159 nm for o-SWNTs [2]. Z-slide 0-4nm.

3.4 Functionalization with fluorescent probe

A fluorescent probe, fluoresceinamine, was coupled to both o-SWNTs [1] and [2], as illustrated in Scheme 3.3, in order to investigate the presence of COOH functional groups on o-SWNTs [1] and [2].

Scheme 3.3: Coupling reaction of oxidized SWNTs [1] and [2] with fluoresceinamine.



In order to remove the excess of non-reacted reagents from f-SWNTs [1] and [2], the samples were dispersed in DMF by sonication and washed with a number of solvents until the filtrate ran clear.

3.5 Spectroscopic analysis of functionalized SWNTs

The fluorescent probe, although not concentrated enough to be seen using UV-Vis/NIR absorption spectroscopy (Figure 3.13), is clearly observable from the emission spectra of both f-SWNT samples excited at 490 nm (Figure 3.14 and Figure 3.15).⁴⁹

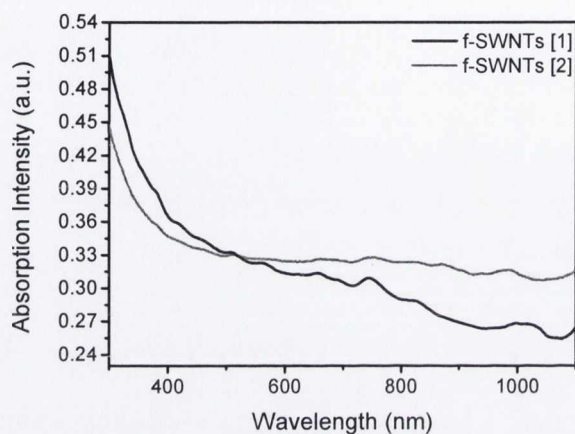


Figure 3.13: UV-Vis/NIR absorption profiles of f-SWNTs [1] and f-SWNTs [2]. The van Hove singularities are still present in both the samples. $[\text{SWNTs}]_i = 1 \times 10^{-1} \text{ mg/mL}$ DMF. The absorption band associated to the fluorescent dye is not present, as an indication of the small amount of fluoresceinamine coupled to the nanotubes.

In order to compare the samples at similar concentrations, they were diluted until equal values of optical absorption were observed (Figure 3.13). Following excitation of these solutions the emission intensities suggest that the degree of functionalization of both samples is comparable, affording similarly functionalized materials. When compared to the fluorescent probe alone in DMF, a red-shift in the maximum emission intensity is observed from 538 to 545 nm for both the f-SWNT [1] and [2]. In order to investigate whether the red-shift originates from covalent attachment or from non-covalent interaction, fluoresceinamine was titrated into a solution of o-SWNTs [2]. This resulted in a slight blue-shift of the emission maximum to 536 nm, strongly indicating that the fluorescent probe is covalently bound to the SWNT structure in the functionalized samples and not simply physisorbed to the surface as previously seen by Dai and co-workers.⁴⁹

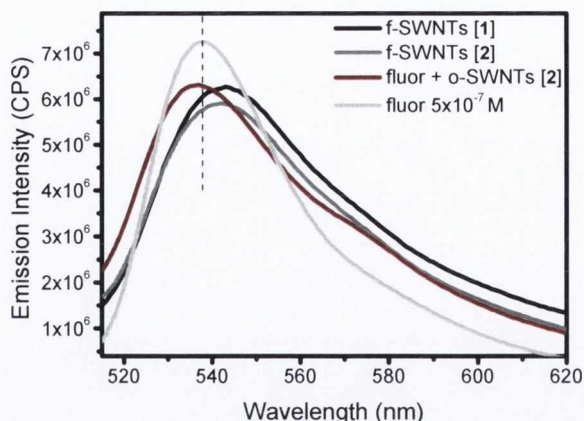


Figure 3.14: Emission profiles ($\lambda_{exc}=490$ nm) of fluoresceinamine, f-SWNTs [1] and [2] and fluoresceinamine π - π stacked to o-SWNTs [2]. The nanotube samples have been diluted until same optical absorption values in DMF.

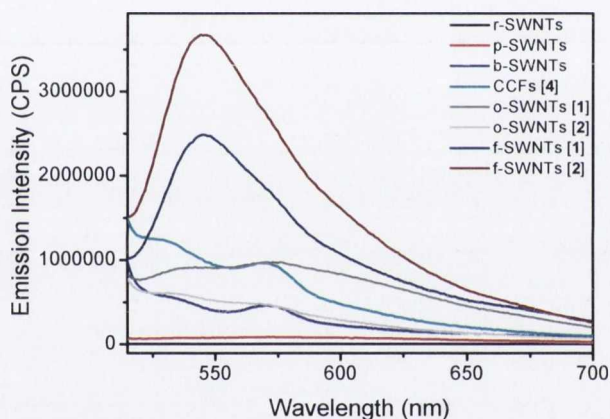


Figure 3.15: Emission profiles ($\lambda_{exc}=490$ nm) of fluoresceinamine functionalized nanotubes f-SWNTs [1] and f-SWNTs [2] compared to r-SWNTs, p-SWNTs, b-SWNTs, o-SWNTs [1], o-SWNTs [2] and CCFs [4]. $[SWNTs]_i = 1 \times 10^{-1}$ mg/mL DMF, $[CCFs]_i = 1 \times 10^{-1}$ mg/mL DMF. Emission peaks at 545 nm are present only in the fluoresceinamine functionalized nanotubes.

The Raman spectra of both batches of the oxidized and functionalized SWNTs are illustrated in Figure 3.16 and interestingly a decrease of the I_D/I_G ratio is observed for both following functionalization. Although the decrease is practically negligible in the case of f-SWNTs [2], a quite substantial drop is evident for f-SWNTs [1], which seem to occur due to the removal of the remaining carbonaceous material from the sample by solvent washing.

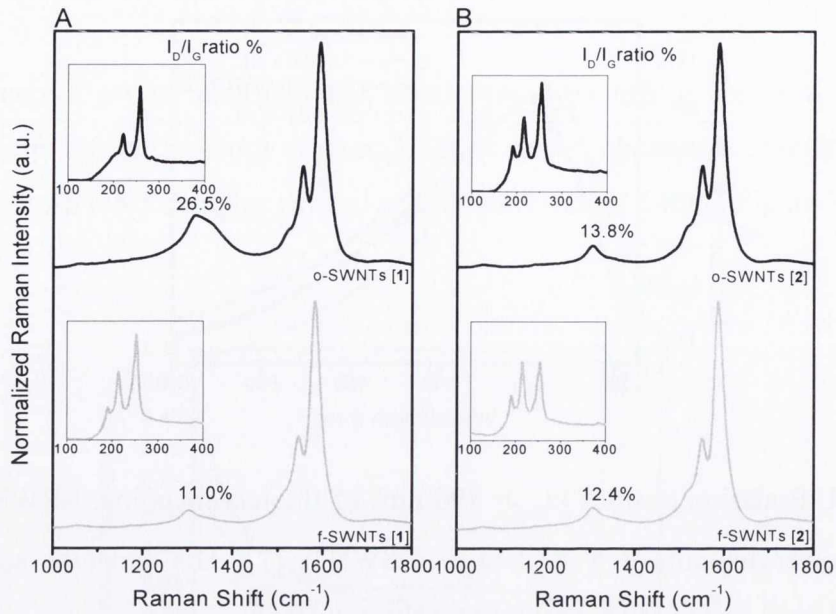


Figure 3.16: Raman spectra ($\lambda_{\text{exc}} = 633 \text{ nm}$) of A) o-SWNTs [1] and f-SWNTs [1] and B) o-SWNTs [2] and f-SWNTs [2] normalized on the G-band. Insets show the RBM bands (scale: 0-0.25 a.u.).

NIR-PL spectra of the functionalized samples are illustrated in Figure 3.17 (and Figure 3.6a in Appendix) and it is evident that structured emission is sustained, indicating retention of the characteristic optical/electronic properties following covalent functionalization.

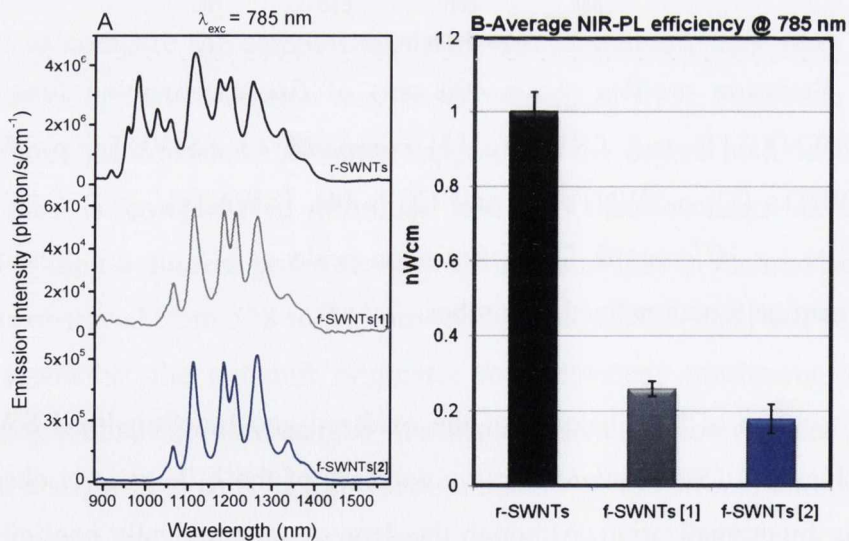


Figure 3.17: A) NIR-PL spectra ($\lambda_{\text{exc}} = 785 \text{ nm}$) of r-SWNTs, f-SWNTs [1] and f-SWNTs [2]. B) Histograms showing the average NIR-PL efficiency at $\lambda_{\text{exc}} = 785 \text{ nm}$ ($n_{\text{measurements}} = 3$).

The removal of the remaining carbonaceous material from the oxidized samples, following solvent washing, is also evident from the reduction in emission in the 880-1000 nm region of the spectrum.

XPS analyses of fluorescein functionalized nanotubes f-SWNTs [1] and [2] have been performed [by our collaborators at the University of Mons, Belgium], and a comparison with the correspondent oxidized samples is reported in Figure 3.18. Following coupling with the fluorescent probe, the contribution associated to the defects content (285.3 eV) stays, as expected, unaltered for f-SWNTs [2], while it slightly increases for f-SWNTs [1]. This is most probably due to the unmasking of defects onto the nanotube surface after removal of residual CCFs, as also suggested by the broad and unsymmetrical D-band in the Raman spectrum of o-SWNTs [1] (Figure 3.16A).

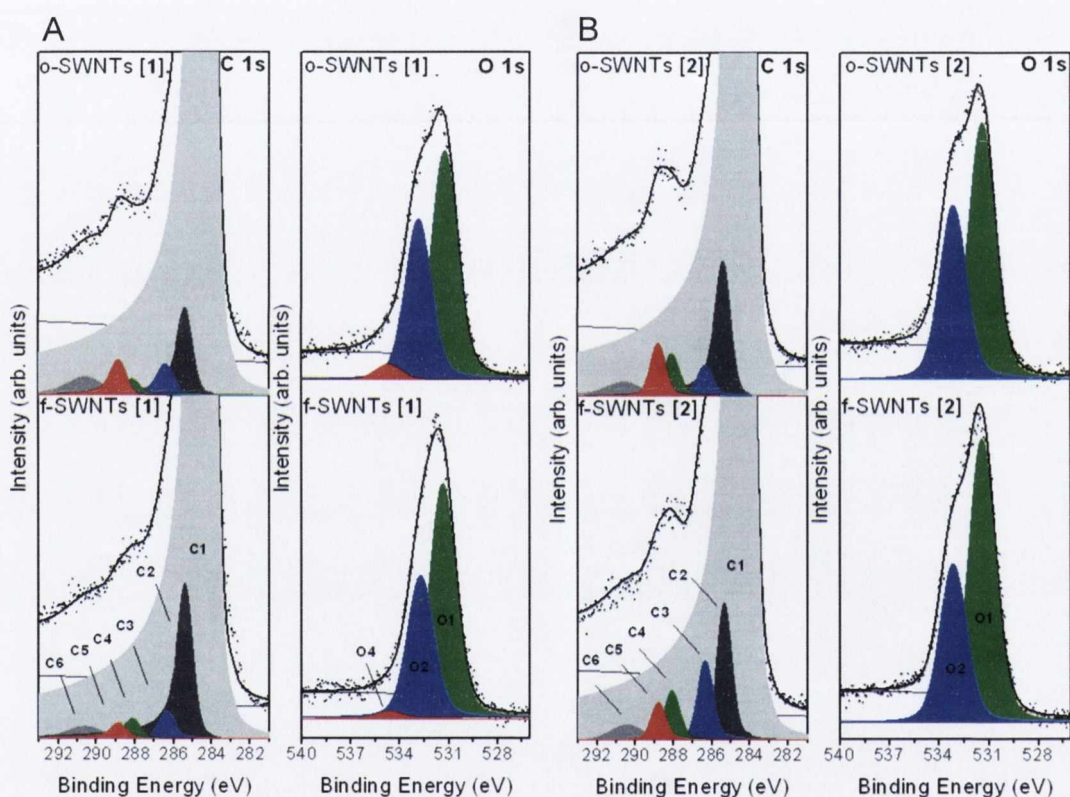


Figure 3.18: XPS C 1s and O 1s spectra of A) o-SWNTs [1] and f-SWNTs [1], and B) o-SWNTs [2] and f-SWNTs [2]. Fitted components are labelled as: **C1**: C-C sp^2 , **C2**: C-C sp^3 , **C3**: C-O, **C4**: C=O, **C5**: (C=O)-O-, **C6**: plasmon loss, and **O1**: (C=O), **O2**: C-O-C/(C=O)-O-/C-OH, **O4**: (C=O)-O-Na.

In both of the considered cases, a reduction in the intensity of the carboxylic acid component (C5) and an increase of the hydroxyl and carbonyl ones (C3 and C4) are

observed, indicating the successful introduction of the fluorescent probe in the nanotube sample. The type of components in f-SWNTs [1] and [2] are visibly the same, which is a proof of the similarity of the two functionalized nanomaterials. However, the relative intensity of the C2-C5 bands in f-SWNTs [2] suggests a slightly higher number of fluorescent probes in the latter when compared to f-SWNTs [1]. The same conclusion can be drawn from (1) the stronger emission intensity when excited at 490 nm, (2) the higher I_D/I_G ratio, and (3) the more pronounced NIR-PL quenching of f-SWNTs [2], as reported in Figure 3.15, 3.16 and 3.17 respectively.

Analysis of the O 1s peak of f-SWNTs [1] reveals a small decrease of oxygen species of lower binding energy (O4), which can be again assigned to residual CCFs removed with by solvent washing. On comparison of f-SWNTs [1] and [2] it is however evident that the oxygen containing functionality in each functionalized sample is really similar following either the NaOH treatment or the solvent washing routes.

3.6 Microscopic analysis of functionalized SWNTs

Representative AFM topographic images of single f-SWNTs [1] and [2] with the height profiles are reported in Figure 3.19.

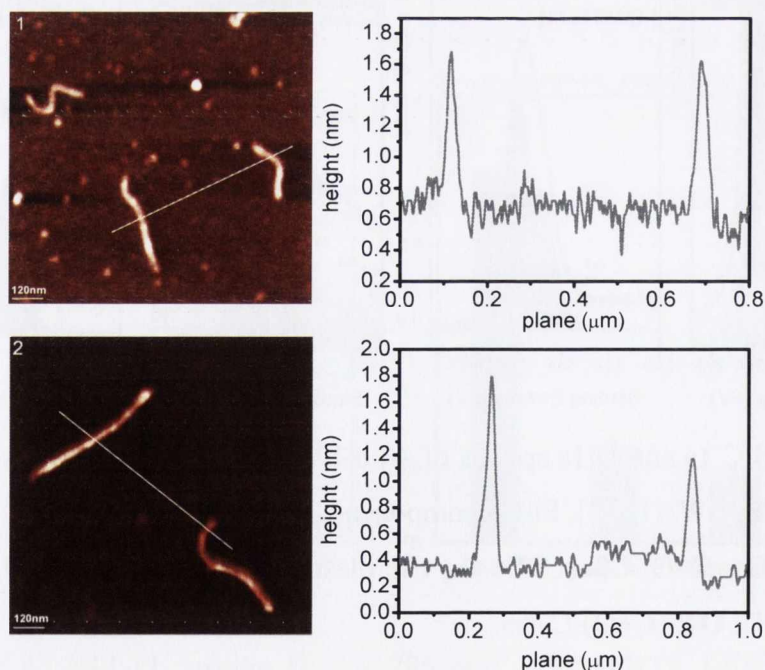


Figure 3.19: AFM topographic images and height profiles of fluoresceinamine functionalized nanotubes. 1] f-SWNTs [1] and 2] f-SWNTs [2]. Z-slide 0-2 nm.

The average lengths of fluorescein functionalized SWNTs have not been calculated as the coupling protocol does not affect the integrity of the nanotube structure.

3.6 Conclusions

Using a well known 2-step purification/oxidation procedure, in the absence of NaOH treatment, we have demonstrated that COOH functionality is introduced directly onto SWNTs, and not only onto carbonaceous material present in the sample, as previously reported for single step nitric acid purification. FT-IR, Raman, NIR-PL and XPS were used to demonstrate that both solvent washing and oxidation procedures are important with regards to the removal of carbonaceous material and conversion of introduced defects to reactive COOH groups, respectively. Covalent functionalization of the oxidized materials was also investigated by attachment of a fluorescent probe, and ultimately, whether treated with base or solvent washed, the resulting materials are close to identical with respect to both their appearance and properties. In addition, we have demonstrated that using either of these purification/oxidation strategies, functionalized materials can be produced that still exhibit their distinctive optical/electronic properties, as demonstrated by sustained structured spectroscopic absorption and emission features.

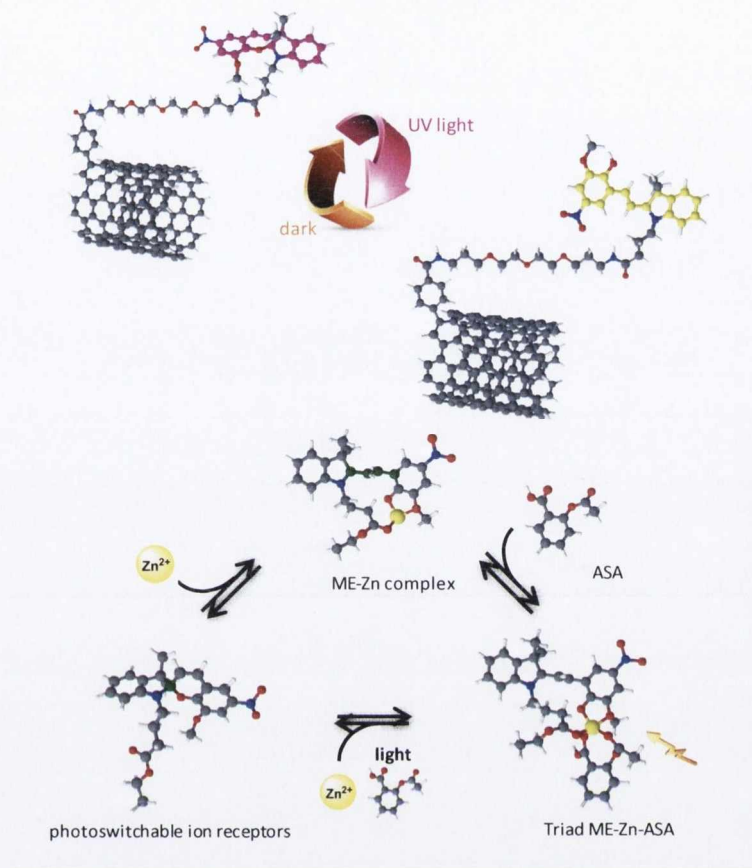
References

- (1) Chen, R. J.; Zhang, Y. G.; Wang, D. W.; Dai, H. J. *Journal of the American Chemical Society* **2001**, *123*, 3838.
- (2) Britz, D. A.; Khlobystov, A. N. *Chemical Society Reviews* **2006**, *35*, 637.
- (3) Banerjee, S.; Hemraj-Benny, T.; Wong, S. S. *Advanced Materials* **2005**, *17*, 17.
- (4) Singh, P.; Campidelli, S.; Giordani, S.; Bonifazi, D.; Bianco, A.; Prato, M. *Chemical Society Reviews* **2009**, *38*, 2214.
- (5) Prato, M. *Nature* **2010**, *465*, 172.
- (6) Syrgiannis, Z.; Gebhardt, B.; Dotzet, C.; Hauke, F.; Graupner, R.; Hirsch, A. *Angewandte Chemie-International Edition* **2010**, *49*, 3322.
- (7) Voiry, D.; Roubeau, O.; Penicaud, A. *Journal of Materials Chemistry* **2010**, *20*, 4385.
- (8) Itkis, M. E.; Niyogi, S.; Meng, M. E.; Hamon, M. A.; Hu, H.; Haddon, R. C. *Nano Letters* **2002**, *2*, 155.
- (9) Niyogi, S.; Hamon, M. A.; Hu, H.; Zhao, B.; Bhowmik, P.; Sen, R.; Itkis, M. E.; Haddon, R. C. *Accounts of Chemical Research* **2002**, *35*, 1105.
- (10) Burghard, M. *Surface Science Reports* **2005**, *58*, 1.
- (11) Strano, M. S.; Dyke, C. A.; Usrey, M. L.; Barone, P. W.; Allen, M. J.; Shan, H. W.; Kittrell, C.; Hauge, R. H.; Tour, J. M.; Smalley, R. E. *Science* **2003**, *301*, 1519.
- (12) Tasis, D.; Tagmatarchis, N.; Bianco, A.; Prato, M. *Chemical Reviews* **2006**, *106*, 1105.
- (13) Haddon, R. C. *Science* **1993**, *261*, 1545.
- (14) Tohji, K.; Goto, T.; Takahashi, H.; Shinoda, Y.; Shimizu, N.; Jeyadevan, B.; Matsuoka, I.; Saito, Y.; Kasuya, A.; Ohsuna, T.; Hiraga, H.; Nishina, Y. *Nature* **1996**, *383*, 679.
- (15) Dillon, A. C.; Gennett, T.; Jones, K. M.; Alleman, J. L.; Parilla, P. A.; Heben, M. J. *Advanced Materials* **1999**, *11*, 1354.
- (16) Hu, H.; Zhao, B.; Itkis, M. E.; Haddon, R. C. *Journal of Physical Chemistry B* **2003**, *107*, 13838.
- (17) Giordani, S.; Colomer, J. F.; Cattaruzza, F.; Alfonsi, J.; Meneghetti, M.; Prato, M.; Bonifazi, D. *Carbon* **2009**, *49*, 578.
- (18) Rinzler, A. G.; Liu, J.; Dai, H.; Nikolaev, P.; Huffman, C. B.; Rodriguez-Macias, F. J.; Boul, P. J.; Lu, A. H.; Heymann, D.; Colbert, D. T.; Lee, R. S.; Fischer, J. E.; Rao, A. M.; Eklund, P. C.; Smalley, R. E. *Applied Physics a-Materials Science & Processing* **1998**, *67*, 29.
- (19) Salzmann, C. G.; Llewellyn, S. A.; Tobias, G.; Ward, M. A. H.; Huh, Y.; Green, M. L. H. *Advanced Materials* **2007**, *19*, 883.
- (20) Shao, L.; Tobias, G.; Salzmann, C. G.; Ballesteros, B.; Hong, S. Y.; Crossley, A.; Davis, B. G.; Green, M. L. H. *Chemical Communications* **2007**, 5090.
- (21) Price, B. K.; Lomeda, J. R.; Tour, J. M. *Chemistry of Materials* **2009**, *21*, 3917.

- (22) Worsley, K. A.; Kalinina, I.; Bekyarova, E.; Haddon, R. C. *Journal of the American Chemical Society* **2009**, *131*, 18153.
- (23) Romanos, G. E.; Likodimos, V.; Marques, R. R. N.; Steriotis, T. A.; Papageorgiou, S. K.; Faria, J. L.; Figueiredo, J. L.; Silva, A. n. M. T.; Falaras, P. *The Journal of Physical Chemistry C* **2011**, *115*, 8534.
- (24) Chen, J.; Hamon, M. A.; Hu, H.; Chen, Y. S.; Rao, A. M.; Eklund, P. C.; Haddon, R. C. *Science* **1998**, *282*, 95.
- (25) Hamon, M. A.; Chen, J.; Hu, H.; Chen, Y. S.; Itkis, M. E.; Rao, A. M.; Eklund, P. C.; Haddon, R. C. *Advanced Materials* **1999**, *11*, 834.
- (26) Kahn, M. G. C.; Banerjee, S.; Wong, S. S. *Nano Letters* **2002**, *2*, 1215.
- (27) Hu, H.; Zhao, B.; Hamon, M. A.; Kamaras, K.; Itkis, M. E.; Haddon, R. C. *Journal of the American Chemical Society* **2003**, *125*, 14893.
- (28) Kostarelos, K.; Lacerda, L.; Pastorin, G.; Wu, W.; Wieckowski, S.; Luangsivilay, J.; Godefroy, S.; Pantarotto, D.; Briand, J. P.; Muller, S.; Prato, M.; Bianco, A. *Nature Nanotechnology* **2007**, *2*, 108.
- (29) Bonifazi, D.; Nacci, C.; Marega, R.; Campidelli, S.; Ceballos, G.; Modesti, S.; Meneghetti, M.; Prato, M. *Nano Letters* **2006**, *6*, 1408.
- (30) Bergeret, C.; Cousseau, J.; Fernandez, V.; Mevellec, J. Y.; Lefrant, S. *Journal of Physical Chemistry C* **2008**, *112*, 16411.
- (31) Movia, D.; Del Canto, E.; Giordani, S. *The Journal of Physical Chemistry C* **2010**, *114*, 18407.
- (32) Del Canto, E.; Flavin, K.; Natali, M.; Perova, T.; Giordani, S. *Carbon* **2010**, *48*, 2815.
- (33) Liu, J.; Rinzler, A. G.; Dai, H. J.; Hafner, J. H.; Bradley, R. K.; Boul, P. J.; Lu, A.; Iverson, T.; Shelimov, K.; Huffman, C. B.; Rodriguez-Macias, F.; Shon, Y. S.; Lee, T. R.; Colbert, D. T.; Smalley, R. E. *Science* **1998**, *280*, 1253.
- (34) Ziegler, K. J.; Gu, Z. N.; Peng, H. Q.; Flor, E. L.; Hauge, R. H.; Smalley, R. E. *Journal of the American Chemical Society* **2005**, *127*, 1541.
- (35) Tobias, G.; Shao, L. D.; Ballesteros, B.; Green, M. L. H. *Journal of Nanoscience and Nanotechnology* **2009**, *9*, 6072.
- (36) Fogden, S.; Verdejo, R.; Cottam, B.; Shaffer, M. *Chemical Physics Letters* **2008**, *460*, 162.
- (37) Biniak, S.; Szymanski, G.; Siedlewski, J.; Swiatkowski, A. *Carbon* **1997**, *35*, 1799.
- (38) Socrates, G. *Wiley* **2008**.
- (39) Lazzeri, M.; Piscanec, S.; Mauri, F.; Ferrari, A. C.; Robertson, J. *Physical Review B* **2006**, *73*, 155426.
- (40) Graupner, R. *Journal of Raman Spectroscopy* **2007**, *38*, 673.
- (41) Estrade-Szwarckopf, H. *Carbon* **2004**, *42*, 1713.

- (42) Jung, A.; Graupner, R.; Ley, L.; Hirsch, A. *physica status solidi (b)* **2006**, *243*, 3217.
- (43) Giordano, R.; Serp, P.; Kalck, P.; Kihn, Y.; Schreiber, J.; Marhic, C.; Duvail, J.-L. *European Journal of Inorganic Chemistry* **2003**, *2003*, 610.
- (44) Datsyuk, V.; Kalyva, M.; Papagelis, K.; Parthenios, J.; Tasis, D.; Siokou, A.; Kallitsis, I.; Galiotis, C. *Carbon* **2008**, *46*, 833.
- (45) Cognet, L.; Tsyboulski, D. A.; Rocha, J. D. R.; Doyle, C. D.; Tour, J. M.; Weisman, R. B. *Science* **2007**, *316*, 1465.
- (46) O'Connell, M. J.; Bachilo, S. M.; Huffman, C. B.; Moore, V. C.; Strano, M. S.; Haroz, E. H.; Rialon, K. L.; Boul, P. J.; Noon, W. H.; Kittrell, C.; Ma, J. P.; Hauge, R. H.; Weisman, R. B.; Smalley, R. E. *Science* **2002**, *297*, 593.
- (47) Strano, M. S.; Huffman, C. B.; Moore, V. C.; O'Connell, M. J.; Haroz, E. H.; Hubbard, J.; Miller, M.; Rialon, K.; Kittrell, C.; Ramesh, S.; Hauge, R. H.; Smalley, R. E. *Journal of Physical Chemistry B* **2003**, *107*, 6979.
- (48) Rinaldi, A.; Frank, B.; Su, D. S.; Hamid, S. B. A.; Schloegl, R. *Chemistry of Materials* **2011**, *23*, 926.
- (49) Nakayama-Ratchford, N.; Bangsaruntip, S.; Sun, X. M.; Welsher, K.; Dai, H. J. *Journal of the American Chemical Society* **2007**, *129*, 2448.

Chapter 4. Single-Walled Carbon Nanotubes as Nanovectors for Biologically Active Metal Cations and Molecules



In this chapter the design, synthesis and complete characterization of a photoresponsive multifunctional nanomaterial composed of a SWNTs vector and SP-based caging molecules are reported. After sidewall functionalization of the nanotube material with a SP based fluorescent receptor, we investigate spectrophotometrically the light modulated reversible caging/releasing properties of such composite towards Zn²⁺ metal ions and a nonsteroidal anti-inflammatory drug (NSAID). The formation of a supramolecular complex between SP, Zn²⁺ ions and the NSAID is suggested by absorption and emission spectroscopy combined with mass spectrometry and NMR. Evidences of the effective functionalization of SWNTs by SP receptors for Zn²⁺ and its light reversible response are offered by thermogravimetric analysis and a number of spectroscopic and microscopic techniques. We report here for the first time a potential photo controllable SP/SWNTs based drug delivery system (DDS) where the nanotubes act as intracellular carriers of light modulated receptors for bioactive metal ions and small organic molecules.

4.1 Introduction

SWNTs have emerged as efficient intracellular vectors of bioactive payloads for alternative drug delivery and cancer therapy applications.¹⁻⁹

As already underscored in the introductory chapter of this thesis, the vast number of covalent, non covalent or encapsulation approaches reported so far opened the way for the design and the realization of new and more complex SWNT-based drug delivery systems (DDSs). Subsequent to the translocation of such nanosized systems through the phospholipid membrane, the therapeutic effect has shown to be initialized by the release of active drugs following enzymatic cleavage of chemical bonds,¹⁰ opening of the capped SWNTs hollow chambers by IR or NIR irradiation,¹¹ or change in the pH of the environment.¹²

To date, a number of spiropyran derivatives have been investigated as receptors and sensors for the recognition and quantification of biomolecules and ions, showing the capability to complex metals cations that can ultimately favour the selective ligation of biologically important anions and amino acids.¹³⁻¹⁵ On the other hand, the exploitation of such supramolecular complexes is still in its early stage, as the number of bioactive organic molecules that can potentially interact with them is certainly vast. To the best of our knowledge, SP derivatives have not been used in medicinal chemistry so far. In our group we recently reported their low toxicity¹⁶ and their behaviour as photoregenerable receptors for Zn^{2+} ions.^{17,18} Therefore, we envisage appealing applications as light controllable zinc ion delivery system when SP is anchored to SWNTs scaffolds.

The essentiality of zinc for humans was discovered almost 50 years ago, but its function as anti-inflammatory agent and adjuvant in cancer prevention has been reported only more recently.¹⁹ Chronic inflammation has been tightly connected to the development of many forms of cancer, and the linkage between the two conditions is now part of an accepted paradigm of carcinogenesis.²⁰⁻²⁴ As a consequence, the control of the inflammatory response to tissue damage has become undoubtedly a key factor in cancer treatment and prevention. Intrigued by the anti-inflammatory ability of zinc and highly motivated by the light modulated reversible chelation of the same metal by SP derivatives developed in our lab, we decided to couple the latter ME-Zn receptor with

the most widely used nonsteroidal anti-inflammatory drug (NSAID), namely the acetylsalicylic acid (ASA). Aspirin was specifically chosen as it has shown to decrease the incidence of several tumor types,²⁴ and also because its geometry allows its interaction with metal ions.²⁵ Following chelation of the zinc ions by the SP derivative and subsequent addition of ASA, we aim to form a supramolecular complex (ME-Zn-ASA) where the anti-inflammatory agents can be released by means of Vis light illumination. Once the structure and the performance of the envisaged ME-Zn-ASA complex are verified, our goal is the development of a novel class of DDS composed by a SWNT scaffold and the ME-Zn-ASA photoresponsive smart delivery unit.

A good DDS candidate requires to (1) be biocompatible,²⁶ (2) have good pharmacokinetic properties (ADME), and to (3) easily release the conjugated bioactive molecule when adequately stimulated. To address the first two requirements, the DDS proposed here, will be composed of catalyst free SWNTs covalently modified by Tour reaction on their sidewalls, and subsequently chemically enriched with PEGylated linkers that have demonstrated to improve the nanomaterial water dispersibility and, as a consequence, to decrease its immunogenicity and to promote its clearance through the urinary excretion route.^{5,8,27-32} The Vis light responsiveness of the designed SP-based delivery system will provide a flexible control of the drug administration, thus meeting the third requisite.

Based on the literature and on the preliminary results reported in this chapter, we envisage the realization of a drug delivery system based on SP photoresponsive receptors loaded on SWNTs. The process steps would consist of (1) shuttling of the anti-inflammatory agents through membranes by SWNTs units,^{2,33} (2) Zn²⁺ and ASA release *in situ* by localized Vis light irradiation, (3) promotion of the beneficial effect consequent to a decreased induction of inflammatory cytokines and chemokines. As a consequence angiogenesis will be slowed down, resulting in diminished invasion and metastatic processes, beside an increased apoptosis in cancer cells.^{19,34}

We believe that the findings reported in this chapter will open the way to the design of novel smart drug delivery systems based on light responsive covalently modified SWNTs composites.

4.2 Purification and Tour reaction on SWNTs

Commercially available raw HiPco SWNTs (Unidym[®]) were purified by successive treatments with nitric acid, sodium hydroxide, and hydrogen peroxide, as reported in Figure 4.1. This protocol, which has been optimized in our lab,³⁵ was specifically chosen as it showed to be effective in the removal of both unwanted metal catalyst and carbonaceous material from the sample without affecting the tubes' integrity.

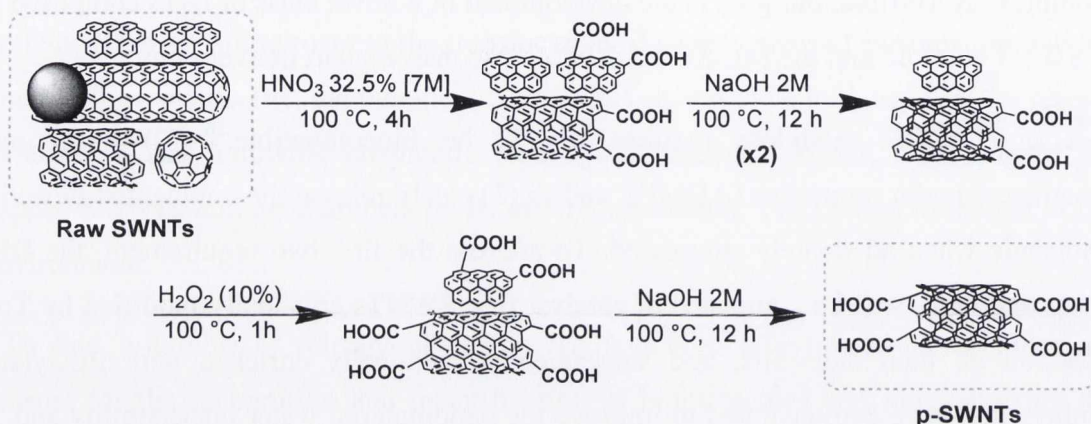


Figure 4.1: Purification of raw SWNTs by nitric acid, sodium hydroxide and hydrogen peroxide treatment.

The purified material (p-SWNTs) was subsequently treated with *in situ* generated 4-carboxybenzenediazonium salts to functionalize the nanotube sidewalls. To ensure a high degree of benzoic acid functionalities and a good dispersibility in solvents the “Tour reaction” was carried out for three consecutive times to afford f-SWNTs (1) (Figure 4.2).³⁶

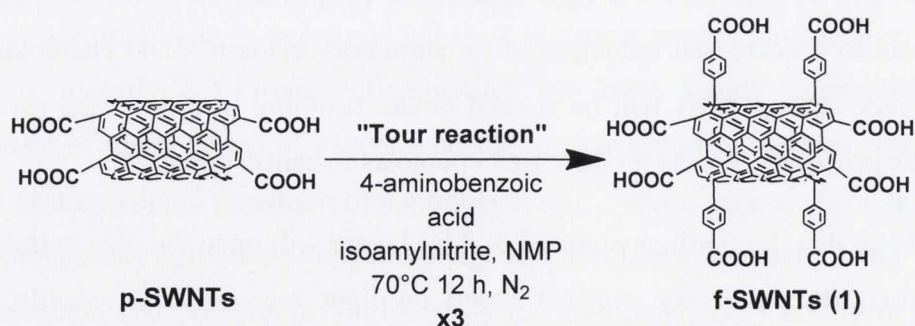


Figure 4.2: Sidewall functionalization of SWNTs with benzoic acid, via the Tour reaction.

4.3 Functionalization of SWNTs with PEG linker and spiropyrans

To further improve the dispersibility of SWNTs in aqueous solvents and to create at the same time a more biocompatible material, Boc-protected PEGylated linker (4) was again chosen as ideal hydrophilic spacer to be interposed between the nanotube scaffold and the photoactive functionality. Compound (4) was coupled to f-SWNTs (1) following activation of the benzoic acid groups to the corresponding ester using NHS and EDC·HCl (Figure 4.3). The Boc protecting group was subsequently removed by trifluoroacetic acid treatment, and the nanotubes bearing free amino groups were reacted with the activated ester of the spiropyran derivative (5) synthesized in our lab,¹⁷ to afford functionalized nanotubes SP f-SWNTs (3).

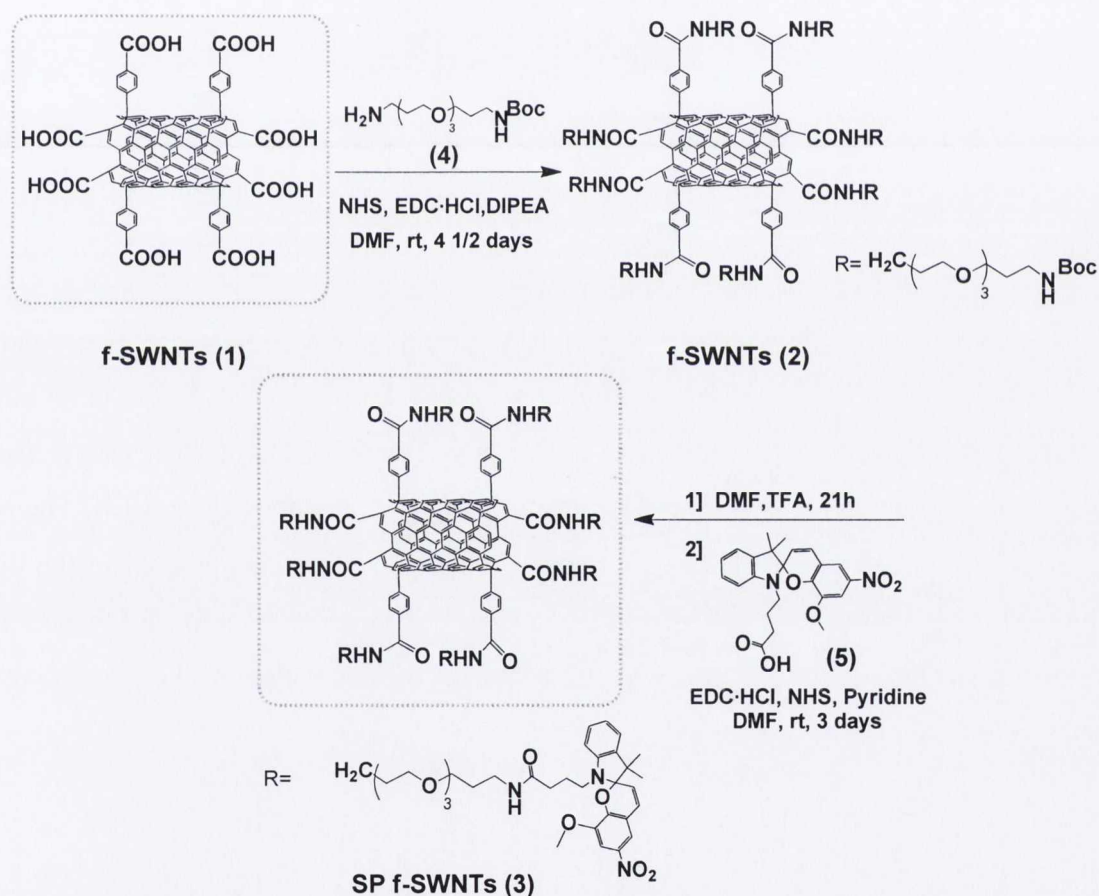


Figure 4.3: Functionalization of Tour reacted nanotubes f-SWNTs (1) with PEG chain and spiropyran photoswitchable derivative.

The improved solubility of SWNT in aqueous solution after covalent sidewall modification is clearly evident from the pictures reported in Figure 4.4, where purified and functionalized samples are compared. The solubility of a nanomaterial in water is of crucial importance if its envisaged applications involve bio environments. As a consequence the demonstrated water solubility of SP-f-SWNTs (3) is paramount as DDS based on such photoactive modular system are here investigated.

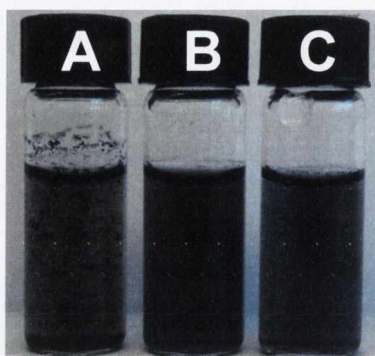


Figure 4.4: Pictures of SWNTs dispersions after A] purification and functionalization with B] benzoic acid and C] SP derivative. [SWNTs]= 0.1 mg/mL distilled H₂O, sonication time 30 min at minimum power. Pictures taken 1 h after sonication ceased.

The amount of functionalities introduced onto the nanotube sidewalls was investigated by Kaiser test.³⁷⁻³⁹ The difference in free primary amino groups before and after coupling reaction of the nanotubes with SP was calculated by measuring their absorbance at 570 nm relative to a blank solution (see Appendix Figure 4.1a). The SP loading was calculated as $\sim 106 \mu\text{g}/\text{mg}$ SWNTs. If this value is compared to the one obtained for SWNTs covalently coupled to SP *via* the defect site approach (chapter 2), the enrichment with a larger number of functional groups is evident in the present case, as expected and aimed.

4.4 Characterization of purified and functionalized SWNTs

4.4.1 Thermogravimetric analysis and TEM images

TGAs were recorded in oxygen atmosphere to assess the successful purification of raw SWNTs after treatment with HNO₃, NaOH and H₂O₂. The residual ash content at 900

°C, which dropped from 48% to 8%, is an indication of the efficient removal of the metal catalyst, as evident from TGA traces in Figure 4.5.

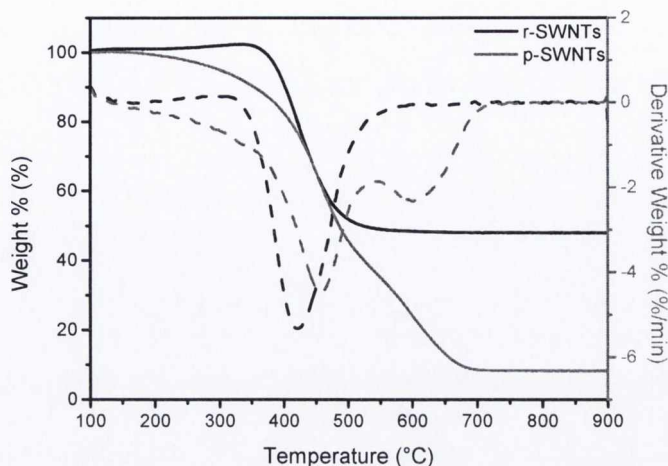


Figure 4.5: Evidences of effective purification of raw SWNTs after treatment with HNO_3 , NaOH and H_2O_2 . TGA (solid lines) and first derivative (dotted lines) traces of raw (r-SWNTs) and purified (p-SWNTs) nanotubes run in air atmosphere.

The 8% value registered after combustion of p-SWNTs can be more likely assigned to the presence of small quantities of residual salt coming from the washing procedure with NaOH . This assumption was confirmed by TEM analysis, where the metal catalyst totally disappeared after the purification protocol, as shown in Figure 4.6.

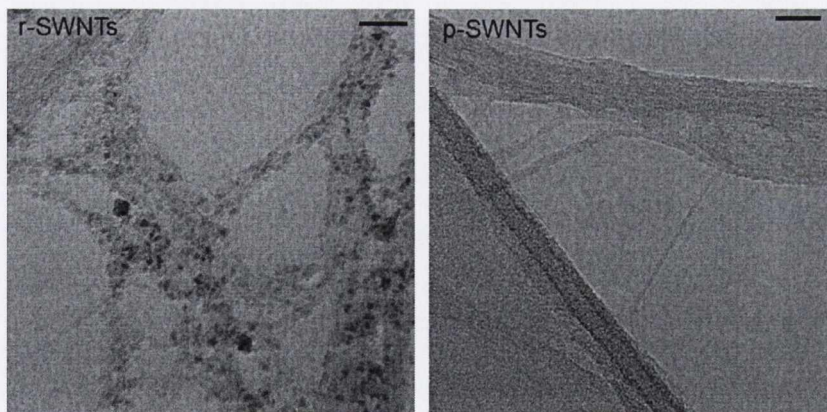


Figure 4.6: HR-TEM images of raw (left) and purified (right) SWNTs on 200 mesh Cu holey carbon grids demonstrating the removal of the metal impurities (black particles) after nitric acid purification and treatment with NaOH and H_2O_2 . Scale bar: 20 nm [analyses run by Dania Movia].

An additional indication of the successful cleaning of the sample from metal particles and carbonaceous impurities was given by the starting decomposition temperature of the SWNTs' graphitic structure. In the presence of impurities, hot spots are usually generated on the SWNTs surface which entail the burning of the material at lower temperatures.⁴⁰ When first derivative traces of r-SWNTs and p-SWNTs were compared (Figure 4.5) the increased oxidative stability of the material from 420 to 460 °C further indicated the effective removal of unwanted impurities after purification and treatment with NaOH and H₂O₂.

To estimate the number of functional groups introduced on the nanotube surface after chemical modification and, more importantly, to determine as to whether functionalization with SP derivative was achieved, TGA analyses were performed in inert nitrogen atmosphere for all the samples (full range traces reported in Appendix Figure 4.2a). As schematized in Table 4.1, the weight loss % at 500 °C, which is attributable to the decomposition of organic functionalities, increased considerably going from raw to purified and SP f-SWNTs (3). This is indicative of the different composition of the materials and, as a consequence of the diverse number of functional groups introduced on their surface. The decreased number of functional groups per carbon atom calculated for SP f-SWNTs (3) is attributed to the removal of residual functionalized carbonaceous fragments following exhaustive solvent washings.

<i>Sample</i>	<i>TGA in nitrogen</i>		
	Weight loss % @ 500°C	1 functional group every	residue % @ 900 °C
raw SWNTs	3	-	70
p-SWNTs	12	-	69
f-SWNTs (1)	28	26C	59
f-SWNTs (2)	35	50C	53
TFA f-SWNTs (2)	30	63C	64
SP f-SWNTs (3)	33	124C	53

Table 4.1: Weight losses % at 500 °C attributed to the decomposition of organic functionalities, estimated number of carbon atoms per organic group and residue percentages after decomposition in nitrogen atmosphere are reported for raw, purified and functionalized SWNTs.

The successful introduction of SP molecules in the nanotube material was confirmed also by the temperature difference maxima between raw SWNTs, p-SWNTs, f-SWNTs (1) and SP f-SWNTs (3) in the 100-500 °C range. As already showed in chapter 2, SP derivative almost completely decomposed at 400 °C displaying two temperature maximum weight loss rates around 180 °C and 240 °C. Also in this case, two maxima appeared for SP f-SWNTs (3), and were again shifted to higher values of 214 °C and 357 °C (Figure 4.7), indicating the presence of SP enriched PEGylated linkers in the nanotube material. By applying the equation reported in chapter 2, the organic loading was calculated as 1 group every 124 C atoms.

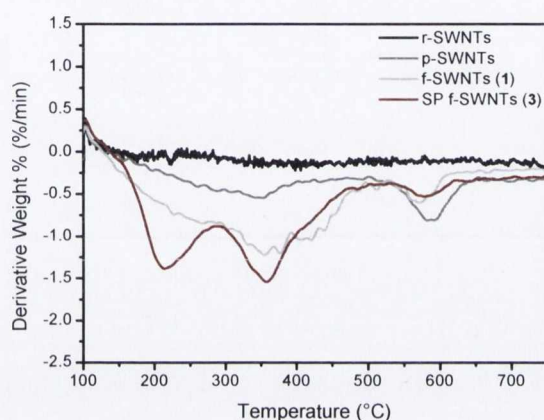


Figure 4.7: TGA first derivative traces in the 100-750 °C range of raw, purified, Tour reacted f-SWNTs (1) and SP functionalized f-SWNTs (5) recorded under nitrogen flow.

4.4.2 FT-IR spectroscopy analysis

The introduction of functional groups onto the nanotube surface was monitored by FT-IR spectroscopy. Characteristic absorption bands assignable to stretching vibrations of specific functional group are clearly evident from the baseline corrected spectra illustrated in Figure 4.8 A and B (non corrected FT-IR spectra in Appendix Figure 4.3a).

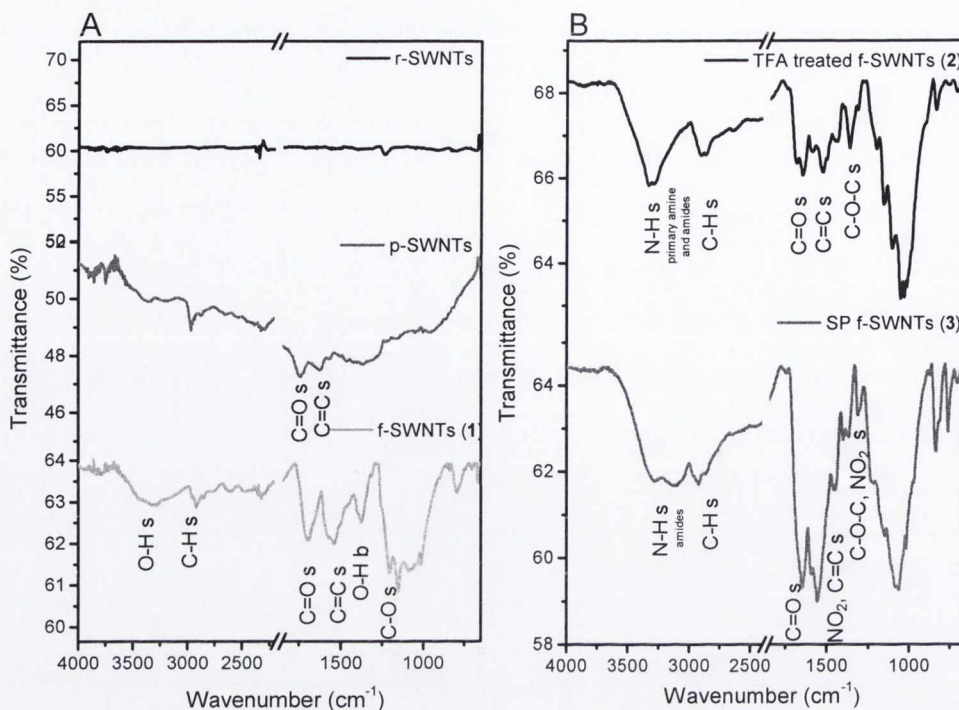


Figure 4.8: ATR/FT-IR spectra of A] raw (r-SWNTs), purified (p-SWNTs) and Tour functionalized (f-SWNTs (1)), B] TFA treated f-SWNTs (2) and SP functionalized (SP f-SWNTs (3)) nanotubes. Spectra have been baseline corrected to improve data visualization.

Following purification with nitric acid and treatment with NaOH and H₂O₂, absorption stretching bands associated to carbonyl groups (1743 cm⁻¹) and C=C bonds of the nanotube structure (1567 cm⁻¹) emerged, thus confirming the introduction of carboxylated functionalities on the nanotube frame by conversion of defect sites to functionalizable -COOH groups.³⁵ After functionalization of the nanotube sidewalls by Tour reaction, new bands appeared in the region where O-H and C-O groups absorb. The latter besides the increased intensity of both carbonyl and C=C signals suggested the effective introduction of benzoic acid groups in f-SWNTs (1). On comparison of TFA treated f-SWNTs (2) spectrum with that of the Tour functionalized material, additional bands that suggested the successful coupling of PEG linker to the benzoic acid residue were observed (peak assignments for all the nanotube samples are reported in the experimental part in chapter 5). Finally when IR measurement were performed on SP f-SWNTs (3) the two distinctive nitro absorption bands at 1553 and 1367 cm⁻¹

appeared (Figure 4.8B), confirming the presence of the spiropyran molecule in the nanomaterial.

4.4.3 Raman spectroscopy analysis

Raman spectroscopy was used as preferential technique to monitor the extent of defects introduction following the chemical processes. The relative intensity of defect (D) and graphitic (G) bands was taken into account as their ratio (I_D/I_G) is commonly calculated to investigate the degree of covalent functionalization on the nanotube structure. An increased I_D/I_G ratio indicates a perturbation of the graphene sheet symmetry that is ascribable to the insertion of defects/edge planes and, as a consequence, functionalities on the nanotube framework.

Figure 4.9 depicts raman spectra of raw, purified and f-SWNTs (1) in addition to I_D/I_G values calculated for all the considered samples. Only slight changes are observed in RBM, 2D- and G- bands, while the D-band is strongly affected following the Tour reaction, indicating covalent functionalization.

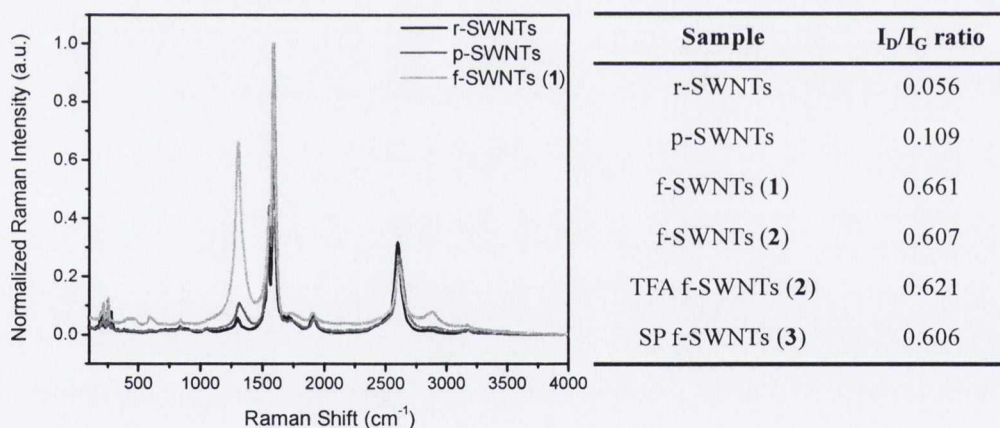


Figure 4.9: Raman analyses ($\lambda_{exc}= 633$ nm). Figure] Raman spectra (normalized on the G-band) of r-SWNTs, p-SWNTs and f-SWNTs (1). Table] I_D/I_G ratio calculations for all the samples.

Following attachment of PEG chain, deprotection from the Boc group and coupling to SP, the intensity of the defect sensitive D-band stayed almost unaltered as expected.

This is evident in Figure 4.10 where enlarged D-, G- and RBM band are reported for all the samples. The sharpening and restored symmetry of the D-band after progressive functional groups enrichment can be explained with the removal of small amounts of residual CCFs by exhaustive washing with solvents.

When the RBM region of raw and purified SWNTs are compared (Figure 4.10B), the destruction of small diameter tubes by nitric acid treatment is confirmed by the disappearance of RBM bands resonant at shifts values $> 280 \text{ cm}^{-1}$.

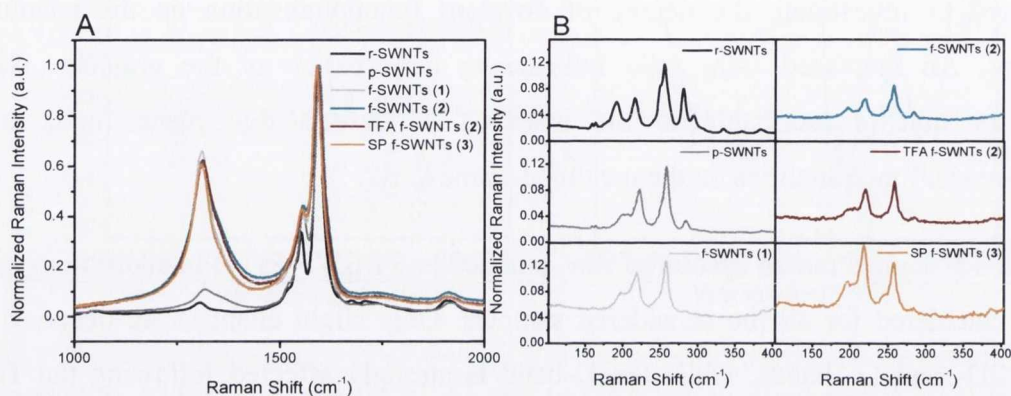


Figure 4.10: Raman analyses ($\lambda_{\text{exc}} = 633 \text{ nm}$) of enlarged A] D- and G- bands, and B] RBM bands of raw, purified and functionalized SWNTs. Spectra normalized on the G-band.

4.4.4 Atomic force microscopy analysis

AFM topographic images were recorded for all the samples dispersed in DMF and sprayed on freshly cleaved mica substrate, with the aim of confirming the cleanliness of the purified material and its effective disentangling after chemical functionalization (Figure 4.11). When r-SWNTs and p-SWNTs are compared, the efficient removal of metal catalyst and impurities is once more confirmed: raw material is composed of a big portion of carbonaceous material and catalytic particles (dots), while following purification only small bundles of clean nanotubes are left. The improved debundling of nanotubes after chemical modification is suggested by the distribution of almost all individual tubes in f-SWNT (1), (2) and (3) samples.

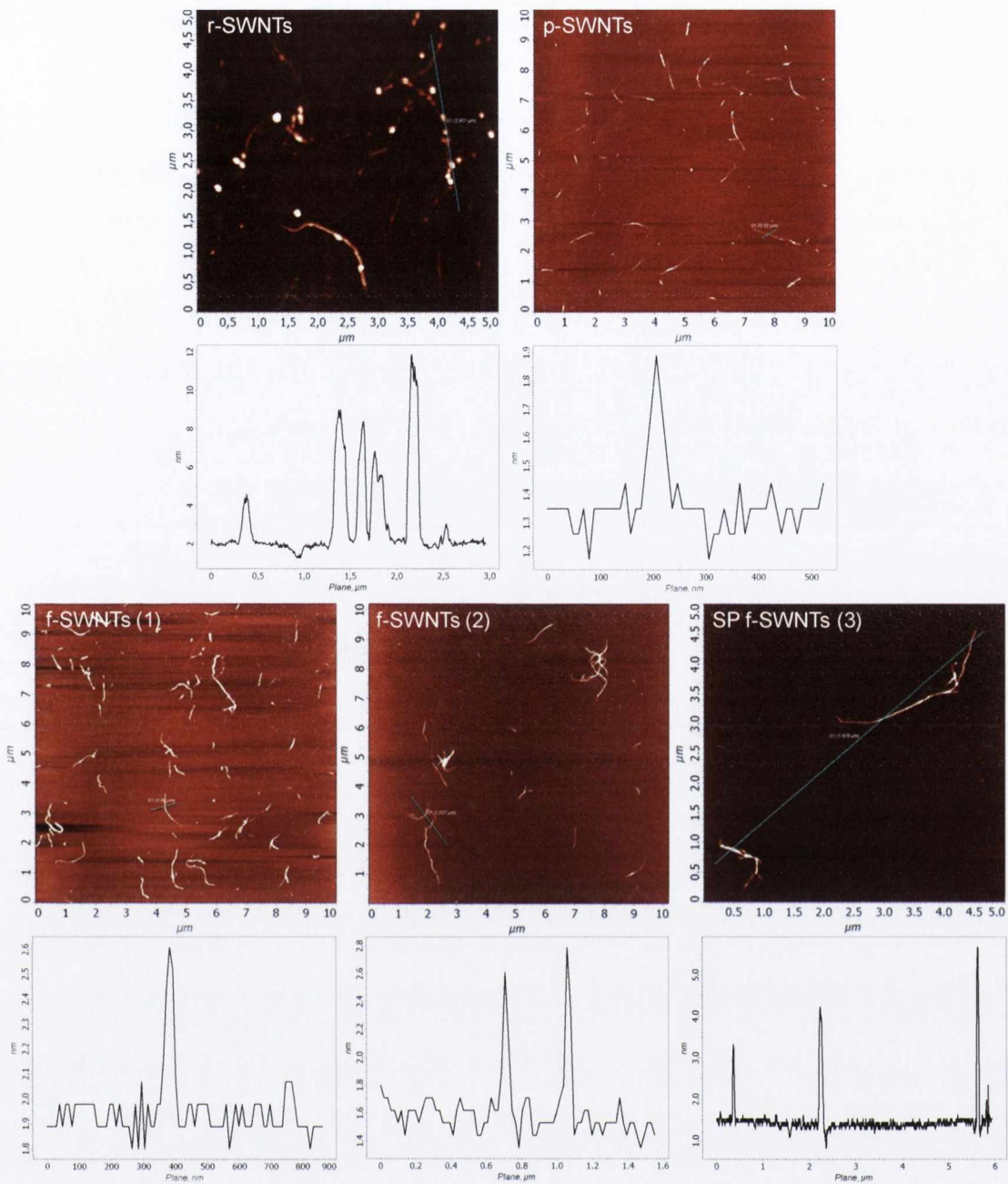


Figure 4.11: AFM topographic images of r-SWNTs, p-SWNTs, f-SWNTs (1), (2) and (3). Z-slide: r-SWNTs 0-10 nm, p-SWNTs and f-SWNTs (1) 0-2.5 nm, f-SWNTs (2) 0-3.7 nm, SP f-SWNTs (3) 0-4 nm.

The chemical protocol here utilized has demonstrated to only slightly affect the tubes' integrity.³⁵

4.5 On-off switching of SWNTs functionalized with spiropyran molecules

Before investigating the switching behaviour of SP f-SWNTs (**3**), the optical changes induced by UV light irradiation and storage in the dark on the correspondent SP derivative in solution were studied.* The reversible interconversion of SP (**6**) in the ME open isomer was demonstrated by modulation of the absorption band at 593 nm following irradiation with UV light (365nm) for 1 minute. This band, that corresponds to the ME form of the dye reverted back to the starting value after 3 minutes in the dark (Figure 4.12B).

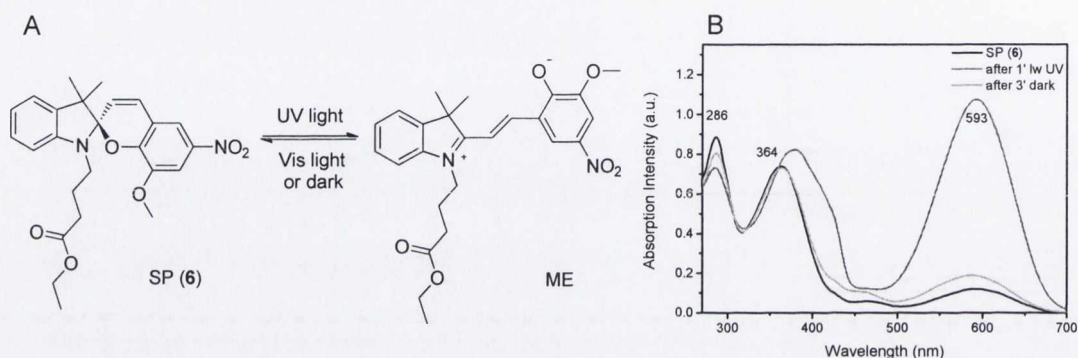


Figure 4.12: A] Photo interconversion of the closed SP (**6**) into the ME open form. B] Absorption spectra of SP (**6**) 10^{-4} M in DMF after 1 min UV illumination (365 nm) and after 3 min storage in the dark.

The electronic properties of raw, purified and sidewall covalently modified SWNTs were evaluated by UV-Vis absorption spectra of DMF solutions (Figure 4.13). Following purification the optical features were retained, while the diazonium treatment resulted in the complete loss of van Hove singularities in agreement with numerous published articles.^{36,41-43} The loss of optical transitions in the absorption spectra of f-SWNTs (**1**), (**2**) and (**3**) is indicative of covalent functionalization. In SP f-SWNTs (**3**) a peak at 416 nm was detectable, which corresponds to the SP closed isomeric form coupled to the PEG linker. As already noticed for SP functionalized nanotubes following the defect site approach (chapter 2), the absorption maximum of SP was red-

* SP (**6**), which is the ethyl ester form of SP (**5**), was specifically chosen as it better resemble the features of that bounded to the SWNTs scaffold.

shifted if compared to the one of the molecule in solution, as an indication of the SP/SWNT interaction.

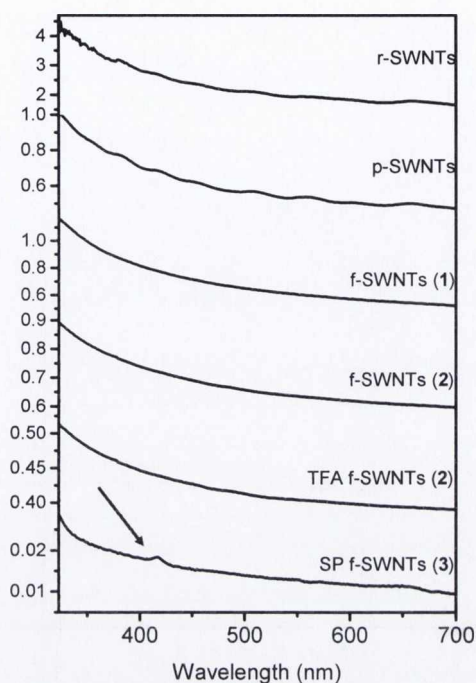


Figure 4.13: UV-Vis absorption spectra of r-SWNTs, p-SWNTs, f-SWNTs (1), (2) and (3) collected on the supernatant of initial 0.1 mg/mL nanotubes in DMF. The arrow indicates the absorption peak ascribable to SP in the nanomaterial.

The photoresponsiveness retention of the SP switch when coupled to SWNTs was investigated via both absorption and emission spectroscopies (Figure 4.14 and 4.15), and the optical changes that occurred after UV irradiation and storage in the dark were measured. UV irradiation resulted, as expected, in an increased absorbance in the ME isomer region (500-600 nm). The reversion of the band at 585 nm to the starting value after storage in the dark is demonstrated in Figure 4.14A. For improving the visualization of the switching behaviour, absorption spectra of SP f-SWNTs (3) were subtracted from the one recorded after UV illumination and darkness (inset Figure 4.14A). As previously observed, the ME absorption maximum blue-shifted compared to the one of the molecule in solution as an indication of π - π interaction between the photoactive molecule and the tubes.⁴⁴ Analogous experiments were performed on raw, purified and all the functionalized SWNTs that showed no photoresponsiveness (spectra

displayed in Appendix Figure 4.4a), thus further supporting the enrichment of SP f-SWNTs (**3**) with the desired photoactive receptor.

It was possible to modulate cyclically and reversibly the switching of the spiro molecule covalently attached to the nanotube material through PEG linker, and the changes in absorption intensity of the band at 585 nm are reported in Figure 4.14B, where on-off switching cycles are depicted.

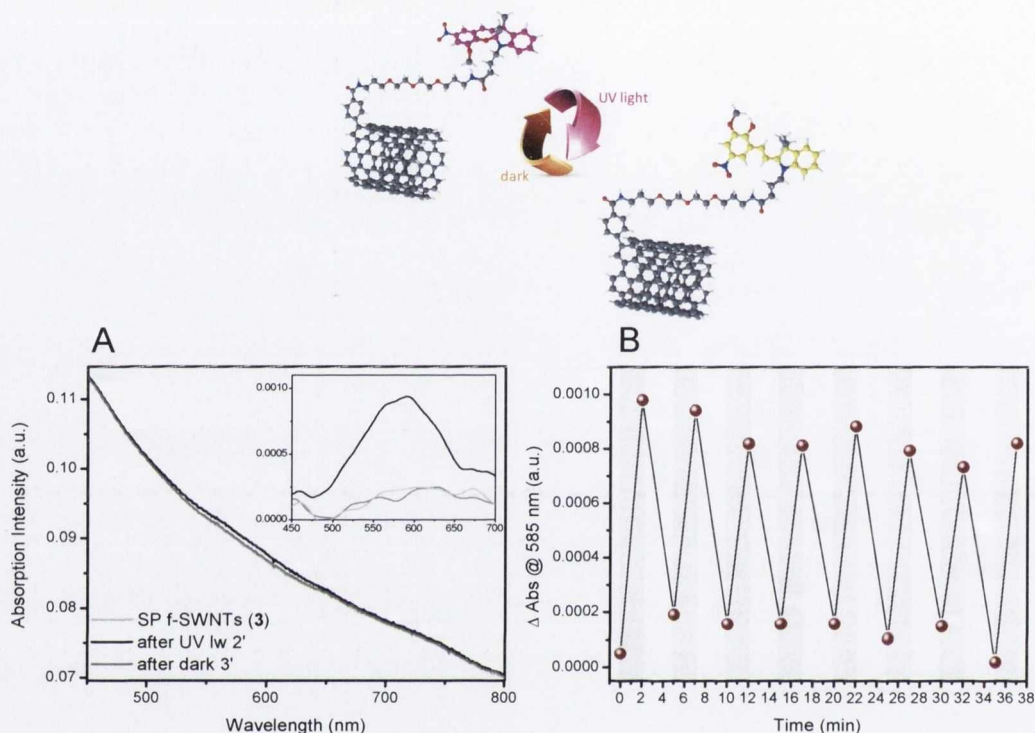


Figure 4.14: On-off switching cartoon of SP f-SWNTs (**3**) and absorption studies. A] SP f-SWNTs (**3**) response to UV (365 nm) illumination for 2 min and dark for 3 min. Inset: difference absorption spectra of SP f-SWNTs (**3**) after 2 min UV, 3 min dark and additional 2 min UV illuminations. B] Absorbance changes at 585 nm of SP f-SWNTs (**3**) solutions following UV (365 nm) and dark cycles. Gray and white bars indicate the UV and the darkness intervals respectively. The spectra were collected on the supernatant of initial 0.1 mg/mL nanotubes in DMF.

The photoswitchability of the SP-SWNTs composite was proved also by emission spectroscopy (Figure 4.15). An emission band at 670 nm, which is associated to the ME open form, was clearly detectable after UV irradiation of SP f-SWNTs (**3**) dispersed in DMF. This emission peak could be cyclically modulated by UV illumination (2 min)

and storage in the dark (5 min), thus confirming the switchability of the nanotube material. Emission spectra, excited at $\lambda_{exc}=593$ nm, of SP f-SWNTs (**3**) before and after UV irradiation, and after storage in the dark are reported in Figure 4.15A, while in Figure 4.15B the on-off switching cycles are shown.

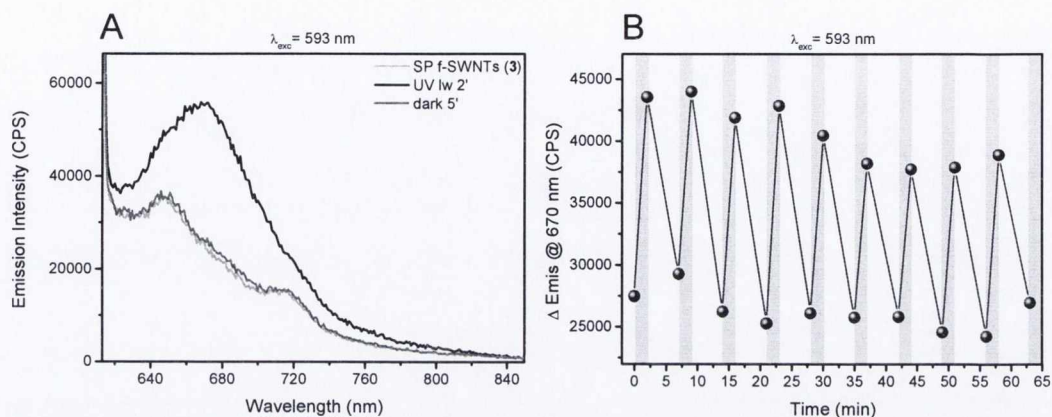


Figure 4.15: Emission studies. A] SP f-SWNTs (**3**) response to UV (365 nm) illumination for 2 minutes and dark for 3 minutes. B] Emission changes at 670 nm of SP f-SWNTs (**3**) solutions following UV (365 nm) and darkness cycles. Gray and white bars indicate the UV and the darkness intervals respectively. The spectra were collected on the supernatant of initial 0.1 mg/mL nanotubes in DMF.

To ensure that the photoswitchable emission band belonged to the SP molecule, the same experiments were performed on f-SWNTs (**2**) before and after removal of the Boc protecting group. In no cases changes were recorded and the emission profiles are reported in Appendix Figure 4.5a. The bands at 650 nm and 715 nm in all the nanotube samples are associated to the emitting behaviour of SWNTs in the visible region when excited at 593 nm.⁴⁵

The emission behavior of the SP alone was recorded and compared to that of the SP f-SWNTs (**3**) (Appendix Figure 4.6a). Bands at a slightly shifted wavelength were observed, which could be ascribable to a change in stabilization of the excited transition state of the molecule in the presence of nanotubes. As a consequence, the interaction between the two constituents of the SP/SWNTs nanodevice synthesized was again confirmed.

4.6 Merocyanine/metal/NSAID complex formation studies

The light modulated reversible chelation of a metal and an NSAID by a spiropyran derivative, when the latter is anchored to a SWNTs scaffold, is here investigated. However, the study of the molecular system performances before its integration in the final nanodevice is good and cautious practice. For this reason the reversible and controlled chelation of Zn^{2+} metal ions and acetylsalicylic acid (ASA) by SP (**6**) derivative in solution, in response to light irradiation, was first considered.¹⁷

The formation and the light controlled modulation of the envisaged supramolecular complex between SP, Zn^{2+} metal ions and ASA was investigated by NMR and mass spectrometry analyses combined with absorption and emission spectroscopy studies.

4.6.1 NMR and mass spectrometry

The approach adopted consisted in the preparation, analysis and comparison of six different solutions containing i) SP, ii) ASA, iii) SP with 1 eq of $Zn(ClO_4)_2$, iv) ASA with 1 eq of $Zn(ClO_4)_2$, v) SP and ASA, and vi) SP, ASA and $Zn(ClO_4)_2$ in equimolar amounts. The combination of NMR and mass spectrometry outcomes led to a number of results that for simplicity are listed here to follow.

1] *SP in CD_3CN + $Zn(ClO_4)_2$ 0.1M in D_2O 1:1 eq ratio.* The complex **ME-Zn** was formed after addition of $Zn(ClO_4)_2$ to the SP solution, as already reported by our group¹⁷ and the evidences are reported in the Appendix paragraph 7.2.1 and Figure 4.16.

2] *SP + ASA in CD_3CN 1:1 eq ratio.* No complex was formed when SP was added of aspirin, as the NMR spectrum consisted of the sum of signals coming from the two molecules with no significant chemical shift changes (Figure 4.16). To exclude proton transfer from the ASA to the SP, NMR studies were performed after a two month period, confirming that the two compounds do not interact (Appendix paragraph 7.2.2).

3] *ASA in CD_3CN + $Zn(ClO_4)_2$ 0.1M in D_2O 1:1 eq ratio.* As expected,²⁵ a complex was formed when aspirin was added of $Zn(ClO_4)_2$ (Appendix paragraph 7.2.3).

4] *SP* in $CD_3CN + Zn(ClO_4)_2$ 0.1 M in $D_2O + ASA$ in CD_3CN 1:1:1 eq ratio. When aspirin was added to a solution containing both *SP* and Zn^{2+} , the appearance of a new peak in the mass spectrum and the recorded NMR signals may be indicative of the formation of a **ME-Zn-ASA** complex, whose hypothetical structure is depicted in Figure 4.16. In the same figure the comparison between the partial 1H -NMR spectra of a solution of spiropyran prior to (*SP*) and after the addition of 1 eq of $Zn(ClO_4)_2$ (**ME-Zn**), 1 eq of aspirin (*SP+ASA*), and the mixture of 1 eq of $Zn(ClO_4)_2$ and 1 eq of aspirin (**ME-Zn-ASA**) are also shown.

The progressive downfield shift of $-OCH_3$ protons (f-f') going from *SP*, to **ME-Zn** and **ME-Zn-ASA** strongly indicated the involvement of the *SP* methoxy group in the complexes coordination. The ester group of the *SP* side chain demonstrated to be also implicated in the metal coordination, as the quartet of protons adjacent to the $-COO$ ester group (p') downshifted with respect to the one in the absence of zinc (p). When *SP* and **ME-Zn** are compared, the protons adjacent to the indolic nitrogen (m-m') shift to lower fields because of the effect of the positively charged N in the open form, and additionally the characteristic coalescence of the *gem* methyl groups (a) in a singlet at 1.82 ppm (a'), due to the symmetry of the *quasi* planar ME, is also observed. The peaks corresponding to the aliphatic protons of the ester chain moved downfield after Zn^{2+} complexation by the *SP* (n-n', o-o') without being further affected after the interaction with ASA. Vinylic (b,c) and aromatic (g,h,i,l) protons disappeared after **ME-Zn** formation, and two distinguishable group of signals appeared in the range of 7.6–7.8 ppm and above 8.5 ppm, as previously reported.¹⁷ In the presence of ASA, the shift of $-COCH_3$ protons (v-v') suggested the involvement of this group in the metal coordination.

An additional proof of the formation of the ternary complex **ME-Zn-ASA** was provided by MALDI-TOF mass spectrometry. Being the latter a soft ionization technique, it allowed the detection of the fragile complex that with other ionization techniques would have been possibly decomposed. In the *SP*- $Zn(ClO_4)_2$ -aspirin solution the two peaks indicating the presence of a $2SP-Zn-ClO_4^-$ and $SP-Zn-ClO_4^-$ complexes were found at 1067 *m/z* and 615 *m/z* respectively. The additional peak at 714 *m/z* suggested the presence of a *SP*- Zn -aspirin- H_2O complex (Appendix paragraph 7.2.4).

We are attempting to obtain crystals of the **ME-Zn-ASA** triad, as their analysis by single-crystal X-ray diffraction would confirm the complex stoichiometry.

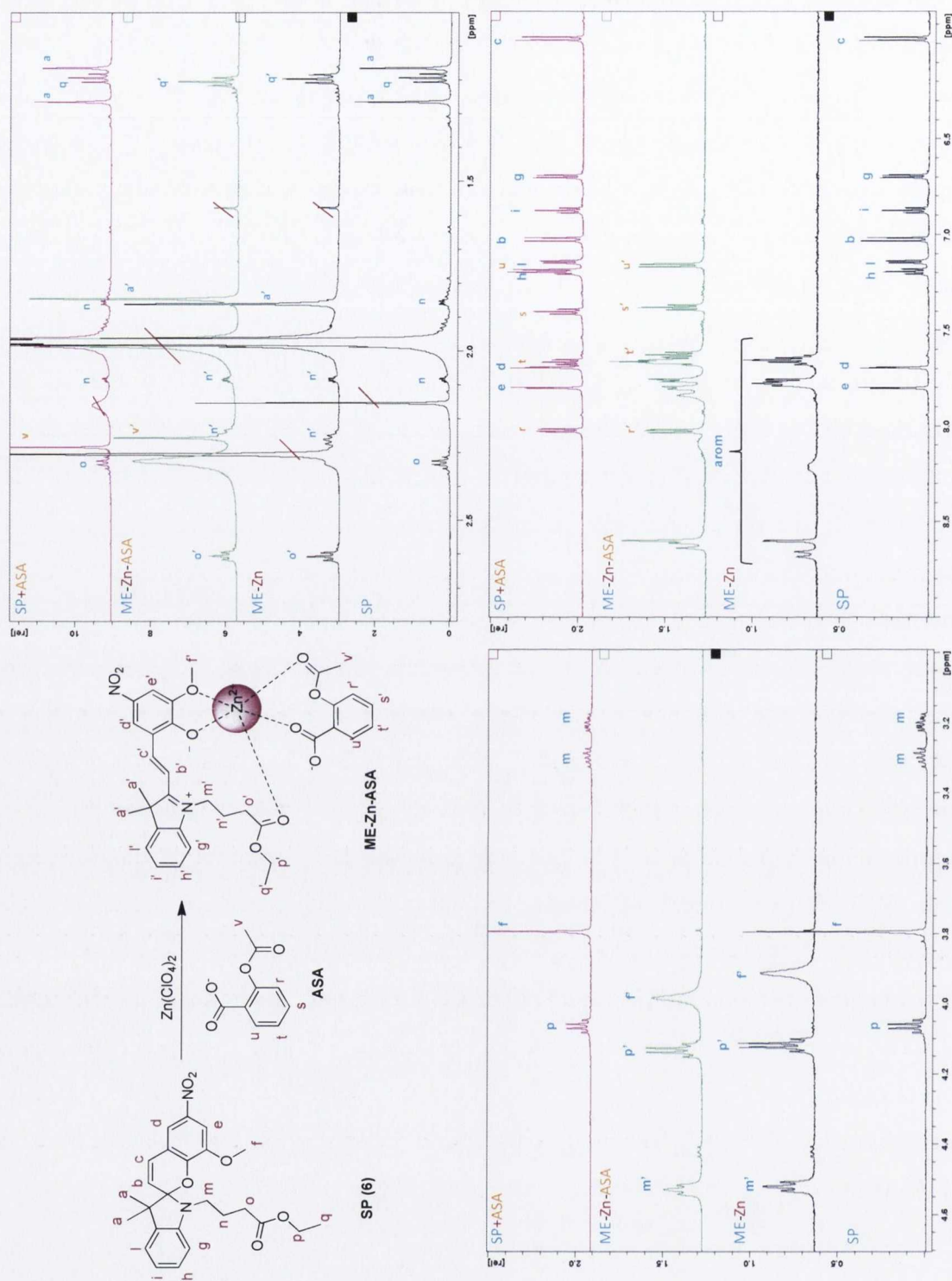


Figure 4.16: Hypothetical structure of the triad **ME-Zn-ASA**, and $^1\text{H-NMR}$ partial spectra of spiropyran prior to (**SP**) and after the addition of 1 eq of $\text{Zn}(\text{ClO}_4)_2$ (**ME-Zn**), 1 eq of aspirin (**SP+ASA**), and 1 eq of $\text{Zn}(\text{ClO}_4)_2$ plus 1 eq of aspirin (**ME-Zn-ASA**).

4.6.2 Absorption and emission spectroscopies

The ternary **ME-Zn-ASA** complex formation, the non-interactions between the two molecules and the chelation of zinc by the ASA drug, were confirmed by UV-Vis spectroscopic analyses. Absorption and emission studies demonstrated the effective light modulated reversible chelation of Zn^{2+} and ASA by the SP derivative.

ME-Zn-ASA triad complex formation. The changes in the absorption spectrum of a solution 10^{-4} M of SP (**6**) in CH_3CN before and after the addition of 1 eq of $\text{Zn}(\text{ClO}_4)_2$ and ASA were monitored and are depicted in Figure 4.17. The absorption spectrum of a solution of SP (picture A) show an absorption band at 358 nm and a low intensity band at 588 nm corresponding to a small amount of the open form isomer at the equilibrium. After the addition of 1 eq of $\text{Zn}(\text{ClO}_4)_2$, the solution turned orange (picture B) and a high intensity band, that corresponds to the **ME-Zn** complex, appeared at 489 nm.¹⁷ The addition of 1 eq of aspirin turned the solution into dark yellow (picture C), the band at 489 nm decreased in intensity, and a shoulder appeared at 430 nm. By comparing the absorption profile of **ME-Zn** before and after the addition of ASA, no intensity changes are detectable in the ME and SP bands. Absorptions below 300 nm and at 430 nm showed an increase in intensity after 1 day and after addition of an excess of aspirin, where the one at a smaller wavelength is due to the ASA molecule (Figure 4.12a in Appendix). The presence of a **ME-Zn** based complex was strongly indicated by the persistence of the band at 489 nm, and its decrease in intensity could be exclusively explained by the interaction of aspirin with the metal ion that is chelated by the ME zwitterion. All the above mentioned considerations brought to the reasonable conclusion that the band at 430 nm can be used as a signal to indicate the formation of the **ME-Zn-ASA** complex.

Control experiments (Figure 4.13a in Appendix) confirmed the attribution of the 430 nm absorption to a species that is not the protonated form of the ME (MEH).

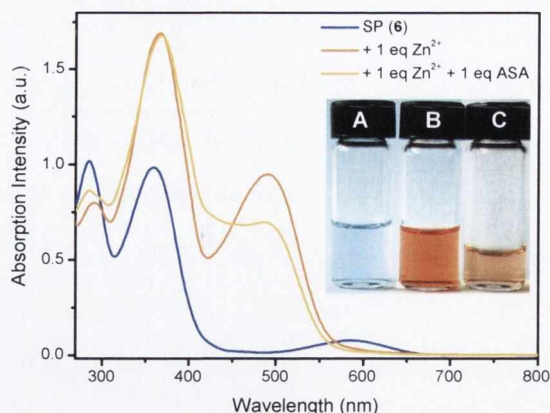


Figure 4.17: Absorption spectra of 10^{-4} M SP (**6**) in CH_3CN (blue) after the addition of 1 eq of Zn^{2+} (orange), and an additional 1 eq of ASA (dark yellow). Pictures of the correspondent solutions are reported in the inset and labelled as A, B and C respectively.

The **ME-Zn** complex formation was monitored by emission spectroscopy at intervals of 30 seconds for nearly one hour (Figure 4.18A). A 10^{-5} M solution of SP (**6**) in CH_3CN was added of 1 eq of $\text{Zn}(\text{ClO}_4)_2$ and irradiated with Vis light (3300K) for 1 minute to ensure the minimum emission of the **ME-Zn** complex at time zero. Upon excitation at $\lambda_{\text{exc}} = 481$ nm, the emission spectra revealed a band at 633 nm, that corresponds to the **ME-Zn** complex.

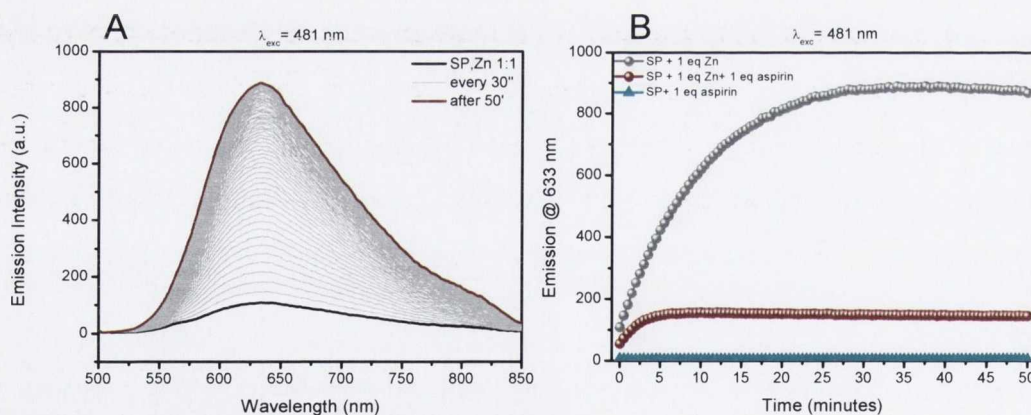


Figure 4.18: Kinetic of **ME-Zn** and **ME-Zn-ASA** complexes formation. A] Emission spectra of a SP solution (10^{-5} M, CH_3CN) after addition of 1 eq of $\text{Zn}(\text{ClO}_4)_2$ (10^{-2} M, H_2O) and Vis irradiation for 1 min. Data interval 30 sec for 50 min. B] Emissions at 633 nm of SP solutions added of Zn, Zn+ ASA or ASA in equimolar amounts.

The same experiment was repeated after the addition of i) 1 eq of $\text{Zn}(\text{ClO}_4)_2$ and 1 eq of ASA and ii) only of 1 eq of ASA to the SP solutions. The emission intensity at 633 nm was again recorded every 30 seconds, and the kinetics of complex formation for the three different solutions are plotted in Figure 4.18B. SP added of only ASA showed no response at 633 nm when excited at 418 nm (cyan), while emission was observed in the presence of the three components. However when the curves of **ME-Zn** (grey) and **ME-Zn-ASA** (wine) are compared, in the latter a lower emission intensity at 633 nm is recorded. We suggest that the interactive force between the metal and the SP dye is modified when ASA is present in solution. The outcomes of our experiments are in good agreement with the one recently reported where a ME-Zn-PPi complex was investigated.¹⁵

Light modulated reversible chelation of Zn/ASA by the SP derivative. The reversible chelation of zinc and ASA by the photoactive molecule was demonstrated by additional absorption and emission experiments and the use of Vis light. The metal cation showed to be fully released by the **ME-Zn** complex after Vis irradiation for just 1 minute, as evident by the disappearance of the emission and absorption bands typical of the complex at 633 nm and 489 nm respectively (Figure 4.14a in Appendix). After storage in the dark the **ME-Zn** complex was fully reconstituted and several light-controlled cycles could be reproduced, as already reported for the same SP derivative bearing a free carboxylic acid.¹⁷ The solution containing the triad **ME-Zn-ASA** was left in the dark for 7 days to equilibrate, and afterwards it was subjected to Vis light illumination. As reported in Figure 4.19A, the absorption features in the 400-600 nm range completely disappeared, as an indication of the release of Zn and ASA. The increased absorption below 300 nm, which is ascribable to the free ASA, further supported the effective release of the NSAID drug after short Vis light illumination. Following storage in the dark for 3 hours the ternary complex **ME-Zn-ASA** was completely restored (Figure 4.19B), as supported by the re-appeared absorption bands in the visible range.

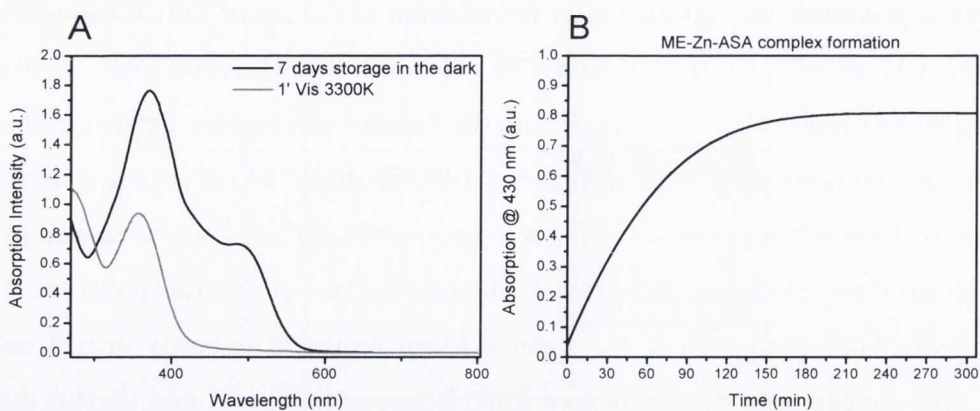


Figure 4.19: Kinetic of **ME-Zn-ASA** complexes formation and release of Zn/ASA by Vis light. A] Absorption spectra of a **ME-Zn-ASA** before and after irradiation with Vis light (3300K) for 1 minute. B] Kinetic of **ME-Zn-ASA** complex formation at 430 nm after Vis light illumination.

No interaction ME/ASA and chelation of zinc ion by ASA. It has been reported that the interaction between a SP and amino acid (AA) can be successfully proved by monitoring the change in fluorescence intensity of the ME opened isomer in the presence of AA.⁴⁶ In our study the same approach was employed to demonstrate the absence of interaction between SP (**6**) and ASA. The solution containing the photoactive molecule was irradiated by UV light (365 nm) for 1 min to ensure its conversion to the open form isomer (ME). The fully conjugated ME displayed an emission band at 705 nm (Figure 4.20A), that almost completely disappeared after 10 min, indicating the spontaneous and fast closure of the structure.

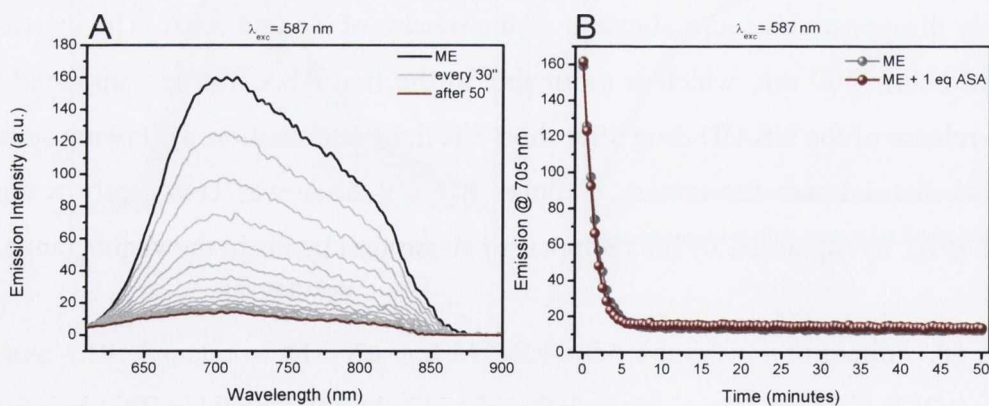


Figure 4.20: A] Emission spectra of ME (**6**) (10^{-5} M, CH_3CN) recorded every 30 sec for 50 min. B] Kinetic of ME (**6**) decay at 705 nm in the presence or absence of ASA.

The same experiment was repeated after the addition of 1 eq of ASA to the ME solution, and the fluorescence decay was monitored (Figure 4.20B). No significant changes were observed, indicating that the ASA is not able to stabilize the zwitterionic ME open form, and thus excluding any interaction between the two organic molecules. This result is in accordance with NMR and mass spectroscopy results.

Finally, following addition of zinc to an ASA solution the appearance of a new absorption band at 310 nm further suggested the complexation of the metal by the drug (Figure 4.15a in Appendix).

4.7 Reversible chelation of zinc by SP f-SWNTs

The complexation and the release of zinc metal ions and acetylsalicylic acid by SP (6) in solution demonstrated to be fully controllable and modulated by light, as pictured in Figure 4.21.

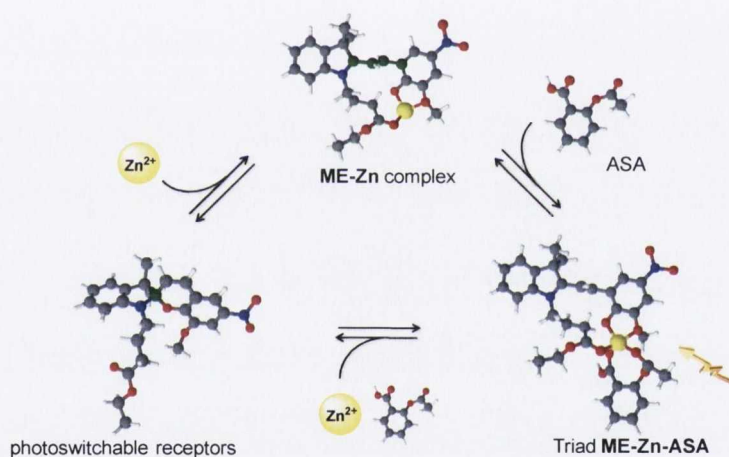


Figure 4.21: Pictorial representation of the cycle of chelation and light modulated release of zinc and ASA by the SP-based receptor.

However, when the photoactive molecule is anchored to a SWNTs scaffold, the simultaneous detection of metal ions and/or small organic molecules becomes more challenging because of the intrinsic optical features and of the strong absorption background of SWNTs. The latter might impede the straightforward assignment or even the detection of signals coming from the non-nanotube fraction by absorption spectroscopy. In the present work, the more sensitive emission spectroscopy will be

used to demonstrate both the chelation and the light modulated release of zinc by the SP f-SWNTs (3).

Furthermore when the performances of smart photoactive receptors in solution are aimed to be reproduced on the same attached to carbon nanotubes, the solubility issue becomes a major limitation. As a consequence, a solvent (or a mixture of solvents) capable to solubilize the tubes and that, at the same time, permits the preservation of the SP-based DDS abilities had to be exploited. A different number of solvents, summarized in Table 4.1a in Appendix, were tested on both SP f-SWNTs (3) and SP (6) before and after addition of zinc. Acetonitrile, the ideal solvent for the detection and performances of the **ME-Zn-ASA** complex, did not dissolve the nanotube material; whereas DMF, one of the solvents of choice for SWNTs, impeded the chelation of Zn^{2+} by the SP because of its solvation effect. Among the non-coordinating solvents, dichlorobenzene (Cl_2Bz) was chosen as, conversely to hexane and dichloromethane, it well dissolved both SPs and nanotubes. To overcome the problem of the non miscibility of the zinc aqueous solution with Cl_2Bz , a ternary mixture composed by Cl_2Bz/CH_3CN in ratio 9:1 and aqueous solution of zinc was used.

Absorption spectroscopy confirmed the reversible photoswitchability of the SP molecule by UV/dark cycles also in Cl_2Bz/CH_3CN 9:1, where the ME band resulted slightly red-shifted (from 588 to 610 nm) as a consequence of the changed polarity of the environment.^{47,48} When fluorescence decays of the ME open isomer in CH_3CN and Cl_2Bz/CH_3CN 9:1 were compared, a faster reversion to the closed SP isomer was recorded in the second case. Absorption and emission profiles of the photoswitchable receptor SP (6) in the two solvents are compared in the Appendix (paragraph 7.2.5, Figure 4.16a).

Zinc chelation studies were performed on SP (6) dissolved in Cl_2Bz/CH_3CN 9:1, following the same protocol adopted for CH_3CN solutions. After addition of 1 eq of $Zn(ClO_4)_2$ the solution turned fluorescent yellow and a new absorption band appeared at 440 nm. The changes in intensity and shape of the latter were monitored with the time, resulting in a clear signal attributable to the **ME-Zn** complex (Figure 4.22).

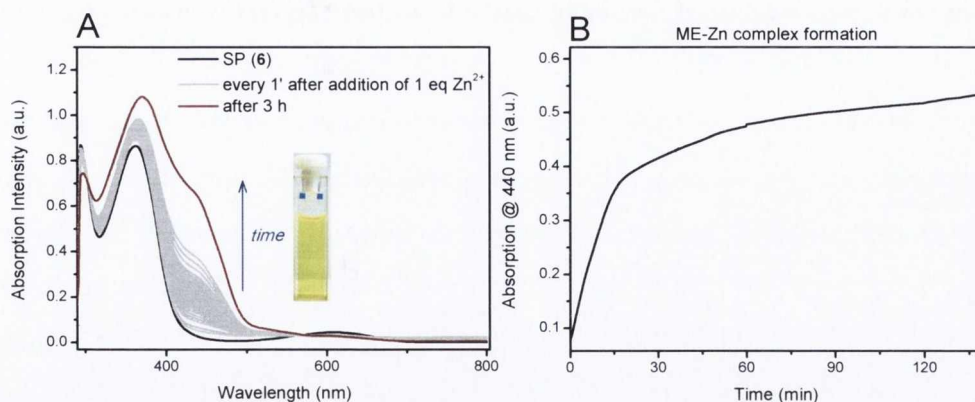


Figure 4.22: Absorption studies. A] Spectra of a SP solution (10^{-4} M, $\text{Cl}_2\text{Bz}/\text{CH}_3\text{CN}$ 9:1) after addition of 1 eq of $\text{Zn}(\text{ClO}_4)_2$ (10^{-1} M, H_2O). Data recorded for 1 h every 1 min, and after 3h. In the inset the colour of the solution after addition of zinc is shown. B] Changes in absorption intensity of **ME-Zn** at 440 nm after Vis light illumination.

Emission studies ($\lambda_{\text{exc}} = 440$ nm) confirmed the absorption outcomes: the intensity of the detected band at 578 nm increased gradually with the time after the addition of the metal to the SP solution, to reach a *plateau* after 30 minutes in the dark, which indicated a fast **ME-Zn** complex formation (Figure 4.23).

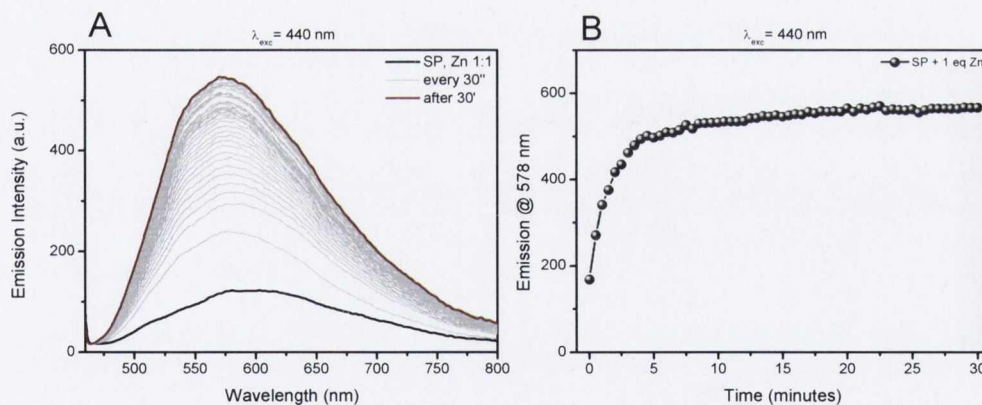


Figure 4.23: Emission studies. A] Spectra of a SP solution (10^{-5} M, $\text{Cl}_2\text{Bz}/\text{CH}_3\text{CN}$ 9:1) after addition of 1 eq of $\text{Zn}(\text{ClO}_4)_2$ (10^{-2} M, H_2O) and Vis irradiation for 1 min. Data recorded for 30 min every 30 sec. B] Changes in emissions intensity of a SP solutions added of Zn in equimolar amount at 578 nm.

The light controlled release of the metal cation from the **ME-Zn** was confirmed also in this solvent mixture (Appendix, Figure 4.17a). After 1 min of Vis light irradiation the solution turned transparent and the peak at 440 nm disappeared. By storing the sample in the dark, the complex spontaneously reformed with the same kinetic showed in Figures 4.21 and 4.22. To again exclude the attribution of the band at 440 nm to the protonated form of the ME (MEH), SP was added of 1 eq of TFA resulting in a different absorption profile in the 400-600 nm region (Appendix, Figure 4.18a). This besides the different colours of the SP solutions after addition of zinc and TFA, and the diverse emission profiles when excited at 440 nm, confirmed the **ME-Zn** complex formation when zinc was added to SP (**6**) dissolved in Cl₂Bz/CH₃CN 9:1.

Once the functioning of the smart photoactive SP based receptor was proved in Cl₂Bz/CH₃CN 9:1, optical measurements were carried out on SP f-SWNTs (**3**) dispersed in the same solvent mixture. Emission spectroscopy was again confirmed as a powerful analytical tool to prove the light responsive nature of the modified nanomaterial. Following UV irradiation of SP f-SWNTs (**3**), the band associated to the zwitterionic ME was detected at 667 nm, and its intensity was modulated by UV and dark cycles of 2 and 5 min respectively. In Figure 4.24 the photoresponsiveness and the on-off switching cycles of the nanotube material covalently functionalized with the SP receptor are once more demonstrated.

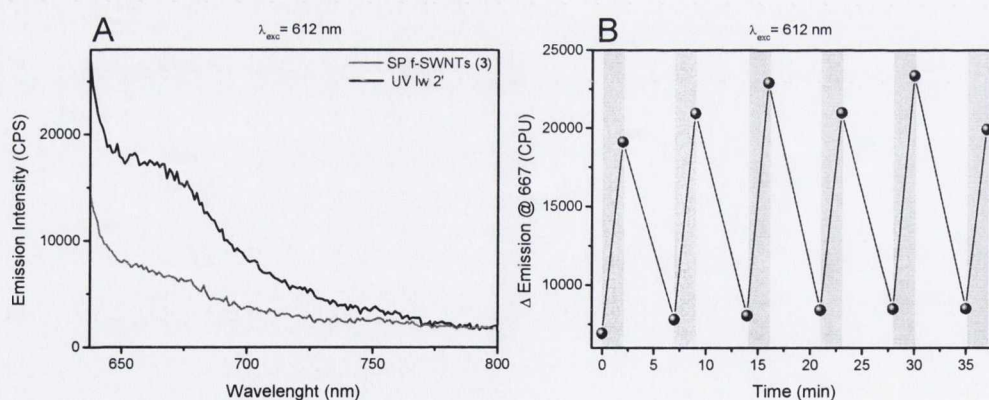


Figure 4.24: Emission studies. A] SP f-SWNTs (**3**) before and after UV (365 nm) illumination for 2 min. B] Emission changes at 667 nm of SP f-SWNTs (**3**) solutions following UV (365 nm) and darkness cycles. Gray and white bars indicate UV (2 min) and darkness (5 min) intervals respectively. Spectra were collected on the supernatant of initial 0.1 mg/mL nanotubes in Cl₂Bz/CH₃CN 9:1.

The SP f-SWNTs (**3**) solution was added of $\text{Zn}(\text{ClO}_4)_2$, left equilibrate in the dark for 5 min and the emission spectrum ($\lambda_{\text{exc}} = 440 \text{ nm}$) was collected. The band recorded at 508 nm was attributed to the formation of the **ME-Zn** complex for two reasons. The first because its shape and shift value are comparable to that of the **ME-Zn** free in solution, the second because its intensity can be modulated by Vis light (Figure 4.25). Sequential conversions between the closed form of the receptor and **ME-Zn** complex anchored to SWNTs scaffolds were recorded after the addition of the metal followed by light and darkness cycles.

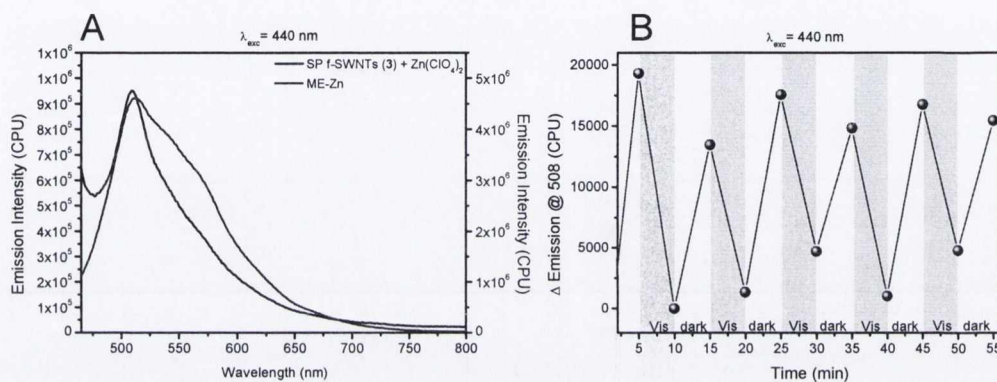


Figure 4.25: Release of zinc by SP f-SWNTs (**3**) triggered by light. A] Emission spectra ($\lambda_{\text{exc}} = 440 \text{ nm}$) of SP f-SWNTs (**3**) added of $\text{Zn}(\text{ClO}_4)_2$ (10^{-1} M , H_2O , $1 \mu\text{L}/\text{mL}$ of NTs) and of the **ME-Zn** complex in $\text{Cl}_2\text{Bz}/\text{CH}_3\text{CN}$ 9:1. B] Emission changes at 508 nm of SP f-SWNTs (**3**) added of Zn^{2+} , following Vis (3300 K) illumination (5 min, grey bars) and dark cycles (5 min, white bars). The spectra were collected on the supernatant of initial $0.1 \text{ mg}/\text{mL}$ nanotubes in $\text{Cl}_2\text{Bz}/\text{CH}_3\text{CN}$ 9:1.

We have previously shown that when ASA is added to a **ME-Zn** solution, the emission of the complex decreased in intensity, suggesting an interactive force between the drug and the metal also when the latter is chelated by the receptor. In the light of this and of the weak emission signal recorded for the complex anchored to SWNTs, experiments involving the addition of ASA to SP-modified nanotubes were not performed. However, the demonstrated zinc-aspirin complex formation besides the successful and reproducible release of zinc metal ions by the photoactive receptor attached to SWNTs (Figure 4.25B), may suggest that when ASA is added to the

nanotube solution it would be released together with the metal following Vis light illumination, as schematized in the cartoon of Figure 4.26.

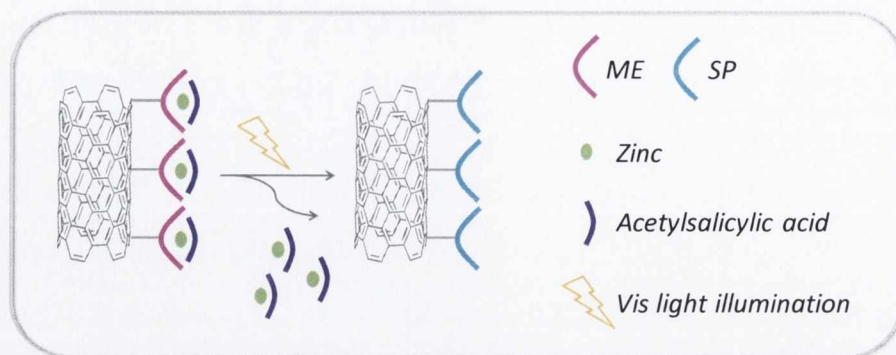


Figure 4.26: Pictorial representation of the envisaged release of bioactive payloads from SWNTs bearing SP photoactive receptors.

Emission studies ($\lambda_{exc} = 440$ nm) were additionally performed on p-SWNTs, f-SWNTs (**1**) and SP f-SWNTs (**3**) and were compared to the emission data recorded for SP f-SWNTs (**3**) after the addition of zinc. In the absence of metal all the nanotube solutions presented a small intensity emission band at 508 nm (Figure 4.19a in Appendix). However, this band remarkably changed both in intensity and in light responsiveness only following addition of zinc to the one functionalized with the SP receptor. This result further confirmed the successful chelation of zinc by the SP photoactive molecule anchored to the SWNT scaffold.

4.8 Epifluorescence microscopy images of SP f-SWNTs

Epifluorescence microscopy images (performed by Dania Movia) of human monocytic leukemia cells (THP-1) treated with SP f-SWNTs (**3**) showed that “macrophage-like” cells grew in close contact with the nanotube aggregates (Figure 4.27A, B and D). Careful microscopy analysis showed active engulfment of such aggregates by THP-1 cells (Figure 4.27C), thus underlining the potential application of SP f-SWNTs (**3**) as drug-delivery platform. Further investigations by TEM would be necessary to better clarify whether THP-1 cells are able to uptake SP f-SWNTs (**3**) inside the cytoplasm.

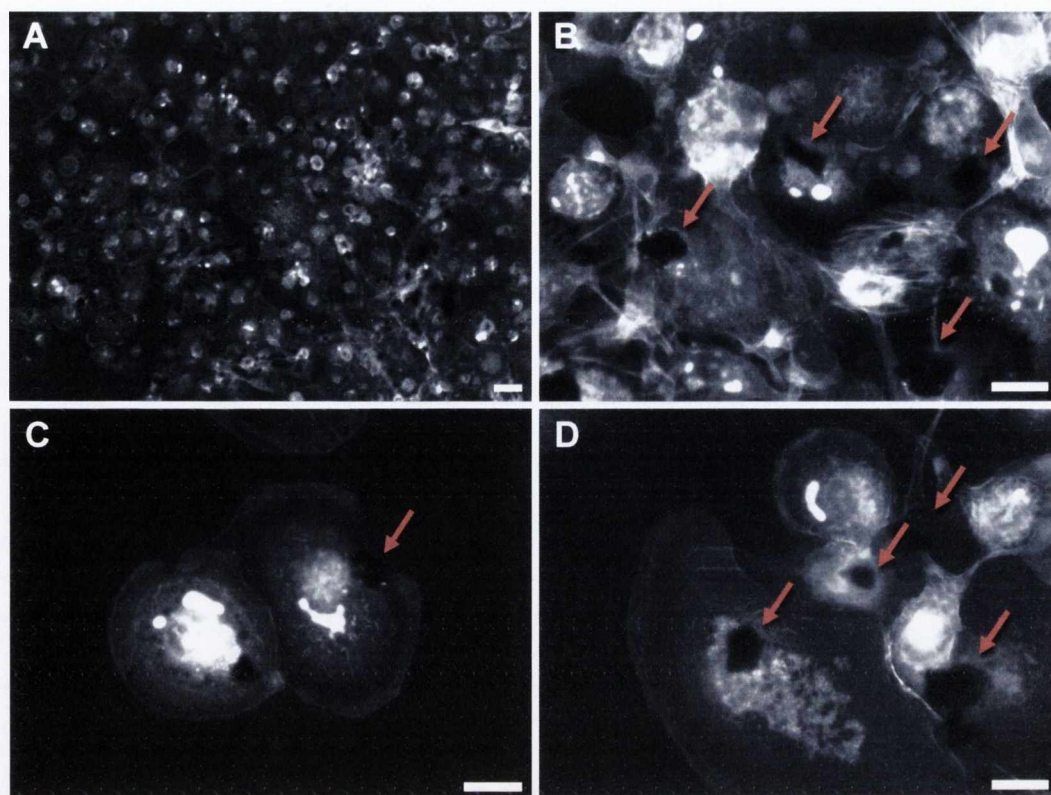


Figure 4.27: Representative epifluorescent microscopy images of PMA-activated, “macrophage-like” THP-1 cells stained with Phalloidin-Alexa 546 conjugate after 24 h exposure to SP f-SWNTs (**3**). (B, D) Arrows point out SP f-SWNTs (**3**) aggregates in close contact with cells. (C) Macrophage engulfing a SWNTs aggregate (red arrow). (B-D) Intensely stained punctate foci of F-actin are visible across the entire cells surface. The punctate F-actin fluorescence along the cell is associated with monocyte-to-macrophage differentiation and it is indicative of adhesive structure formation.⁴⁹ Scale bar: 20 μm : (A) 10 \times , (C-D) 50 \times magnification.

4.9 Conclusions

We have demonstrated the light modulated release of anti-inflammatory zinc ions by a smart multifunctional material composed of spiropyrans and SWNTs. The exploitation of a number of complementary characterization technique allowed the investigation of both composition and performance of chemically purified and sidewall functionalized nanotubes. The suitability of the synthesized SP/SWNT material for potential applications in bio-systems was suggested by (1) the removal of toxic metal catalyst

particles, as confirmed by TGA and TEM images, and by (2) their increased debundling and dispersibility in common solvents and water, as gathered by AFM topographic images and solubility tests. The introduction of PEGylated biocompatible linkers and SP photoactive molecules was confirmed by characteristic vibrations of the functional groups in FT-IR spectra, by increased weight loss below the graphitic decomposition temperature in TGA analyses, and by the higher I_D/I_G ratio in Raman spectra after functionalization. The introduction of a high number of organic pendants on the tubes' surface was achieved by Tour reaction and was confirmed by Kaiser test.

UV-Vis spectroscopy has been decisive in proving the photoswitchability of the SP receptor both when free in solution and when anchored to the SWNT scaffold. Emission and absorption studies, combined with mass spectrometry and $^1\text{H-NMR}$ demonstrated the formation of a supramolecular complex between SP, Zn^{2+} ions and acetylsalicylic acid, coined as ME-Zn-ASA. Visible light illumination showed to trigger the release of both metal and NSAID drug from the ternary complex in a controlled manner. The successful and reproducible release of zinc metal ions by the photoactive receptor loaded on the tubular nanosized scaffold was also proved by UV-Vis spectroscopic studies. The set of data presented in this work and the evidences gathered so far, suggest that the delivery of ASA together with zinc is potentially achievable when the latter is chelated by SP f-SWNTs.

We presented here for the first time a potential photo controllable SP/SWNTs based drug delivery system (DDS) where the nanotubes act as intracellular carriers of light modulated receptors for anti-inflammatory agents.

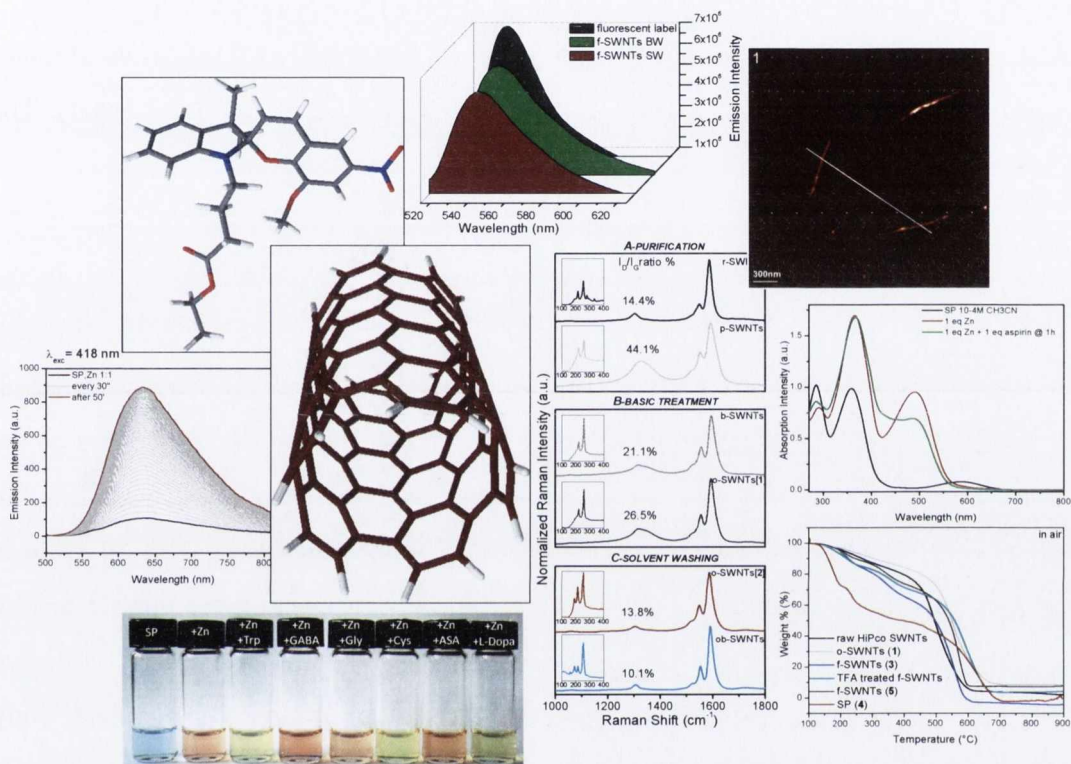
References

- (1) Kam, N. W. S.; O'Connell, M.; Wisdom, J. A.; Dai, H. *Proceedings of the National Academy of Sciences of the United States of America* **2005**, *102*, 11600.
- (2) Pantarotto, D.; Briand, J. P.; Prato, M.; Bianco, A. *Chemical Communications* **2004**, 16.
- (3) Pantarotto, D.; Singh, R.; McCarthy, D.; Erhardt, M.; Briand, J. P.; Prato, M.; Kostarelos, K.; Bianco, A. *Angewandte Chemie-International Edition* **2004**, *43*, 5242.
- (4) Liang, F.; Chen, B. *Current Medicinal Chemistry* **2010**, *17*, 10.
- (5) Kostarelos, K.; Bianco, A.; Prato, M. *Nature Nanotechnology* **2009**, *4*, 627.
- (6) Su, Z.; Zhu, S.; Donkor, A. D.; Tzoganakis, C.; Honek, J. F. *Journal of the American Chemical Society* **2011**, *113*, 6874.

- (7) Khazaei, A.; Rad, M. N.; Borazjani, M. K. *International journal of nanomedicine* **2010**, *5*, 639.
- (8) Prato, M.; Kostarelos, K.; Bianco, A. *Accounts of Chemical Research* **2008**, *41*, 60.
- (9) Kam, N. W. S.; Dai, H. J. *Journal of the American Chemical Society* **2005**, *127*, 6021.
- (10) Chen, J.; Chen, S.; Zhao, X.; Kuznetsova, L. V.; Wong, S. S.; Ojima, I. *Journal of the American Chemical Society* **2008**, *130*, 16778.
- (11) Chaban, V.; Prezhdo, O. *Acs Nano* **2011**, ASAP.
- (12) Ito, Y.; Venkatesan, N.; Hirako, N.; Sugioka, N.; Takada, K. *International Journal of Pharmaceutics* **2007**, *337*, 357.
- (13) Shao, N.; Jin, J. Y.; Cheung, S. M.; Yang, R. H.; Chan, W. H.; Mo, T. *Angewandte Chemie-International Edition* **2006**, *45*, 4944.
- (14) Shao, N.; Gao, X.; Wang, H.; Yang, R.; Chan, W. *Analytica Chimica Acta* **2009**, *655*, 1.
- (15) Shao, N.; Wang, H.; Gao, X.; Yang, R.; Chan, W. *Analytical Chemistry* **2010**, *82*, 4628.
- (16) Movia, D.; Prina-Mello, A.; Volkov, Y.; Giordani, S. *Chemical Research in Toxicology* **2010**, *23*, 1459.
- (17) Natali, M.; Aakeroy, C.; Desper, J.; Giordani, S. *Dalton Transactions* **2010**, *39*, 8269.
- (18) Natali, M.; Soldi, L.; Giordani, S. *Tetrahedron* **2010**, *66*, 7612.
- (19) Prasad, A. S.; Beck, F. W. J.; Snell, D. C.; Kucuk, O. *Nutrition and Cancer* **2009**, *61*, 879
- (20) Moore, M. M.; Chua, W.; Charles, K. A.; Clarke, S. J. *Clinical Pharmacology & Therapeutics* **2010**, *87*, 504.
- (21) Balkwill, F.; Mantovani, A. *Clinical Pharmacology & Therapeutics* **2010**, *87*, 401.
- (22) Rakoff-Nahoum, S. *Yale Journal of Biology and Medicine* **2006**, *79*, 123.
- (23) Goswami, B.; Rajappa, M.; Sharma, M.; Sharma, A. *International Journal of Gynecological Cancer* **2008**, *18*, 591.
- (24) Mantovani, A.; Allavena, P.; Sica, A.; Balkwill, F. *Nature* **2008**, *454*, 436.
- (25) Singla, A. K.; Wadhwa, H. *International Journal of Pharmaceutics* **1994**, *108*, 173.
- (26) Kohane, D. S.; Langer, R. *Chemical Science* **2010**, *1*, 441.
- (27) Dumortier, H.; Lacotte, S.; Pastorin, G.; Marega, R.; Wu, W.; Bonifazi, D.; Briand, J.-P.; Prato, M.; Muller, S.; Bianco, A. *Nano Letters* **2006**, *6*, 1522.
- (28) Sayes, C. M.; Liang, F.; Hudson, J. L.; Mendez, J.; Guo, W.; Beach, J. M.; Moore, V. C.; Doyle, C. D.; West, J. L.; Billups, W. E.; Ausman, K. D.; Colvin, V. L. *Toxicology Letters* **2006**, *161*, 135.
- (29) Shi Kam, N. W.; Jessop, T. C.; Wender, P. A.; Dai, H. *Journal of the American Chemical Society* **2004**, *126*, 6850.

- (30) Schipper, M. L.; Nakayama-Ratchford, N.; Davis, C. R.; Kam, N. W. S.; Chu, P.; Liu, Z.; Sun, X.; Dai, H.; Gambhir, S. S. *Nature Nanotechnology* **2008**, *3*, 216.
- (31) Porter, A. E.; Gass, M.; Bendall, J. S.; Muller, K.; Goode, A.; Skepper, J. N.; Midgley, P. A.; Welland, M. *Acs Nano* **2009**, *3*, 1485.
- (32) Mutlu, G. M.; Budinger, G. R. S.; Green, A. A.; Urich, D.; Soberanes, S.; Chiarella, S. E.; Alheid, G. F.; McCrimmon, D. R.; Szeleifer, I.; Hersam, M. C. *Nano Letters* **2010**, *10*, 1664.
- (33) Bianco, A.; Kostarelos, K.; Partidos, C. D.; Prato, M. *Chemical Communications* **2005**, 571.
- (34) Barreto, J. A.; O'Malley, W.; Kubeil, M.; Graham, B.; Stephan, H.; Spiccia, L. *Advanced Materials* **2011**, H18.
- (35) Flavin, K.; Kopf, I.; Navio, C.; Bittencourt, C.; Giordani, S. *Journal of Materials Chemistry* **2011**, in revision.
- (36) Flavin, K.; Lawrence, K.; Bartelmess, J.; Tasiar, M.; Navio, C.; Bittencourt, C.; O'Shea, D. F.; Guldi, D. M.; Giordani, S. *Acs Nano* **2011**, *5*, 1198.
- (37) Kaiser, E.; Colescot, R. I.; Bossinge, C. D.; Cook, P. I. *Analytical Biochemistry* **1970**, *34*, 595.
- (38) Pantarotto, D.; Browne, W. R.; Feringa, B. L. *Chemical Communications* **2008**, 1533.
- (39) Quintana, M.; Prato, M. *Chemical Communications* **2009**, 6005.
- (40) Rinaldi, A.; Frank, B.; Su, D. S.; Hamid, S. B. A.; Schloegl, R. *Chemistry of Materials* **2011**, *23*, 926.
- (41) Bahr, J. L.; Tour, J. M. *Journal of Materials Chemistry* **2002**, *12*, 1952.
- (42) Dyke, C. A.; Tour, J. M. *Nano Letters* **2003**, *3*, 1215.
- (43) Price, B. K.; Hudson, J. L.; Tour, J. M. *Journal of the American Chemical Society* **2005**, *127*, 14867.
- (44) Sayama, K. H.; Ohga, Y.; Shinpou, A.; Suga, S.; Arakawa, H. *New Journal of Chemistry* **2001**, *25*, 200.
- (45) Movia, D.; Del Canto, E.; Giordani, S. *The Journal of Physical Chemistry C* **2010**, *114*, 18407.
- (46) Ipe, B. I.; Mahima, S.; Thomas, K. G. *Journal of the American Chemical Society* **2003**, *125*, 7174.
- (47) Murugan, N. A.; Chakrabarti, S.; Ågren, H. *The Journal of Physical Chemistry B* **2011**, *115*, 4025.
- (48) Wojtyk, J. T. C.; Wasey, A.; Kazmaier, P. M.; Hoz, S.; Buncel, E. *The Journal of Physical Chemistry A* **2000**, *104*, 9046.
- (49) DeFife, K. M.; Jenney, C. R.; Colton, E.; Anderson, J. M. *Journal of Histochemistry & Cytochemistry* **1999**, *47*, 65.

Chapter 5. Experimental Procedures



5.1 General Procedures

TGA analyses were performed on a PerkinElmer Thermogravimetric Analyzer Pyris 1 TGA. The method used for performing TGA measurements both in air and nitrogen is as follows: 5 minute isothermal step at 30 °C (to equilibrate the sample); heat from 30 °C to 100 °C at a rate of 10 °C min⁻¹; 20 minute isothermal step at 100 °C (to ensure evaporation of the solvents); heat from 100 °C to 900 °C at a rate of 10 °C min⁻¹.

FT-IR spectra were measured in the solid state on a PerkinElmer FT-IR Spectrometer Spectrum 100 with a universal ATR sampling accessory (diamond/ZnSe crystal). The spectra were recorded at 256 scans with a 4 cm⁻¹ resolution.

Micro-Raman scattering measurements were carried out at room temperature in the backscattering geometry using RENISHAW 1000 micro-Raman system equipped with a CCD camera and a Leica microscope. An 1800 lines mm⁻¹ grating was used for all measurements, providing a spectral resolution of ~ 1 cm⁻¹. As an excitation source the Ar⁺ laser with 457 and 514 nm excitation lines and the He-Ne laser with 633 nm excitation with variable powers were used. Measurements were taken with 20 seconds of exposure time and 4 accumulations. The laser spot was focused on the sample surface using a 50x objective with short-focus working distance. Raman spectra were collected on numerous spots on the sample and recorded with Peltier cooled CCD camera. Only one spectrum was collected per spot. Frequency shifts were calibrated by a Si reference. The intensity ratio I_D/I_G was obtained by taking the peak intensities after baseline corrections. The data were collected and analyzed with Renishaw Wire and GRAMS software.

Raman mapping measurements were collected at room temperature using RENISHAW in-Via Raman system coupled with CCD camera. Samples were deposited on glass cover slides No 1. The laser spot was focused on the sample surface using a 100x oil immersion objective (N.A. = 1.4). As excitation source laser at 488 nm with 9 mW power was used. An 1800 lines mm⁻¹ grating was used, providing a spectral resolution of ~ 1 cm⁻¹. Raman maps were taken with 0.2 seconds of exposure time, one accumulation and total number of points 128x128. The data were collected and analyzed with Wire 3.1 software and NT-MDT Nova software.

XPS measurements were performed in a VERSAPROBE PHI 5000 from Physical Electronics, equipped with a Monochromatic Al $K\alpha$ X-Ray source with a highly focused beam size which can be selected from 10 μm to 300 μm . The energy resolution was 0.6 eV. For the compensation of built up charge on the sample surface during the measurements a dual beam charge neutralization composed of an electron gun (~ 1 eV) and the Argon Ion gun (≤ 10 eV) was used.

The UV-Vis and the UV-Vis-NIR Absorption spectra were recorded on a Perkin Elmer UV/Vis Spectrometer Lambda 35 and a Perkin Elmer UV-Vis-NIR Spectrometer Lambda 1050 respectively. All the data were recorded after 1 cycle, with an interval of 1 nm, slit width of 2 nm and scan speed of 240 nm min^{-1} . The nanotube samples were dispersed in HPLC grade solvents by sonication (tip and/or bath), centrifuged for a minimum time of 90 min at 4000 rpm and the absorption spectra were recorded on the supernatant of initial SWNT concentration of 0.1mg/mL or 0.01 mg/mL, except as otherwise stated.

Samples were illuminated by using a portable UVP ultraviolet lamp equipped with a combination of shortwave (254 nm)/longwave (365 nm) and a Schott KL 1500 LCD Visible lamp (560-900 nm).

Emission spectra were taken in a HORIBA Jobin Yvon Fluorolog-3 Spectrofluorometer equipped with a 450 xenon CV lamp after 1 cycle, with slit width of 10 nm and integration time 0.1 s. The nanotube samples were dispersed in HPLC grade solvents by sonication (tip and/or bath), centrifuged for a minimum time of 90 min at 4000 rpm and the emission spectra were recorded on the supernatant of initial SWNT concentration of 0.1mg/mL or 0.01 mg/mL, except as otherwise stated.

NIR-PL studies were carried out in triplicate on supernatants in a L.O.T. ORIEL NS1 NanoSpectralyzer[®] (diode lasers; λ_{exc} = 638 nm, 683 nm and 785 nm) with an integration time of 1 second and 5 accumulations. Samples were dispersed in aqueous sodium dodecylbenzene sulfonate (SDBS) at an SWNTs:SDBS weight ratio of 1:25. The dispersions were obtained by sonication and centrifuged at 4000 rpm for 90 min. Additional details are reported later on this chapter together with the emission efficiency calculation.

AFM topographic images were collected in semi-contact mode with an NT-MDT inverted configuration system. Silicon tips with reflectance gold coated on the back, tip apex radius 10 nm, force constant 2 N/m and frequency 170 kHz were used. The data were collected and analyzed with NT-MDT Nova software. Samples were prepared for analysis by dispersing the nanotubes in high purity DMF by sonication and spin coating on mica substrates (results in Chapter 2) or by dispersing the nanotubes in high purity DMF by sonication, spray coated onto freshly cleaved mica substrates and dried overnight in oven at 90° C (results in Chapter 3).

For High Resolution Transmission Electron Microscopy (HR-TEM) SWNTs powders were dispersed in high purity DMF ($[SWNTs]_i = 0.1 \text{ mg/mL}$) by sonic tip and sonic bath. The samples were prepared by dropping an aliquot (10 μL c.a.) of the dispersions on 200 mesh Cu holey carbon grids and incubating for some minutes. The grids were then drained, dried for 1 day at 37 °C and visualized under a Jeol 2100 operating at 200 kV with a Lanthanum Hexaborise emission source.

Proton Nuclear Magnetic Resonance spectra were recorded on a Bruker DPX 400 MHz spectrometer in CDCl_3 (solvents standardized with respect to TMS). Chemical shifts are reported in ppm and coupling constants in Hertz. Carbon NMR spectra were recorded on the same instrument (100 MHz) with total proton decoupling.

The Kaiser test is a qualitative and quantitative method for the identification of free amine groups.¹⁻³ This test was originally designed to monitor solid-state protein coupling, and it has been also successfully applied to characterize amino-functionalized nanotubes.⁴

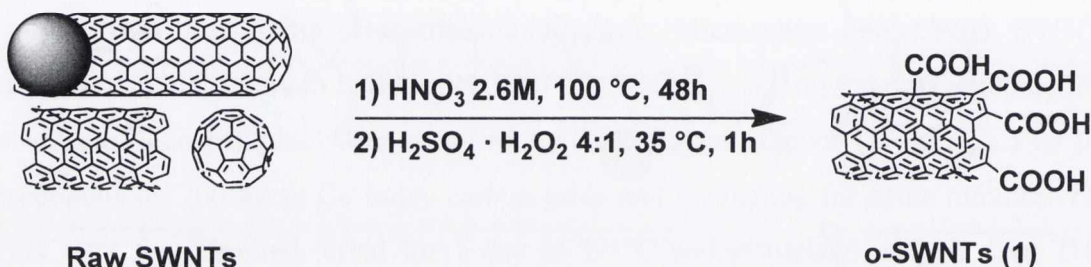
The standard procedure used in all the Kaiser tests was performed as follows:

- Exact weight of 1.0 mg of f-SWNTs
- Addition of 75 μL of solution 1 (80 g of phenol in 20 ml of EtOH)
- Addition of 100 μL of solution 2 (2 ml of KCN 1mM in 98 ml of pyridine)
- Addition of 75 μL of solution 3 (1 g of ninhydrin in 20 ml of EtOH)
- Solution heating at 100°C for 7 minutes under vigorous stirring
- Dilution with EtOH until the volume of 5 ml
- Sonication for 7 minutes.

5.2 Experimental for Chapter 2

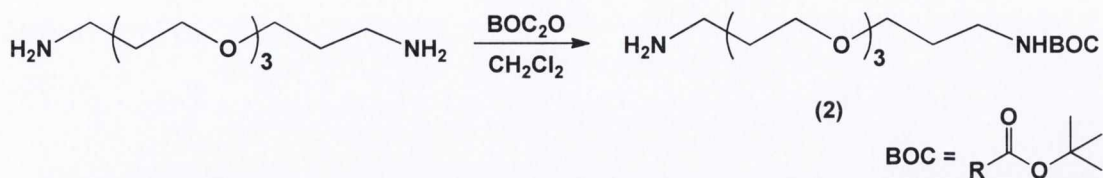
5.2.1 Materials. SWNTs produced by the HiPco technique were purchased from Unidym[®], Inc. (Lot no. R0546). Reagents and solvents were purchased as reagent-grade from Fisher Scientific Ireland Ltd, or Sigma-Aldrich Ireland and used without further purification.

5.2.2 Preparation of o-SWNT (1)



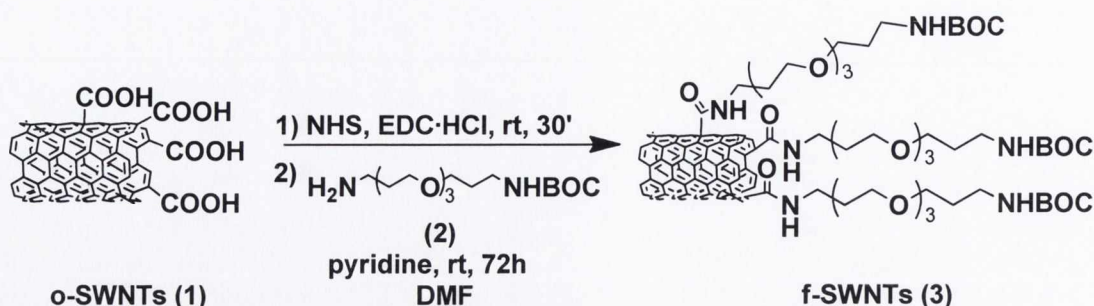
HiPco pristine SWNTs (Unidym[®] lot R0546) were weighted (100 mg) and dispersed in 100 mL aqueous solution of HNO_3 (2.6 M). The dispersion was stirred under reflux at 100 °C for 48 h. After cooling down to room temperature the dispersion was filtered through a Millipore system (on a 0.2 μm Isopore filter) and the black solid powder collected on the filter was rinsed with distilled water (until the pH value of the filtrate was neutral) and dried overnight at 60 °C under vacuum. The purified nanotubes were subsequently dispersed in distilled water, sonicated for 10 min and treated with 100 mL of piranha solution ($\text{H}_2\text{SO}_4_{\text{conc}} \cdot \text{H}_2\text{O}_2$ (30%) at a 4:1 ratio) and the mixture was stirred at 35 °C for one hour. After cooling down to room temperature the mixture was diluted with ice and filtered through a Millipore system (on a 0.2 μm Isopore filter) and the residue rinsed with distilled water (~ 500 mL) until the pH of the filtrate was neutral. After drying at 60 °C under vacuum overnight 78 mg of oxidized and shortened o-SWNTs (1) were obtained. **FT-IR** ν (cm^{-1}): 3004, 2900, 2836 (C-H), 1740, 1714 (C=O), 1603, 1492, 1431 (C=C), 1384, 1310 (C-C), 1283, 1207, 1156 (C-O-C).

5.2.3 Preparation of tert-Butyl 3-(2-(2-(3-aminopropoxy)ethoxy)propyl)carbamate (2)



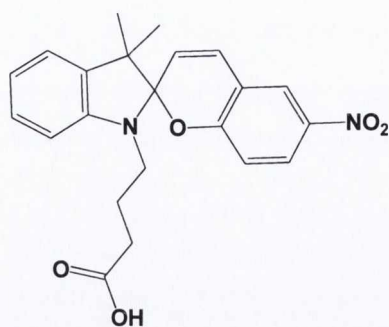
A solution of 4,7,10-trioxa-1,13-tridecanediamine (17.53 mL, 2 equiv, 80.0 mmol) in 60 mL of dichloromethane (DCM) was added drop wise to a solution of tert-butoxycarbonyl anhydride (Boc₂O) (8.74 g, 1 equiv, 40.0 mmol) in 60 mL of DCM over a three and a half hour period at 0 °C. The solution was then stirred at room temperature for 24 h. The solvent was evaporated and the residue was added to distilled water (~100 mL). The bis-Boc protected derivative, insoluble in water, appeared as a white precipitate. The latter was removed by filtration on celite. The water was extracted 5 times with dichloromethane (15 mL). The organic phases were unified and dried with Na₂SO₄ anhydrous. After solvent evaporation under reduced pressure the product (2) was obtained as yellowish oil. **Yield** 68%. *R_f* = 0.8 (CH₂Cl₂:MeOH 9:1). **¹H-NMR** (400 MHz, CDCl₃): δ = 1.43 (s, 9H, Boc), 1.71-1.85 (m, 4H, CH₂), 2.90 (t, 2H, *J* = 6.0 Hz, CH₂NH₂), 3.23 (d, 2H, *J* = 5.5 Hz, CH₂NH), 3.35-3.41 (m, 2H, CH₂), 3.53-3.64 (m, 10H, CH₂), 5.16 (bs, 1H, NH). **¹³C-NMR** (100 MHz, CDCl₃): δ = 28.0 (3CH₃), 29.2 (CH₂CH₂NH₂), 31.3 (CH₂CH₂NH), 38.0 (CH₂NH), 39.1 (CH₂NH₂), 69.2 (CH₂), 69.6 (CH₂), 69.7 (CH₂), 70.0 (CH₂), 70.1 (CH₂), 74.1 (CH₂), 78.5 (C Boc), 155.7 (COO). **FT-IR** ν (cm⁻¹): 3351 (NH), 2929, 2866 (C-H), 1693 (C=O), 1517 (N-H), 1364 (C-tBut), 1249 (CO-O-C), 1105 (C-O-C). **HRMS (*m/z* -ES)**: Found: 321.24 (M+ H⁺, C₁₅H₃₂N₂O₅ Requires: 320.43).

5.2.4 Preparation of f-SWNTs (3)



o-SWNTs (1) were weighted (70 mg) and dispersed in approximately 50 mL of dimethylformamide (DMF) by sonication in a water bath for 10 min. N-hydroxysuccinimide (NHS) (30 mg in 5 mL of DMF) was added to the dispersed o- (1) and the dispersion was sonicated for another 10 min. 1-Ethyl-3-(3-dimethylaminopropyl)carbodiimide hydrochloride (EDC·HCl) (46 mg in 5 mL of DMF), was added to the dispersion of o-SWNTs and the sonication continued for an additional 10 min. The reaction mixture was stirred at room temperature for 30 min and tert-butyl 2-(2-(2-aminoethoxy)ethoxy)ethylcarbamate (2) (138 mg in 25.5 mL of DMF) was added. Pyridine (5.4 mL) was added and the reaction mixture was stirred at room temperature for 3 days under N₂. The functionalized SWNTs (3) were collected as a black precipitate and filtered twice through Millipore system (on a 0.2 μm fluoropore FG filter). The black solid collected on the filter was dissolved in DMF, sonicated for 10 min and filtered again on a new 0.2 μm fluoropore FG filter. The product was washed with increasing polarity solvents toluene, diethyl ether, dichloromethane and methanol to remove the excess of non-reacted products. The black solid was dried under vacuum overnight to afford 76 mg of f-SWNTs (3). **FT-IR** ν (cm⁻¹): 3252 (NH), 2915, 2845, 2603 (C-H), 1739 (C=O), 1570, 1522 (N-H), 1435 (C-tBu), 1150 (C-O-C).

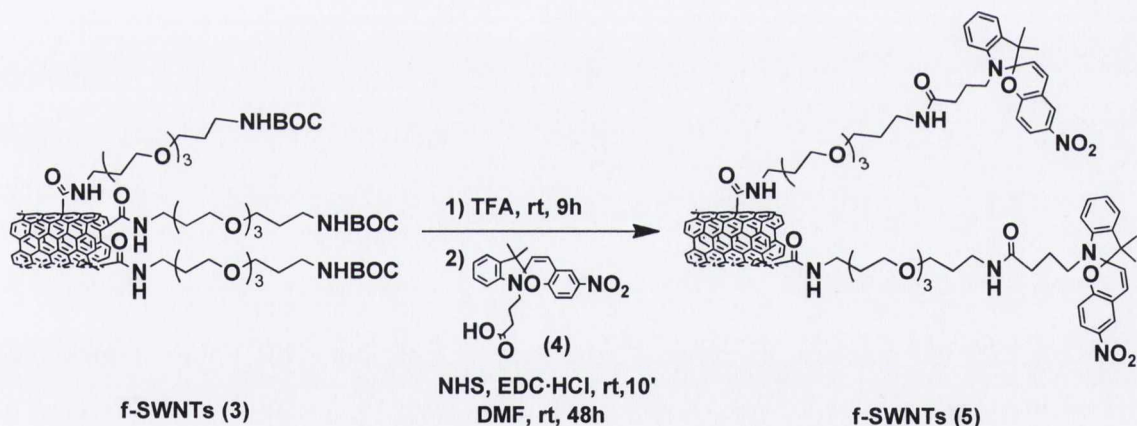
5.2.5 Preparation of SP (4)



(4)

The spirocyan 4-(3',3'-dimethyl-6-nitrospiro[chromene-2,2'-indoline]-1'-yl)butanoic acid (4) was synthesized by Manuel Natali according to the literature procedure previously reported⁵ followed by a basic hydrolysis to generate the carboxylic acid.

5.2.6 Preparation of f-SWNTs (5)



A 66 mg quantity of the previously obtained f-SWNTs (3) was dispersed in 25 mL of DMF and sonicated in sonic bath for 20 min. A 4.5 mL aliquot of trifluoroacetic acid (TFA) was added and the mixture was stirred at room temperature for 9 h. The black product was filtered through a Millipore system (on a 0.2 μm fluoropore FG filter) and washed in order with pyridine, dimethylformamide, toluene, diethyl ether, dichloromethane and methanol. The black solid was dried under vacuum to afford 57.8 mg of f-SWNT. **FT-IR** ν (cm^{-1}): 3261 (NH), 3061, 2866 (C-H), 1737, 1651 (NH-CO), 1651, 1571 (N-H), 1431 (C-C), 1054 (C-O-C). Solutions of spirocyan (7 mg in 1 mL),

NHS (2.2 mg in 1 mL) and EDC·HCl (3.3 mg in 1 mL) in DMF were added sequentially. The solution was stirred at room temperature for 10 min in order to activate the carboxylic groups and the sonicated deBoc f-SWNTs (40 mg in 60 mL of DMF) and pyridine (1.2 mL) were added. The reaction mixture was stirred at room temperature for 2 days under a nitrogen atmosphere. The product was collected as a black precipitate and was filtered through a Millipore system (on a 0.2 μm fluoropore FG filter). The residue was collected, dissolved in 10 mL of DMF and sonicated for 10 min. The f-SWNTs (**5**) were refiltered through Millipore system (on a 0.2 μm fluoropore FG filter) and washed with toluene, diethyl ether, dichloromethane and methanol to completely remove any unreacted products. The black solid was dried under vacuum overnight to afford 36 mg of spiropyran f-SWNT (**5**). **FT-IR** ν (cm^{-1}): 3265 (N-H), 2908, 2844 (C-H), 1732 (NH-CO), 1577, 1362 (NO_2), 1478 (C-C), 1520 (C=C), 1217, 1114, 1091 (C-O-C).

5.3 Experimental for Chapter 3

5.3.1 Materials. SWNTs produced by the HiPco technique were purchased from Unidym[®], Inc. (Lot no. R1912). Reagents and solvents were purchased as reagent-grade from Fisher Scientific Ireland Ltd, or Sigma-Aldrich Ireland and used without further purification.

5.3.2 NIR-PL measurements and efficiency calculation. NIR-Photoluminescence (NIR-PL) measurements were carried out on r-SWNTs, p-SWNTs, b-SWNTs, o-SWNTs [1], o-SWNTs [2], ob-SWNTs, f-SWNTs [1], f-SWNTs [2] and CCFs dispersed in aqueous sodium dodecylbenzene sulphonate (SDBS) ($[\text{SWNTs}]_i = 8 \times 10^{-2}$ mg/mL; $[\text{CCFs}]_i = 8 \times 10^{-2}$ mg/mL) at a SWNTs:SDBS and CCFs:SDBS weight ratio of 1:25. The dispersions were obtained by sonication (sonic tip and sonic bath) and the final pH of the dispersions was equal to the neutral value. The dispersions were then centrifuged at 4000 rpm (corresponding to $900 \times g$) for 90 min. NIR-PL studies were carried out in triplicate on supernatants in a L.O.T. ORIEL NS1 NanoSpectralyzer[®] (diode lasers; $\lambda_{\text{exc}} = 638$ nm, 683 nm and 785 nm) with an integration time of 1 second and 5 accumulations.

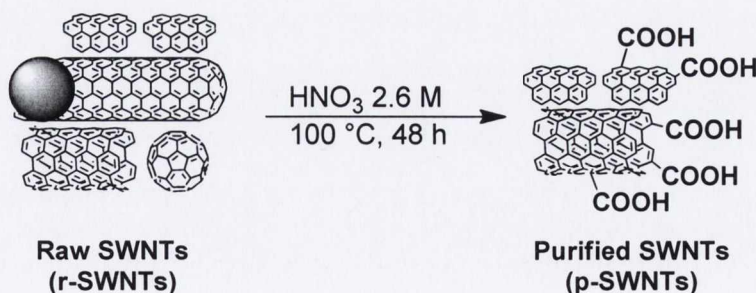
NIR-PL efficiency calculations: The NIR-PL transitions of SWNTs are strictly correlated with the specific (n,m) nanotube structure.^{6,7} Therefore, a quantitative comparison of the NIR emission based on the intensity of a specific NIR-PL band was not possible among SWNTs samples treated with different chemical procedures, which introduce defects on the nanotubes surface and may influence the sample (n,m) composition.

To allow a simple quantitative comparison of the NIR-PL intensity of the various SWNTs samples, their emission efficiency was therefore estimated. This value represents the spectrally integrated emission values adjusted to the fraction of excitation light absorbed by the sample. The emission efficiency was determined for the three λ_{exc} as follow:

$$\text{Emission efficiency} = \text{total emission power} / \text{absorption at } \lambda_{exc}$$

where the total emission power value corresponds to the integer of the total NIR emission spectrum. The term referring to the absorption at the selected λ_{exc} was included to avoid interference due to small differences in the SWNTs concentration of the samples. NIR-PL spectra were acquired three times for each sample to increase the significance of the estimation. The emission intensity was then calculated as average value ($n_{exp} = 3$) \pm standard deviation. The results are normalised on the emission efficiency of r-SWNTs.

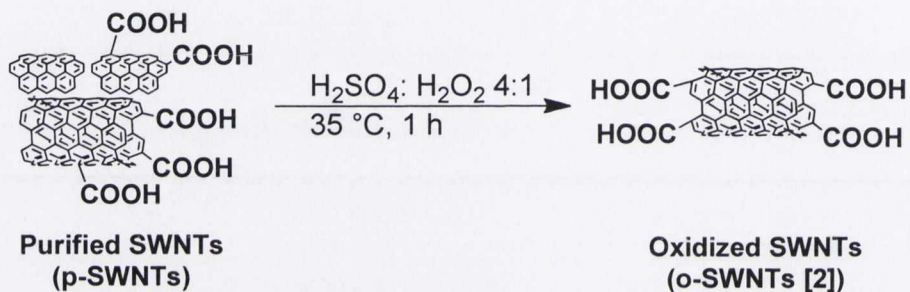
5.3.3 Preparation of purified single walled carbon nanotubes p-SWNTs



As received raw HiPco SWNTs (300 mg) were added to HNO_3 aqueous solution (2.6 M, 300 mL). The dispersion was stirred under reflux at 100 °C for 48 h.⁸⁻¹² After cooling down to room temperature the dispersion was filtered through a Millipore

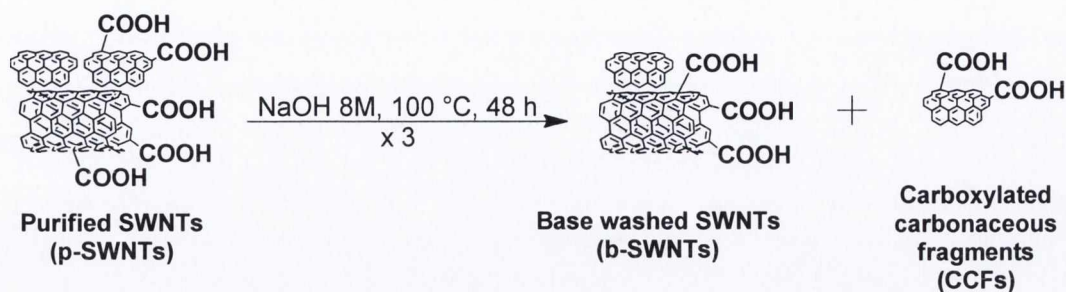
system (on a 0.2 μm Isopore filter) and the black solid on the filter was rinsed with distilled water (3 L, until the pH value of the filtrate was neutral). The tubes were subsequently removed from the filter (mud form), dispersed in DMF (100 mL), sonicated for 30 min and filtered on a 0.2 μm Millipore Fluoropore membrane. The residue was washed with DMF (500 mL) until the filtrate ran clear. The sample was resuspended in NMP (100 mL) and sonicated for 60 min and filtered on a new 0.2 μm Millipore Fluoropore membrane. After careful washing with NMP (100 mL), DMF (200 mL) and MeOH (200 mL) respectively, the sample was collected, dispersed in water (100 mL), sonicated for 60 min and freeze dried to obtain the p-SWNTs (270 mg).

5.3.4 Preparation of oxidized single walled carbon nanotubes o-SWNTs [2]



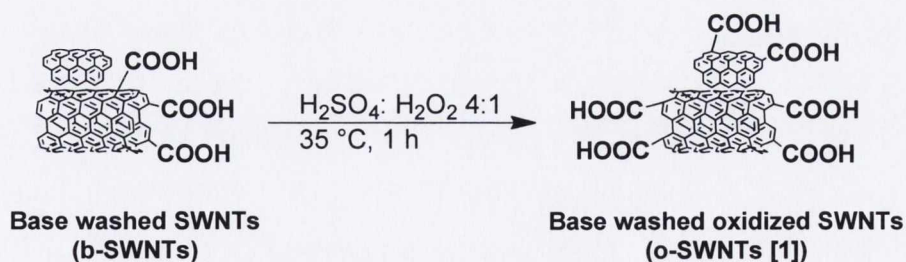
The p-SWNTs (100 mg) were added to distilled water (10 mL), sonicated for 20 min and stirred in piranha solution (H_2SO_4 conc : H_2O_2 (30%)) at a 4:1 ratio, 100 mL) at 35 $^\circ\text{C}$ for one hour. After cooling to room temperature and diluting with ice (500 g) a filtration through a Millipore system (on a 0.2 μm Isopore filter) was carried out. The residue was rinsed with distilled water (3.5 L, until the pH of the filtrate was neutral), removed from the filter before completely dry, dispersed in DMF (100 mL) and sonicated for 30 min. After the filtration through a 0.2 μm Fluoropore membrane the nanotubes were washed with DMF (300 mL) until the filtrate ran clear, removed from the membrane (mud form), suspended NMP (100 mL), sonicated for 60 min and filtered on a new 0.2 μm Millipore Fluoropore membrane. The sample was dispersed in NMP, dialyzed against water for 48 hours and subsequently freeze dried to afford the o-SWNTs [2] (40 mg). **FT-IR** ν (cm^{-1}): 3150 (O-H), 2907, 2880 (C-H), 1730 (C=O), 1580 (C=C), 1322 (C-O), 1237, 1220, 1155 (C-O-C), 1080 (C-O).

5.3.5 Preparation of base treated purified single walled carbon nanotubes b-SWNTs¹³



The nitric acid treated sample p-SWNTs (100 mg) was added to a NaOH solution (8 M, 100 mL) and sonicated for 30 min. The mixture was stirred at 100 °C for 48 h in a Teflon[®] container under nitrogen atmosphere. After cooling down to room temperature the nanotubes were isolated by filtration on a 0.2 μm Millipore Fluoropore membrane. The residue on the filter was washed with deionized water (3L) until neutral pH was reached. The brown filtrate was collected, neutralized with 0.1 M HCl, washed with water and concentrated under vacuum. The basic treatment was repeated two additional times on the residue left on the filter. The three neutralized filtrates were unified to afford CCFs (20 mg) and the residue was freeze dried to afford b-SWNTs (50mg). **FT-IR** ν (cm⁻¹): 3223 (O-H), 2957, 2871 (C-H), 1718 (C=O), 1570, 1498 (C=C) 1370 (C-H)

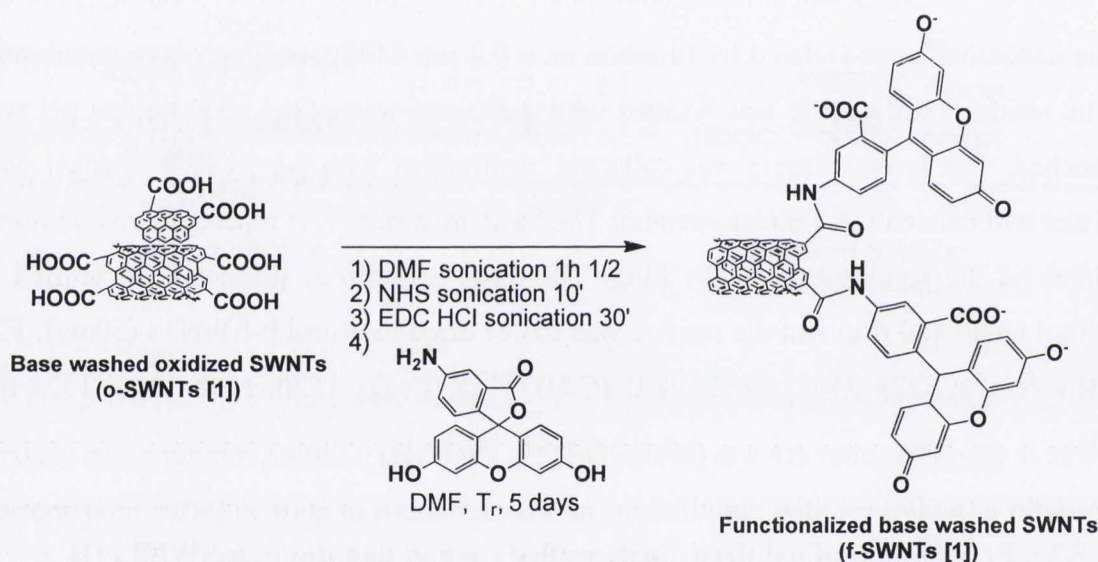
5.3.6 Preparation of oxidized single walled carbon nanotubes o-SWNTs [1]



The b-SWNTs (30 mg) were added to distilled water (3 mL), sonicated for 20 min and stirred in piranha solution (H_2SO_4 conc : H_2O_2 (30%) at a 4:1 ratio, 30 mL) at 35 °C for one hour. After cooling down and diluting the reacted nanotubes with ice (100 g) a filtration through a Millipore system (on a 0.2 μm Isopore filter) was carried out. The

residue was rinsed with distilled water (2 L, until the pH of the filtrate was neutral), removed from the filter before completely dry, dispersed in DMF (50 mL) and sonicated for 30 min. After the filtration on a 0.2 μm Fluoropore membrane the nanotubes were washed with DMF (200 mL) until the filtrate ran clear and finally with MeOH (200 mL). The sample dispersed in water was sonicated for 2 hours and freeze dried to afford the o-SWNTs [1] (21 mg). **FT-IR** ν (cm^{-1}): 3335 (O-H), 2907, 2868 2846 (C-H), 1724 (C=O), 1576 (C=C), 1363, 1312 (C-C), 1201, 1148 (C-O-C), 1052 (C-O).

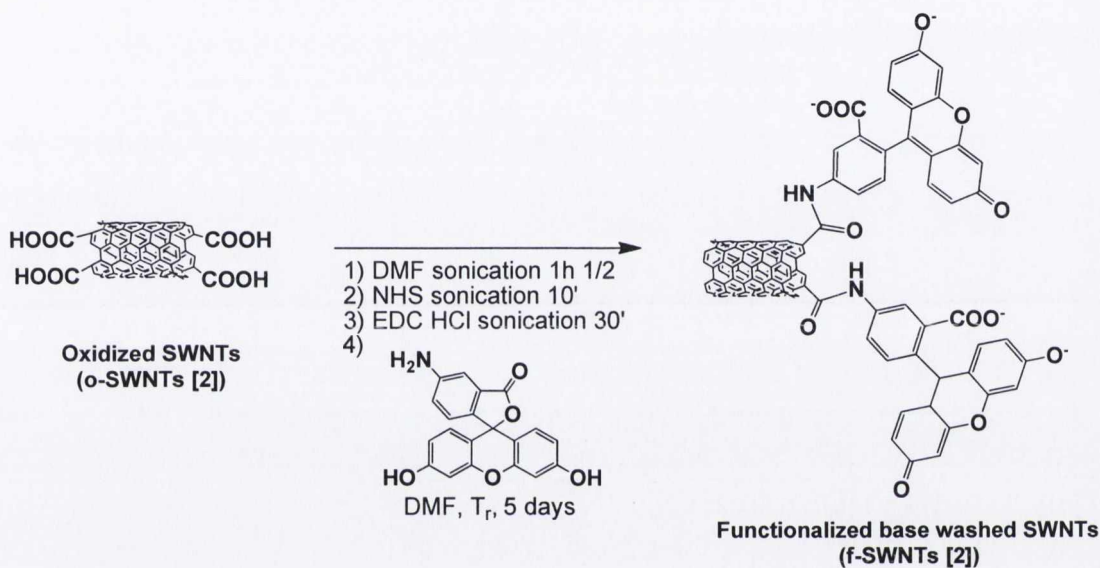
5.3.7 Preparation of fluorescein functionalized single walled carbon nanotubes f-SWNTs [1]



10 mg of o-SWNTs [1] were dispersed in DMF (30 mL) by sonication in a water bath for one hour and half. N-hydroxysuccinimide (NHS) (4 mg in 10 mL of DMF) was added and the dispersion was sonicated for another 10 min. 1-Ethyl-3-(3-dimethylaminopropyl)carbodiimide hydrochloride (EDC·HCl) (6 mg in 2 mL of DMF) was added to the dispersion and the sonication continued for an additional 30 min. The sample was subsequently added to fluoresceinamine isomer I (14 mg in 3 mL of DMF) and the reaction mixtures were stirred at room temperature for 3 days. The functionalized SWNTs [1] were collected as a black precipitate and filtered through Millipore system (on a 0.2 μm fluoropore FG filter). The black solid collected on the filter was washed with DMF (1 L), redissolved in DMF (50 mL), sonicated for 30 min

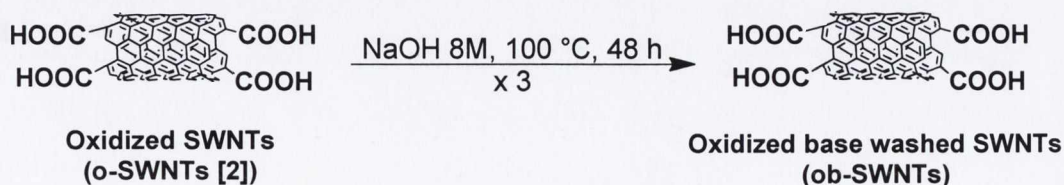
and filtered again on a new 0.2 μm fluoropore FG filter. The product was carefully washed with DMF (250 mL) and MeOH (250 mL) to remove the non-reacted starting material and dried under vacuum to afford 6.5 mg of f-SWNTs [1]. **FT-IR** ν (cm^{-1}): 3128 (O-H), 2911, 2843 (C-H), 1721 (C=O), 1571 (C=C), 1405 (O-H), 1201, 1212, 1147 (C-O-C).

5.3.8 Preparation of fluorescein functionalized single walled carbon nanotubes f-SWNTs [2]



10 mg of o-SWNTs [2] were functionalized using the same procedure as shown for fluorescein functionalized single walled carbon nanotubes (f-SWNTs [1]), affording 9 mg of f-SWNTs [2]. **FT-IR** ν (cm^{-1}): 3179 (O-H), 2914, 2844 (C-H), 1732 (C=O), 1571 (C=C), 1437 (O-H), 1211, 1154, 1030 (C-O-C).

5.3.9 Preparation of base treated oxidized single walled carbon nanotubes ob-SWNTs

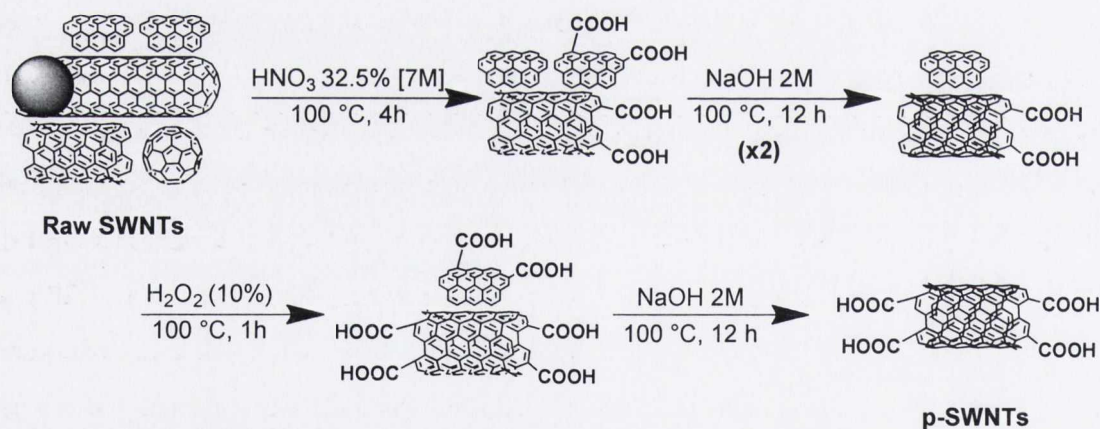


A small amount of oxidized sample o-SWNTs [2] (8 mg) was added to a NaOH solution (8 M, 100 mL) and sonicated for 30 min. The mixture was stirred at 100 °C for 48 h in a Teflon[®] container under nitrogen atmosphere. After cooling down to room temperature the nanotubes were isolated by filtration on a 0.2 µm Millipore Fluoropore membrane. The residue on the filter was washed with deionized water until neutral pH was reached, and dried under vacuum to afford the base treated oxidized ob-SWNTs (8 mg). **FT-IR** ν (cm⁻¹): 3178 (O-H), 2953, 2915, 2845 (C-H), 1722 (C=O), 1570 (C=C), 1359 (C-O), 1219, 1183 (C-O-C), 1052 (C-O).

5.4 Experimental for Chapter 4

5.4.1 Materials. SWNTs produced by the HiPco technique were purchased from Unidym[®], Inc. (Lot no. R0513). Reagents and solvents were purchased as reagent-grade from Fisher Scientific Ireland Ltd, or Sigma-Aldrich Ireland and used without further purification.

5.4.2 Preparation of purified single walled carbon nanotubes p-SWNTs



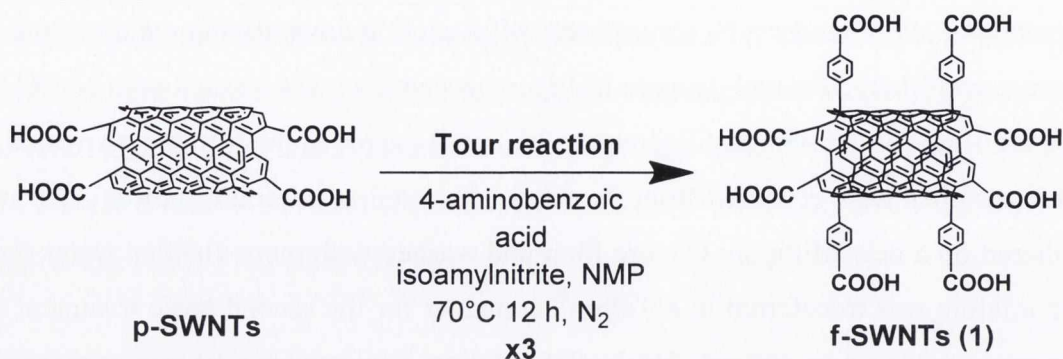
As received raw HiPco SWNTs (200 mg, 1.64 of wet cake) were added to HNO_3 aqueous solution (32.5%, 800 mL), the dispersion was sonicated for 15 min at variable powers and stirred at 100°C for 4 hours. After quenching with ice (1 Kg) the mixture was filtered through Millipore system (on a 0.2 µm Isopore filter) and the black solid on the filter was washed with a copious amount of distilled water (6 L, until the pH of the filtrate was neutral). The tubes were subsequently removed from the filter (mud form), dispersed in distilled water (250 mL), sonicated for 5 min, filtered on a new 0.2 µm

Millipore Isopore membrane and washed with distilled water (2L). The mixture was transferred to a Teflon[®] container and was made up to 400 mL 2M NaOH solution (32g NaOH). The dispersion was sonicated for 10 min at maximum power and stirred overnight at 100°C under a N₂ atmosphere. After cooling down to room temperature the mixture was filtered through Isopore Millipore system and was washed with NaOH 2M (400 mL) and further with distilled water (3 L) until the pH of the filtrate was neutral.

The nanotubes were removed from the filter, sonicated at minimum power for 5 min, refiltered on a new Millipore Isopore filter and washed with more distilled water (1 L). The mixture was transferred to a Teflon[®] container for the second basic treatment and was again made up to 400 mL 2M NaOH solution, sonicated for 10 min at maximum power and stirred overnight at 100°C under a N₂ atmosphere. After cooling down to room temperature the dispersion was filtered, washed with NaOH 2M (400 mL) and further with distilled water until the pH of the filtrate was neutral (3 L).

The nanotubes were collected (wet cake), transferred to a round bottom flask and added of H₂O₂ 10% (400 mL). After sonication for 15 min at variable powers the mixture was stirred at 100°C for 1 hour. It was subsequently quenched with ice, filtered through a Millipore Isopore filter and washed with distilled water (1 L). The residue left on the filter was dispersed in water, sonicated for 5 min at full power, refiltered on a new Millipore filter and washed with distilled water (1 L). The nanotubes were transferred to a Teflon container and were made up to 400 mL 2M NaOH solution. The dispersion was sonicated for 10 min at maximum power and stirred overnight at 100°C under a N₂ atmosphere. After cooling down to room temperature, the solution was again filtered, washed with NaOH 2M (400 mL) and further with distilled water (2L) until the pH of the filtrate was neutral. The mixture was sonicated, filtered on new Millipore filters and washed with distilled water for two additional times. Finally the nanotubes were added of HCl 3.5% (400 mL) and rinsed with distilled water (2 L). The sample was collected, dispersed in water (100 mL), sonicated for half an hour and freeze dried to obtain the purified p-SWNTs (84.5 mg). **FT-IR** ν (cm⁻¹): 3357 (O-H), 2967, 2934, 2878 (C-H), 1743, 1626 (C=O), 1567 (C=C), 1369 (C-C).

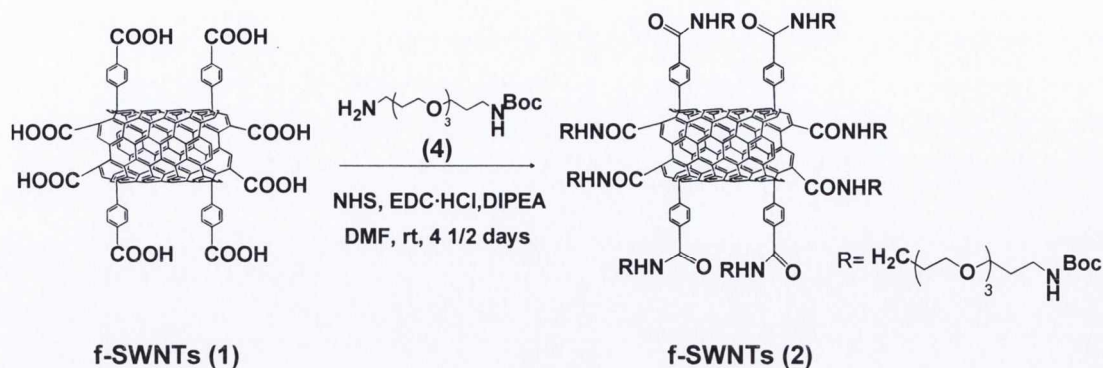
5.4.3 Preparation of benzoic acid functionalized single walled carbon nanotubes f-SWNTs (1)



60 mg of p-SWNTs were dispersed in NMP (250 mL) by sonication at full power for 30 min. Following addition of p-aminobenzoic acid (1.37 g, 0.01 moles, 2 equiv) the mixture was sonicated at full power for additional 15 min. Isoamyl nitrite (2 mL, 0.015 moles, 3 equiv) was added and the mixture was stirred at 70°C overnight under nitrogen atmosphere. After cooling down to room temperature, the nanotubes were filtered through a 0.2 μm Millipore Fluoropore filter and washed with NMP (300 mL). The latter procedure was repeated three times.

The nanotube mixture was finally filtered through a 0.2 μm Millipore Fluoropore filter and rinsed with NMP (300 mL) and DMF (400 mL). The residue was collected, dispersed in DMF (100 mL), sonicated at full power for 20 min and filter on a new Millipore filter. The residue was finally washed with MeOH (500 mL) and dried under vacuum to afford the benzoic acid functionalized f-SWNTs (**1**) (75.5 mg). **FT-IR** ν (cm^{-1}): 3305 (O-H), 2958, 2920, 2851 (C-H), 1699 (C=O), 1572, 1539 (C=C), 1378 (O-H), 1401, 1314 (C-C), 1205 (C-O-C), 1151 (C-O).

5.4.4 Preparation of PEG functionalized single walled carbon nanotubes f-SWNTs (2)

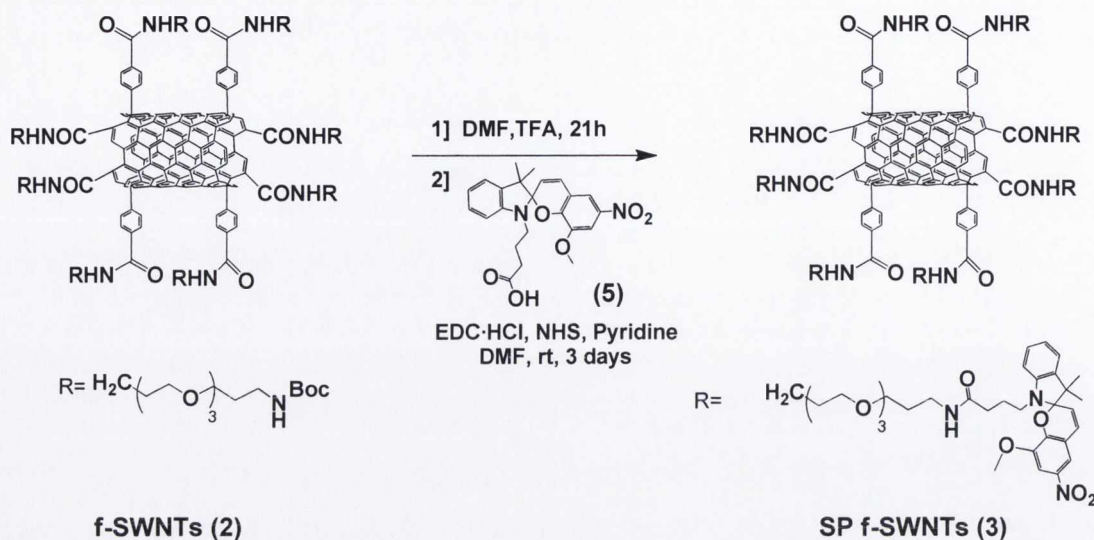


40 mg of f-SWNTs (1) were dispersed in DMF (100 mL) by sonication at full power for 90 min. After cooling down in ice bath, the nanotube solution was added of 1-Ethyl-3-(3-dimethylaminopropyl)carbodiimide hydrochloride (EDC·HCl) (49 mg in 10 mL of DMF) and sonicated for additional 45 min in sonic bath. The mixture was subsequently stirred in ice bath for 30 min in order to activate the COOH groups. N-hydroxysuccinimide (NHS) (32 mg in 10 mL of DMF) was added and the dispersion was sonicated for another 30 min and cooled down in ice bath.

89 mg of tert-Butyl 3-(2-(2-(3-aminopropoxy)ethoxy)ethoxy) propylcarbamate (4) were dissolved in DMF (10 mL) and added to the mixture in small excess. After the addition of *N,N*-Diisopropylethylamine (DIPEA) (100 μL) the nanotube mixture was stirred at room temperature for 4 and half days.

The functionalized nanotubes were collected as a black precipitate and filtered through a Millipore system (0.2 μm Fluoropore FG filter). The solid was washed with DMF (600 mL) and was then re-dispersed in DMF (100 mL) by sonication in sonic bath at full power for 20 min. The material was filtered on a new Millipore FG filter and washed with DMF (500 mL) and MeOH (500 mL). The residue was dried under vacuum to afford f-SWNTs (2) (42.4 mg). **FT-IR** ν (cm^{-1}): 3287 (N-H), 2916, 2849 (C-H), 1688, 1642 (C=O), 1587, 1530, 1443 (C=C), 1364 (C-O), 1213, 1158 (C-O-C).

5.4.5 Preparation of spiropyran functionalized single walled carbon nanotubes f-SWNTs (3)



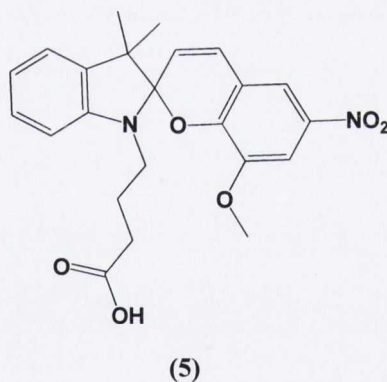
A 37.5 mg quantity of previously obtained f-SWNTs (2) was dispersed in DMF (400 mL) and sonicated in sonic bath at full power for 120 min. A 3 mL aliquot of trifluoroacetic acid (TFA) was added and the mixture was stirred at room temperature for 21 h. The black product was filtered through a Millipore system (on a 0.2 μm fluoropore FG filter), washed with DMF (150 mL) and quenched with triethylamine (3 mL). The residue on the filter was collected, re-dispersed in DMF (100 mL) and sonicated in sonic bath for 10 min. The dispersion was filtered again through a new 0.2 μm Millipore Fluoropore filter. The filtered off solution was brown and, to ensure that no nanotubes passed through the filter, the filtering procedure was repeated 3 times. This still resulted in a brown filtrate due to the high quantity of carbonaceous material removed from the sample. The functionalized nanotubes left on the filter were washed with DMF (150 mL), toluene (50 mL), Et₂O (50 mL), CH₂Cl₂ (50 mL) and MeOH (250 mL). The sample was dried under reduced pressure to afford 33.7 mg of Boc deprotected f-SWNTs. **FT-IR** ν (cm⁻¹): 3332, 3281 (N-H), 2905, 2864 (C-H), 1687, 1648 (C=O), 1590, 1526, 1498, 1446 (C=C), 1364 (C-O), 1204, 1158 (C-O-C).

10 mg of the spiropyran (SP, 5) were dispersed in dry DMF (20 mL), added of EDC·HCl (4.8 mg) and stirred in ice bath for 10 min under a N₂ atmosphere, until the activated ester was formed (motored by TLC in hexane/EtOAc 2:8). NHS (5 mg) and

pyridine (~ 1 mL) were added and the mixture was stirred in ice bath for 1 h under a N₂ atmosphere.

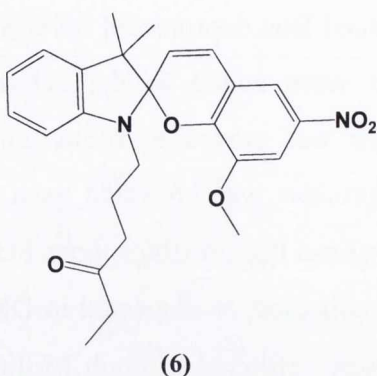
30 mg of previously obtained Boc deprotected f-SWNTs were sonicated in dry DMF (100 mL) for 5 min, and were added to the activated spiropyran solution. The spiropyran-nanotube mixture was stirred at room temperature for 3 days under a nitrogen atmosphere. The product was collected as a black precipitate, was filtered through a Millipore system (on a 0.2 μm fluoropore FG filter) and washed with DMF (300 mL). The residue was collected, re-dispersed in DMF (100 mL) and sonicated for 2 min. The f-SWNTs (**3**) were refiltered through Millipore system (on a new 0.2 μm fluoropore FG filter) and washed with DMF (150 mL), toluene (100 mL), Et₂O (100 mL), CH₂Cl₂ (300 mL) and MeOH (200 mL) to completely remove any unreacted products. The black solid was dried under reduced pressure to afford 29 mg of SP f-SWNT (**3**). **FT-IR** ν (cm⁻¹): 3285, 3120 (N-H), 2917, 2866 (C-H), 1646 (C=O), 1553, 1367 (NO₂), 1565, 1447 (C=C), 1311, 1225, 1150 (C-O-C).

5.4.6 Preparation of SP (**5**)



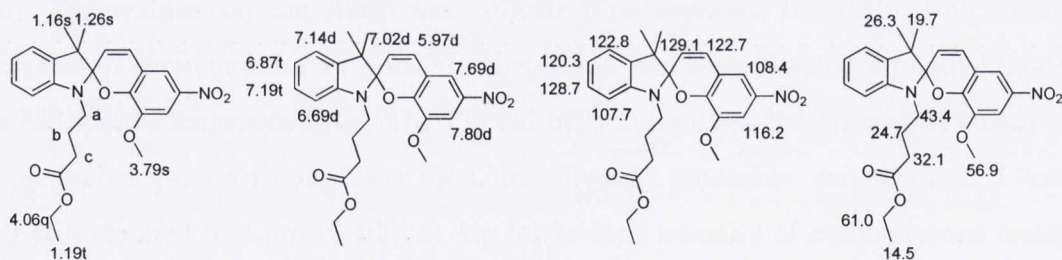
The spiropyran 4-(8-methoxy-3',3'-dimethyl-6-nitrospiro[chromene-2,2'-indolin]-1'-yl)butanoic acid (**5**) was synthesized by Manuel Natali according to the literature procedure previously reported.¹⁴

5.4.7 Characterization SP (6)

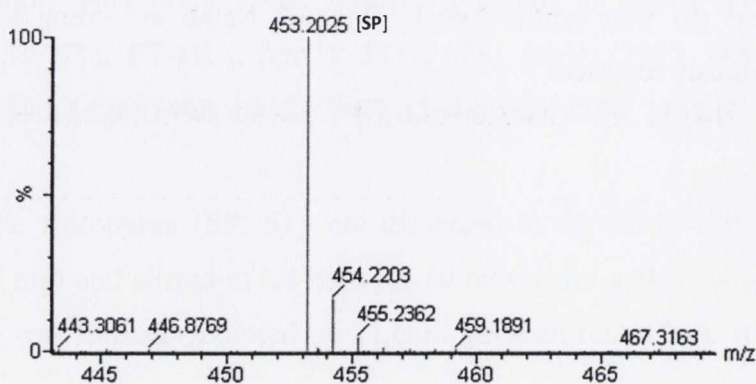


$^1\text{H-NMR}$ (600 MHz, CD_3CN): δ = 1.16 (s, 3H, CH_3), 1.19 (t, 3H, J = 7.2 Hz, CH_3), 1.26 (s, 3H, CH_3), 1.84-1.86 (m, 1H, CH_2), 2.07-2.09 (m, 1H, CH_2), 2.31-2.35 (m, 2H, CH_2CO), 3.17-3.32 (m, 2H, CH_2N), 3.79 (s, 3H, OCH_3), 4.06 (q, 2H, J = 7.1 Hz and 14.1 Hz, CH_2), 5.97 (d, 1H, J = 10.4 Hz, CH), 6.69 (d, 1H, J = 7.8 Hz, arom.), 6.87 (t, 1H, J = 7.2 Hz arom.), 7.02 (d, 1H, J = 10.4 Hz, CH), 7.14 (d, 1H, J = 6.7 Hz arom.), 7.19 (t, 1H, J = 7.0 Hz, arom), 7.69 (d, 1H, J = 2.3 Hz, arom), 7.80 (d, 1H, J = 2.6 Hz, arom).

$^{13}\text{C-NMR}$ (150 MHz, CD_3CN): δ = 14.5, 19.7, 24.7, 26.3, 32.1, 43.4, 53.3, 56.9, 57.8, 59.4, 61.0, 107.7, 107.9, 108.4, 116.2, 119.6, 120.3, 122.7, 122.8, 128.7, 129.1, 137.0, 148.0, 149.9, 173.8.



HRMS (m/z -ES): Found: 453.2025 (M^+ , $\text{C}_{25}\text{H}_{28}\text{N}_2\text{O}_6$ Requires: 452.1947)



5.4.8 NMR studies. Proton Nuclear Magnetic Resonance spectra were recorded on a Bruker Avance II 600MHz NMR Spectrometer with a 5mm TCI cryoprobe operating at 600.13 MHz for proton and 150.62 MHz for carbon. The solvents (CD₃CN and d-DMSO) were standardized with respect to TMS. Chemical shifts are reported in ppm and coupling constants in Hertz. Standard solutions of zinc chloride (0.442 M) were prepared in D₂O. An aliquot of this solution (10 µl) was added to 990 µl of spiropyran solution 4.42 x10⁻³ M in CD₃CN. Another aliquot of the zinc solution (10 µl) was added to 980 µl of spiropyran solution 4.42 x10⁻³ M in CD₃CN, and 10 µl acetylsalicylic acid solution 0.1M in CD₃CN. All the samples were irradiated with UV light (long wavelength) for 5 min, equilibrated overnight at room temperature in the dark, and afterwards the spectra were collected.

5.4.9 Mass spectrometry. MALDI-TOF MS spectra were acquired using a Waters MALDI-Q TOF Premier spectrometer. The instrument was operated in positive or negative reflectron mode as required. The laser operated at 337 nm. Samples were run using DCTB *trans*-2[3(4-*tert*-Butylphenyl)-2-methyl-2-propenylidene]malononitrile as a MalDI matrix dissolved in DCM (2 mg/ml). Matrix solutions were mixed with complex solutions with ratio 1:1 and 1 µl of the resulting mixture was spotted on the MALDI plate and allowed to dry. The machine was calibrated using PEG. The internal lock mass used was [Glu¹] Fibrinopeptide B, 1570, 6774 m/z (M+H)⁺. MassLynx 4.1 software was used to carry out post run analysis.

ESI mass spectra were acquired using a Micromass time of flight mass spectrometer (TOF) interfaced to a Waters 2690 HPLC. The instrument was operated in positive or negative mode as required. Leucine Enkephalin was used as an internal lock mass. Mass were recorded over the range 100-1000 m/z. Operating conditions were as follows: ESI capillary voltage 2500V, cone voltage 25V, desolvation temperature 200° C, source temperature 100°C. The ESI gas was nitrogen. MassLynx 4.0 software was used to carry out the analysis.

All samples consisted of CD₃CN dilution of that used for NMR analyses.

5.4.10 Dispersion of SP f-SWNTs (3). Dry powder SP f-SWNTs (3) was weighted and added to sterile DMSO at a concentration of 0.1 mg/mL (stock solution). Stock solution was sonicated (sonic bath, 4h). 9 mL of RPMI 1640 cell media (supplemented with 2 mM L-glutamine, 10% foetal bovine serum (FBS) and 10 mg/ml penicillin-streptomycin) was mixed with 1 mL of stock solution, thus obtaining a final SWNTs concentration of 10 µg/mL (done by Dania Movia).

5.4.11 Cell culture. Human monocytic leukemia (THP-1) cells were obtained from the American Tissue Culture Collection (ATCC). Briefly, THP-1 cells were cultured in suspension in modified RPMI 1640 media (supplemented with 2 mM L-glutamine, 10% foetal bovine serum (FBS) and 10 mg/ml penicillin-streptomycin) and incubated at 37 °C and 5% CO₂. At 60% confluence, cells were diluted in modified RPMI 1640 media at concentrations appropriate for experimental procedure. The passage number was restricted between five and fifteen (done by Dania Movia).

5.4.13 Incubation with SP f-SWNTs (3) dispersions. THP-1 cells were seeded on glass cover slips in 24-well plates and activated with phorbol-12-myristate-13-acetate (PMA) (Sigma-Aldrich, USA) for 72 h to induce differentiation into adherent macrophages and stop their natural proliferation. After removing the cell media, adherent THP-1 cells were exposed to SP f-SWNTs (3) dispersions in supplemented RPMI 1640 cell media. After 24 h incubation cells were carefully recovered from the wells and placed on a HistoBond microscope slide (RA Lamb, UK). Samples were then fixed with 90% ethanol and subsequently rinsed with saline. F-actin was labeled by adding 2U/mL of Phalloidin-Alexa 546 conjugate (Invitrogen, UK). The slides were incubated at room temperature in the dark for 30 min, rinsed with saline and mounted in Vectashield (Vector, UK) prior to epifluorescence and confocal microscopy. Specimens were examined with an Olympus BX51M reflection epi-fluorescence microscope equipped with standard PC and the Cell-D image acquisition/processing software (Soft Imaging System, SIS, GmbH) (done by Dania Movia).

References

- (1) Kaiser, E.; Colescot, R. I.; Bossinger, C. D.; Cook, P. I. *Analytical Biochemistry* **1970**, *34*, 595.
- (2) Sarin, V. K.; Kent, S. B. H.; Tam, J. P.; Merrifield, R. B. *Analytical Biochemistry* **1981**, *117*, 147.
- (3) Fontenot, J. D.; Ball, J. M.; Miller, M. A.; David, C. M.; Montelaro, R. C. *Peptide Research* **1991**, *4*, 19.
- (4) Quintana, M.; Prato, M. *Chemical Communications* **2009**, 6005.
- (5) Aakeroy, C. B.; Hurley, E. P.; Desper, J.; Natali, M.; Douglawi, A.; Giordani, S. *CrystEngComm* **2010**, *12*, 1027.
- (6) Weisman, R. B.; Bachilo, S. M. *Nano Letters* **2003**, *3*, 1235.
- (7) Bachilo, S. M.; Strano, M. S.; Kittrell, C.; Hauge, R. H.; Smalley, R. E.; Weisman, R. B. *Science* **2002**, *298*, 2361.
- (8) Giordani, S.; Colomer, J. F.; Cattaruzza, F.; Alfonsi, J.; Meneghetti, M.; Prato, M.; Bonifazi, D. *Carbon* **2009**, *49*, 578.
- (9) Del Canto, E.; Flavin, K.; Natali, M.; Perova, T.; Giordani, S. *Carbon* **2010**, *48*, 2815.
- (10) Movia, D.; Del Canto, E.; Giordani, S. *Physica Status Solidi B-Basic Solid State Physics* **2009**, *246*, 2704.
- (11) Movia, D.; Del Canto, E.; Giordani, S. *The Journal of Physical Chemistry C* **2010**, *114*, 18407.
- (12) Bonifazi, D.; Nacci, C.; Marega, R.; Campidelli, S.; Ceballos, G.; Modesti, S.; Meneghetti, M.; Prato, M. *Nano Letters* **2006**, *6*, 1408.
- (13) Salzmann, C. G.; Llewellyn, S. A.; Tobias, G.; Ward, M. A. H.; Huh, Y.; Green, M. L. H. *Advanced Materials* **2007**, *19*, 883.
- (14) Natali, M.; Aakeroy, C.; Desper, J.; Giordani, S. *Dalton Transactions* **2010**, *39*, 8269.

Chapter 6. Conclusions and Future Work



6.1 Conclusions

In this research project we have designed, synthesized and fully characterized novel smart multifunctional nanodevices composed of spiropyrans and SWNTs. The preservation of the switchability of the photochromic dye between its two isomeric forms has been explored when anchored to the nanotube scaffold, as a first step toward the assembly of more complex devices for potential sensing and bio applications.

The achievements of the presented studies can be listed as follows:

- first example of a continuous on-off switching of a SP-SWNT material in solution;
- evidence that following two different washing strategies (NaOH or solvents) the final shortened covalently functionalized SWNT materials look close to identical in both their appearance and sustained electronic properties;
- first example of uptake and release of Zn^{2+} ions from a SP receptor covalently attached to SWNT vectors controllable by Vis light irradiation;
- detection of the spontaneous assembly of SP photoactive molecules, zinc metal ions and acetylsalicylic acid into a ME-Zn-ASA ternary complex when concomitantly in solution;
- evidence of the Vis light controlled release of antiinflammatory agent (Zn^{2+} and ASA) from the photoactive receptor offering the first example of SP-based DDS.

We strongly believe that our research should open new opportunities in the design and development of novel SWNT-based composite for drug delivery applications, where the bioactive payloads vehicled intracellularly by the tubes can explicate their action following visible light impulses.

6.2 Future work

The production of a drug delivery system that is nanometric in size, that easily penetrates the cell membrane and is biocompatible, that specifically binds to receptors expressed in target cells, and that releases the transported drugs *in situ* in response to an external stimulus, will be of particular importance in the near future. The light responsive DDS proposed in this thesis, where anti-inflammatory Zn^{2+} and aspirin demonstrated to be released by means of Vis radiation from SP derivative, can be regarded as a good candidate especially when covalently anchored to SWNT carriers enriched with specific receptor binding units.

Among the bioactive molecules envisaged as potentially deliverable by the reported SP f-SWNTs nanovector, we will next consider the neurotransmitter GABA (γ -aminobutyric acid), some essential amino acids (AA) like glycine, tryptophan, tyrosine, cysteine and 5-hydroxytryptophan, and finally the AA derivative L-DOPA. They have been specifically chosen for their similarity in structure bearing common functional groups ($-COOH$, $-NH_2$), and because they have shown to be involved in the control of a number of pathologies ranging from hypertension to cancer, and neurological diseases like Alzheimer and Parkinson.

AAs are good candidates, as they have shown good affinity for both SP derivatives and ME-metal complexes. By following the same chemical and analytical approach reported in chapter 4, we aim to create light controllable ME-Zn-AA ternary complexes (Figure 6.1) and to exploit SWNTs transport properties to deliver the bioactive molecules to target cells.

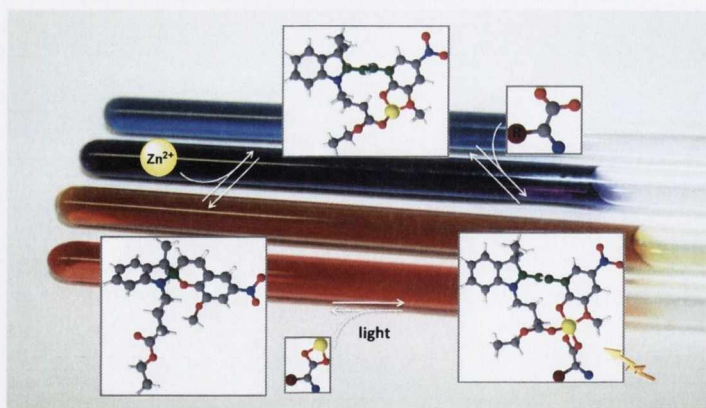


Figure 6.1: Pictorial representation of the light modulated cycle of chelation and release of Zn^{2+} and AA by a SP-based receptor.

Chapter 7. Appendix



7.1 Appendix for Chapter 3

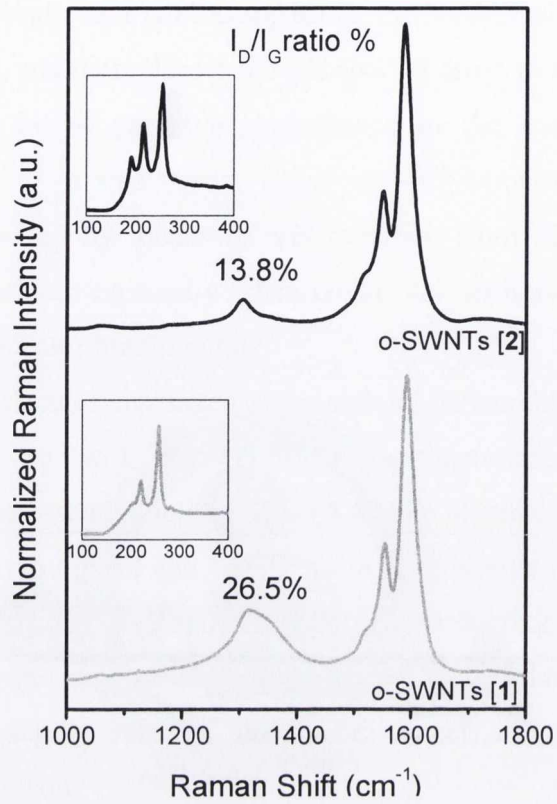


Figure 3.1a: Raman spectra ($\lambda_{\text{exc}} = 633 \text{ nm}$) of o-SWNTs [1] and o-SWNTs [2]. Spectra have been normalized on the G-band. The insets show RBMs enlargement (scale: 0-0.25 a.u.).

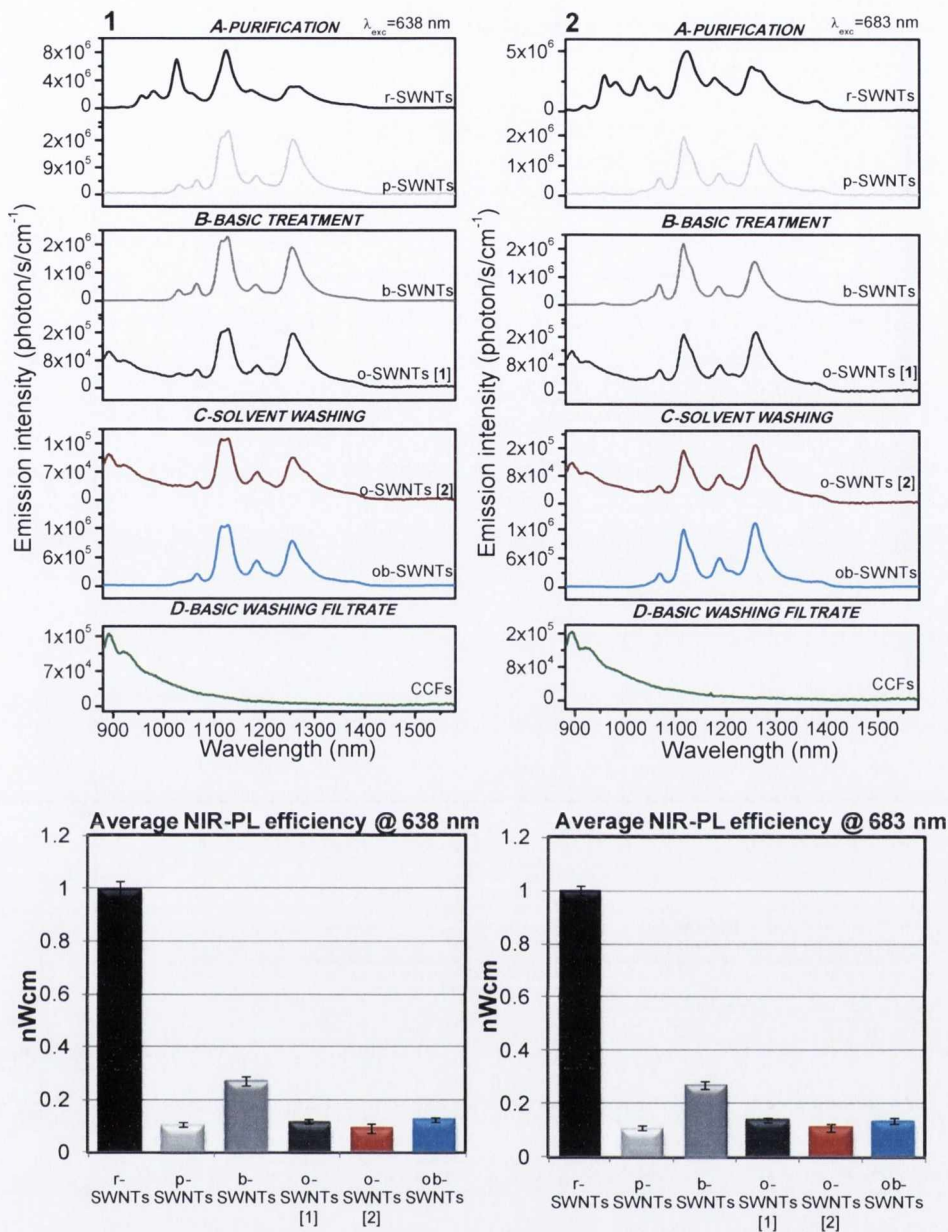


Figure 3.2a: NIR photoluminescence (PL) spectra of r-SWNTs, p-SWNTs, b-SWNTs, o-SWNTs [1], o-SWNTs [2], ob-SWNTs and CCFs. ($[SWNTs]_i = 8 \times 10^{-2}$ mg/mL; $[CCFs]_i = 8 \times 10^{-2}$ mg/mL; SWNTs:SDBS weight ratio = 1:25; CCFs: SDBS weight ratio = 1 :25). 1] $\lambda_{exc} = 638$ nm 2] $\lambda_{exc} = 683$ nm. On the bottom, histograms showing the average NIR-PL efficiency at $\lambda_{exc} = 638$ nm and $\lambda_{exc} = 683$ nm ($n_{measurements} = 3$).

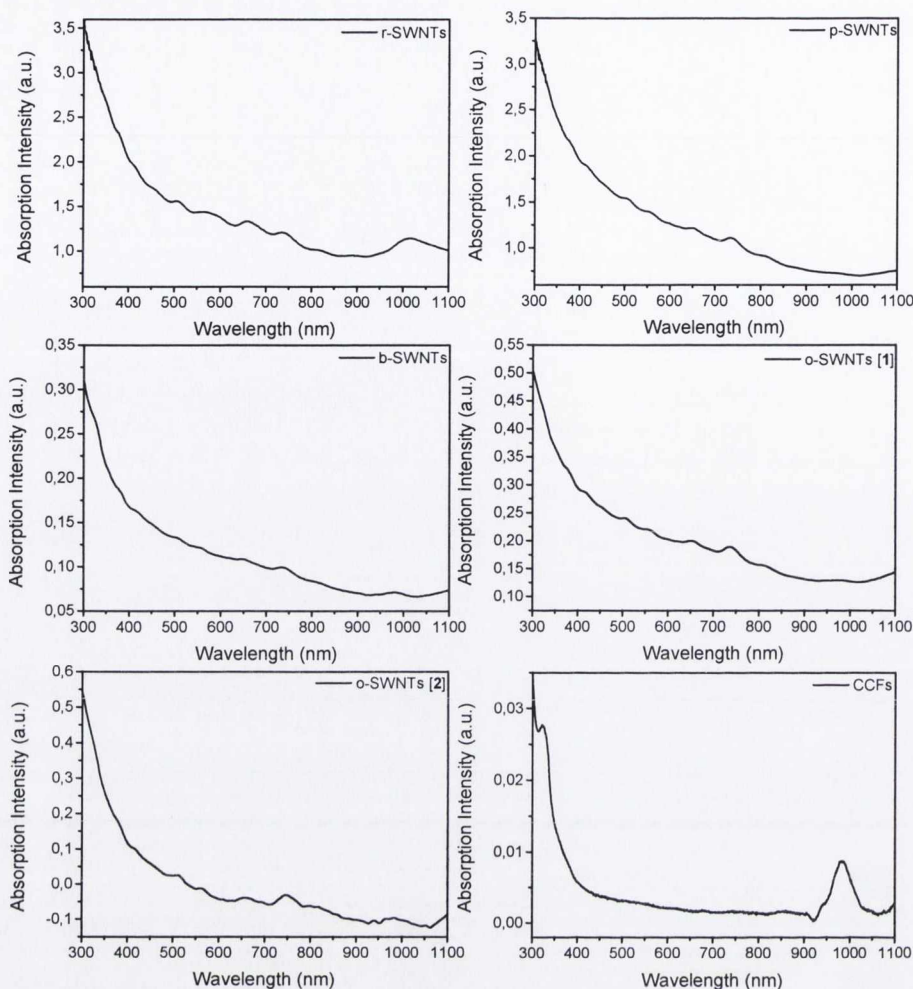


Figure 3.3a: UV-Vis/NIR absorption profiles of r-SWNTs, p-SWNTs, b-SWNTs, o-SWNTs [1], o-SWNTs [2] and CCFs. [SWNTs]_i = 1×10^{-1} mg/mL DMF. Spectra with actual absorption intensity values are reported.

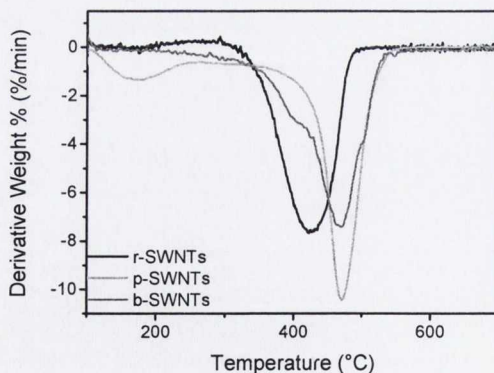


Figure 3.4a: TGA first derivative traces of r-SWNTs, p-SWNTs and b-SWNTs performed in air atmosphere. The shift of the graphitic decomposition temperature to higher values going from raw to p-SWNTs is indicative of the increasing purity of the material.

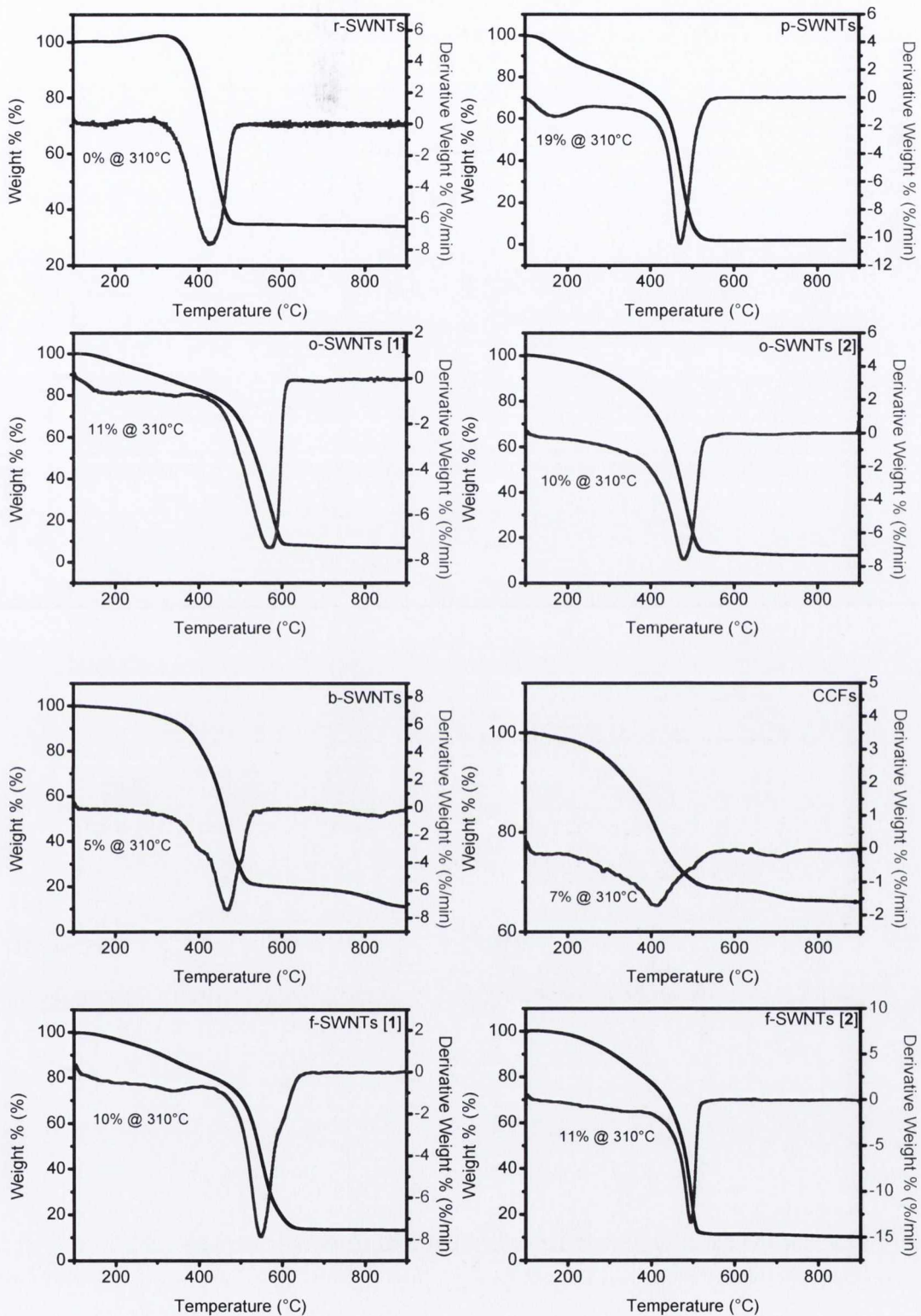


Figure 3.5a: TGA traces of r-SWNTs, p-SWNTs, b-SWNTs, CCFs, o-SWNTs [1] and [2], f-SWNTs [1] and [2]. The weight losses % at 310 °C attributed to the decomposition of organic groups in the nanotube samples are reported. All the experiments have been run in air atmosphere with a temperature rate of 10 °C min⁻¹.

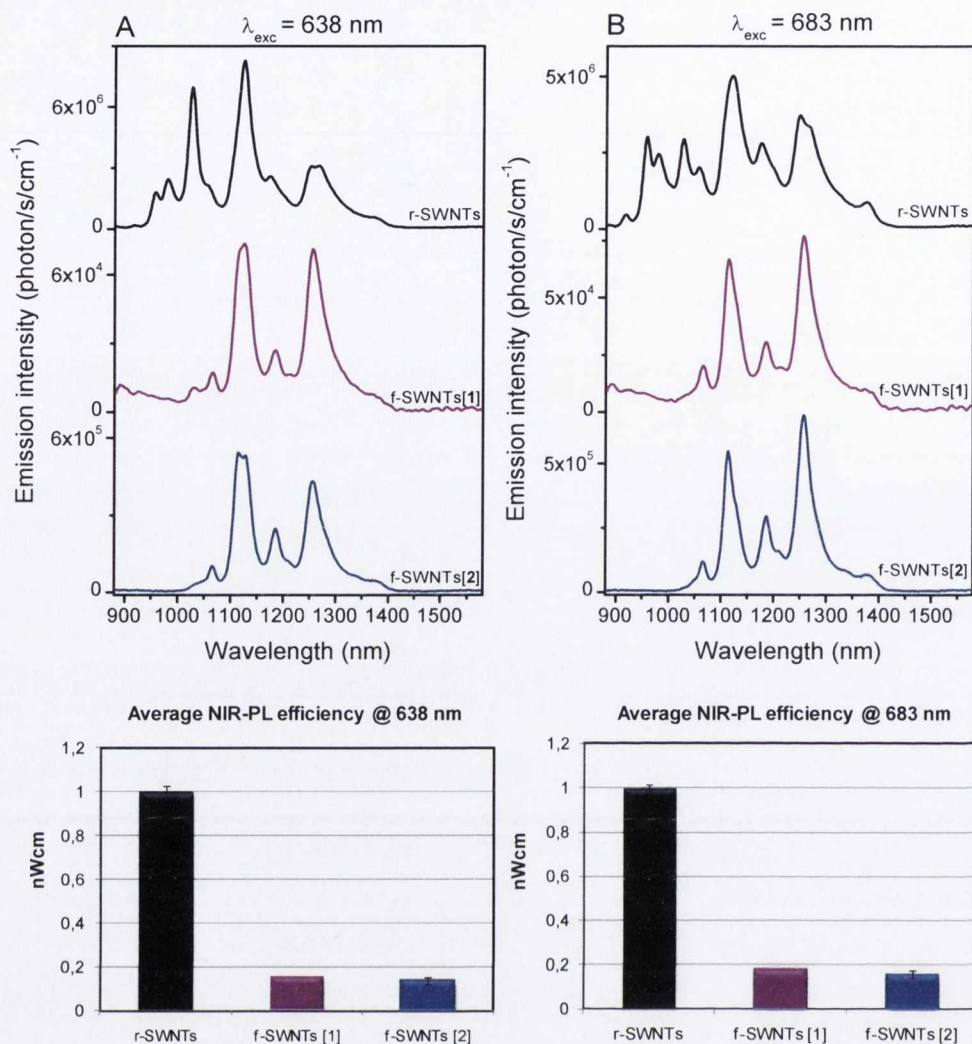


Figure 3.6a: NIR photoluminescence (PL) spectra of f-SWNTs [1] and f-SWNTs [2]. ([SWNTs]_i = 8×10^{-2} mg/mL; SWNTs:SDBS weight ratio = 1:25). A] $\lambda_{exc} = 638 \text{ nm}$ B] $\lambda_{exc} = 683 \text{ nm}$. On the bottom, histograms showing the average NIR-PL efficiency at $\lambda_{exc} = 638 \text{ nm}$ and $\lambda_{exc} = 683 \text{ nm}$ ($n_{\text{measurements}} = 3$).

7.2 Appendix for Chapter 4

The amine loading was calculated from the equation:

$$\frac{\mu\text{mol}}{\text{g}} = \frac{[\text{Abs sample} - \text{Abs blank}] \cdot \text{dilution (ml)} \cdot 10^6}{\text{extinction coeff.} \cdot \text{sample weight (mg)}}$$

where the extinction coefficient, also known as molar absorptivity, represents how efficiently a chemical species absorbs light at a given wavelength. For CNTs this coefficient has a value of $15000 \text{ M}^{-1} \text{ cm}^{-1}$. The amine loading was calculated as $383 \mu\text{mol/g}$ of material for TFA treated f-SWNTs and as $134 \mu\text{mol/g}$ for SP f-SWNTs (3), therefore the difference of $249 \mu\text{mol/g}$ constituted the amino groups that reacted with the SP derivative. SP loading: $249 \mu\text{mol/g} \times 424.45 \mu\text{g}/\mu\text{mol} = 105.7 \mu\text{g SP/mg SWNTs}$.

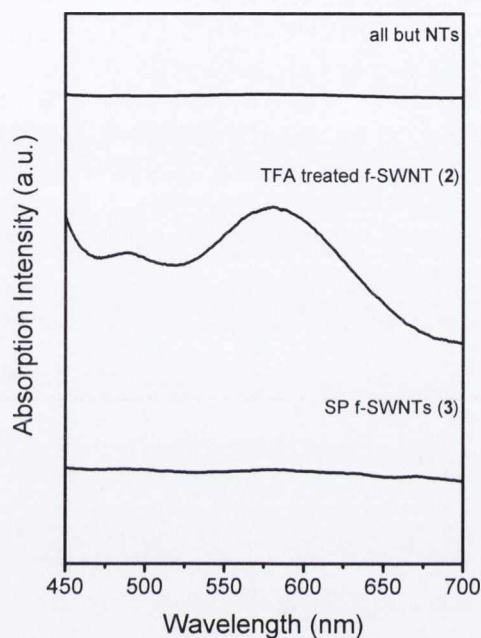


Figure 4.1a: UV-Vis absorption profiles of TFA treated f-SWNTs (2) and SP f-SWNTs (3) compared with a blank solution (all but nanotubes) which has been treated in the same way.

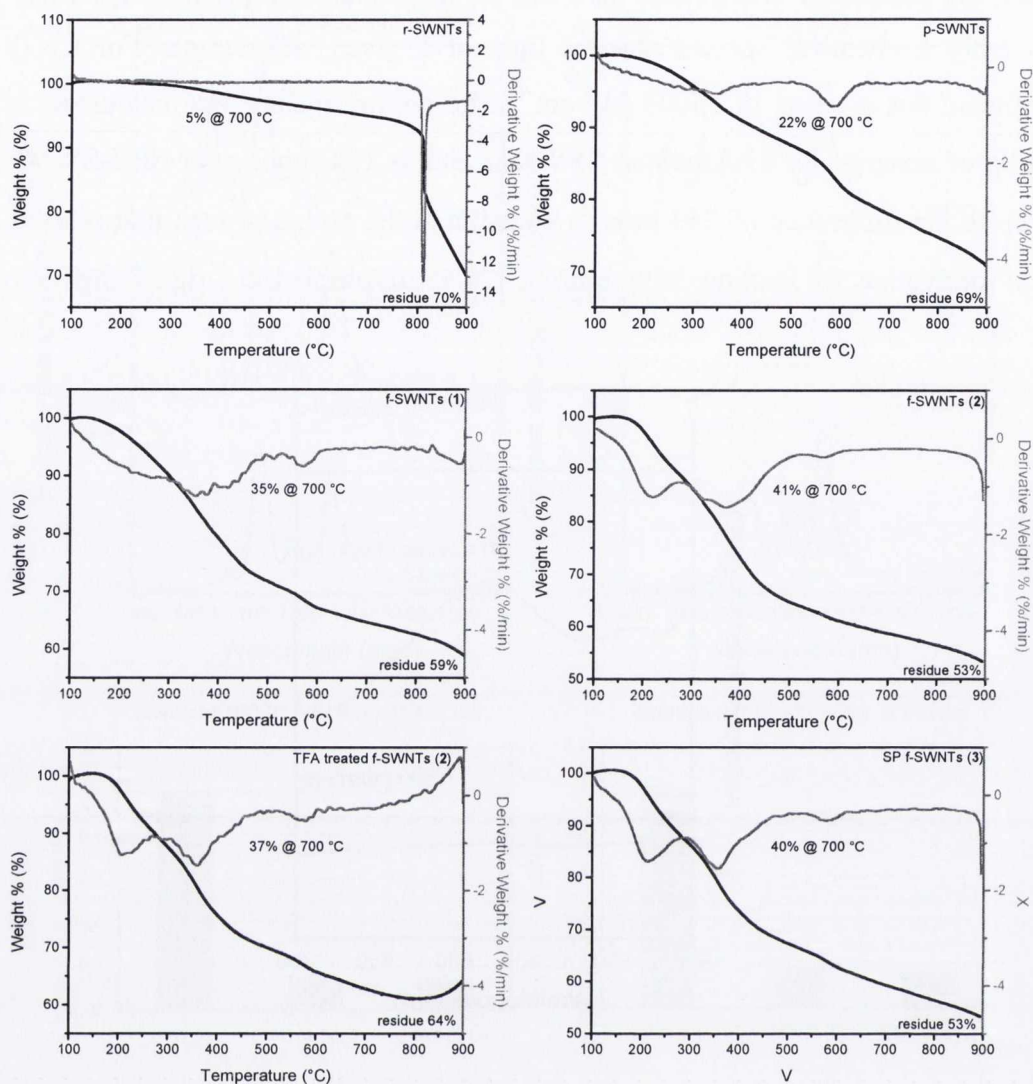


Figure 4.2a: TGA traces of r-SWNTs, p-SWNTs, f-SWNTs (1), f-SWNTs (2), TFA treated f-SWNTs (2) and SP f-SWNTs (3). The weight losses % at 700 °C attributed to the decomposition of organic groups in the nanotube samples are reported. All the experiments have been run in N₂ atmosphere with a temperature rate of 10 °C min⁻¹.

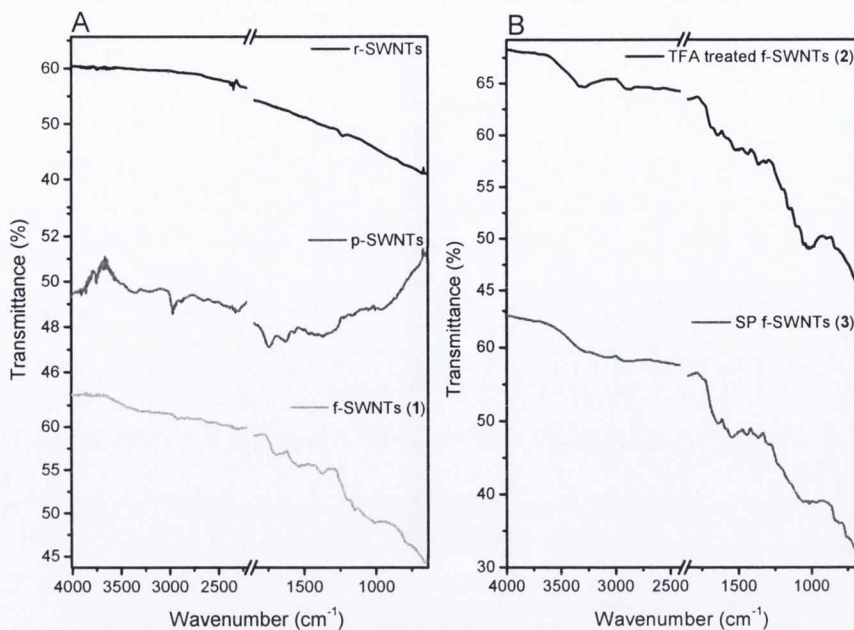


Figure 4.3a: ATR/FT-IR spectra of A] raw (r-SWNTs), purified (p-SWNTs) and Tour functionalized (f-SWNTs (1)), B] TFA treated and SP functionalized (SP f-SWNTs (3)) nanotubes.

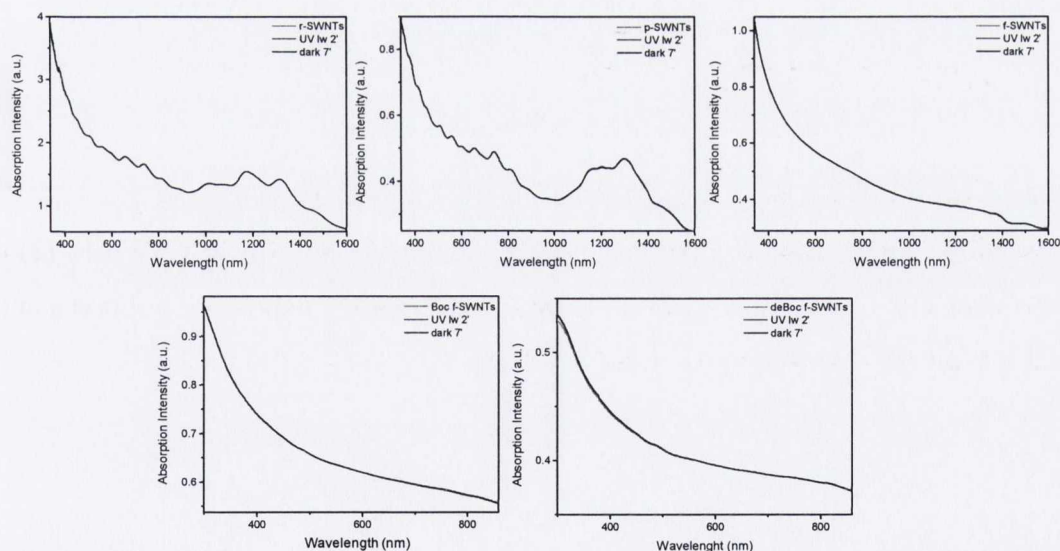


Figure 4.4a: UV-Vis absorption spectra of r-SWNTs, p-SWNTs, f-SWNTs (1), f-SWNTs (2) and TFA treated f-SWNT (2) after UV illumination for 2 min and storage in the dark for 7 min.

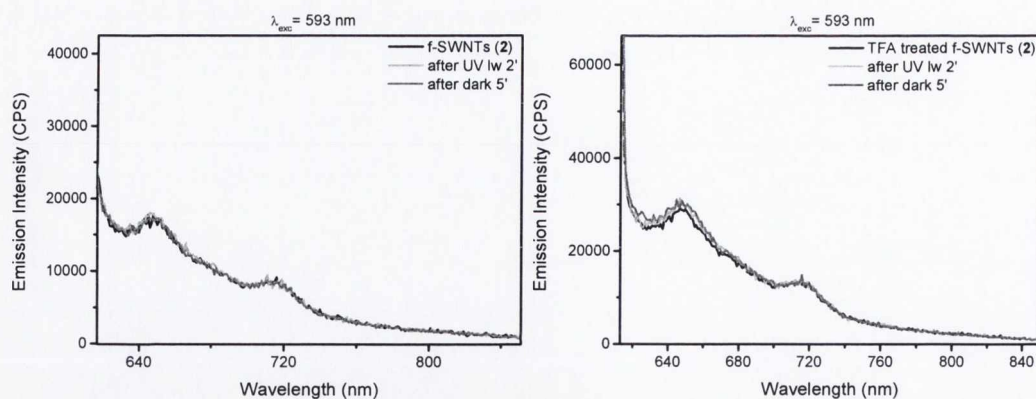


Figure 4.5a: Emission profiles ($\lambda_{\text{exc}} = 593 \text{ nm}$) of f-SWNTs (2) before and after removal of the Boc protecting group by TFA recorded after UV illumination for 2 min and storage in the dark for 5 min.

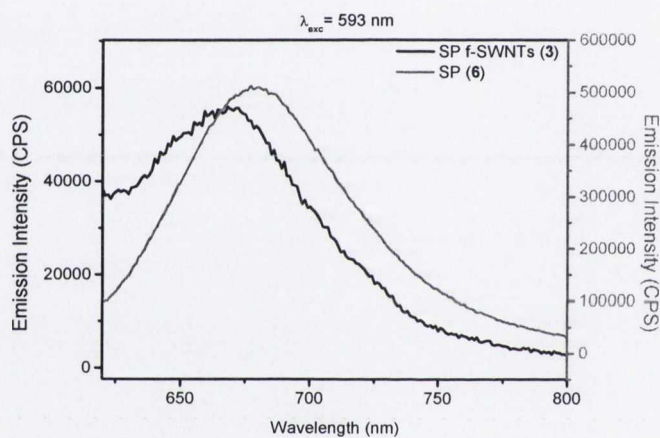


Figure 4.6a: Comparison of emission profiles ($\lambda_{\text{exc}} = 593 \text{ nm}$) of SP f-SWNTs (2) and SP (5) after UV illumination (365 nm) for 2 min in DMF. [SWNTs] = supernatant of initial 0.1 mg/mL, [SP] = 10^{-5} M .

7.2.1 ME-Zn complex formation

Sample preparation. SP (**6**) was dissolved in CD₃CN and added of 1 eq of a 0.1M D₂O solution of Zn(ClO₄)₂. It was subsequently illuminated with UV light (365 nm) for 2 min and left equilibrate overnight at room temperature in the dark before recording ¹H, ¹³C, H-H and C-H COSY NMR spectra.

Results

¹H-NMR (600 MHz, CD₃CN): 1.19 (t, 3H, *J*= 7.1 Hz, CH₃), 1.86 (s, 6H, CH₃), 2.24-2.28 (m, 2H, CH₂), 2.60 (t, 2H, *J*=6.7 Hz, CH₂CO), 3.91 (s, 3H, OCH₃), 4.11 (q, 2H, *J*=7.1 Hz and 14.3 Hz, CH₂), 4.52 (t, 2H, *J*=7.5 Hz), 7.63-7.79 (m, 6H, arom. and CH), 8.60 (d, 1H, *J*= 2.3 Hz, arom), 8.67 (d, 1H, *J*= 15.8 Hz, arom).

HRMS (*m/z* –MALDI-TOF): Found: 1067.2675 (M, C₅₀H₅₆N₄O₁₆ Cl Zn Requires: 1067.2671) [2SP+ Zn+ ClO₄⁻] Found: 615.0822 (M, C₂₅H₂₈N₂O₁₀ Cl Zn Requires: 615.0724) [SP+ Zn+ ClO₄⁻]. Spectrum is reported in Figure 4.7a.

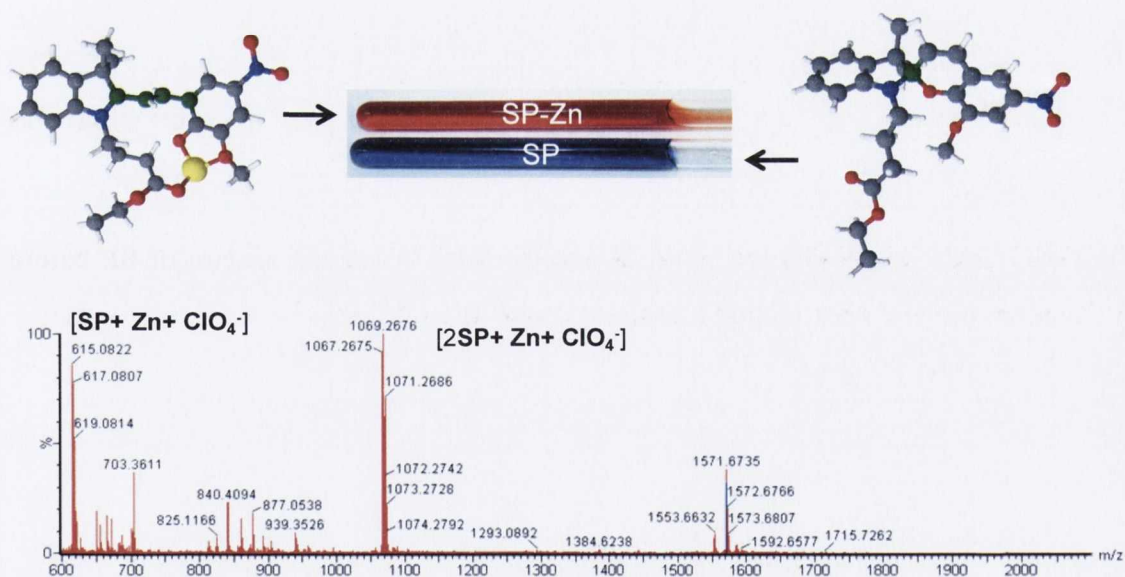


Figure 4.7a: Top] NMR tubes containing SP before and after the addition of zinc. Bottom] MALDI-TOF mass spectrum of **ME-Zn** complex in CD₃CN.

7.2.2 ME and ASA: no interaction

Sample preparation. SP (**6**) was dissolved in CD₃CN and added of 1 eq of ASA in CD₃CN. It was subsequently illuminated with UV light (365 nm) for 2 min and left equilibrate overnight at room temperature in the dark before recording ¹H and H-H NMR studies. After a two month time the same solution was again analyzed by ¹H-NMR.

Results

¹H-NMR (600 MHz, CD₃CN): δ = 1.16 (s, 3H, CH₃), 1.19 (t, 3H, J = 7.2 Hz, CH₃), 1.26 (s, 3H, CH₃), 1.84-1.86 (m, 1H, CH₂), 2.07-2.09 (m, 1H, CH₂), 2.28 (s, 3H, CH₃ ASA), 2.31-2.35 (m, 2H, CH₂CO), 3.17-3.32 (m, 2H, CH₂N), 3.79 (s, 3H, OCH₃), 4.06 (q, 2H, J = 7.1 Hz and 14.1 Hz, CH₂), 5.97 (d, 1H, J = 10.4 Hz, CH), 6.69 (d, 1H, J = 7.8 Hz, arom.), 6.87 (t, 1H, J = 7.2 Hz arom.), 7.02 (d, 1H, J = 10.4 Hz, CH), 7.14 (d, 1H, J = 6.7 Hz arom.), 7.19 (t, 1H, J = 7.0 Hz, arom.), 7.19 (d, 1H, J = 8.1 Hz, arom. ASA), 7.40 (m, 1H, arom. ASA), 7.66 (m, 1H, arom. ASA), 7.69 (d, 1H, J = 2.3 Hz, arom.), 7.80 (d, 1H, J = 2.6 Hz, arom.), 8.01 (m, 1H, arom. ASA), 9.56 (m, 1H, OH).

The signal at 9.56 ppm disappeared with the time, indicating deprotonation of ASA. However, no opening of the SP molecule and generation of protonated ME (MEH) was observed (Figure 4.8a).

The same result was confirmed by mass spectrometry where the spectra of SP before and after addition of ASA looked identical (Figure 4.9a).

HRMS (m/z -ES): Found: 453.2025 (M⁺, C₂₅H₂₈N₂O₆, Requires: 452.1947).

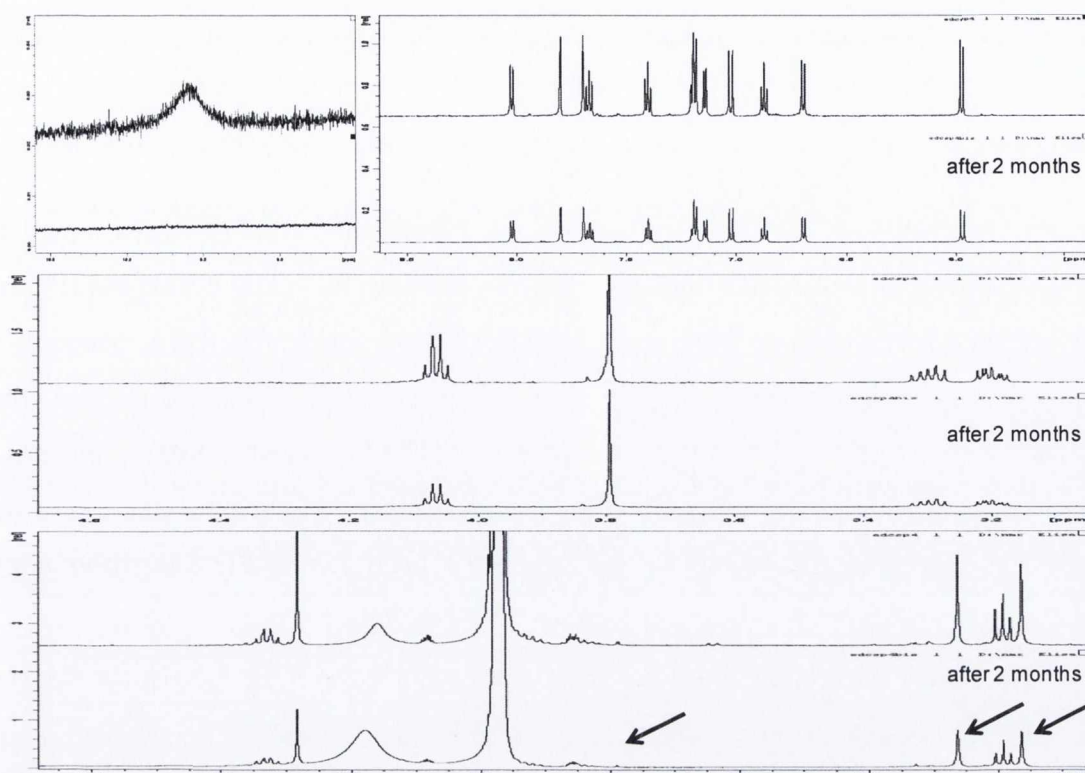


Figure 4.8a: $^1\text{H-NMR}$ partial spectra of a CD_3CN solution of SP (6) containing ASA after overnight (top spectra) and two month time (bottom spectra) storage in the dark. The arrows indicate the peaks that would have changed if an interaction between the two molecules occurred.

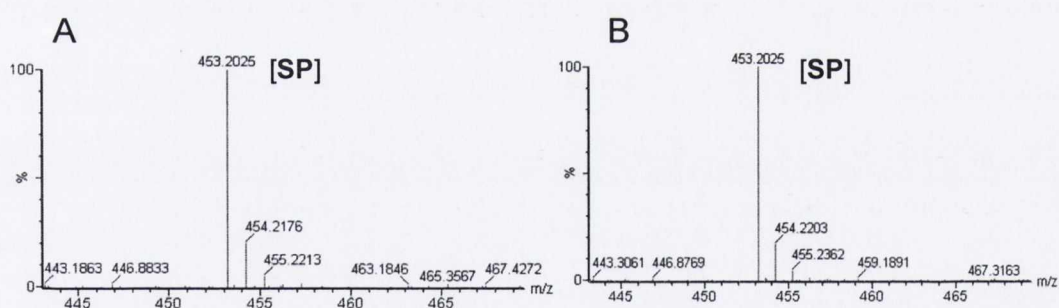


Figure 4.9a: ES mass spectra of SP (6) A] before and B] after the addition of 1 eq of ASA in CD_3CN .

7.2.3 ASA and Zn^{2+} metal ion complex formation

Sample preparation. ASA was dissolved in CD_3CN and added of 1 eq of a 0.1M D_2O solution of $\text{Zn}(\text{ClO}_4)_2$. It was subsequently illuminated with UV light (365 nm) for 2

min and left equilibrate at room temperature in the dark before recording NMR studies. In the present case UV light irradiation was used to reproduce all the experimental parameters.

Results. $^1\text{H-NMR}$ and HRMS looked significantly different to the spectra recorded in the absence of Zn^{2+} thus indicating interaction/chelation of the ion by the aspirin (Figure 4.10a). Three set of signals were recorded in $^1\text{H-NMR}$, suggesting the presence of 3 systems in solution in the ratio 1:0.5:0.3 that can be more likely assigned to ASA, Zn-ASA and $[\text{Zn-ASA}]_2$ respectively. Maldi TOF and $^{13}\text{C-NMR}$ spectra further confirmed the complexation of zinc by the NSAID. The exact stoichiometry and mechanism of the interaction between the metal ion and the ligand are currently under investigation in our lab.

$^1\text{H-NMR}$ aspirin (600 MHz, CD_3CN): $\delta = 2.28$ (s, 3H, CH_3), 7.19 (d, 1H, $J = 8.1$ Hz, H_a), 7.40 (m, 1H, H_c), 7.66 (m, 1H, H_b), 8.01 (m, 1H, H_d).

HRMS (m/z – MALDI-TOF): Found: 379.09 (M, $\text{C}_9\text{H}_{12}\text{ClO}_{10}\text{Zn}$ Requires: 379.05) [$\text{aspirin} + \text{Zn} + \text{ClO}_4^- + 2\text{H}_2\text{O}$]. Found: 663.18 (M, $\text{C}_{20}\text{H}_{23}\text{ClNO}_{14}\text{Zn}_2$ Requires: 663.93) [$2\text{aspirin} + 2\text{Zn} + \text{ClO}_4^- + 2\text{H}_2\text{O} + \text{CH}_3\text{CN}$].

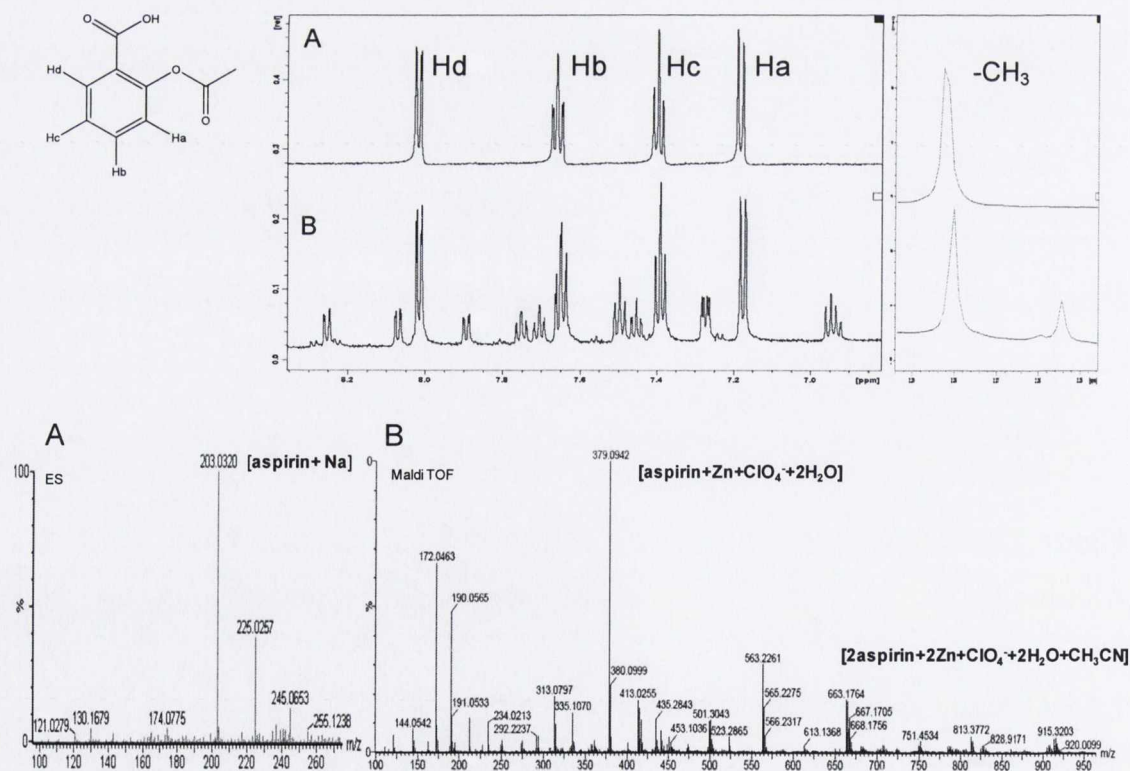


Figure 4.10a: $^1\text{H-NMR}$ partial spectra (top) and mass spectra (bottom) of a CD_3CN solution of ASA A] before and B] after the addition of 1 eq of $\text{Zn}(\text{ClO}_4)_2$ in D_2O .

7.2.4 ME-Zn-ASA complex formation

Sample preparation. . SP (6) was dissolved in CD₃CN and added of 1 eq of a 0.1M D₂O solution of Zn(ClO₄)₂. 1 eq of acetylsalicylic acid dissolved in CD₃CN was subsequently added, the solution was illuminated with UV light (365 nm) for 2 min and left equilibrate overnight at room temperature in the dark before recording ¹H, ¹³C, H-H and C-H COSY NMR spectra.

Results

HRMS (m/z –MALDI-TOF): Found: 1067.2698 (M, C₅₀H₅₆N₄O₁₆ Cl Zn Requires: 1067.2671) [2SP+ Zn+ ClO₄⁻] Found: 615.0724 (M, C₂₅H₂₈N₂O₁₀ Cl Zn Requires: 615.0724) [SP+ Zn+ ClO₄⁻] Found: 714.1575 (M, C₃₄H₃₆N₂O₁₀ Zn Requires: 714.1767) [SP+ Zn+ aspirin+H₂O] (Figure 4.11a).

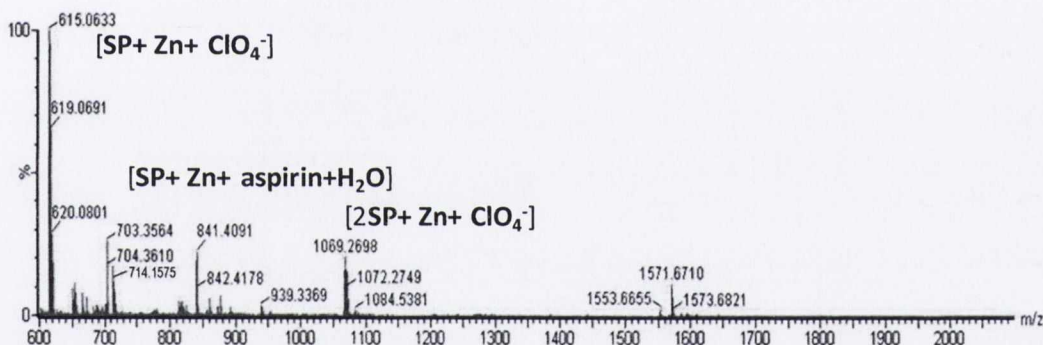


Figure 4.11a: MALDI-TOF mass spectrum of ME-Zn-ASA in CD₃CN.

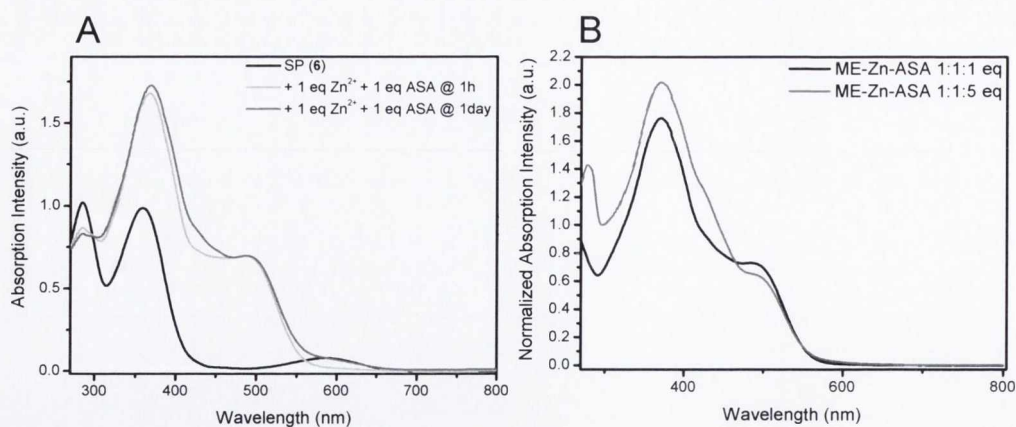


Figure 4.12a: Absorption spectra of 10^{-4} M SP (6) in CH_3CN after A] addition of Zn^{2+} and ASA in equimolar amounts recorded after 1 hour and 1 day, B] addition of Zn^{2+} and ASA in equimolar amounts and excess of ASA.

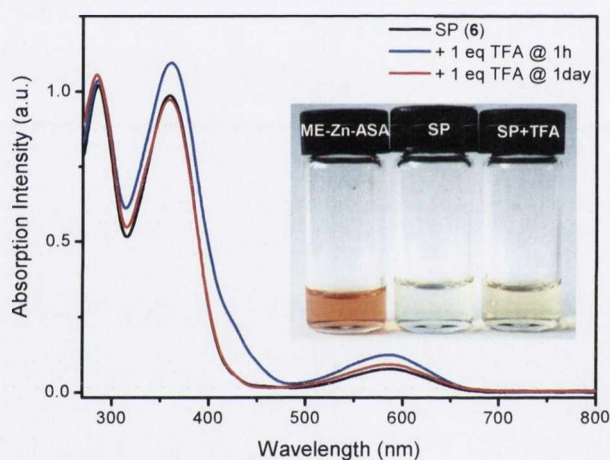


Figure 4.13a: Absorption spectra of 10^{-4} M SP (6) in CH_3CN recorded before and after the addition of 1 eq of trifluoroacetic acid (TFA) at 1 hour and 1 day. The absence of an increased absorption band at 430 nm following addition of TFA after 1 day, excluded its correlation to newly formed MEH. Inset] Pictures of SP (6) solution before and after the addition of Zn^{2+} /ASA and TFA. The different colours further confirmed the non similarity of the three SP samples.

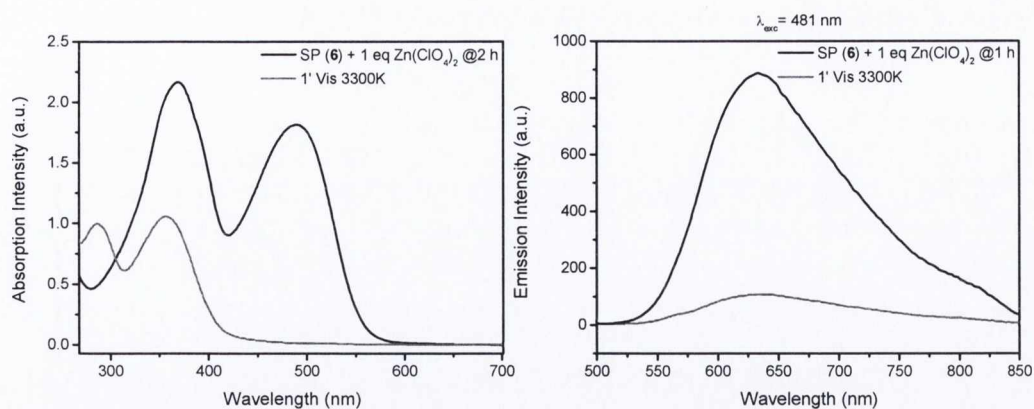


Figure 4.14a: Light modulation of the **ME-Zn** complex. Absorption and emission spectra of **ME-Zn** before and after Vis irradiation (3300K) for 1 min.

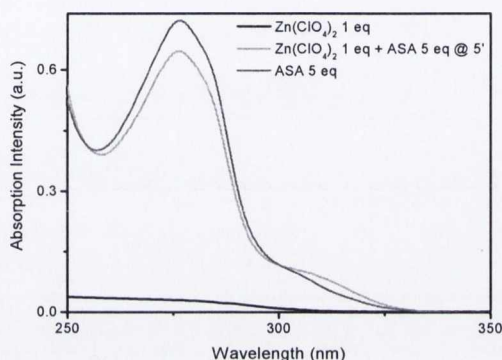


Figure 4.15a: Absorption spectra of CH_3CN solutions added of $\text{Zn}(\text{ClO}_4)_2$, ASA or the two together. The absorption shoulder at 310 nm suggests the complexation of zinc by the drug.

<i>Solvent</i>	<i>Without SWNTs</i>		<i>With SWNTs</i>	
	SP switch	Zn chelation	SP switch	Zn chelation
CH_3CN	√	√	X	X
DMF	√	X	√	X
MeOH	X	X	X	X
DBPS	√	X	X	X
DBPS/EtOH	√	X	X	X
$\text{CH}_3\text{CN}/\text{DMF}$ (9:1)	√	√ (but not reversible)	X	X

Table 4.1a: Solvents and mixtures of solvents tested for the solubilization and detection of performances of SP-based DDS anchored to SWNTs or in solution. Positive and negative results are schematized with √ or X respectively. DBPS: Dulbecco's phosphate buffered saline.

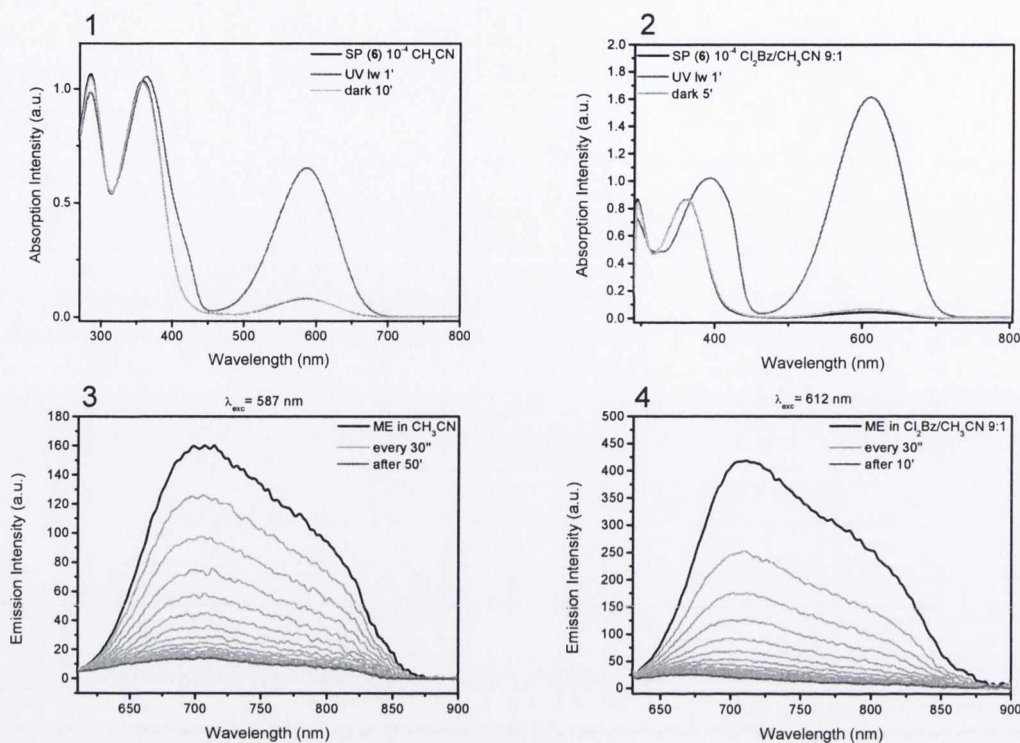
7.2.5 SP switchability and Zn²⁺ chelation in Cl₂Bz/CH₃CN 9:1

Figure 4.16a: Comparison of absorption and emission spectra of SP (6) dissolved in CH₃CN (1, 3) or Cl₂Bz/CH₃CN 9:1 (2, 4). 1,2] Absorption profiles of 10⁻⁴ M SP solutions before and after UV (356 nm) irradiation for 1 min, and after storage in the dark. 3,4] Fluorescence decay of 10⁻⁵ M SP solutions after irradiation with UV light (365 nm) for 1 min recorded at intervals of 30 sec.

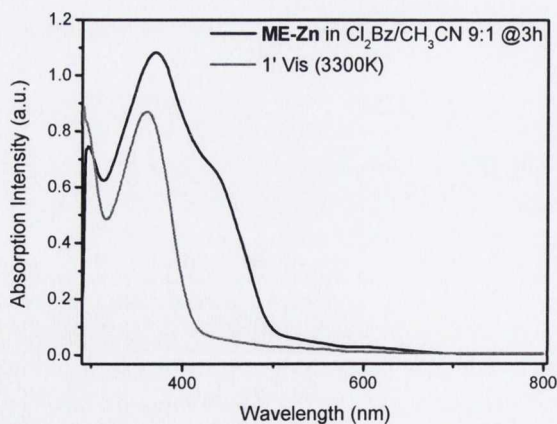


Figure 4.17a: Absorption spectra of ME-Zn in Cl₂Bz/CH₃CN 9:1 before and after irradiation with Vis light (3300K) for 1 min. The band at 440 nm disappeared indicating release of the metal ion and closure of the receptor to the SP isomer.

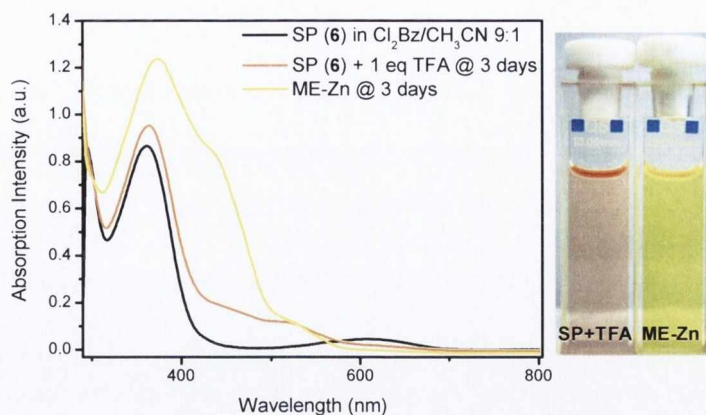


Figure 4.18a: Absorption spectra of a SP (**6**) solution (10^{-4} M, $\text{Cl}_2\text{Bz}/\text{CH}_3\text{CN}$ 9:1) before and after the addition of 1 eq of $\text{Zn}(\text{ClO}_4)_2$ (10^{-1} M, H_2O) and 1 eq of TFA. Pictures of the SP solutions after addition of the acid (SP+TFA) and the metal ion (ME-Zn) are reported on the right.

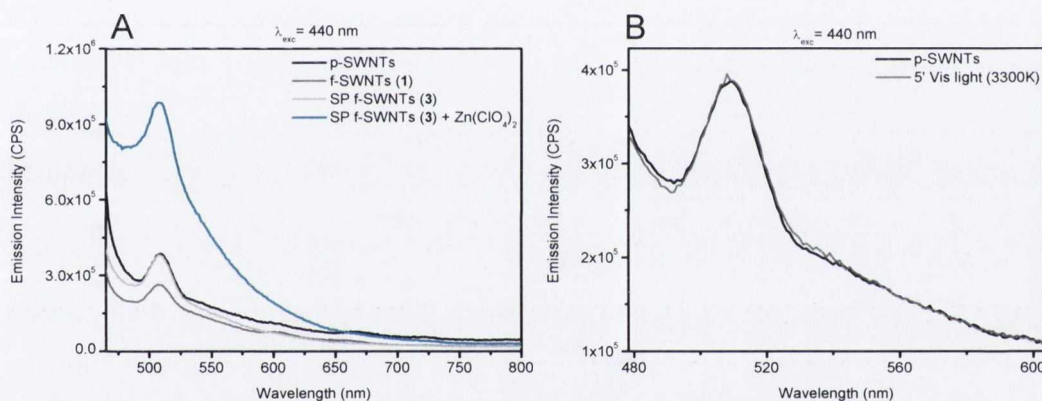


Figure 4.19a: Emission spectra ($\lambda_{\text{exc}} = 440$ nm) of A] p-SWNTs, f-SWNTs (**1**) and SP f-SWNTs (**3**) before and after the addition of $\text{Zn}(\text{ClO}_4)_2$ (10^{-1} M, H_2O , $1\ \mu\text{L}/\text{mL}$ of NTs), B] p-SWNTs before and after irradiation with Vis light (3300K) for 5 min. Spectra collected on the supernatant of initial $0.1\ \text{mg}/\text{mL}$ nanotubes in $\text{Cl}_2\text{Bz}/\text{CH}_3\text{CN}$ 9:1.

List of publications

- 1] Movia D., Del Canto E. and Giordani S. "Spectroscopy of single-walled carbon nanotubes in aqueous surfactant dispersion" *Phys. Stat. Sol. B* **2009**, 246, 2704-2707.
- 2] Del Canto E., Flavin K., Natali M., Perova T. and Giordani S. "Functionalization of single-walled carbon nanotubes with optically switchable spiropyrans" *Carbon*, **2010**, 48, 2815-2824.
- 3] Movia D., Del Canto E. and Giordani S. "Purified and Oxidized Single-Walled Carbon Nanotubes as robust near-IR fluorescent probes for molecular imaging" *J. Phys. Chem. C*, **2010**, 114, 18407-18413
- 4] Del Canto E., Flavin K., Movia D., Navio C., Bittencourt C. and Giordani S. "Critical Investigation of Defect Site Functionalization on Single-Walled Carbon Nanotubes" *Chem. Mater.*, **2011**, 23, 67-74.
- 5] Di Crescenzo A., Aschi M., Del Canto E., Giordani S., Demurtas D. and Fontana A. "Structural Modifications of Ionic Liquid Surfactants for improving the Capability to Disperse Single-Walled Carbon Nanotubes in Water: an Experimental and Theoretical Study" *Phys. Chem. Chem. Phys.*, **2011**, 13, 11373–11383.
- 6] Del Canto E., Flavin K., Movia D. and Giordani S. "Oxidized Single-Walled Carbon Nanotubes: removal of carbonaceous functionalized material by washing with solvents or base" *Proc. MRS Spring Meeting*, **2011**, ASAP.
- 7] Di Crescenzo A., Germani R., Del Canto E., Giordani S., Savelli G. and Fontana A. "Effect of surfactant structure on carbon nanotube sidewalls adsorption", *Eur. J. Org. Chem.*, **2011**, DOI: 10.1002/ejoc.201100720.
- 8] Flavin K., Kopf I., Del Canto E., Navio C., Bittencourt C. and Giordani S. "Controlled Carboxylic Acid Introduction: A Route to Highly Purified Oxidised Single-Walled Carbon Nanotube", *J. Mater. Chem*, **2011**, accepted.

Conference abstracts and presentations

- 1] Giordani S., Natali M., Del Canto E. and Perova T. "Functionalization of Carbon Nanotubes with Molecular Switches" ChemOnTubes 2008, Saragoza, Spain, 6-9 April 2008.
- 2] Giordani S., Del Canto E., Natali M. and Perova T. "Molecular switches on tubes" NT'08, 9th International Conference on the Science and Application of Nanotubes Tubes, Montpellier, France 29 June-4 July 2008 (Poster presentation).
- 3] Giordani S., Del Canto E. and Natali M. "Molecular switches on tubes" 236th ACS National Meeting, Philadelphia, 17-21 August 2008.
- 4] Del Canto E., Natali M., Perova T. and Giordani S. "Spiropyran Dye Molecules on Single Walled Carbon Nanotubes" Intel European Research and Innovation Conference 2008, Leixlip, 10-12 September 2008 (Poster presentation).
- 5] Del Canto E., Natali M., Perova T. and Giordani S. "Spiropyran Dye Molecules on Single Walled Carbon Nanotubes" AFM Forum and Workshop, University College Dublin (UCD), 20-21 November 2008 (Poster presentation).
- 6] Movia D., Del Canto E. and Giordani S., "Spectroscopy of Single-Walled Carbon Nanotubes in Aqueous Surfactant Dispersion" XXIIIrd International winterschool on electronic properties of novel materials 2009, Kirchberg/Tirol Austria, 7-14 March 2009.
- 7] Movia D., Del Canto E., Flavin K. and Giordani S., "Spectroscopic characterization of acid-treated single-walled carbon nanotubes" 61st Irish Universities Chemistry Colloquium DIT, 17-19 June 2009 Dublin.
- 8] Movia D., Del Canto E. and Giordani S. "Microscopy and Spectroscopic Characterization of Acid-Treated Single-Walled Carbon Nanotubes" Microscopical Society of Ireland 33rd Annual Symposium 26 – 28 August 2009 Astra Hall, Student Centre University College Dublin.
- 9] Del Canto E., Natali M., Perova T. and Giordani S., "Micro and Tip Enhanced Raman Spectroscopies on Spiropyran Functionalized Single Walled Carbon Nanotubes" Intel European Research and Innovation Conference 2009 Leixlip, 8-10 September 2009 (Poster presentation).

- 10] Prina-Mello A., Movia D., Del Canto E., Mohammed M.B., Tian F., Coey J.M.D., Volkov Y., Giordani S. "Investigation of functionalised SWNTs toxicity and biocompatibility by multiparametric high content screening analysis" Nanocarbon 2009, 8-11 September 2009, Italy.
- 11] Del Canto E., Flavin K., Natali M., Perova T. and Giordani S., "Synthesis and Characterization of Spiropyran Functionalized Single Walled Carbon Nanotubes" 2009 IRCSET Symposium "Innovation fuelling the Smart Society", RDS Ballsbridge Dublin, 25 September 2009.
- 12] Del Canto E., Flavin K., Natali M. and Giordani S. "Functionalization of single walled carbon nanotubes with optically switchable spiropyrans" 239th ACS National Meeting, San Francisco, 21-25 March 2010.
- 13] Giordani S., Del Canto E., Flavin K., Natali M. "Functionalization of Single Walled Carbon Nanotubes with Optically Switchable Spiropyrans", ChemOnTubes 2010, International Meeting on the Chemistry of Nanotubes and Graphene Arcachon, France, 11-15 April 2010.
- 14] Del Canto E., Flavin K., Movia D. and Giordani S. "A critical investigation into the purification and covalent functionalization of Single Walled Carbon Nanotubes", ChemOnTubes 2010, International Meeting on the Chemistry of Nanotubes and Graphene Arcachon, France, 11-15 April 2010 (Poster presentation).
- 15] Movia D., Del Canto E. And Giordani S. "NIR-Photoluminescence of Chemically Treated Single-Walled Carbon Nanotubes", ChemOn Tubes 2010, International Meeting on the Chemistry of Nanotubes and Graphene Arcachon, France, 11-15 April 2010.
- 16] Del Canto E. and Giordani S." Covalent functionalization and characterization of single walled carbon nanotubes", Dublin Chemistry Graduate Seminar Series, 26 May, UCD, Dublin (talk).
- 17] Del Canto E. and Giordani S." Covalent functionalization and characterization of single walled carbon nanotubes", SFI site review, 6 August, TCD, Dublin [Reviewers Prof. Colin Nuckolls, Prof. Michael Strano, Prof. Kari Rissanen] (talk).
- 18] Del Canto E., Flavin K., Movia D., Natali M. and Giordani S." Design, synthesis and characterization of Single Walled Carbon Nanotubes", Intel European Research and

Innovation Conference 2010, Intel Ireland Campus, Collinstown Industrial Park, Leixlip, 12-14 October 2010 (Poster presentation).

19] Giordani S., Del Canto E., Flavin K., and Natali M. “Functionalizing Nanotubes with Molecular Switches for Smart and Sensitive Devices”, Intel European Research and Innovation Conference 2010, Intel Ireland Campus, Collinstown Industrial Park, Leixlip, 12-14 October 2010.

20] Movia D., Del Canto E. And Giordani S. “NIR-Photoluminescence of Chemically Treated Single-Walled Carbon Nanotubes”, INSPIRE BioNano Postgraduate Research Workshop, Conway Institute, University College Dublin, Dublin, 20-21 October 2010.

21] Di Crescenzo A., Del Canto E., Pieraccini S., Masiero S., Spada G.P., Giordani S. and Fontana A. “Lipophilic Guanosine Derivatives as Carbon Nanotubes Dispersing Agents”, European-Winter School on Physical Organic Chemistry (E-WiSPOC), Bressanone 30 January-4 February 2011.

22] Del Canto E., Flavin K., Movia D. and Giordani S. “A critical investigation into the purification and covalent functionalization of Single Walled Carbon Nanotubes”, 2011 MRS Spring Meeting and Exhibit, San Francisco California, 25-29 April 2011.

23] Del Canto E., Movia D., and Giordani S. “Purified and oxidized single-walled carbon nanotubes: potential NIR fluorescent probes for molecular imaging” 2011 MRS Spring Meeting and Exhibit, San Francisco California, 25-29 April 2011.

24] Di Crescenzo A., Germani R., Del Canto E., Giordani S., Savelli G. and Fontana A. “Effect of Surfactant Structure in Carbon Nanotube Sidewalls Adsorption”, TUMA, Perugia, Italy, 30 June-1 July 2011.

25] Di Crescenzo A., Aschi M., Del Canto E., Giordani S. and Fontana A. “Structural modifications for improving the dispersibility of single-walled carbon nanotubes”, XXIV Congresso Nazionale della Societa' Chimica Italiana (National Congress of the Italian Chemical Society), Lecce, Italy, 11-16 September 2011.